Cubic Phase Templating of Mesoporous Platinum – Synthesis, Characterisation & Electrocatalytic Properties.

Afnan Qabil Alshammari

Thesis submitted for the degree of Doctor of Philosophy

Department of Chemistry

May 2024

University of Reading

Declaration

I confirm that this is my own work and the use of all material from other sources has been properly and fully acknowledged.

Afnan Qabil Alshammari

Abstract

The synthesis and application of mesoporous platinum materials with novel 3D cubic morphology and large pore spacing by utilising two amphiphilic molecules Brij® 58 and F127 as structure-directing agents was explored. Brij® 58 and F127, when mixed with water or hexacholorplatinic acid (HCPA), were found to form stable mesophases such as the face centred cubic (FCC), body centred cubic (BCC), hexagonal ($\mathrm{H_I}$), and lamellar ($\mathrm{L}_\propto$), according to small angle x-ray scattering (SAXS) and cross polarising light microscopy (CPLM) data. This versatility made these systems ideal for mesoporous platinum synthesis. Interestingly, mesoporous platinum nanoparticles, ranging from 23 to 57 nm, were fabricated through a polyol synthesis-like mechanism at 80 °C utilising Brij® 58/HCPA at concentrations ranging from 30 to 60 wt% with no additional reducing agent. Mesoporous platinum electrodes (MPEs) were created using FCC (40 wt% of Brij® 58) and BCC templates (30 wt% of Brij® 58 and 50 wt% of F127).

The FCC template from Brij® 58/HCPA was employed to create MPEs at various potentials. The electrodes exhibited interesting surface features and an internal 3D cubic morphology most likely to be a diamond structure with pore diameters varying from 3.0 to 3.5 nm and lattice parameters ranging from 6.3 to 7.1 nm. They also demonstrated high electrochemically active surface areas (ECSA) with values up to ~27.6 $\mathrm{m^2\ g^{-1}}$ and improved catalytic activity towards ethanol in acidic media. They illustrated high J_F/J_B ratios reaching a maximum of 1.19 and low onset potentials (E_{onset}) reaching a minimum of 0.35 V. Electrochemical impedance spectroscopy (EIS) emphasised small charge transfer resistance (R_{ct}) and large double layer capacitance (C_{dl}) values for the MPEs. All films also demonstrated good long-term stability.

The BCC template of Brij® 58/HCPA was utilised to fabricate the MPEs at different potentials. The electrodes revealed exciting surface morphology and an internal 3D cubic morphology most likely to be a primitive structure with pore diameters ranging from 3.0 to 3.5 nm, and lattice parameters between 6.4 and 6.8 nm. Films revealed high ECSA reaching up to a maximum of ~ 31.2 $\mathrm{m^2\,g^{-1}}$ for thin films and all films exhibited excellent catalytic activity towards ethanol oxidation. They demonstrated high J_F/J_B ratios reaching a maximum of 1.38 and low E_{onset} values reaching a minimum of 0.33 V. All films also exhibited excellent long-term stability.

The BCC template of F127/HCPA was used for electrodeposition of MPEs at various potentials. These MPEs revealed an internal 3D cubic morphology most likely to be a primitive structure with large pore diameters of between 7.8 and 8.2 nm and lattice parameters from 16.4 to 17.4 nm. Electrodes presented high ECSA ranging up to ~ 24.5 $\mathrm{m^2\ g^{-1}}$ and superior catalytic activity for ethanol oxidation as recognised by high J_F/J_B ratios increasing to a maximum of 1.05 and low E_{onset} values with a minimum of 0.37 V. EIS analysis highlighted good efficiency for ethanol oxidation, represented by low values of R_{ct} and large C_{dl} values. The electrodes also displayed good long-term stability.

All MPEs in this study demonstrated, high ECSA and excellent catalytic activity for ethanol oxidation as evidenced by high J_F/J_B ratios, low E_{onset} values and enhanced stability. This behaviour, coupled with the interesting external surface morphology and internal cubic mesoporosity, suggests the potential for further applications (batteries, capacitors and other types of electrocatalysis) of these materials.

Acknowledgements

First and foremost, I would like to praise Allah the Almighty, the Most Gracious and the Most Merciful for His blessings given to me during my study and in completing this thesis.

I would like to express my sincere gratitude and special appreciation to my supervisor, Dr Joanne Elliott, for her patient guidance, continuous support, and encouragement throughout this journey. Without her, this research would not have been possible.

I also want to express my immense gratefulness to my second supervisor, Dr Roger Bannett, for his advice and assistance. Additionally, I would like to thank Amanpreet Kaur for her help with atomic force microscopy and Nicholas Spenser for his assistance with X-ray diffraction.

To my friends in the Department of Chemistry, your friendship and shared joy brightened my PhD journey. Thank you so much for your support.

I am deeply thankful to all members of my family, particularly my parents. To my father, Qabil, thanks for your continuous support and for inspiring me with the invaluable lesson that nothing is impossible with perseverance. To my mother, Duhamah, I am profoundly indebted to your endless love and care. Your ceaseless prayers provided me with enduring motivation. A heartful and huge thanks to all my siblings for everything they have contributed.

I am incredibly grateful to my beloved husband, Dr Abdulrahman Alshammari, for his unwavering love, support, consistent encouragement, and constant belief in me, which have been continual sources of strength. I extend my exceptional thanks to my lovely daughter, Hoor, whom I love to the sun and back. Thank you for the love, happiness, and cheerful smiles you bring into our lives every day. You truly light up our world. My love for you is infinite.

Finally, I would like to take this opportunity to extend my sincere gratitude to the government of Saudi Arabia and Jouf University for the financial support and assistance in funding my PhD studies.

Table of Contents

Abbreviations	**Term**
A	Geometrical surface area
AE	Auger electrons
AFM	Atomic force microscopy
Ar	Relative atomic mass
BCC	Body centred cubic
$\text{BCC}_{\text{Brij® 58}}$	Brij® 58 with BCC structure template
BCC_{F127}	F127 with BCC structure template
BES	Backscattered electrons
C_{dl}	Double layer capacitance
CMC	Critical micelle concentration
CMT	Critical micellisation temperature
CoV	Coefficient of variation
CP	Cloud point
CPLM	Cross-polarising light microscopy
CPP	Critical packing parameter
CV	Cyclic voltammetry
ECSA	Electrochemical active surface area
EIS	Electrochemical impedance spectroscopy
E_{onset}	Onset potential
F	Faraday constant
FCC	Face centred cubic
$\text{FCC}_{\text{Brij® 58}}$	Brij® 58 with FCC structure template
F_{I}	Final current
HCPA	Hexachloroplatinic acid
$\mathrm{H_{I}}$	Hexagonal
$\mathrm{H_{II}}$	Inverse hexagonal
H_{upd}	Hydrogen underpotential
I	Current in mA
I_{B}	Current for backward oxidation peak
I_{F}	Current for forward oxidation peak
$\mathrm{I_{I}}$	Micellar cubic
$\mathrm{I_{II}}$	Inverse micellar cubic
J	Current density from the real area in mA cm^{-2}
J_{B}	Current density for backward peak
J_{F}	Current density for forward peak in mA cm^{-2}
$\mathrm{L}_{\propto}$	Lamellar
$\mathrm{L_{I}}$	Micellar solution
$\mathrm{L_{II}}$	Inverse micellar solution

LLC	Lyotropic liquid crystal
MPEs	Mesoporous platinum electrodes
MPE-n	Mesoporous platinum electrode (n = the deposition voltage)
MPE_n	Mesoporous platinum electrode (n = the deposition times)
M_{Pt}	Mass of platinum
Mr	Molecular weight
m_{Pt}	Moles of platinum
m_e	Moles of electron
Mpt	Melting point
n	Exponent term
σ	Charge density
Q	Constant phase element
Q_{dep}	Total deposition charge
Q_{HUP}	Charge associated with the hydride region
r	Micelle radius
RSA	Real surface area
R_{ct}	Charge transfer resistance
RF	Roughness factor
R_s	Solution resistance
SAXS	Small angle X-ray scattering
SEM	Scanning electron microscopy
SE	Secondary electrons
Stdev	Standard deviation
TEM	Transmission electron microscopy
w''_{max}	Frequency of maximum imaginary impedance Z''
x^2	Chi-squared
XRD	X-ray diffraction
Y_0	Pre-exponent term
Z_w	Warburg diffusion element

Chapter 1- Introduction

1.1 Overview

This thesis describes research undertaken to create mesoporous platinum with novel 3-dimensional (3D) cubic morphology and large pore spacing. It also describes work undertaken to investigate the catalytic properties of the high surface area platinum electrodes. This study exploits two types of amphiphilic molecules as structure-directing agents: Brij® 58 and Pluronic F127.

A primary aim of this thesis is to enrich the understanding of lyotropic liquid crystal (LLC) phase interactions with hexachloroplatinc acid (HCPA) and extend the range of novel cubic phases available for use as structure-directing agents to produce mesoporous platinum materials. A secondary aim of this thesis is to provide insightful knowledge of the surface morphology and internal structure of 3D cubic mesoporous platinum materials. A final aim of this thesis is to extend knowledge of the electrochemical properties of 3D cubic mesoporous platinum electrodes (MPEs).

This introductory chapter briefly introduces mesoporous platinum materials and their fabrication process. Also, a general overview is given regarding LLC, the role of critical packing parameters (CPP) in the interfacial curvature of molecular aggregations, and distinctions between type I and type II phases. Following this, an overview of the phase behaviour of Brij® 58 and F127 is presented based on the literature. Finally, a brief discussion of the applications of mesoporous platinum, such as ethanol oxidation, is provided.

1.2 Mesoporous materials

Over the previous years, porous materials have attracted considerable interest due to their unique properties such as high surface area, porosity and stability. The porous materials are divided into three classes according to the IUPAC convention; microporous (<2 nm), mesoporous (2–50 nm) and macroporous (>50 nm).[1,2] The mesoporous silica was first reported in 1990, and was produced by the reaction of a layered polysilicatekanemite with alkyl trimethylammonium cationic surfactants (C_n-TMA) with controlled pore sizes achieved by changing the C_n-TMA's alkyl number.[3] Since this discovery, advancements have been made in developing new mesoporous materials through improved mesostructured templating utilising poly (ethylene oxide) surfactant and block copolymer to produce mesoporous materials.[4,5] In 1997, Attard *et al*.[6] established a different organic structural templating method. Their method differs from the previous work and is based on the self-assembled liquid crystal template made from a high surfactant concentration (>30 wt% surfactant). This approach produces thin-film metals via the electrodeposition of metallic compounds dissolved in the aqueous lyotropic liquid phase. Various publications have since employed the procedure of LLC templating to create mesoporous films with repeat distances in the range of 3–10 nm of platinum[7–9], tin[10] and other metals. Nowadays, it is widely established that employing the soft templating approach produces porous materials featuring regular mesoporous structures with high surface areas.[11–13] Mesoporous metals have drawn considerable attention due to their metallic frameworks, including high surface area, ordered structure and narrow distribution of pore size.[12,14] Mesoporous metals offer various potential applications based on their high surface area and tunable pore size, such as electronic devices, biosensors, magnetic recording media, and metal catalysts.[12–17] The mesoporous structures allow easy access to the inner surface of materials and use micelles as templates where the size of the micelles can directly influence the size of the pores. Amongst mesoporous metals, mesoporous platinum is particularly interesting due to its highly catalytic and chemical stability.

1.2.1 Mesoporous platinum films

Mesoporous platinum materials have attracted interest due to their attractive properties for applications like chemical and biochemical sensors and catalytic applications, including the oxidation of ethanol and methanol in fuel cells.[17–19] Various studies have reported the deposition of platinum throughout the template approach of LLC reported by Attard *et al*.[6] The LLC is formed from the self-assembly of amphiphilic molecules and is discussed in section 1.3 in detail. Many studies have utilised the LLC templating approach to produce various nanostructures with nanochannels positioned in 2-dimensions (2D) such as hexagonal ($\mathrm{H_I}$) and complex 3D networks of nanochannel-like cubic structures. For example, mesoporous platinum with the 2D $\mathrm{H_I}$ structure was fabricated via the $\mathrm{H_I}$ structure of the LLC containing octaethyleneglycol monohexadecyl ether ($C_{16}EO_8$) and Brij® 56.[6,9,20] These mesoporous platinum films revealed pores with sizes of 1.8 to 4.0 nm and an electrochemical active surface area (ECSA) between 17 and 23 $m^2\ g^{-1}$. The diameter of the pores can be monitored by employing a longer or shorter chain surfactant, hydrocarbon additives or polymeric surfactants.[7] The $\mathrm{H_I}$ morphology of mesoporous platinum/ ruthenium alloy was also produced using Brij 76, which is polyoxyethylene (10) stearyl ether ($C_{18}EO_{10}$) as a structural directing agent. The fabricated mesoporous platinum/ ruthenium alloy showed a pore diameter of 3.7 nm and ECSA of 80 $m^2\ g^{-1}$.[21] These films exhibited good catalytic activity toward methanol oxidation and nonenzymatic glucose selectivity.[21,22]

It has been observed that the 3D nanostructure has some advantages compared to the 2D and 1D structures. For instance, it can overcome problems in the orientation and connectivity related to the 1D and 2D nanostructures. It also prevents pore blockage, increases mechanical stability and electrocatalytic performance, and facilitates charge transport and diffusion.[8] The fabrication of the 3D mesoporous platinum has been achieved using double gyroid mesoporous silica as a template.[23] Also, the direct electrochemical templating of the bicontinuous cubic phase shows the best choice for the fabrication of the 3D mesoporous platinum.[24] However, the constrained availability and increased viscosity of the cubic phases in the phase diagram have impeded direct electrochemical templating due to the high resistance to the flow of the cubic phases during the templating process. Akbar *et al*. have reported the facile route for producing 3D mesoporous platinum via the direct electrochemical templating of a thin layer of the double diamond phase of phytantriol.[24] The produced mesoporous platinum, which showed an ordered 3D network with high ECSA estimated to be > 40 $m^2\ g^{-1}$ with a pore size of 9 nm.[8] The applied deposition potential has significantly influenced the fabricated 3D mesoporous platinum morphology.[24] Recently, Akbar *et al*. developed the phytantriol templating method which showed the ability to control the nanoscale size of the metal by the addition of a cosurfactant (Brij® 56). This method reduces the lipid bilayer curvature by the presence of surfactants that swell the template lattice parameter.[25] This approach used Brij® 56 with different concentrations of 0, 7.5 and 20% showed the mesoporous platinum with lattice parameters 13.9, 15.2 and 19.9 nm have ECSA of 40, 27 and 23 $m^2\ g^{-1}$, respectively.[25] More recently, Akbar *et al*. reported the production of mesoporous platinum with a primitive structure via the chemical and electrochemical deposition of a phytantriol/ Brij® 56 template with a bicontinuous cubic phase (Im3m symmetry).[26] Mesoporous platinum films are typically characterised using X-ray scattering, electron microscopy, and electrochemical analysis.[25]

1.2.2 Porous platinum nanoparticles

Porous metal nanoparticles, particularly platinum nanoparticles, have attracted significant attention and have been extensively used due to their properties and wide range of catalytic applications.[27–32] Recent interests focus on controlling the size and shape of platinum nanoparticles to ensure high performance. The synthesis of dendritic and mesoporous morphology of platinum nanoparticles is highly favourable due to their high surface area, facilitating greater catalytic activity.[33]

In the fabrication process, surfactants are commonly added as stabilising and structure-directing agents for shape-controlling nanoparticles in colloidal and polyol synthesis.[34] Colloidal synthesis involves the reduction of platinum in the presence of appropriate reducing agents through heat treatment, UV light exposure, or even at room temperature in the subject of effective reducing agents.[35] The commonly used surfactants are polyvinylpyrrolidone (PVP)[36], cetyltrimethylammonium bromide (CTAB)[37], and non-ionic surfactants such as polyvinyl alcohol (PVA)[38], Pluronic F127[33,39] and Brij® 58[28,29,40,41] Notably, a recent review by Quinson and Jensen[35] highlighted the limited understanding of surfactant's role in the preparation of the platinum nanoparticles. Polyol synthesis utilises polyalcohol solvent as a reducing agent for metal reduction, often in the presence of some additives such as NaOH.[42] The shape of mesoporous platinum nanoparticles obtained through this method varies depending on the solvent utilised and the growth mechanism conditions. Moreover, temperature and pressure greatly affect the structure and size of platinum nanoparticles. [43] For instance, Yamauchi *et al*. observed a larger size of dendritic platinum nanoparticles produced at high temperatures using Brij®58 and l-ascorbic through a sonochemical method.[40] Generally, the polyol process utilises a high temperature above 100 °C to facilitate the production of nanoparticles.[43] The formation mechanism of mesoporous platinum nanoparticles commonly involves three steps: reduction, nucleation and growth.[35] The synthesised porous platinum particles are generally characterised using different techniques such as UV–Visible spectroscopy, energy-dispersive spectroscopy (EDS), scanning electron microscopy (SEM), transmission electron microscopy (TEM), atomic force microscopy (AFM), and others.[44]

1.2.3 Fabrication of platinum nanostructure materials

Hard and soft templates - Nanostructure metals are commonly prepared via templating methods, in which nanostructured materials replicate the structure of the used template. In the hard-templating approaches, the inorganic materials, such as silica, act as templates, and the metals are deposited in the sites between the inorganic materials. Following this, the template is removed by chemical etching to produce a reverse replica of the template. This approach was initially used for preparing mesoporous carbon by Ryoo's group[45], which reported the use of MCM-48 and SBA-15 silica templates.[45,46] Shin *et al.* extended the hard-template process to synthesising metallic systems and produced platinum nanowires using MCM-48 silica as a template, and the final structure was an inverse replica of the template.[47] In this project, the hard-template process is not preferred due to the multi-step process, and typically, the hard template requires removing chemicals that might cause undesirable remains of silica trapped within the mesoporous network.[48]

The soft-templating approach uses organic molecules, such as amphiphilic molecules, as templates to produce an ordered mesoporous structure, which is achieved after the removal of the template. The LLC phase acts as a structural directing agent in the soft template method. The schematic for the soft template approach is presented in Figure 1.1.

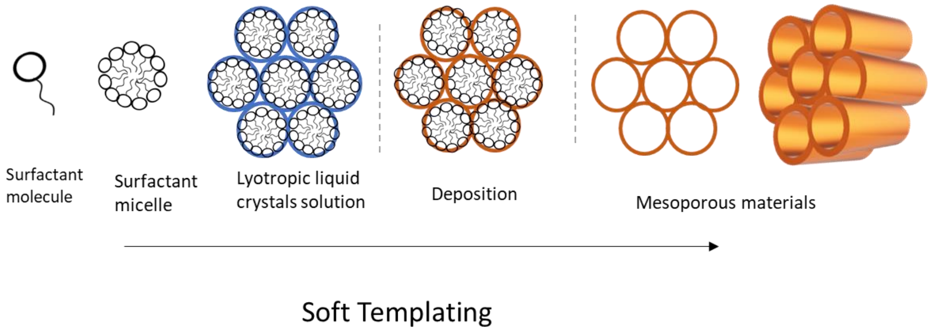

Figure 1.1 The synthetic procedure for the soft-template process to prepare metal-based nanomaterials was adapted from Yamauchi and Kuroda[16].

Figure 1.1 shows the soft templating process that started with the self-assembly of amphiphilic molecules driven by a combination of various intermolecular forces, including hydrophobic interactions, van der Waals forces, hydrogen bonding, and electrostatic interactions to produce a specific phase of LLC. Subsequently, metal deposition happens around the channels of different phases, as seen in the orange colour. After that, the template is easily removed due to the solubility of organic molecules, which demonstrates the straightforward removal process. Afterwards, the produced nanostructure metal could exhibit a replica structure for the template. The LLC phases can be changed by varying surfactant's alkyl chain length, and subsequently, the pore size.[49]

Reduction of platinum metal ions - The chemical or electrochemical reduction of metal salts is important for the preparation of nanostructured materials. The electrochemical process requires an external power supply for the reduction. In contrast, chemical reduction needs electrons that can be provided by a reducing agent.

The electrochemical reduction of platinum is normally carried out in an electrochemical cell containing two or three electrodes. The deposition of platinum metal is carried out in a highly conductive substrate with suitable potential. This approach is used to produce different nanostructures of metal. The commonly used platinum precursor is HCPA. The electrodeposition of platinum is complicated and might involve at least two redox processes.[7,50,51]

$$\mathbf{[PtCl_6]^{2-} + 2e^- \rightarrow [PtCl_4]^{2-} + 2Cl^-}$$

Equation 1.1

E° = 0.726 V vs NHE [7]

$$\mathbf{[PtCl_4]^{2-} + 2e^- \rightarrow Pt_{(s)} + 4Cl^-}$$

Equation 1.2

E° = 0.758 V vs NHE [7]

These reactions are irreversible two-electron reduction. The electrodeposition of platinum from HCPA has been widely used for the production of mesoporous platinum. This method creates different film thicknesses related to the amount of charge passed during the deposition. The quality of the nanostructure metals depends on the rate of the deposition.[52] The applied potential can control the rate of the deposition. Elliott *et al*. investigated the effect of the applied potential in the 2D structure of mesoporous films.[7] The exploration of electrodeposition at different potentials from +0.10 to -0.30 V vs SCE showed that a highly ordered structure was obtained at potentials greater than -0.10 V vs SCE while those deposited at -0.20 V vs SCE exhibited an irregular nanostructure. Deposition potentials less than -0.20 V vs SCE did not show any observable nanostructure due to the presence of unwanted side reactions at these potentials. Akbar *et al*. also reported similar results for depositing 3D mesoporous films. They exhibited that the deposition potential, whether lower or higher than the optimal value of -0.20 V, led to a deterioration of the structure for mesoporous platinum, resulting in a less ordered mesoporous structure with irregular pore sizes and decreased overall structural integrity.[24]

Another procedure for platinum reduction is the chemical process in the presence of a reducing agent. Commonly cited reducing agents are detailed in a review by Jin-Kim *et al*. [44], such as sodium borohydride ($NaBH_4$), potassium bitartrate ($KC_4H_5O_6$), methoxy polyethene glycol ($CH_3O(CH_2CH_2O)_nH$), dimethylamine borane (C_2H_7BN) and ascorbic acid ($C_6H_8O_6$).[44] The chemical reduction pathway of platinum typically goes through the reduction of $[PtCl_6]^{-2}$ to $[PtCl_4]^{-2}$ and then undergoes reduction to Pt(0).[35] Despite this general scheme, several studies observed the formation of some intermediate species before the production of Pt(0).[53] Consequently, the accurate nature of the reduction mechanism remains uncertain and varies among different systems.[35] The suitable reducing agent controls the deposition rate in the chemical process. Notably, when sodium borohydride is used as a reducing agent, it introduces disordered mesoporous materials due to multi-nucleation processes.[54] In contrast, the use of the dimethylamine borane as a reducing agent creates highly ordered mesoporous structures due to the slow metal deposition.[54]

1.3 Lyotropic Liquid crystals

The LLCs are formed by amphiphile molecules (i.e. surfactant or amphiphilic block copolymers) that can self-assemble to form various liquid crystal structures when mixed with a polar solvent, such as water. Amphiphilic molecules consist of two or more parts. One of those parts is soluble in water, known as the hydrophilic head, while the other is not soluble in water and is called the hydrophobic tail, and they are covalently linked. When the molecule dissolves in water, the hydrophilic part interacts favourably with water molecules, forming hydrogen bonds and increasing the entropy of the system. This interaction contributes to lowering the overall energy of the system. On the other hand, the hydrophobic part of the molecule tends to avoid contact with water, reducing the unfavourable interactions between the hydrophobic part and water molecules, further lowering the system's energy. Therefore, the overall energy of the system is reduced, leading to a decrease in surface tension. Subsequently, the surface concentration is saturated, and the micelles are self-assembled (as shown in Figure 1.2).[55]

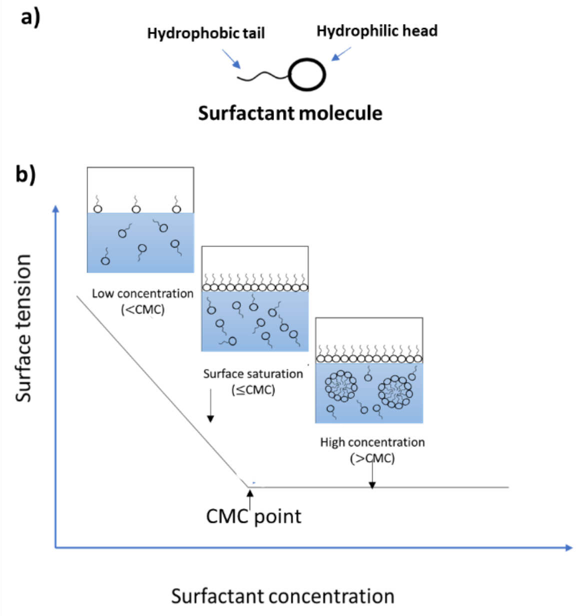

Figure 1.2 a) Surfactant molecule with the head and tail parts, b) surface tension of a surfactant solution with increasing concentration, and micelle formation. CMC means the critical micellar concentration.

The micelles are produced at a specific concentration known as critical micelle concentration (CMC). The hydrophilic part of the surfactant can be non-ionic, ionic or zwitterionic, whereas the tail part can be hydrocarbon or fluorocarbon.[56] Therefore, surfactants are classified into cationic, anionic and non-ionic depending on their charge.

Block copolymers have several advantages when compared to surfactants.[57,58] The morphology control is more flexible as the properties of block copolymers, such as compositions, molecular weights, and volume fraction, can be controlled to modify their packing parameters. Moreover, block copolymers with high molecular weight (Mr) can synthesise mesoporous materials with large pore sizes (10–60 nm) and thick pore walls, which are useful for some applications. Block copolymers are classified into anionic amphiphilic and cationic amphiphilic block copolymers. The LLCs form various phases depending on the molecular structure, temperature, and concentration of amphiphile molecules.

1.3.1 Critical Packing parameter

The CPP can determine the shape of the micelle. The CPP for amphiphilic molecules is calculated from the volume (v) taken by the hydrophobic group in the micellar core, the length of the hydrophobic groups in the core (l_c), and the area (a_0) taken by the hydrophilic group in the micelle solution, as highlighted by Israelachvili *et al*.[59]

$$CPP = \frac{v}{a_0 l_0} \qquad \text{Equation 1.3}$$

Quantifying the CPP gives the means to determine the packing behaviour of surfactant molecules. The CPP is a dimensionless number that relates the size and shape of surfactant molecules to the curvature of the interfaces they form. Therefore, the determination of the CPP enables the study of the interfacial curvature, which plays a crucial role in various phenomena, including micelle formation, vesicle formation, and emulsion stability. The CPP is influenced by several factors, including the size and shape of the surfactant head and tail groups.[60] For example, surfactants with a large head group compared to the tail group (resulting in a small CPP) tend to form micelles with a positive curvature, known as type I phases. On the other hand, surfactants with a small head group compared to the tail group (resulting in a large CPP) tend to form micelles with a negative curvature, known as type II phases.[61,62] The illustration schematic of CPP is presented in Figure 1.3. Additionally, the length of the hydrocarbon chain, the nature of the solvent, and the temperature can also affect the CPP.[63] Modifying the surfactant structure can alter the CPP and, consequently, the behaviour of the surfactant at interfaces. For instance, increasing the length of the hydrocarbon chain while keeping the head group constant can decrease the CPP, leading to changes in surfactant packing and micelle formation. The consequences of changing the surfactant shape or structure are significant. Changes in the head group size relative to the tail group can affect the curvature of the micelles formed. This, in turn, can impact the stability and properties of the surfactant micelle.

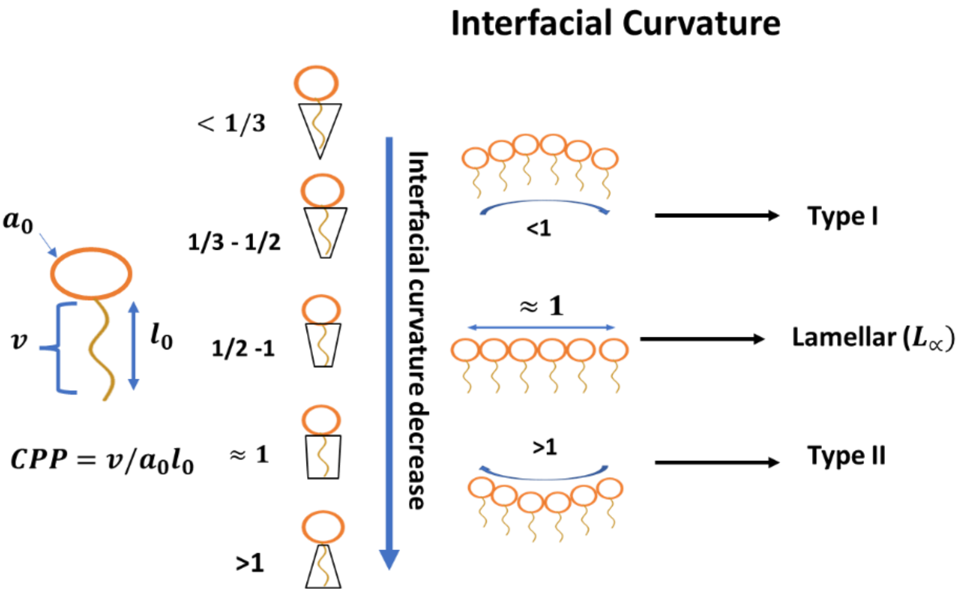

Figure 1.3 The self-assembled structure determined by packing parameters, adapted from Israelichvili et al. and M. Salim et al. [64–66]

1.3.2 Type I and Type II phases

Depending on the curvature's directions, the LLC can be classified into type I (normal phase) and type II (inverse phase). All the phases have some curvatures except the lamellar phase ($L_\propto$), which consists of a series of bilayer sheets, and the interface between water and amphiphile molecules is flat. The type I phase happens normally when the interface curves away from the water, such as in a micellar solution (L_I), micellar cubic (I_I), hexagonal (H_I) and bicontinuous cubic. In contrast, type II phases occur when the interface curves to the water, such as inverse micellar (L_{II}), inverse micellar cubic (I_{II}), inverse hexagonal (H_{II}), and inverse bicontinuous cubic. The schematics of the phases of type I and type II are shown in Figure 1.4.

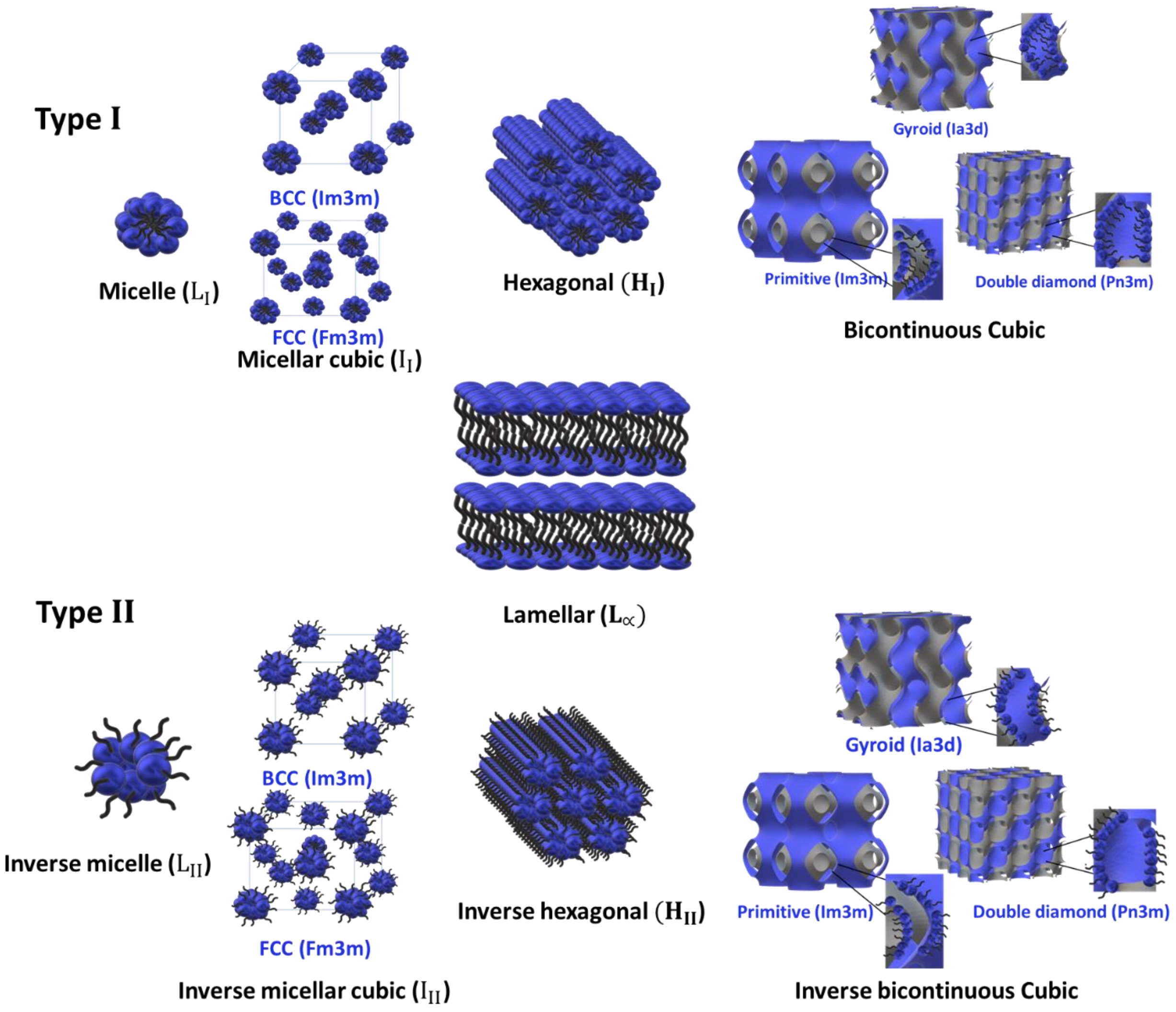

Figure 1.4 A normal and reverse types of self-assembled surfactant structures. The images were generated using MSLattice and FreeCAD software.

Figure 1.4 shows the phases of type I and type II of LLCs. Surfactant content leads to the structure transition. Cross-polarising light microscopy (CPLM) and small angle X-ray scattering (SAXS) are common techniques characterising the LLC structures.

The $\mathrm{I_I}$ phase - The $\mathrm{I_I}$ structure contains micelles organised in a cubic lattice structure known as discontinuous cubic. In micelles, the position of the hydrophilic head depends on surfactant's curvature and can be in the core or at the outer surface of micelles for $\mathrm{I_I}$ or $\mathrm{I_{II}}$, respectively. This structure has two kinds of cubic: body centred cubic (BCC) and face centred cubic (FCC). The cubic systems appear dark under CPLM because their isometric nature leads to the absence of birefringence, which is the ability to split light into colourful patterns. The distinction between the cubic phases can be achieved using the SAXS technique. From the SAXS analysis, the position of Bragg peaks can estimate the space group for each phase. The BCC has the space group of Im3m, while the FCC has the space group of Fm3m. It should be highlighted that the space group Im3m corresponds to three different phases: P-surface bi-continuous cubic and the BCC phases.[67]

The H_I phase - The H_I structure is built of cylindrical micelles that are closely packed and self-organised into a hexagonal lattice structure. Also, the hydrophilic head in the H_I structure depends on surfactant's curvature and can be in the core or outer surface of micelles for the H_I or H_{II} , respectively. The H_I phase under CPLM shows a birefringent texture. The separation between the channels can vary based on the proportion of surfactant to water.

The $L_\propto$ phase - The $L_\propto$ phase occurs under zero curvature. The hydrophilic head for the amphiphilic molecule is arranged towards the water, while the tail is far from the water. It also exhibits birefringent texture under CPLM.

Bicontinuous cubic - The bicontinuous cubic represents a complex subset within LLC. The bicontinuous cubic is an interesting phase but is uncommon in LLC structures. These structures exhibit unique continuous but nonintersecting nanochannels in both aqueous and non-aqueous domains, forming the complex structure.[68] These nanochannels are separated by a curved bicontinuous layer, which can be a hydrophilic head group or hydrophobic tail group that depends on the curvatures to produce the normal and inverse bicontinuous cubic structure. The X-ray crystallographic investigations present that there are three main types: primitive (space group Im3m), double-diamond lattice (space group Pn3m) and double-gyroid lattice (space group Ia3d).[67]

1.4 Liquid crystalline in this study

This study focuses on the utilisation of Brij® 58 and Pluronic F127 as a structural directing agent for the fabrication of mesoporous platinum materials. Brij® 58, known as polyoxyethylene (20) cetyl ether, is a non-ionic surfactant belonging to the Brij series. Brij® 58 consists of a hydrophilic head made of polyoxyethylene (PEO) and a hydrophobic tail formed of an alkyl chain. Pluronic F127 is a tri-block copolymer composed of the hydrophilic part, which is poly (ethylene oxide) (PEO) and the hydrophobic part, which is the poly (propylene oxide) (PPO) blocks.[69,70] These surfactants play crucial roles in various industries, and understanding their properties is essential.

1.4.1 Chemical / physical properties of Brij® 58 compared to Brij® 56

In this section, the Brij® 58 was compared to the Brij® 56 surfactant, another Brij family member commonly used to produce nanostructure metals. Both surfactants are composed of polyoxyethylene (PEO) and alkyl chin, but Brij® 56 has a smaller headgroup compared to Brij® 58. Therefore, Brij® 56 was selected for comparison. The structure of Brij® 58 and Brij® 56 is shown in Figure 1.5.

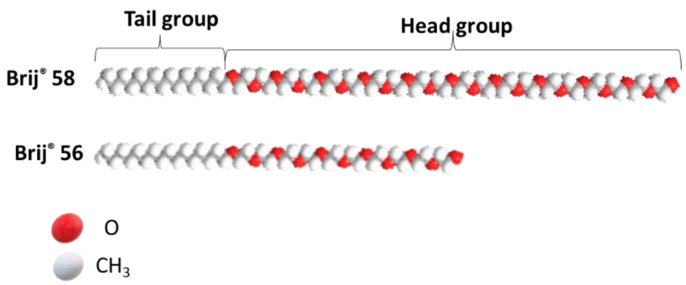

Figure 1.5 The structure of Brij® 58 ($C_{16}EO_{20}$) and Brij® 56 ($C_{16}EO_{10}$).

The main difference between Brij® 58 and Brij® 56 is the size of the hydrophilic head group, with Brij® 58 (n=20) being twice the size of Brij® 56 (n=10). Subsequently, the Mr and CMC are larger for Brij® 58 compared to Brij® 56, as shown in Table 1.1.

*Table 1.1 The properties of Brij 58 and Brij 56, presenting their respective molecular weights (Mr) , critical micelle concentrations (CMC), melting point (mpt) and micelle radius (r) (*estimated from the lattice parameter of the lamellar phase($L_\propto$) reported in Ref [71]).*

Surfactant	Mr / g mol^{-1}	CMC / wt%	mpt / ℃	r / nm	Ref
Brij® 58	1124	0.79	38	4.4	[72]
Brij® 56	683	0.24	32-34	2.8*	[71]

Table 1.1 shows that the radius for Brij® 58 micelle is 4 nm, while for Brij® 56, it was estimated to be 2.8 nm. In polar solutions, the micelles of Brij® 56 and Brij® 58 consist of a hydrophobic core and hydrophilic shell. As mentioned above, the CPP value decreases with the increase of the headgroup size, leading to an increase in the micelle size. Therefore, Brij® 58 has a larger micelle size compared to Brij® 56. Several studies have undertaken a comparative analysis of the Brij® 58 system and Brij® 56, focusing on various aspects. One such study by Ghosh investigated the reverse micelle sizes of Brij surfactants, including Brij® 58 and Brij® 56, in nonpolar solvents such as benzene and ethyl ammonium nitrate.[63] The results showed that as the ratio of the concentration of ethyl ammonium nitrate to surfactant concentration increased, the reverse micelle's size decreased. The Brij® 58 exhibited larger reverse micelles compared to Brij® 56 under these conditions.[63]

Moreover, Bhadane and Patil examined the cloud point (CP) of pure Brij® 56 and Brij® 58, both independently and in the presence of some additives.[73] The CP of a surfactant is the temperature at which it transitions from a homogenous solution to a two-phase system, resulting in a cloudy appearance caused by reduced solubility. Their findings reported that the CP for both Brij® 56 and Brij® 58 decreased with an increase in the concentration of surfactants as well as with an increase in the PEO head group due to an increase in micelle concentration.[73] Specifically, at a concentration of 0.5 wt%, the CP value of pure Brij® 56 and Brij® 58 were measured as 66.0 ℃ and 96.3 ℃, respectively. Increasing the concentration to

5 wt% changed the CP value to 58.6 ℃ and 91.7 ℃, for Brij® 56 and Brij® 58, respectively.[73] Both Brij® 58 and Brij® 56 are soluble in water and have been utilised due to their low toxicity and flexibility in forming stable colloidal systems.

In a comprehensive study of the Brij® 58 water system, Gibaud *et al*. found the transition from liquid at low concentrations $>$ 35 wt% to the formation of a transparent gel between 35 wt% and 70 wt% and a turbid gel above 80 wt%.[72] The Brij® 58 micelles, termed "hairy" micelles, consist of hydrocarbon cores covered with extended poly(ethylene oxide) (PEO) arms.[74] The hydrophilic shell thickness of Brij® 58 was reported to decrease from 2.66 nm at 5 wt% to 1.78 nm at 25 wt%, while the core radius increased from 1.70 nm at 5 wt% to 2.0 nm at 25 wt%, this was attributed to reduction in water quantity with increasing Brij® 58 concentration.[72] This led to a decrease in the distance between micelles from 7.6 nm at 5 wt% to 4.3 nm at 25 wt% of Brij® 58, revealing a closer arrangement at higher concentration.[72]

1.4.2 Phase behaviour of Brij® 58

The phase behaviour of Brij® 58 has been reported previously by Gibaud *et al*. and Mahanthappa *et al*.[72,74] An earlier study by Gibaud *et al*. demonstrated the phase behaviour of Brij® 58 in water over a wide range of concentration from 30 to 95 wt% at room temperature which exhibited various mesophase structures of FCC, BCC, $\mathrm{H_I}$ and $\mathrm{L_\propto}$ phases with the increase of Brij® 58 concentrations.[72] A subsequent study by Mahanthappa *et al.* reported the presence of a new phase Frank−Kasper (FK) A15 phase at 55 wt% Brij® 58, which transferred to BCC and then to $\mathrm{H_I}$ with the increase of the temperature.[74] The results also indicated that the rapid quenching of the $\mathrm{H_I}$ phase from 70 ℃ to 25 ℃ created the FK σ phase.[74] These results confirmed how the thermal process influences the self-assembly morphology. In general, many other factors can also affect the structure of the phase.

Examples include external factors such as pressure[75] and light[76,77], as well as the concentration of surfactants[78], the shape of the amphiphilic molecule[79] and the addition of chemical compounds, solvents and some additives.[80,81]

1.4.3 Chemical / physical properties of Pluronic F127

Pluronic F127 (F127) belongs to Pluronic copolymers with an approximate molecular formula of $(PEO)_{99}(PPO)_{69}(PEO)_{99}$, $(PEO)_{100}(PPO)_{70}(PEO)_{100}$ or $(PEO)_{106}(PPO)_{70}(PEO)_{106}$, and the Mr varies depending on the hydrophobic and hydrophilic parts, from about 12000 to 13400 g mol^{-1}.[55] F127 molecule is longer than the Brij® 56 and Brij® 58 with micelles of a diameter size of 20 ± 0.7 nm.[82] The chemical structure of F127 is shown in Figure 1.6.

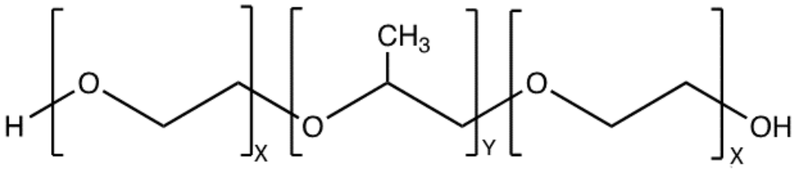

Figure 1.6 Chemical structures of Pluronic F127, X=99, 100 or 106 and Y=69 or 70.

Generally, Pluronic copolymers are uncharged and soluble in water at low temperatures (<15°C). F127 can form both isotropic and anisotropic liquid crystalline gels. The Pluronic copolymers' gel regions appear at concentrations higher than 20 wt% with a temperature higher than the critical micellisation temperature (CMT).[83] The gelation of F127 was reported by Wu *et al.* to be the lowest gelation concentration at room temperature compared to other Pluronic copolymers.[55] The gelation indicates the transition from a liquid to a gel state, where the material transforms into a semi-solid structure. For F127, the solutions at ≤ 5 ℃ with a concentration of 18 wt% to 30 wt% are freely flowing liquids, and the gel phase forms when the temperature increases to ≥ 20 ℃.[84]

The hydrophobic PPO groups for Pluronic micelles are located in the micellar core, and the hydrophilic PEO chains surround them.[84] Albano *et al*. reported that F127 is a linear triblock copolymer with two hydrophilic tails.[85] Therefore, the $L_\propto$ phase can be formed by an extended monolayer (S-shape) or a bilayer with the copolymer molecules directing their tails to the same water phase (U-shape), and this principle also applies to the micellar.[85] Thus, the aggregation behaviour of F127 is complicated, and the CMC depends strongly on the temperature compared to the low molecular weight surfactant. For example, Wu *et al*. and Wanka *et al*. indicated that the increase in temperature causes an increase in the PPO block's hydrophobicity and, consequently, causes micelle formation, which results in a decrease in the CMC.[55,86]

1.4.4 Phase behaviour of Pluronic F127

Several studies have reported the phase behaviour of F127-water mixtures.[87,88] Wanka *et al.*[87] reported the phase diagrams and aggregation behaviour for the Pluronic copolymers, including F127 with a molecular formula of $(PEO)_{106}(PPO)_{70}(PEO)_{106}$, using CPLM.[87] The results showed three major phase regions of isotropic, cubic and cubic + crystalline with a thin two-phase region at the interface between the isotropic and cubic phases. Besides, they expressed that the different samples of F127 displayed satisfactory reproducibility under small-angle neutron scattering (SANS) measurements compared to other Pluronic. In 2013, Jang *et al.* investigated the phase behaviour of F127 with a molecular formula of $(PEO)_{100}(PPO)_{70}(PEO)_{100}$, using SAXS, and reported that the phase transition of the F127 in water goes through isotropic, FCC, BCC, H_I, and $L_\propto$ phases as the concentration is increased.[88]

1.5 Catalytic applications of mesoporous platinum

Commercial bulk metals have been used mainly in energy conversion and storage, catalysis, sensing, adsorption and separation. However, the surface area and particle size could greatly affect such applications.[89] Therefore, mesoporous metals with features such as uniform pore sizes and high surface areas enhance their performance in supercapacitors, batteries and optical sensors compared to bulk metals.[90] The electrochemical sensors are the most popular sensors based on mesoporous metals due to their high conductivity, high surface area and chemical stability.[91]

Ethanol oxidations - The ethanol oxidation reaction and the methanol oxidation reaction were examined as potential fuel cells (for generating energy).[90,92,93] The fuel cells have attracted attention due to their high fuel conversion and electrical efficiency.[94] Commonly, there are two types of fuel cells, including methanol direct fuel cells (DMFC) and ethanol direct fuel cells (DEFC).[95] Direct ethanol fuel cells show more advantages over direct methanol fuel cells, including higher safety during transportation and storage, besides lower cost and easier handling for ethanol.[95] Also, ethanol oxidation is preferred over methanol due to having higher energy density in the complete oxidation to CO_2, which releases 12 electrons. However, the major challenge for ethanol oxidation is the various reaction paths that can occur. The oxidation of ethanol can be performed in both acidic and alkaline electrolytes.[96] In the acidic medium, platinum effectively serves as an electrocatalyst for ethanol oxidation. In the electrochemical reaction, water at the anode experiences consumption to produce CO_2, protons and electrons and is regenerated at the cathode by oxygen reduction. As time progresses, the ethanol concentration reduces at the anode, necessitating replacement, while the water content at the cathode requires replenishment or removal to prevent flooding and fuel cross-over issues.[95,96] In acidic media, the activity of platinum is the highest owing to fewer blockages in active sites and the dissolution of salts generated during the reaction.[95] The ethanol oxidation process cannot be completed in the catalyst with poor activity, and several byproducts are generated, such as acetaldehyde and acetic acid, which limits the transition of ethanol to CO_2.[97] Although several studies have reported the mechanisms of ethanol oxidation reaction, further research is still needed as it is a complicated multi-step reaction.[95,98,99] The products of the ethanol oxidation reaction are expected to encompass both the total oxidation product (CO_2) and the partial oxidation products, including acetaldehyde and acetic acid[99], as shown in Figure 1.7.

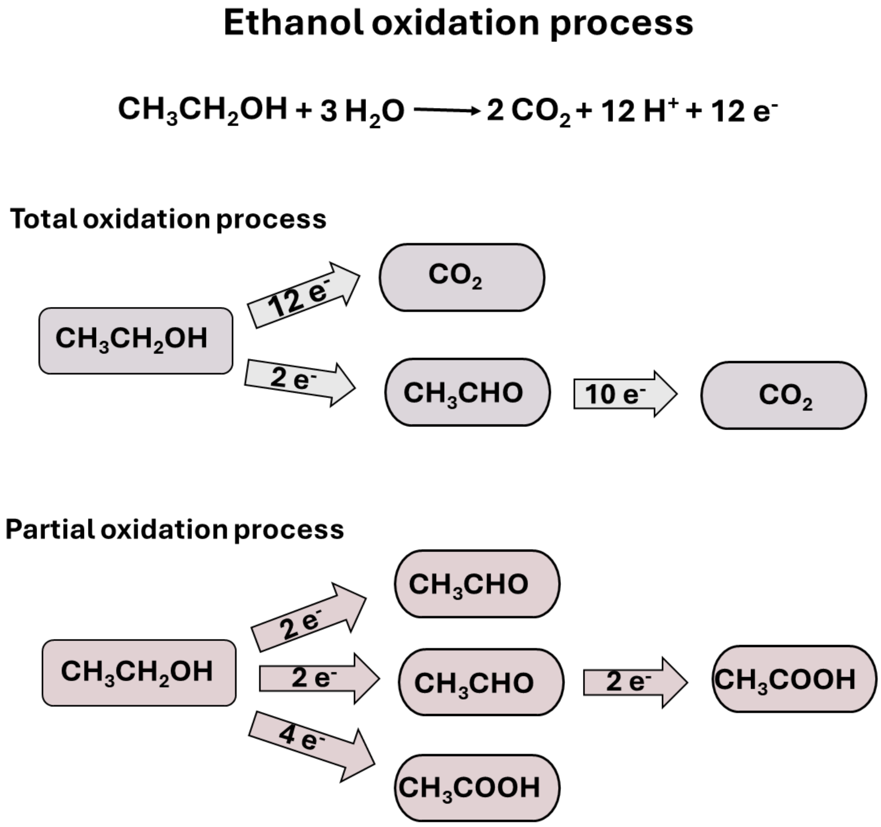

Figure 1.7 Diagram of the pathways during ethanol oxidation reaction in acid media adapted from Zheng et al. [97]

Figure 1.7 shows the total pathway describing the complete ethanol oxidation, which produces CO_2 that occurs by releasing 12 electrons.[99] However, the partial oxidation pathway reveals the formation of acetic acid and acetaldehyde that release 4 or 2 electrons, respectively. The reason for the partial oxidising of ethanol is the difficulty of breaking the C-C bonds, which reduces efficiency.

A recent review by Yaqoob *et al.* [95] discussed the ethanol oxidation mechanism on platinum surfaces in acid media. They emphasised two mechanisms that the reaction could go through. Firstly, they highlighted that a good agreement indicates acetic acid and acetaldehyde are the main products on the platinum surface in acid media. The C-C bond was reported to stay intact at a potential 0.60 V, yielding either 2 or 4 electrons, undergoing a splitting in the C-C bond with continuous oxidation following the readsorption of acetaldehyde and forming the CO_{ads} intermediate.[95,97] The presence of CO_{ads} restricts the adsorption of the reactants by blocking the active sites of platinum. Nevertheless, at potentials beyond 0.60 V, water oxidation prompts the formation of Pt–OH or Pt–O on the platinum surface, facilitating CO_{ads} oxidation to CO_2. Consequently, CO_2 is exclusively produced at higher potentials.[98] Secondly, they reported another mechanism on the platinum surface, which started with a reaction of the platinum metal with alcohol and the production of CO_2 accompanied by alcohol dehydrogenation. The alcohol dehydrogenation results in the formation of the intermediate Pt-OR. Then, platinum hydrolysis produces the intermediate Pt-OH with a proton and electron. After that, both intermediate Pt-OR and Pt-OH combine and regenerate platinum accompanied by CO_2, a proton and electron, and ethanol oxidise entirely.

The intermediates, such as CO_{ads} and acetaldehyde, formed during the ethanol oxidation reaction cause the poisoning at the surface of a platinum catalyst.[100] Subsequently, this poisoning effect on the surface leads to a sluggish kinetic reaction and weak overall performance.[97] Therefore, there have been numerous endeavours to develop electrocatalysts of platinum with enhanced activity and durability. For ethanol oxidation, the catalytic activity and durability play important roles in shaping the efficiency and longevity of the catalytic process. The catalytic activity measures the rate at which ethanol is converted to its oxidised derivatives and their efficiently at low potential.[95,97] This can be indicated by the high current of the oxidation peak, the low onset potential (E_{onset}) reflecting the initial oxidation of ethanol and the increase in the ratio of the forward peak to the backward peak, which replicates its tendency to oxidise the CO more efficiently.

The review by Yaqoob *et al*. displays a valuable contribution, providing comprehensive and significant insight into the electrochemical data of platinum catalysts employed for ethanol oxidation under various conditions, including efforts to develop binary or ternary platinum-based catalysts or control the microstructure of platinum catalysts.[95] The electrocatalytic activity of the nanostructured platinum materials is affected by their shape, size [101], and morphology.[102,103] Therefore, the controlled microstructure of platinum catalysts leads to the increase of the ECSA and the active sites, which show excellent catalytic activity due to the efficient movement of reactants.[104] Mesoporous metals have the advantage of supporting better performances of the alcohol oxidation reactions, such as a high ECSA for the mesoporous structure that facilitates a fast proton and electron pathway in the electrochemical reaction.[105]

1.6 Work overview

The structure of this thesis is as follows:

Chapter 2 presents an overview of the methods and techniques used in this work for the analytical investigations.

Chapter 3 studies the phase behaviour of Brij® 56 and Brij® 58 in water at different compositions using SAXS and CPLM. Moreover, it investigates the effect of the presence of

HCPA on the phase behaviour of Brij® 58 at different compositions as well. It also describes the chemical reactivity of Brij® 58 ($\geq$ 30 wt%) in aqueous HCPA at high temperatures and the subsequent formation of mesoporous platinum nanoparticles.

Chapter 4 illustrates the electrochemical production of the 3D mesoporous platinum using Brij® 58 based FCC phases at different potentials. The morphological characterisation uses SEM, TEM, AFM and XRD techniques. The surface area of produced mesoporous platinum is estimated, and the catalytic activity towards ethanol oxidation is also investigated.

Chapter 5 investigates the electrochemical fabrication of the 3D mesoporous platinum using Brij® 58 based BCC phase at different deposition potentials and fixed time. Moreover, it examines their morphology, surface area and the catalytic activity towards ethanol oxidation. It also explores the electrodeposition of platinum at different deposition times and fixed potential. It then investigates their morphology, surface area and the catalytic activity towards ethanol oxidation.

Chapter 6 describes the phase behaviour of F127 in water and HCPA. It also explores the utilisation of the BCC phase of F127 as a template for the electrochemical fabrication of 3D mesoporous platinum. Furthermore, it investigates their structure, surface area and catalytic activity towards ethanol oxidation.

Finally, a summary of conclusions and some of the future works are provided.

Chapter 2- Techniques and methods

2.1 Overview

All the analytical techniques used in this work are illustrated in this chapter. A brief description of the theoretical background of the analytical techniques is reported. The techniques used throughout this examination are cyclic voltammetry (CV), potential step, electrochemical impedance spectroscopy (EIS), CPLM, SAXS, X-ray diffraction (XRD), electron microscopy (SEM and TEM), and atomic force microscopy (AFM).

2.2 Chemicals and materials

All of the compounds were used as received. Brij® 56 (Polyoxyethylene 10 cetyl ether, $C_{16}EO_{10}$), Brij® 58 (Polyoxyethylene 20 cetyl ether, $C_{16}EO_{20}$) and Pluronic F127 (poly(ethylene oxide)$_{100}$-poly(propylene oxide)$_{70}$-poly(ethylene oxide)$_{100}$, PEO_{100}-PPO_{70}-PEO_{100}) were purchased from Aldrich and were used as surfactant templates. Hexachloroplatinic acid (HCPA) (H_2PtCl_6) solution (8 wt % in water) was purchased from Aldrich and was used as the electrolyte for platinum fabrication. Ultra-pure deionised water was also used for solution preparations and general cleaning (18.2 MΩ cm at 25 °C). Decon 90 was purchased from Fisher Scientific and used to clean all glassware by soaking in 2 vol% solution for at least 3 hours, followed by rinsing with ultra-pure deionised water. 0.5 M aqueous sulfuric acid (H_2SO_4) solution was prepared from p.a-grade concentrated acid from various sources such as Merck and used as an electrolyte. Ethanol (C_2H_5OH) (99.8%) was purchased from Aldrich and used to prepare 0.5 M ethanol with 0.5 M sulfuric acid as an electrolyte. Alumina in two grades, 1.0 and 0.3 µm, and polishing pads (microcloth PSA) were purchased from Fisher Scientific for electrode cleaning.

Platinum disc electrodes (2 mm diameter) were purchased from IJ Cambria Scientific Ltd and used for the majority of electrochemical studies. Platinum foils (0.25 mm thickness) were purchased from Goodfellow and used as additional substrates for platinum electrodeposition. An Ag/AgCl reference electrode was purchased from IJ Cambria Scientific Ltd in 1 M KCl and used for all electrochemical studies. A platinum flag and platinum gauze were used as counter electrodes.

2.3 Equipment

A digital mini scale with high precision (50 g / 0.001 g) was used for weighing samples. A mini dry bath was purchased from Appleton and used for heating samples. Mini Centrifuge 100-240 V, 50/60 Hz, was purchased from Fisher brand and used for mixing samples. Capped glass vials and reliable microcentrifuge tubes that were sealed even with prolonged boiling (1.5mL) were purchased from Fisher brand and used to prepare samples. Three types of potentiostat were used: Autolab was used with the Nova software for most of the electrochemical studies, PalmSens3 was used for the electrodeposition of platinum, and PalmSens4 with PSTrace software was used for the impedance studies. Polarised light microscopy Axioskop 40 was provided with a Linkam TMS90 heating/cooling stage to control the temperature, and a Canon camera was used to collect some images of the phase behaviour of the mixtures. Microscope slides and cover slips from various sources, such as AmScope, were used for the sample loading in CLPM. The small-angle X-ray Bruker Nanostar AXS with Cu K alpha (45 kV, 650 mA) source was also used to investigate the phase behaviour of the LLC and the structure of mesoporous platinum. The X-ray diffraction Bruker D8 ADVANCE X-ray diffractometer was used to study the mesoporous platinum foils. Scanning electron microscope FEI Quanta FEG 600 equipped with a Quorum PP2000T Cryo rotating stage was used to study the surface morphology of the electrodes. Transmission electron microscope JEOL JEM-2100Plus LaB6 equipped with AMT XR401 digital camera with Engine Software was used to explore the structure of mesoporous platinum. Carbon film 300 mesh was purchased from Sigma-Aldrich. Atomic force microscope Cypher from Oxford Instruments was also used to study surface morphology.

2.4 Preparation of liquid crystalline mixtures

Samples of different wt % compositions of Brij® 56, Brij® 58 and F127 were prepared. The samples were prepared by weighing an appropriate amount of surfactant and ultra-pure deionised water or 0.195 M HCPA solution in plastic vials. The mixtures were mixed manually or centrifuged until the samples became homogeneous, as indicated by looking at them under CPLM. The precise conditions and amount of surfactants are detailed in the relevant chapters.

2.5 Background to techniques

2.5.1 Electroanalytical techniques

The electroanalytical techniques used in this study are CV, potential step and EIS. Before all electrochemical experiments, the platinum disc working electrodes were polished with alumina in two grades (1.0 and 0.3 µm) using a polishing pad until the surface was as shiny as a mirror. In contrast, the platinum foils were cleaned by flaming them for a few seconds before the electrodeposition. For the electroanalytical investigation, a typical electrochemical cell was prepared that consists of a potentiostat which controls the electroanalytical process, the three electrodes and the electrolyte solution. The three-electrode system is preferred for its accuracy and ability to control experimental conditions effectively. A schematic of the three electrodes of an electrochemical cell is shown in Figure 2.1.

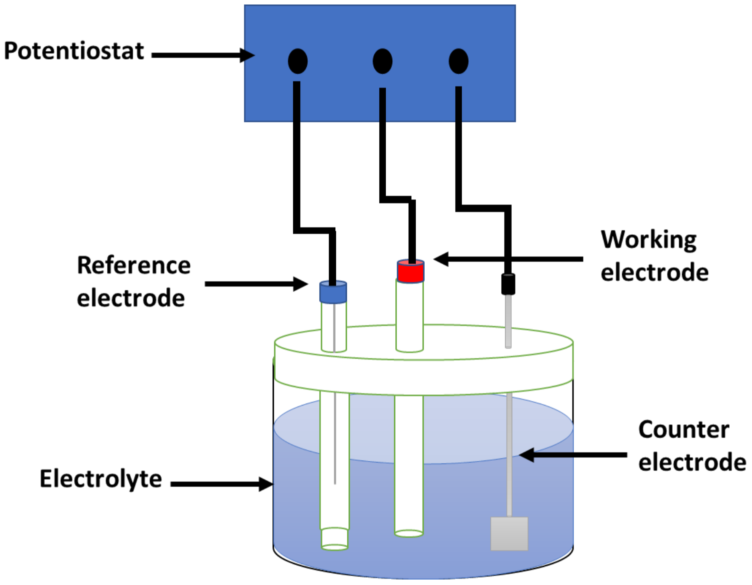

Figure 2.1 Three-electrode electrochemical cell.

In this typical cell, the platinum disc electrode or platinum foil is used as a working electrode. Ag/AgCl was used as a reference electrode, and the platinum flag was used as a counter electrode. The electrolyte varied depending on different systems and measurements. For instance, 0.5 M H_2SO_4 electrolyte was used in CV to clean the electrodes and study the surface area of the electrodes.

2.5.1.1 Potential step

The electrochemical fabrication of nanostructure platinum was carried out at room temperature by potential step deposition of the LLC template. The mesoporous platinum films were deposited at the platinum disc electrode (with an area of 3.142 x 10^{-2} cm^2) and platinum foil (with an area of ~ 0.2 - 0.5 cm^2). Electrodeposition was carried out using different templates and variable conditions as specified in the relevant chapters.

The potential was applied to the working electrode, which instantly transitions from one value (E1) to another more negative value (E2). These values were chosen based on the previous paper of platinum deposition.[7] The current is measured as a function of time. At the E1 value, platinum reduction is unfavourable; at the E2, platinum species become close to the surface and then reduced. The reduction of platinum occurs at E2. As a result, the platinum species flows toward the electrode surface and is followed by a reduction to solid platinum. The potential step records are current with respect to time, and their integration produces the total deposition charge (Q_{dep}). Q_{dep} is then used to calculate ECSA, as shown later. When time passes, the Q_{dep} increases and the thickness of the deposited platinum increases according to Faraday's law.[106]

After the fabrication, the platinum disc and foil electrodes were removed from the templating cell and soaked in ultra-pure deionised water, which was replaced after one hour; this process was repeated several times. The platinum disc electrodes and foils were stored in ultra-pure deionised water at room temperature. Further cleaning of the platinum disc electrodes was carried out using CV and scanned five times in 0.5 M H_2SO_4 at 100 mV s^{-1} between potential limits of +1.2 and -0.30 V vs. Ag/AgCl. The gradual formation and elimination of oxide/hydride layers effectively clean the impurities on the electrode surface.

2.5.1.2 Cyclic voltammetry

CV is the most common electrochemical technique that is generally involved in considering molecular species' reduction and oxidation processes. This technique is used to determine the active surface area of the mesoporous materials. The CVs data are represented according to the IUPAC principle, where the positive values indicate the oxidation (anodic) currents.[107] In CV, the x-axis shows the applied potential, while the y-axis exhibits the resulting current. The typical CV for the platinum electrodes in 0.5 M H_2SO_4 at room temperature at a scan rate of 50 mV s^{-1} is shown in Figure 2.2.

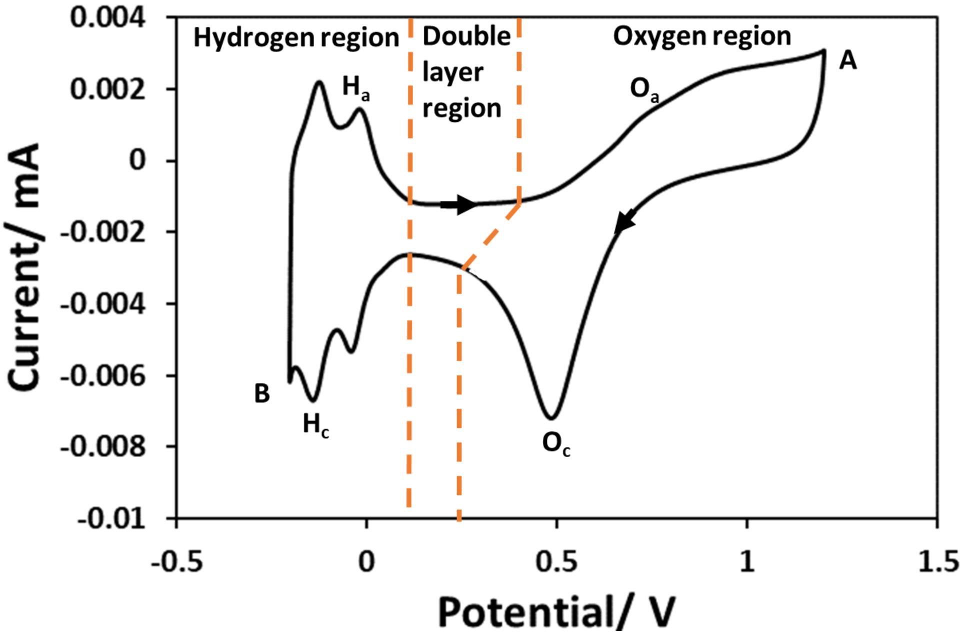

Figure 2.2 A representative cyclic voltammogram for a polished platinum electrode in 0.5 M H_2SO_4 at a scan rate of 50 mV s^{-1}.

During the forward scan, the surface of the working electrode oxidises and generates the anodic current. Similarly, the surface of the working electrode reduces during the backwards scanning and produces the cathodic current.

The typical platinum CV shows three distinct regions: the hydride, oxide, and double-layer regions.[108] As the potential becomes more positive, the anodic current flows attributed to adsorbed oxygen or platinum oxide (O_a) formation. Then, point A represents the start of the bulk oxygen evolution. In the backward scanning, the cathodic current flows due to the reduction of the surface platinum oxide (O_c). As the potential becomes increasingly negative while passing the double-layer region, hydride peaks appear to be attributed to the formation of adsorbed hydrogen or platinum hydride (H_c). Following this, point B represents the start of the bulk hydrogen evolution. At this point, the potential is reversed, and the anodic current flows again due to the desorption of the platinum hydride (H_a).[106,109] The size, shape and number of the observed peaks at the hydride region depends on the platinum crystal planes.[106,108,110,111]

The CV in 0.5 M H_2SO_4 was used to characterise the mesoporous platinum films and work out the ECSA. It can be expressed by the roughness factor (RF), which can be obtained from the formula:

$$RF = \frac{RSA}{A} \qquad \textit{Equation 2.1}$$

Where, (RSA) (cm^2) is the real surface area and A (cm^2) is the geometrical surface area. It is essential to highlight that the error associated with the determination of RF for the MPEs was thoroughly examined in this study using Nova and PlamSens3 software. The Nova software showed more accurate data, which was preferable for all the CV investigations. The calculated error shows a value of ± 9 for the high surface area electrodes with RF > 100. This error was assessed across the CVs at a scan rate of 50 mV s^{-1}. Consequently, it should be made aware that all the RF values for the MPEs presented in this work include an uncertainty of ± 9.

The RSA can be calculated by integrating the charge associated with the hydrogen adsorption/ desorption region and using the conversion factor of 210 x 10^{-6} C cm^{-2} which corresponds to the charge associated with the adsorption/desorption of a monolayer of hydrogen on a platinum surface.[108,109,112]

$$RSA = \frac{Q_{HUP}}{210\times 10^{-6}} \qquad \textit{Equation 2.2}$$

Where Q_{HUP} (C) is the charge associated with the hydride region, Q_{HUP} is determined by:

$$Q_{HUP} = \frac{Q - Q_D}{2} \qquad \textit{Equation 2.3}$$

The Q (C) is the charge associated with the formation and removal of a hydrogen monolayer on the surface of the electrode and can be calculated by integrating the current (I) passed with respect to time (t) for the hydride region during the forward and reverse cycles. The Q_D is the charge associated with the double-layer region.

The ECSA (m^2 g^{-1}) for platinum can be estimated by:[108,113]

$$ECSA = \frac{RSA}{M_{Pt}} \qquad \textit{Equation 2.4}$$

Where the M_{Pt} (g) is the mass of platinum and can be calculated by:

$$M_{Pt} = Ar \times m_{Pt} \qquad \textit{Equation 2.5}$$

Ar is the relative atomic mass (for platinum 195.084 g mol^{-1}), and m_{Pt} is the number of moles of platinum, which can be measured from the moles of electron (m_e) divided by four as the deposition of platinum metal is a four-electron process:

$$m_{Pt} = \frac{m_e}{4} \qquad \textit{Equation 2.6}$$

The number of moles for the electron (m_e) can be determined from the Q_{dep} in the deposition:

$$m_e = \frac{Q_{dep}}{F} \qquad \textit{Equation 2.7}$$

Where Q_{dep} (C) is calculated by integrating the current (I) passed with respect to time (t), and F is the Faraday constant (96485 C mol^{-1}).

It should be highlighted that the CV was also used to investigate ethanol oxidation for the mesoporous platinum films. The CVs were carried out in 0.5 M H_2SO_4 + 0.5 M C_2H_5OH electrolyte at room temperature and various scan rates between potential limits of +1.2 and -0.30 V vs Ag/AgCl. However, only the CVs at a scan rate of 50 mV s^{-1} are presented in this thesis.

2.5.1.3 Electrochemical impedance spectroscopy

EIS was performed at room temperature in 0.5 M H_2SO_4 + 0.5 M C_2H_5OH with a frequency range from 100 kHz to 0.2 Hz and an AC amplitude of ± 10 mV. EIS is an analytical method that offers kinetic and mechanistic data of various electrochemical systems. It is a valuable tool for distinguishing between polished and porous electrodes. Its application extends to investigating the accessibility of the internal surface for mesoporous materials, which can improve knowledge of the electrochemical behaviour of mesoporous films.[114–116] EIS generates a detailed frequency-dependent impedance spectrum by applying small amplitude alternating currents through the system and measuring the resulting voltage response.[117] This spectrum enables a deep examination of diverse electrochemical processes in the electrolytic cells, giving insights into factors such as solution resistance (R_s), charge transfer resistance (R_{ct}), double-layer capacitance (C_{dl}) and mass transport limitation.[118] These elements determine the physical processes for the system, such as R_s, which is associated with the diffusion and mass transfer of active species, while R_{ct} is linked to the transfer of electrons at the interface between the electrode and the electrolyte. The C_{dl} results from the separation of ions in the electrolyte and the charges on the electrode surface. Interpreting EIS data involves expressing electrical circuit elements as combinations of resistors, capacitors and inductors. The Nyquist plots for the simple electrical circuit containing a single resistor and capacitor elements are produced using PSTrace software and shown in Figure 2.3.

Figure 2.3 a) shows that when the circuit contains only a resistor, the real part equals R, while the imaginary part is zero. Therefore, a single point lies on the x-axis in the Nyquist plot. Figure 2.3 b) exhibits the circuit that contains only a capacitor. The imaginary part is inversely proportional to the capacitance and frequency, while the real part is zero. Therefore, a straight line lies on the y-axis in the Nyquist plot. Values close to zero relate to high frequencies, while lower frequencies relate to higher impedance values.

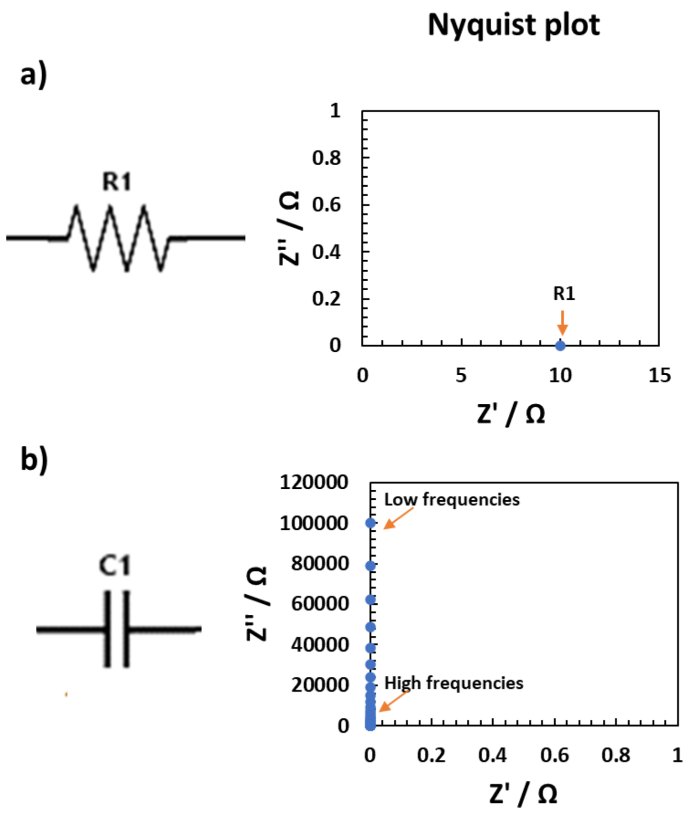

Figure 2.3 Nyquist plots of some model circuits for a) resistor and b) capacitor only.

A circuit behaves resistively when the resistor R is connected in series at low and high frequencies. When a circuit exhibits resistive behaviour, its impedance is essentially real, meaning it lies on the real axis of the complex impedance plane.[119] Therefore, the semicircle observed in the Nyquist plot is often analogous to the impedance response and can be applied to different circuits. Examples of different model circuits used in this study are shown in Figure 2.4.

Figure 2.4 a) shows an R(RC) circuit, and this model can be applied when the semicircle is symmetrical. The high-frequency intercept of the semicircle determines the R_s. The R_{ct} is equal to the diameter of this semicircle.

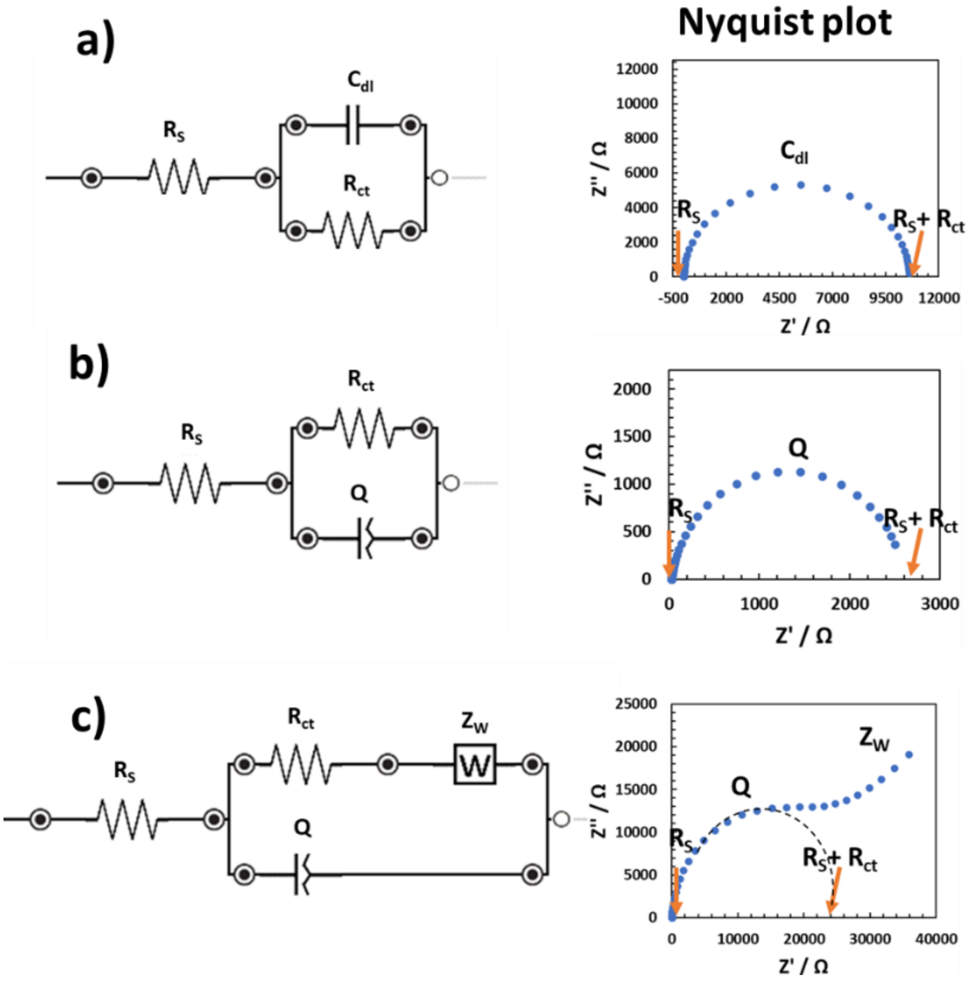

Figure 2.4 Nyquist plot of different model circuits produced using PSTrace software.

Figure 2.4 b) shows the R(RQ) circuit applied when the semicircle is depressed. This is due to non-ideal capacitor behaviour due to the surface heterogeneity at the double-layer interface. Therefore, the C_{dl} is replaced with a constant-phase element (Q) parallel with R_{ct}.[117,119,120] Surface roughness, chemical inhomogeneity, and electrode-electrolyte interface heterogeneity due to ion adsorption all have an impact on constant-phase elements.[121] The impedance of Q is described by :

$$Z_Q = \frac{1}{Y_0(iw)^n} \qquad \textit{Equation 2.8}$$

Where, the Y_0 ($s^n\ \Omega^{-1}$) is the pre-exponent term, n is the exponent term, and the w (2πf Hz) is the angular frequency.[117,119] The Y_0 is $s^n\ \Omega^{-1}$ does not give a clear physical interpretation compared to the C_{dl}, which is s Ω^{-1} or F. Therefore, the conversion of Y_0 data to C_{dl} is essential. Hsu and Mansfeld proposed an approach in their technical note.[122]

$$C_{dl} = Y_0(w''_{max})^{n-1} \qquad \textit{Equation 2.9}$$

Where, w''_{max} is the frequency where the maximum value of the imaginary component of impedance (Z'') is observed.

Figure 2.4 c) displays the Randles circuit, which can be used when the semicircle is followed by a rise to a nearly vertical line at low frequencies. The Randell circuit consists of Q parallel with R_{ct} and a Warburg diffusion element (Z_w). The Z_w is a general component that describes diffusion impedance and can be defined further to identify behaviour at low frequencies.[121]

If the impedance data shows more than one semicircle, it indicates the need for additional resistors/capacitors in the circuit. For instance, if two semicircles exist, a pair of R and Q elements will be added to the circuit. Therefore, the number of resistors and capacitors in the circuits corresponds to the number of semicircles observed.[117] The goal of using the suitable model circuit is to get the best alignment between the data obtained from experiments and the curve generated by the model, and the precision of the fit can be assessed by examining the chi-squared values (x^2).[120] As the complexity of a model increases, a challenge arises, and it may fit every impedance, or multiple intricate models could effectively match an impedance spectrum. Therefore, equivalent-circuit simulation may sometimes lead to inaccurate conclusions, and results must therefore be carefully considered, and sensible interpretations made.[119]

2.5.2 Analytical techniques

2.5.2.1 Cross-polarising light microscopy

The CPLM was used to investigate the phase behaviour of the LLC. In the CPLM, the sample is viewed through a pair of polarizing filters positioned in a crossed configuration. One filter, the analyzer, is placed above the sample, which is sandwiched between two glass plates, while the other filter, the polarizer, is situated below. The polarizer permits only light waves vibrating in a particular direction to pass through, whereas the analyzer selectively allows light waves vibrating in a plane perpendicular to its axis to pass. This setup helps in observing the optical properties of the sample under different orientations of polarized light. In the absence of a sample, the microscope image appears black because no light passes through. However, in the presence of the sample, the light passes through and is split into two orientations of rays, as the polarizing filters allow only specific light waves to pass through. Consequently, the sample can appear either isotropic or anisotropic under the microscope, depending on its properties, as shown in Figure 2.5.

Anisotropic refers to materials whose properties vary depending on the direction, whereas isotropic describes materials with direction-independent properties. These terms are fundamental in basic crystallography for explaining material properties. From Figure 2.5, samples split polarised light into two perpendicular directions in the anisotropic phase. These rays are termed "ordinary" (o-ray) and "extraordinary" (e-ray) rays, which travel in all orientations and hit the second polariser (the analyser).[123] Their recombination results in constructive interference, and therefore, the anisotropic phase exhibits characteristic optical textures (birefringence) under the CPLM.[124]

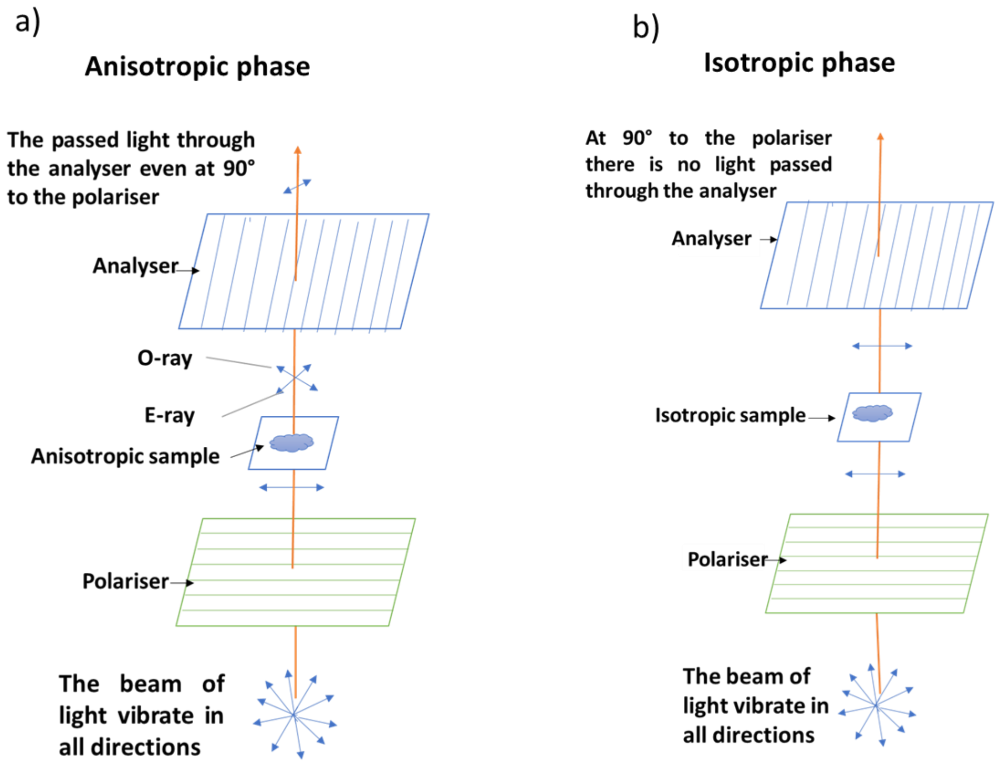

Figure 2.5 Schematic of CPLM in a) anisotropic and b) isotropic materials redrawn and adapted from Roychoudhuri and Pedrotti.[125]

On the other hand, the isotropic phase has the same optical properties in all orientations. When the light hits the sample, the o-ray and e-ray vibrate in phase with each other; they cancel each other by means of destructive interference. Consequently, the sample appears dark under the polariser. Thus, the phases of LLC can be identified under CPLM by their textures that are revealed under the CPLM, depending on the phase structure and its alignment.

Sample preparation - Small amounts of mixtures were placed on microscope slides and subsequently covered with a coverslip. The coverslip was pressed to ensure the mixture spread and reduce the sample thickness. Besides, the heating/cooling rate was maintained at 5 °C min^{-1}. The temperature varied from 25 °C to 65 °C and was gradually cooled to 25 °C. A Canon camera was used to take images of the different phases of the mixtures under microscopy.

Analysis of sample under CPLM- The identification of liquid crystals via CPLM can be investigated through the phase's birefringent textures, bubble shape, or viscosity under CPLM.[126,127] The different phases of the LLC are shown in Figure 2.6.

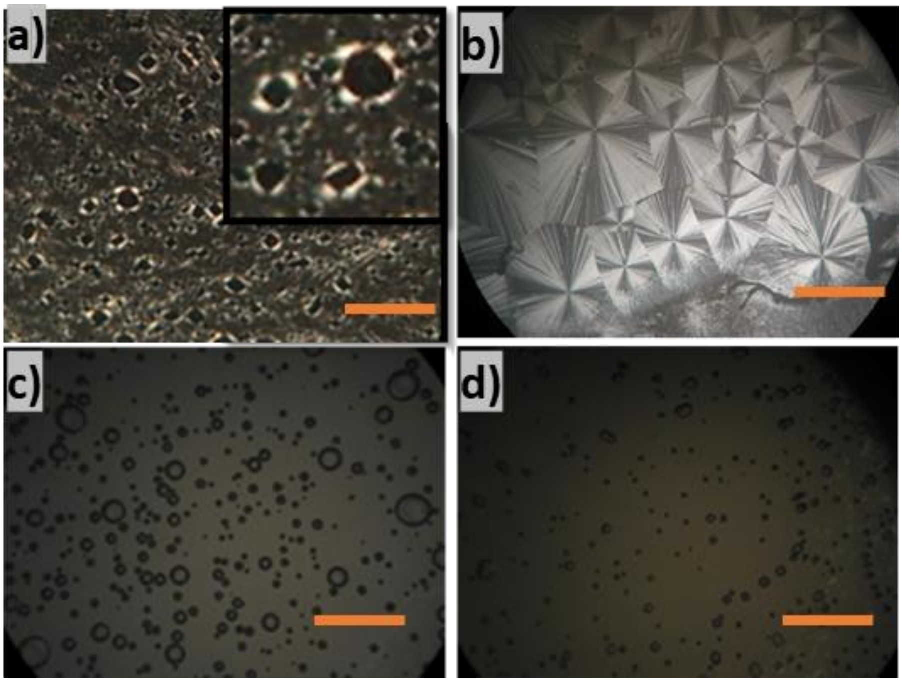

Figure 2.6 CPLM images for a) lamellar $L_{\propto}$ and the inset exhibits spherulite, b) hexagonal H_I shows the anisotropic fan-like texture, c) inverse micellar L_{II} and d) cubic phase. The scale bar on the CPLM image =500 µm.

In lyotropic systems, the $\mathrm{L}_{\propto}$, H_{I} and H_{II} phases exhibit birefringence, with two distinct refractive indices perpendicular to each other. These liquid crystal phases display specific optical textures when viewed under a polarising microscope.[126] The H_{I} and H_{II} phases are viscous phases that contain angular air bubbles. While the $\mathrm{L}_{\propto}$ phase is relatively viscous but less viscous than the H_{I} phase with spherulite air bubbles. In contrast, the cubic (V_{I}) and inverse micellar (L_{II}) phase has an isotropic nature and appears dark. Therefore, the viscosity of materials can distinguish the isotropic phases. The L_{II} phase exhibits low viscosity due to the flat interface between micelles, while the cubic phases reveal high viscosity because of the highly structured interface within the cubic lattice.[128]

2.5.2.2 Small angle X-ray scattering

The SAXS instrument used in this study was calibrated against silver behenate at a d-spacing of 58.3 Å. Scattering patterns were obtained using X-ray radiation with a wavelength of 1.54 Å and a beam size of 0.1 mm by 0.1 mm, with a sample-to-detector distance of 1063.5 mm.

SAXS is a non-destructive analytical method that analyses the sample as a function of the scattering angle to determine the X-ray scattered intensities. It provides information on nanoscale dimensions, size, and internal structure of colloidal and material objects.[129] SAXS explores the structure of nanostructured materials by measuring the scattering intensity at scattering angles 2θ close to 0°. The structure shows symmetry, and the interaction of X-ray radiation with the sample's nanostructure can produce a diffraction pattern, showing constructive interference at specific angles. This phenomenon is described by Bragg's law:

$$n\lambda = 2d\,sin(\theta) \qquad \text{Equation 2.10}$$

Where λ (nm) is the X-ray radiation wavelength, d (nm) is the distance between reflection sites, θ (°) is the scattering angle, and n is an integer. A schematic illustration of Bragg's law is shown in Figure 2.7.

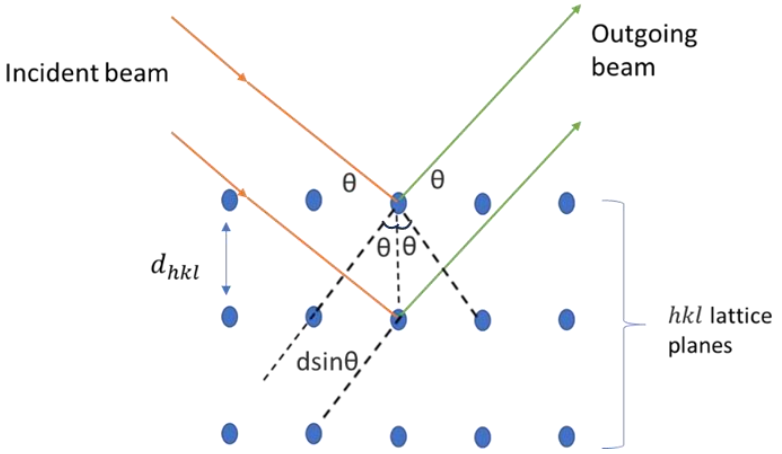

Figure 2.7 A schematic illustration of Bragg's Law.

The diffraction spots in a SAXS pattern are generated by different combinations of three integers, h, k, l known as Miller indices. These indices represent specific lattice planes within the crystal structure that diffract X-rays at particular angles, resulting in the formation of diffraction spots at corresponding positions in the pattern. The distance between these lattice planes is referred to as the interplanar spacing, denoted as d_{hkl}. The relationship between the Miller indices and the lattice parameter determines the interplanar spacing and varies depending on the lattice system of the crystal.

The SAXS instrument is typically configured with an X-ray beam source and a 2D detector, as shown in Figure 2.8. The X-ray beam strikes the sample and enters the vacuum chamber to prevent air from scattering the beam. The scattered radiations are then collected by the 2D X-ray detector, which generates a 2D pattern that can be converted to a 1D pattern for analysis.[130]

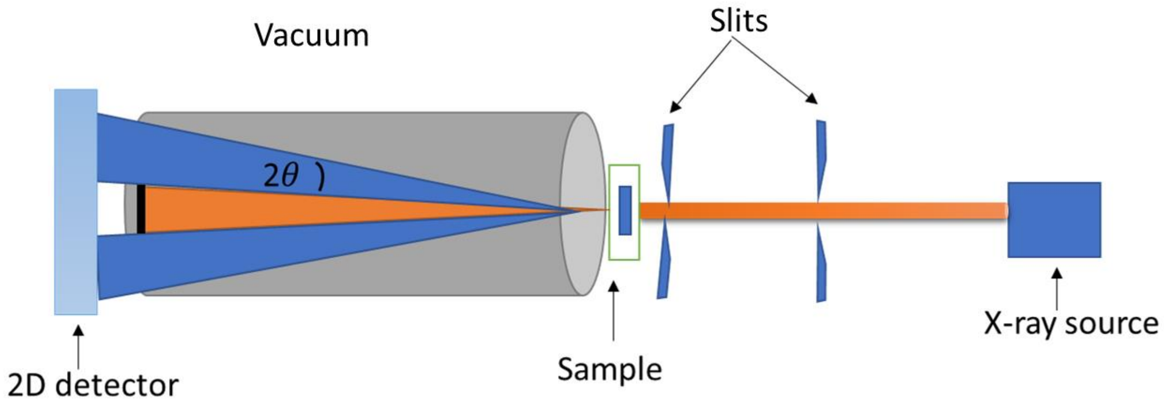

Figure 2.8 Schematic illustration showing a typical setup of the SAXS instrument adapted from M.Gräwert et al.[131]

Sample loading - Electrodeposited platinum films were directly attached to the sample grid with the help of polyimide sticky tape. In contrast, the LLC mixture samples were sandwiched between two layers of polyimide tape supported by a Viton sheet, as shown in Figure 2.9.

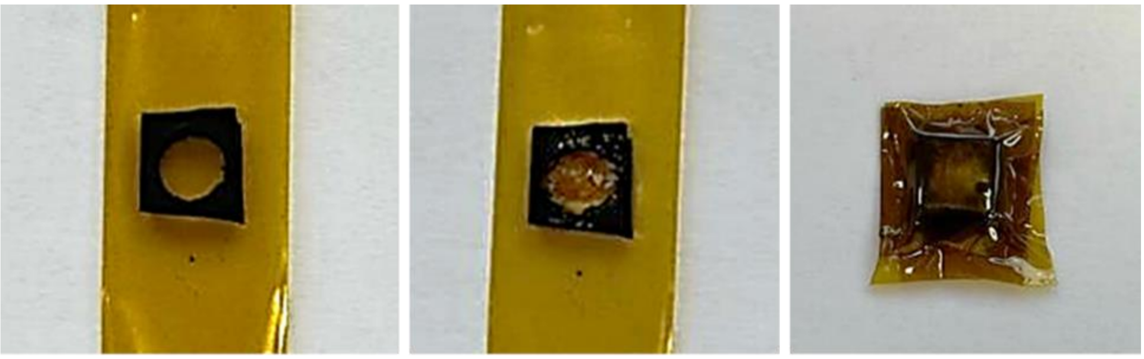

1- A hole in a Viton sheet, adhered to polyamide tape.

2- The mixture is placed inside the hole.

3- The cell is covered with polyamide tape.

Figure 2.9 LLC sample preparation for the SAXS, the diameter of the hole is 1 cm.

Analysis of SAXS samples - The SAXS data was displayed as 2D SAXS patterns and then converted to a 1D pattern using Image J software with macros available in-house. These two patterns, 1D and 2D, were used to identify the symmetry structure.[67] In SAXS analysis, the refractive index of the sample and the scattering vector q are important parameters. The refractive index influences the scattering behaviour of X-rays in the sample, affecting the intensity and distribution of the scattered radiation. The scattering vector q is defined as:

$$q = \frac{4\pi}{\lambda} sin(\theta) \qquad \textit{Equation 2.11}$$

Where λ is the wavelength of the X-ray radiation and θ is the scattering angle. The scattering vector q provides information about the size and arrangement of scattering centers in the sample. For periodic structures, such as those found in crystals or ordered mesoporous materials, the q is related to the spacing between the scattering centers (d) by:

$$q = \frac{2\pi}{\mathrm{d}} \qquad \textit{Equation 2.12}$$

Where d is the spacing between the scattering centers, therefore, in SAXS analysis, the reciprocal of the spacing between scattering centers ($1/d$) is often used to measure the arrangement of scattering centers in the sample.

In this study, the symmetry structure of the samples was identified from the 1D pattern, which exhibits a ratio of diffraction peaks for each Bragg peak. To ensure the accuracy of phase identification, an Excel spreadsheet was developed to calculate the d-spacing for all phases at different diffraction peaks. These calculated d-spacing values were then compared with expected values for various phases, with the phase showing matching d-spacing values being identified as the correct phase. The diffraction peaks can be converted to d-spacings, and then the lattice parameter can be calculated. The lattice parameter is the repeating distance between the lattice planes. Table 2.1 shows the ratio of diffraction peaks for the different symmetries and the lattice parameter.

Table 2.1 shows the ratio of diffraction peaks for different symmetry and the lattice parameter.[126,132,133]

Structure	Bragg's ratio	Lattice parameter
Lamellar	$1:2:3:4:5\ldots$	$a_{L_\propto} = d$
Hexagonal	$1:\sqrt{3}:\sqrt{4}:\ \sqrt{7}:\sqrt{9}:2\sqrt{3}\ldots$	$a_{H_I} = \dfrac{2d}{\sqrt{3}}$
Discontinuous cubic **BCC(Im3m)** **FCC(Fm3m)**	$1:\sqrt{2}:\sqrt{3}:\sqrt{4}:\sqrt{5}:\sqrt{6}\ldots$ $\sqrt{3}:\sqrt{4}:\sqrt{8}:\sqrt{11}:2\sqrt{3}\ldots.$	$a_{cubic} = \sqrt{h^2+k^2+l^2} \times d$ Where, d (Å) is d-spacing h, k, l= miller indices
Bicontinuous cubic **Gyroid (la3d)** **Double diamond (Pn3m)** **Primitive (Im3m)**	$\sqrt{3}:\sqrt{4}:\sqrt{7}:\sqrt{8}:\sqrt{10}:\sqrt{11}\ldots$ $\sqrt{2}:\sqrt{3}:\sqrt{4}:\sqrt{6}:\sqrt{8}:\sqrt{9}\ldots$ $\sqrt{2}:\sqrt{4}:\sqrt{6}:\sqrt{8}:\sqrt{10}\ldots$	

The lattice parameter calculation depends on the mesophase structure. The schematic for the lattice parameter of the $L_\propto$, H_I, BCC and FCC phases are illustrated in Figure 2.10.

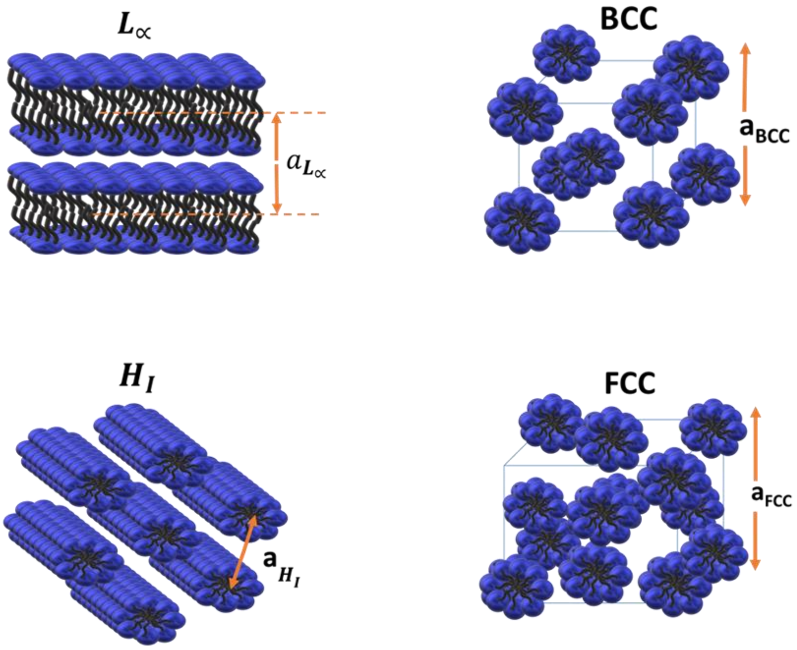

Figure 2.10 The lattice parameter for lamellar ($L_\propto$), hexgonal (H_I), body centerd cubic (BCC) and face centered cubic (FCC).

Figure 2.10 shows the lattice parameter for the $\mathrm{L}_\propto$ structure where the d-spacing is the repeating distance that is equal to the lattice parameter. While in the H_I symmetry, the lattice parameter (a) is calculated from the distance between two cylinders, and it depends on the amount of water and amphiphile. On the other hand, the lattice parameter for the cubic phases (BCC and FCC) is the distance from the middle of the micelle to the middle of the next micelle.

2.5.2.3 Wide X-ray powder diffraction

This work used XRD patterns run in a normal 2θ scan with a Cu tube at a wavelength of (λ = 1.54 Å), voltage of 40 kV and current of 40 mA. The detector used is a Lynxeye XT. In XRD, a powder diffractometer captures the intensity of monochromatic X-rays diffracted by a sample at various angles specified by the user. This results in a pattern shown in a relationship between the intensity and the angle of incidence of the X-ray beam (2θ). It is used to study the structure of unknown crystalline materials. The discovery of phases is achieved by matching the XRD pattern achieved from an unknown sample with patterns of a reference database.[134] The peaks in the plot indicate the crystal's lattice plane, the width of peaks indicates the size of crystals, where broader peaks indicate smaller crystal sizes. Conversely, the intensity of the peaks indicates the orientations of the platinum crystallites, which also vary depending on the orientation of the pores.

This work used XRD to study the deposited nanostructured platinum films. The XRD principally gives information about the arrangement of atoms in a crystal lattice. Therefore, it is expected to show the FCC structure for platinum films. However, it can also provide some information about the effect of the mesoporous structure, such as the crystal size. It may not directly provide information about porosity. The presence of certain peaks or the broadening of peaks in the XRD patterns may indicate a certain degree of disorder or order structure, which can be further analyzed using peak positions, intensities, and shapes, as well as advanced techniques like Rietveld refinement.

Sample preparation - The mesoporous platinum foils were stuck to the holder with Kapton tape.

Sample analysis - The 2D data were converted to 1D using the data conversion program ConvX. The data then were compared to the standard data of the International Centre for Diffraction Data.

2.5.2.4 Scanning electron microscopy

The SEM is one of the electron microscopy techniques employed for surface imaging, designed to show features of the sample at the nanoscale level.[135] The SEM can produce high-resolution images of the surface. In the SEM analysis, the electron beam is directed over a sample possessing a conductive surface, as shown in Figure 2.11. When the beam interacts with the sample, it generates physical phenomena consisting of the emission of high-energy backscattered electrons (BES), secondary electrons (SE), Auger electrons (AE) and X-ray emission. Detectors gather the signals and transmit them to a screen for image display. The secondary electron is the most commonly used for studying the surface morphology. Meanwhile, the electron waves are utilised in different fields. For instance, the X-ray spectra can be used for the elemental analysis: energy-dispersive spectrometer (EDX).[136]

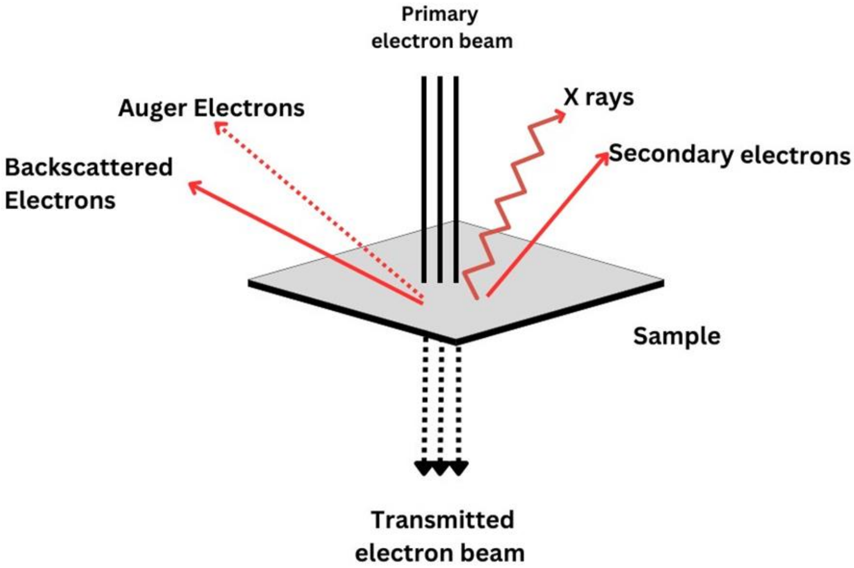

Figure 2.11 Types of electrons emitted from the surface when the primary electron beam interacts in scanning electron microscopy (SEM) adapted and redrawn from Zhou et.al [137]

Sample loading - No pre-treatments were required for SEM, and the electrodes were placed in the sample holder inside the chamber. Carbon tape was used to connect the electrode to the sample holder to be conductive, as shown in Figure 2.12. Then, the SEM imaging was carried out under vacuum at a working distance of 6-7 mm and accelerating voltages of 20 kV.

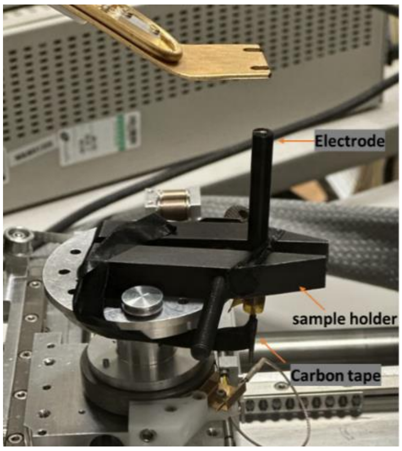

Figure 2.12 Sample loading in SEM

Sample analysis - A range of magnifications (250-30000x) was applied. The SEM data were analysed using INCA microanalysis software in order to identify the deposited material. The morphology of the sample was investigated through a visual observation of the SEM images.

2.5.2.5 Transmission electron microscopy

TEM is a technique used to exhibit the size and morphology of nanoparticles. This technique can be used to observe the sample's morphology, lattice spacing, and crystal orientation.[138] The TEM has the same basic principle as the light microscope, but instead of using visible light, it employs a beam of electrons to generate images. A schematic of the beam interaction with sample in TEM is shown in Figure 2.13.

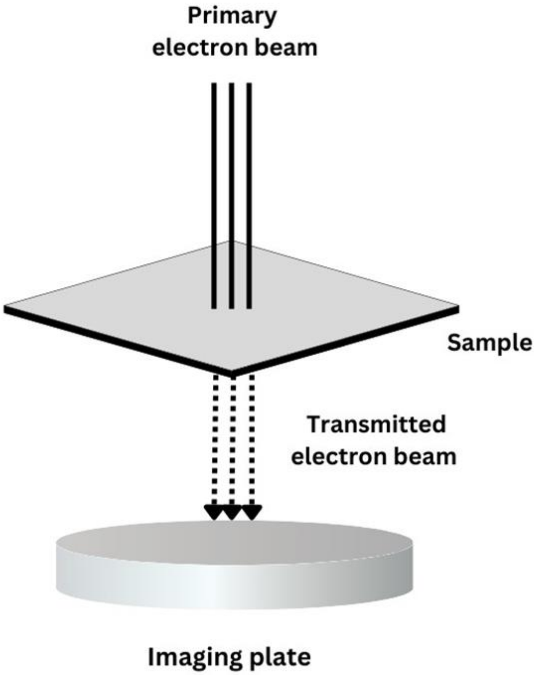

Figure 2.13 Interaction of the primary electron beam with the sample in transmission electron microscopy (TEM) adapted from Mo et al. [139]

In TEM, only thin samples, which allow a fraction of the incident electron beam to go through the sample, can be studied. Thicker or denser samples appear darker under TEM. The images of the sample depend on the interaction of the high-energy electron beam with the sample when the beam is passed through the specimen. In TEM, the beam of electrons is transmitted through the ultra-thin sample. Following this, the transmitted electron from the sample hits the fluorescent screen and produces the image.[139]

Sample loading - In this study, the electrodeposited mesoporous platinum films were carefully scratched off from the substrate with the help of a scalpel and placed on a copper grid with a supporting carbon film (300 mesh). The copper grid was placed on the sample holder and loaded inside the chamber for analysis.

Analysis of the sample - The TEM images at different magnifications were collected to investigate the shape of the mesoporous platinum. Image J software was used to measure the lattice parameter and the pore diameter manually.

2.5.2.6 Atomic force microscopy

AFM is a class of scanning probe microscopes that can produce 3D images of various material surfaces with the ability to see the structures at the atomic level. It can scan surfaces and provides dimensions, roughness, topography, and other material characteristics.[140] The information is collected by touching a mechanical probe with the surface. The 3D images are generated by measuring the force between the sharp probe and the surface. The fundamental operation of the AFM is shown in Figure 2.14.

Figure 2.14 shows a sharp tip at the end of the probe connected to a cantilever interacting with the sample's surface. A laser projects light onto the cantilever, and reflected light is detected by a position-sensitive photodetector, which measures the deflection of the cantilever. The sample is placed on a piezoelectric scanning stage, and the tip-sample position is adjusted in 3D with nanometre accuracy. Throughout the scanning, the feedback loop ensures that the tip-sample interaction is constant, allowing for the mapping of the sample's topography due to the constant adjustment of the tip's height to maintain a constant force.[140]

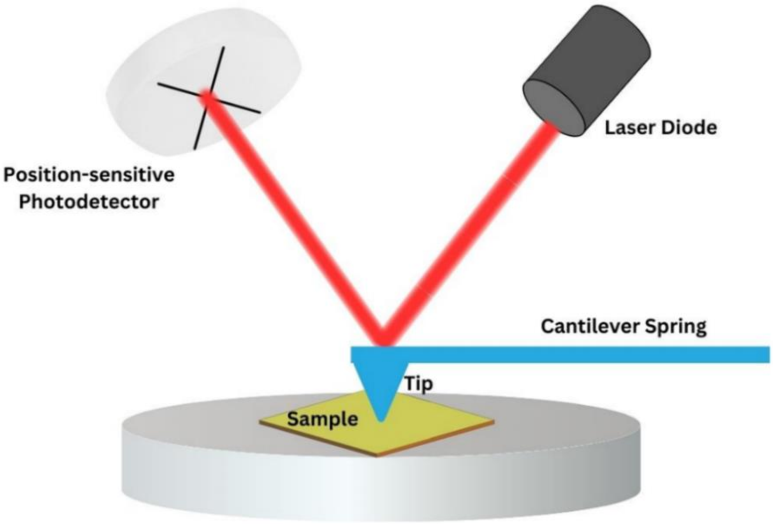

Figure 2.14 a typical atomic force microscope(AFM) instrument setup adapted from Zeng et al. [141]

Sample loading - The samples were made by attaching the electrodeposited platinum film to the specimen disc using double-sided carbon tape and placing it into the AFM chamber, as shown in Figure 2.15.

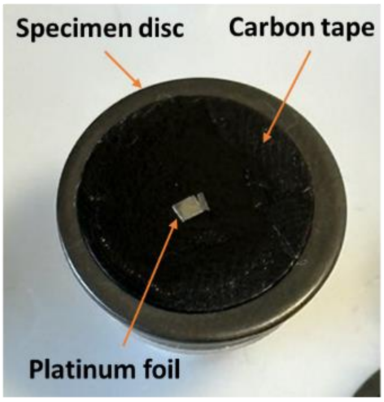

Figure 2.15 Sample for the AFM

Sample analysis - Gwyddion software was used to analyse the AFM images. This study obtained the mean square roughness (RMS) and the average feature size (AFS) using Gwyddion. This software can obtain the RMS from height irregularities data and the AFS from the 2D autocorrelation function that is used to evaluate rough surface anisotropy.

Chapter 3- Head group size effects in phase behaviour (Brij® 56 and Brij® 58) and in-situ phase reactivity for platinum nanoparticle synthesis (Brij® 58)

3.1 Introduction

Non-ionic surfactants are commonly used as LLC to prepare replica platinum nanostructured materials following the approach of Attard *et al.*[6] For instance, Brij® 56 has been commonly used as a structural directing agent for producing mesoporous platinum materials.[71,142,143] The specific structure of the LLC can significantly affect the properties of the produced metal nanostructured materials.[49,126,144] Therefore, understanding the phase behaviour of the LLC makes it conceivable to modify the structures and properties to meet specific application requirements. This can involve modifying some factors to cause a phase transition or changing the surfactant structure to support forming a selected phase.[145] In this study, the Brij® 56 was selected for comparison with Brij® 58, which has larger micelles. The phase behaviour of both Brij® 56 [142] and Brij® 58 [72,74] have been studied earlier. Brij® 56 is a substance that contains $C_{16}EO_8$ as a key component and has been widely employed in the production of a $\mathrm{H_I}$ structure of mesoporous platinum through the electroreduction of LLC containing HCPA.[6,20,114] The presence of HCPA on the LLC has been investigated for $C_{12}EO_8$ and $C_{16}EO_8$ by Attard *et al.*[127] The results showed that increasing the HCPA concentration influenced the phase boundaries by increasing the transition temperatures of the $\mathrm{I_I}$ and $\mathrm{H_I}$ phases.[127] Considering that the $C_{16}EO_8$ is the crucial component for the Brij® 56, it responded similarly in the presence of HCPA. Furthermore, Ashgar *et al.* reported a model for predicting how the volume fraction determines the $\mathrm{H_I}$ and gyroid cubic phase lattice for lyotropic phases of Brij® 56 mixtures containing water or HCPA.[71]

This current study shifts its interest to non-ionic Brij® 58. Understanding the interaction of Brij® 58 with HCPA becomes necessary in this investigation, as it is essential for optimising conditions for the fabrication of mesoporous platinum. Several studies that used Brij® 58 in a micelle assembly approach (i.e. low concentration just above the CMC) to produce porous platinum nanoparticles in the presence of some reducing agents are listed in Table 3.1.

Table 3.1 Comparison of using Brij® 58 with K_2PtCl_4 in water to fabricate platinum nanoparticles at different conditions (US) means Ultrasonic cleaner, (AA) means ascorbic acid.

K_2PtCl_4/ mM	Wt% of Brij® 58	Additives/ Treatment	Description	Particle size/ nm	Pores size/ nm	Ref
20	10%-20%	US at room temperature 0.1 M AA	Mesoporous platinum nanoparticle	30-40	2	[28]
20	1.0%	US at 20 °C US at 60 °C 0.1 M l-AA	Dendritic platinum nanoparticle	23 60	2-4	[40]
5	0.01% 0.05% 1.0% 5.0% 10.0% 15.0% 20.0%	0.0125 M AA / Ethanol at room temperature	Mesoporous platinum nanoparticle	170 90 68 55 40 30 26	n.a	[41]
40	20%	0.1 M AA Ketjen black at room temperature	Dendritic platinum	4.45 (Pt/C-1) 7.98 (Pt/C-2)	n.a	[29]

Interestingly, while K_2PtCl_4 is the most commonly used salt, this work utilises H_2PtCl_6 (HCPA) salt instead. There is limited literature on the specific application of LLC containing Brij® 58 (i.e. concentration ≥ 30 wt%) to produce a distinct structure of mesoporous platinum, suggesting the need for further investigation in this area.

Aims:

- To confirm how the head group size affects the micelle size and phase behaviour of Brij® 56 versus Brij® 58 in water. Additionally, to investigate for the first time the interaction of aqueous HCPA with the head group of Brij® 58. For example, the suggested micelle sizes for Brij® 56 and Brij® 58 in water and Brij® 58 in HCPA are shown in Figure 3.1; as can be seen, the micelle size is believed to increase for the Brij® 58 systems, and it is also believed that more highly curved phases will be favoured. One of the aims of this work is to confirm this behaviour.

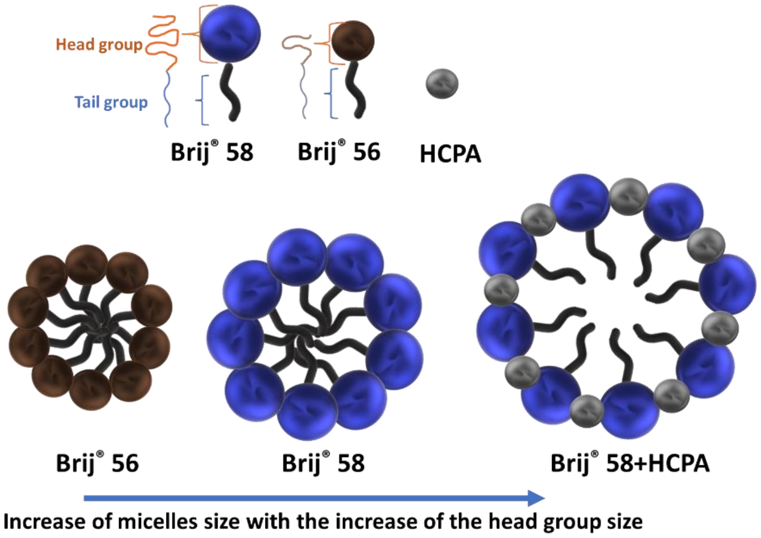

Figure 3.1 The average size of micelles increases with the increase in the polar head group.

- To investigate for the first time the in-situ reactivity of Brij® 58 (≥ 30 %) in aqueous HCPA at variable temperatures and to explore the potential to fabricate platinum nanoparticles without any additional reductant. The suggested in-situ reactivity of Brij® 58 with HCPA is shown in Figure 3.2. It is believed, based on current literature, that when Brij® 58 and HCPA are mixed and heated, mesoporous platinum will be produced because the Brij® 58 will act as an in-situ reductant and structural directing agent.

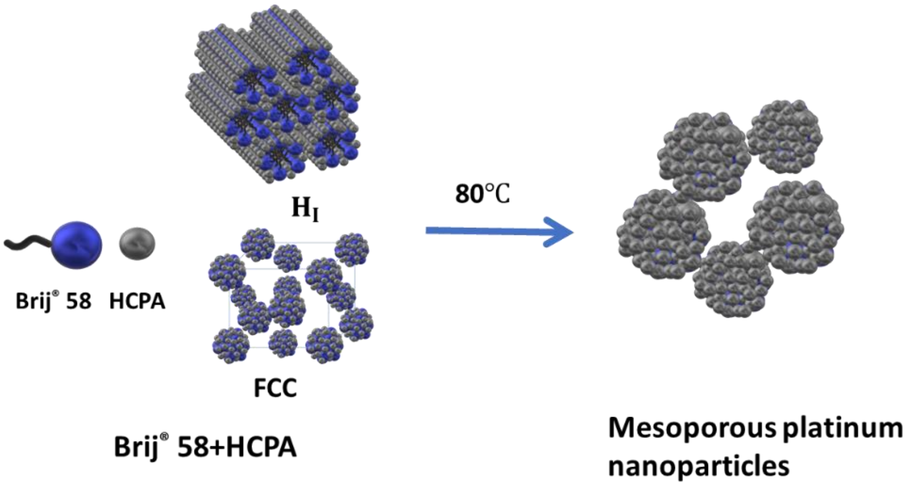

Figure 3.2 Schematic illustrates the in-situ fabrication of platinum nanoparticles in this study.

3.2 Methodology

The methodology is presented in two main sections in accordance with the aims.

3.2.1 Phase behaviour of Brij® 56 and Brij® 58 in water and Brij® 58 in HCPA

3.2.1.1 Preparation of lyotropic liquid crystals

An appropriate amount of Brij® 56 and Brij® 58 and ultra-pure deionised water, or 0.195 M HCPA, were placed in plastic vials. The plastic vials containing the mixtures were heated in the dry bath at 70 °C for approximately 15 minutes and then centrifuged for about 5 minutes. Sealed vials were used to prevent the evaporation of water molecules at high temperatures, which might influence the structures of the LLC mesophases. The heating and centrifugation cycles were repeated four times until the mixtures became homogenous following a process similar to that of Attard *et al.*[127]

Then, the samples were stored in sealed vials at room temperature. The exact amounts of surfactants and solvents are presented in Tables 3.2 to 3.4.

Table 3.2 Different compositions of Brij® 56 and water mixtures used in this study.

Mass of Brij® 56 /g	Mass of H_2O /g	Wt% of Brij® 56
0.151	0.350	30.14± 0.165%
0.197	0.304	39.32± 0.128%
0.252	0.254	49.80±0.098%
0.303	0.203	59.92±0.082%
0.348	0.148	70.16± 0.071%
0.395	0.104	79.16± 0.073%

Table 3.3 Different compositions of Brij® 58 and water mixtures used in this study.

Mass of Brij® 58 /g	Mass of H_2O /g	Wt% of Brij® 58
0.155	0.347	30.80 ± 0.161%
0.195	0.296	39.72 ± 0.128%
0.253	0.248	50.50 ±0.098%
0.302	0.198	60.40 ± 0.082%
0.351	0.156	69.29 ± 0.072%
0.394	0.096	80.41 ± 0.063%

Table 3.4 Different compositions of Brij® 58 and HCPA mixtures used in this study.

Mass of Brij® 58 /g	Mass of HCPA /g	Wt% of Brij® 58
0.152	0.351	30.22 ± 0.164%
0.201	0.297	40.36± 0.124%
0.248	0.252	49.60± 0.101%
0.297	0.194	60.49± 0.084%
0.352	0.147	70.54± 0.071%
0.399	0.101	79.80± 0.062%

3.2.1.2 Exploration of the phase behaviour

CPLM and SAXS were used to study the phase behaviour of Brij® 56 and Brij® 58 in water and Brij® 58 in HCPA. For CPLM, the samples were heated throughout the analysis from 20 to 65

℃ at a scan rate of 5 ℃ min^{-1} employing the heating stage with an accuracy of ± 0.1 ℃. For SAXS, the 2D pattern was converted to the 1D pattern using Image J software. Then, the 1D pattern was analysed from the ratio of diffraction peaks for each Bragg peak, as described in Chapter 2.

3.2.2 Investigation of the in-situ reactivity of Brij® 58 ≥ 30 wt%

3.2.2.1 Samples preparation

The experiment involved several steps, starting with the typical preparation of the homogenous Brij® 58 and HCPA mixtures at various concentrations from 30 to 80 wt% of Brij® 58. The details of the preparation process are listed below:

- On day 1, new samples of Brij® 58/HCPA mixtures were prepared as described above by repeating four heating and centrifugation cycles until the mixtures became homogenous. The amount of Brij® 58 and HCPA are presented in Table 3.5.

Table 3.5 Different compositions of Brij® 58 and HCPA mixtures used in this study.

Mass of Brij® 58 /g	Mass of HCPA /g	Wt% of Brij® 58
0.060	0.143	29.56± 0.416%
0.079	0.122	39.30± 0.316%
0.101	0.100	50.25± 0.247%
0.121	0.082	59.61± 0.206%
0.140	0.062	69.31± 0.178%
0.162	0.040	80.20± 0.154%

- On day 2, the mixtures underwent two cycles of heating at 80 ℃ for 20 minutes, followed by centrifugation for 10 minutes, and the colour of the mixtures changed to brownish.

- On day 3, the mixtures were heated at 80 ℃, and 50 and 60 wt% of Brij® 58/HCPA mixtures exhibited a noticeable colour change to black within 10 minutes of heating. Further heating was applied for an additional 30 minutes, resulting in a colour change to black for the mixtures ranging from 30 to 60 wt% Brij® 58/HCPA.

  Washing of chemical deposits - Washing of chemical deposits was carried out by centrifuging with ultra-pure deionised water for 25 minutes, and then the water was replaced; this process was repeated several times until the nanostructured platinum powder was separated. The Brij® 58 is soluble in water; therefore, removing the template was easy by sequential washing with water. After washing, the nanostructured platinum powder was kept moist in order to avoid inhalation.

3.2.2.2 Characterisation of platinum nanoparticles

TEM and SAXS were used to study the produced platinum nanoparticles. The analysis of the TEM images was based on manually measuring the diameter of each particle using ImageJ software.

3.3 Results and discussion

The results are presented and discussed in two main sections in accordance with the aims.

3.3.1 Phase behaviour of Brij® 56 and Brij® 58 in water and Brij® 58 in HCPA

The phase behaviour of Brij® 56 and Brij® 58 in water (Brij® 56/ water and Brij® 58/water) and Brij® 58 in HCPA (Brij® 58/ HCPA) were studied using CPLM and SAXS.

3.3.1.1 Cross-polarising light microscopy

For CPLM analysis, identifying each phase was following the method in section 2.5.2.1, and the assessment was based on visual observations of the phases under CPLM. The different phases can be distinguished by comparing the sample's birefringence, viscosity and shape of the bubbles. For instance, the $\mathrm{I_I}$ phase exhibits an isotropic texture, while the $\mathrm{H_I}$ phase shows an anisotropic texture. Also, the shape of the bubbles is essential for phase identification, and the angular bubbles indicate the $\mathrm{H_I}$ phase, while the spherulite bubbles indicate the $\mathrm{L_\propto}$ phase. CPLM images with the polariser in were collected at 20 ℃, and the constructed phase diagrams at different temperatures and compositions of Brij® 56/water, Brij® 58/water and Brij® 58/HCPA are presented in Figure 3.3 , Figure 3.4 and Figure 3.5, respectively.

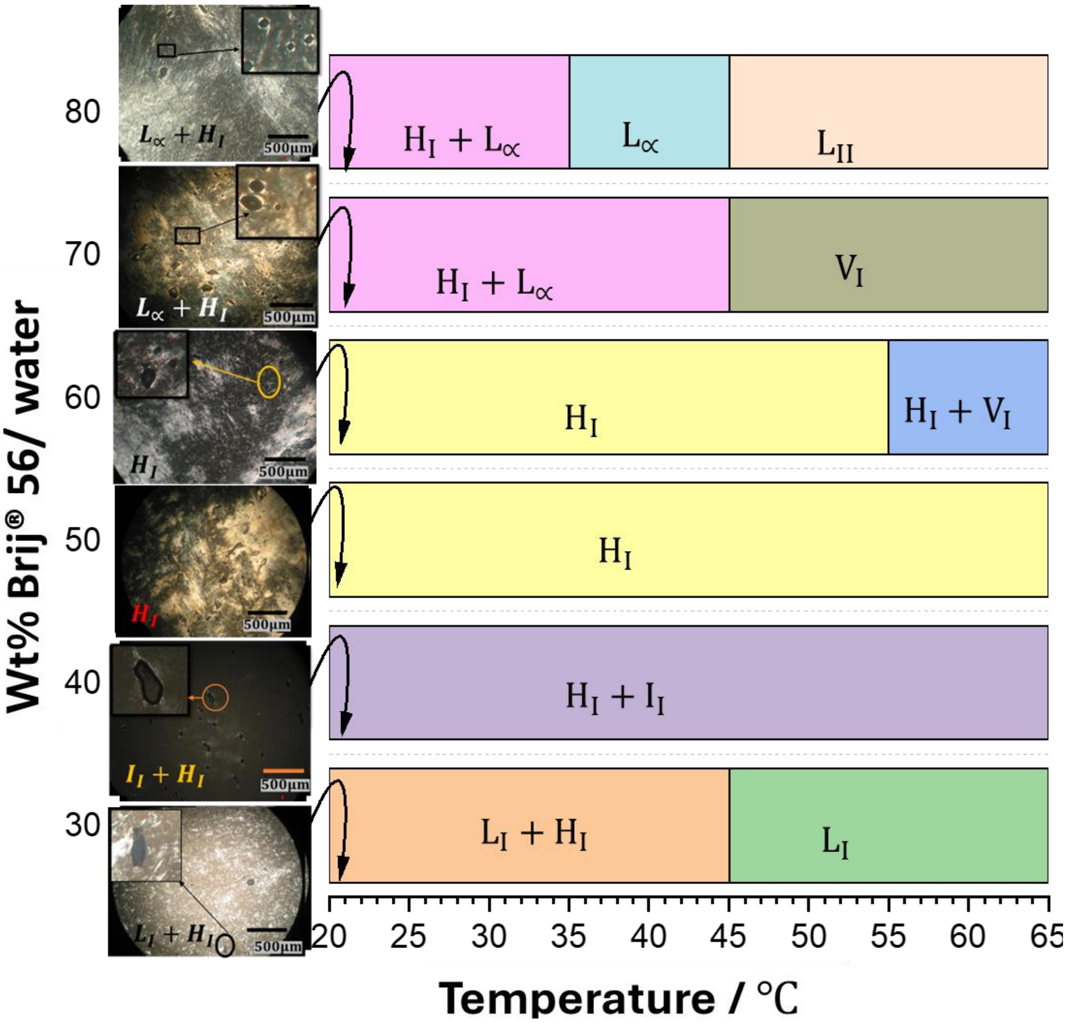

Figure 3.3 Phase diagram of Brij® 56 in water at various temperatures and compositions, accompanied by CPLM images taken at 20 ℃ for different systems: some features, such as the shape of the bubbles, are identified in CPLM images. The different phases are presented in the diagrams for the micellar solution (L_I) micellar cubic (I_I) hexagonal (H_I) lamellar ($L_\propto$), cubic (V_I) and invers micelles (L_{II}). The (+) illustrate the mixed phase and the (*) illustrate the phase separation. The scale bar on the CPLM image =500 µm.

Figure 3.3 shows the CPLM analysis of Brij® 56/water mixtures. At 30 wt% of Brij® 56, there is phase separation, which generally occurs at the CP and is distinguished by an anisotropic runny texture for the $\mathrm{H_I}$+$\mathrm{L_I}$ phases from the CPLM image. This phase separation remains stable up to 45 ℃ $\pm$ 1 ℃ then transferred to the $\mathrm{L_I}$ phase. At 40 wt% Brij® 56/water, the mixture reveals $\mathrm{H_I}$+$\mathrm{I_I}$ phase, illustrated by the presence of both isotropic and anisotropic textures with angular bubbles, and was stable up to 65 ℃. As the concentration increases, the samples reveal the $\mathrm{H_I}$ phase and converts to biphasic of $\mathrm{H_I}$ and $\mathrm{V_I}$ at a higher temperture ≥ 55 ℃ $\pm$ 1 ℃ for the 60 wt% Brij® 56/water. Further increasing the composition of Brij® 56/water, results in biphasic of $\mathrm{H_I}$+$\mathrm{L_\propto}$ phases, which are indicated by an anisotropic texture with angular and spherulite bubbles. The $\mathrm{H_I}$+$\mathrm{L_\propto}$ phases convert at high temperatures to the $\mathrm{V_I}$ and $\mathrm{L_{II}}$ for 70 and 80 wt% Brij® 56/water, respectively. These findings are in agreement with the previous study by Elliott *et al.*[142], which reported that the mesophases range from the $\mathrm{I_I}$, mixed phase of $\mathrm{I_I} + \mathrm{H_I}$ and $\mathrm{L_\propto}$ phases with the increase of Brij® 56 concentrations.[142]

The phase behaviour of Brij® 58/water at different compositions and temperatures is presented in Figure 3.4.

Figure 3.4 illustrates the CPLM analysis of Brij® 58/water. At 30 and 40 wt% of Brij® 58/water, the samples show the $\mathrm{I_I}$ phase, characterised by a viscous isotropic texture with angular bubbles. The $\mathrm{I_I}$ phase remains stable up to 55 ℃ $\pm$ 1 ℃ and then converts to $\mathrm{L_I}$ phase, confirmed by a runny isotropic texture. For 50 and 60 wt% of Brij® 58/water, a biphasic of $\mathrm{H_I} + \mathrm{I_I}$ is observed, remaining stable until 35℃ $\pm$ 1 ℃ , which then transitions to the $\mathrm{H_I}$ phase up to 65 ℃.

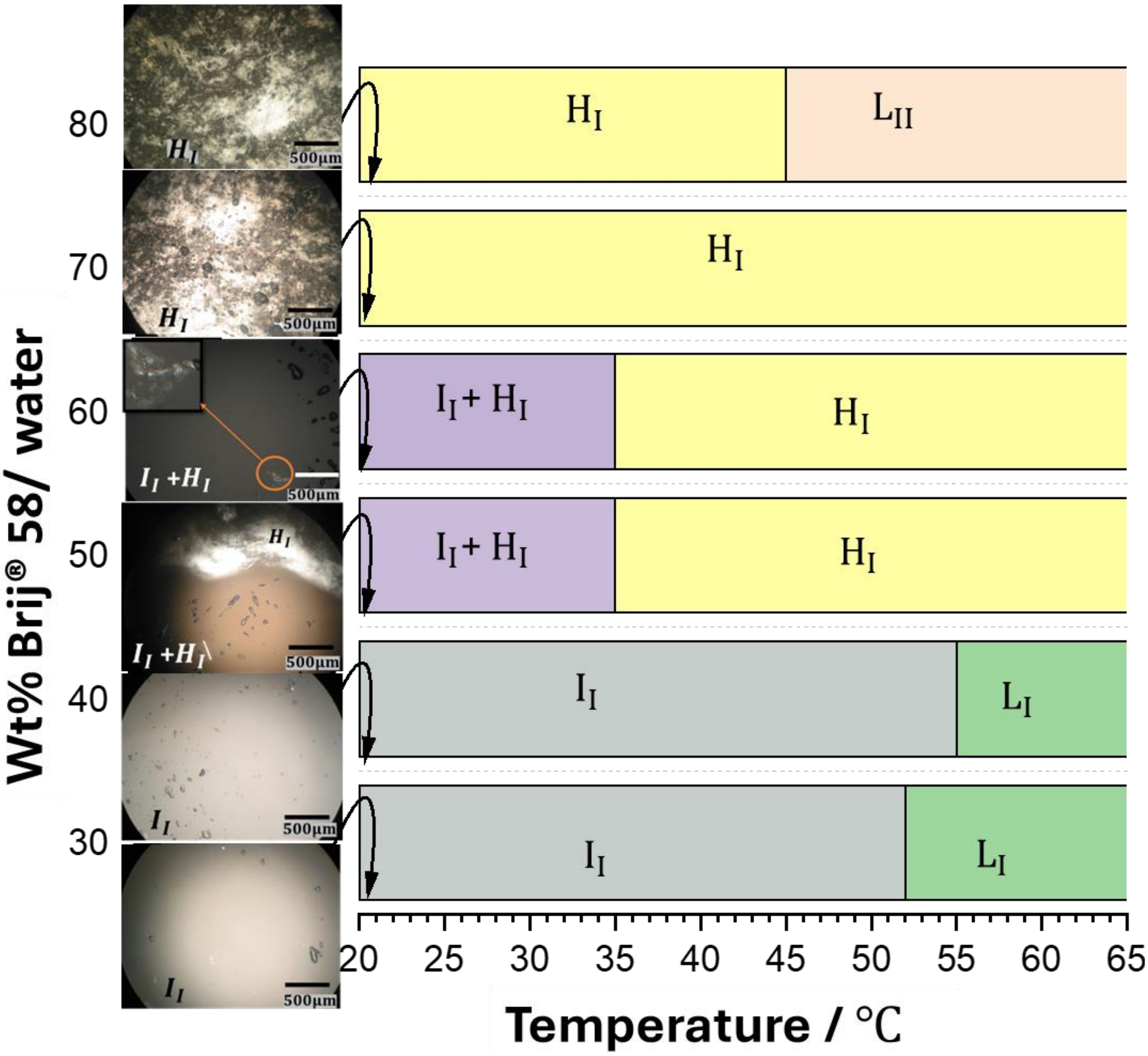

Figure 3.4 Phase diagram of Brij® 58 in water at various temperatures and compositions, accompanied by CPLM images taken at 20 ℃ for different systems: some features, such as the shape of the bubbles, are identified in CPLM images. The different phases are presented in the diagrams for the micellar solution (L_I) micellar cubic (I_I) hexagonal (H_I) lamellar ($L_\propto$), cubic (V_I) and invers micelles (L_{II}). The (+) illustrate the mixed phase. The scale bar on the CPLM image =500 µm

At 70 and 80 wt% Brij® 58/water, the samples exhibit the $\mathrm{H_I}$ phase, with stability up to 65 °C for 70 wt%, while for 80 wt% it converts to $\mathrm{L_{II}}$ at 45 $\pm$ 1 °C. These findings are in agreement with the previous studies by Gibaud *et al.*[72], who investigated the phase behaviour exclusively at room temperature and Mahanthappa *et al.*[74], who focused on the compositions from 30 to 65 wt% Brij® 58 at different temperatures. Mahanthappa *et al.*[74] reported the presence of the

A15 phase at 55 % Brij® 58, which is not an exact wt% studied here and cannot be identified through CPLM.

The phase behaviour of Brij® 58/HCPA at different compositions and temperatures is presented in Figure 3.5.

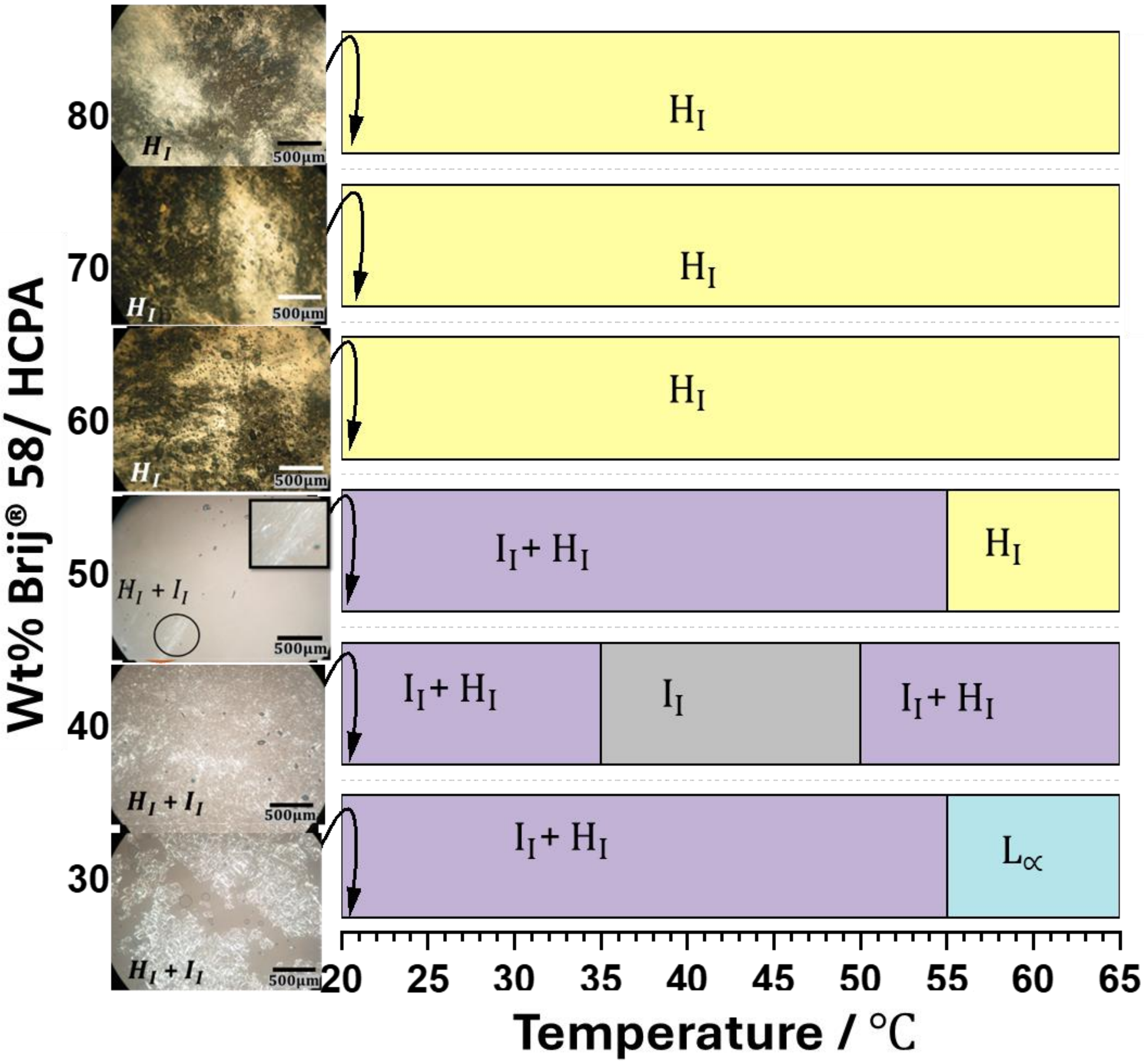

Figure 3.5 Phase diagram of Brij® 58 in HCPA at various temperatures and compositions, accompanied by CPLM images taken at 20 ℃ at different compositions from 30% to 80%. The different phases are presented in the diagrams for the micellar solution (L_I), micellar cubic (I_I), hexagonal (H_I) and lamellar ($L_\propto$). The (+) illustrate the mixed phase and the scale bar on the CPLM image =500 µm.

Figure 3.5Figure 3.4 exhibits the CPLM images and phase behaviour of Brij® 58/HCPA mixtures. Interestingly, the presence of HCPA on Brij® 58 at the compositions from 30 wt% to 50 wt% of

Brij® 58 induces an anisotropic texture for the $\mathrm{H_I}$ phase along with the isotropic texture for the $\mathrm{I_I}$ phase. This mixed phase $\mathrm{H_I}$+$\mathrm{I_I}$ at 30 wt% Brij® 58/ HCPA remains stable up to 55 $℃ \pm 1$ ℃. Then, the $\mathrm{L_\propto}$ phase appears at higher temperatures. At 40 wt% Brij® 58/ HCPA, this biphasic of $\mathrm{H_I}$+$\mathrm{I_I}$ transfers at 35 $℃ \pm 1$ ℃ to the $\mathrm{I_I}$ phase, and then the biphasic state reemerges as the temperature increases to 50 $℃ \pm 1$ ℃. At 50 wt% Brij® 58/ HCPA, this biphasic of $\mathrm{H_I}$+$\mathrm{I_I}$ transfers to $\mathrm{H_I}$ phase at 45 $℃ \pm 1$ ℃ . Interestingly, at higher concentrations from 60 to 80 wt% Brij® 58/ HCPA, the samples reveal the $\mathrm{H_I}$ phase to be stable up to 65 ℃.

Although the CPLM gives a general idea of the phase behaviour of mixtures, it cannot identify the symmetry structure of mixtures or the spacing. Therefore, advanced analyses were carried out using SAXS to study the phases' exact structure and lattice parameters.

3.3.1.2 Small angle X-ray scattering

The SAXS was used to investigate the phase behaviour of Brij® 56/water, Brij® 58/water and Brij® 58/HCPA at room temperature, as shown in Figure 3.6.

Figure 3.6 a) shows the 1D SAXS data collected for Brij® 56/water. The SAXS data show some broad peaks with low intensity, which might indicate the $\mathrm{H_I}^*$ in the phase separation. This sample indicates $\mathrm{H_{I+}L_I}$ under CPLM, as discussed in Figure 3.3. At 40 wt% Brij® 56/water, the data show four Bragg peaks with a ratio of $1{:}\sqrt{2}:\sqrt{3}:\sqrt{4}$ consistent with the BCC phase. As the concentration increases to 50 wt%, the data show the $\mathrm{H_I}$ phase characterised by three Bragg peaks in a ratio of $1{:}\sqrt{3}:\sqrt{4}$. At concentrations from 60 to 80 wt% of Brij® 56/water, new peaks appear along with the $\mathrm{H_I}$ phase for the $\mathrm{L_\propto}$ phases with a ratio of 1:2:3. These SAXS data are in agreement with the CPLM and previous study by Elliott *et al.*[142]

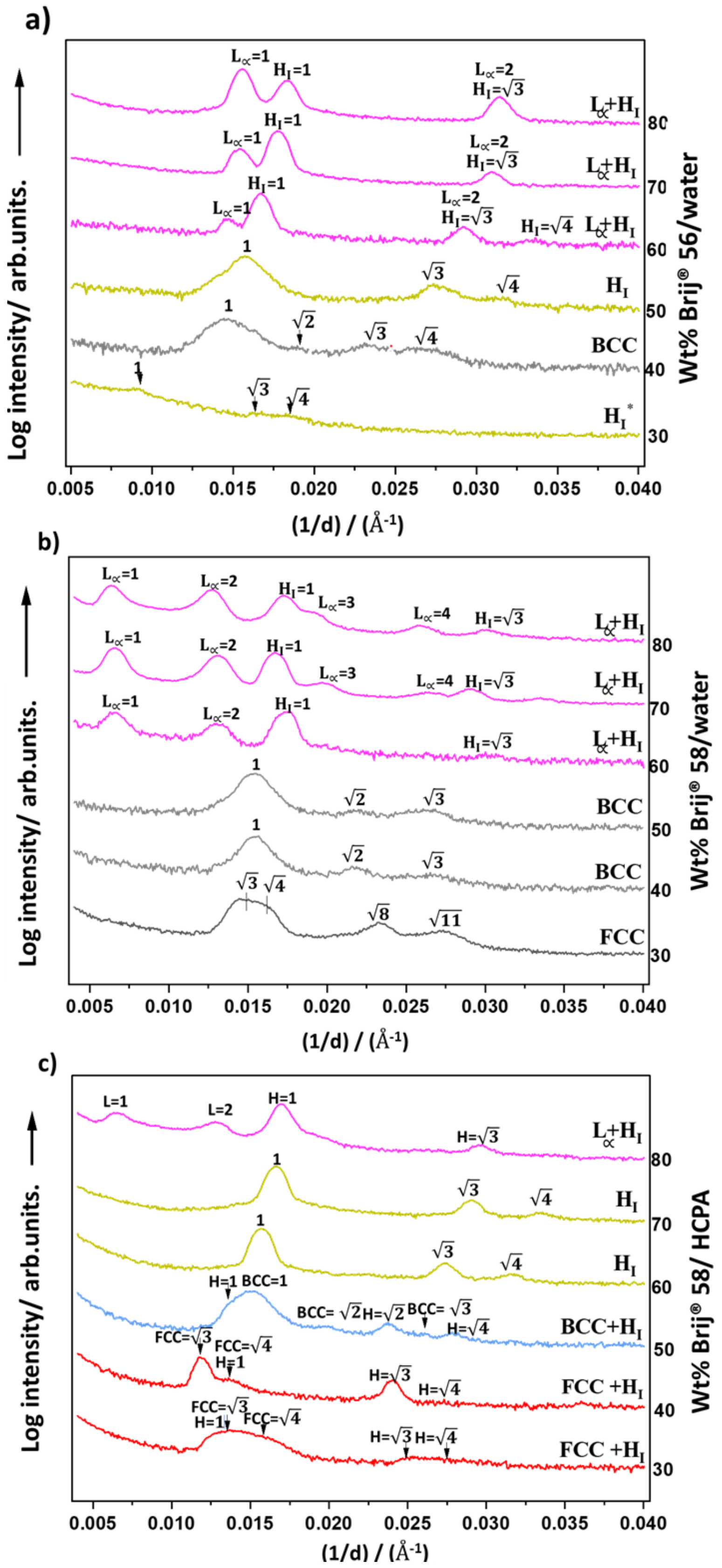

Figure 3.6 SAXS intensities of a) Brij® 56 in water, b) Brij® 58 in water and c) Brij® 58 in HCPA at different concentrations at room temperature. The relative peak position ratios are presented in the plots for hexagonal (H_I) lamellar ($L_\propto$), face centred cubic (FCC) and body centred cubic (BCC). The intensity profiles are plotted on the logarithmic scale.

Figure 3.6 b) indicates the 1D SAXS pattern for Brij® 58/water. At 30 wt% Brij® 58/water, the data exhibit three Bragg peaks with a peak ratio of $\sqrt{3}$: $\sqrt{4}$: $\sqrt{8}$: $\sqrt{11}$ related to the FCC phase. At 40 and 50 wt% of Brij® 58/water, the SAXS data show three Bragg peaks with the ratio of 1: $\sqrt{2}$: $\sqrt{3}$ corresponding to the BCC structure. At higher concentrations from 60 to 80 wt% Brij® 58/ water, the data reveal biphasic $\mathrm{H_I} + \mathrm{L_\propto}$ which is indicated by the Bragg peaks that can be indexed with either the $\mathrm{H_I}$ (1: $\sqrt{3}$: $\sqrt{4}$) or $L_\propto$ (1:2:3) phases. The results are consistent with the previous studies by Gibaud *et al.*[72] and Mahanthappa *et al.*[74]

Figure 3.6 c) reveals the 1D SAXS patterns for Brij® 58/HCPA. The effect of HCPA on the composition of the 30 to 50 wt% Brij® 58 samples, induces the $\mathrm{H_I}$ phase along with the BCC and FCC phases. At 30 and 40 wt% Brij® 58/HCPA the SAXS data reveal FCC + H_I while the 50 wt% Brij® 58/HCPA indicate the BCC + $\mathrm{H_I}$ phases. This unusual phase behaviour was confirmed by the presence of an anisotropic texture for the $\mathrm{H_I}$ phase along with the isotropic texture for the $\mathrm{I_I}$ phase under CPLM (shown in Figure 3.5).

The comparison of the phase diagrams for the Brij® 56 and Brij® 58 systems obtained from CPLM (Figure 3.3, Figure 3.4 and Figure 3.5) with SAXS measurements (Figure 3.6) indicate similar results. However, some differences were observed in biphasic samples due to the difficulties associated with identifying such co-existing phases.

Both CPLM and SAXS data for Brij® 56/ water and Brij® 58/ water reveal the effect of the head group size on the phase behaviour. The noticeable changes in phases are discussed further below:

- The phase separation occurred at 30 wt% of Brij® 56 but not for Brij® 58, due to the differences in the CP. This observation is consistent with the previous study by Bhadane and Patil [73], which showed an increase in the CP with a larger head group.

Consequently, Brij® 58, with a larger head group, exhibited no phase separation at low concentrations in contrast to Brij® 56.

- The FCC and BCC phases were observed over a large domain of the phase diagram for Brij® 58/water mixtures compared to Brij® 56/water. A likely explanation for this behaviour is that the FCC and BCC phases have a highly curved structure, and the increase of the head group size for Brij® 58 favours a greater degree of curvature. Therefore, Brij® 58 creates a more tightly packed and highly curved structure. The findings correspond with the prior research results [146], indicating that the cubic phase is dominant for the system with the larger head group.
- The position of Bragg peaks for the $\mathrm{L}_{\propto}$ phases in Brij® 58/water are shifted to the left compared to the $\mathrm{L}_{\propto}$ phases in Brij® 56/water which mean*s* an increase in the lattice parameter for Brij® 58. This shift in the peak position is due to the differences in the molecular structure, especially the head group size, which leads to a change in the size of micelles.

As this investigation has an interest in exploring the effect of the presence of the HCPA on the phase behaviour of Brij® 58, the visible variations from both CPLM and SAXS are discussed further below:

- The presence of HCPA exhibits unusual phase behaviour for Brij® 58 at low wt%, and the phase transformation series varies from that of Brij® 58/water. At 30, 40 and 50 wt%, the presence of HCPA induced the $\mathrm{H_I}$ phase alongside the FCC and BCC phases for Brij® 58.
- The presence of HCPA with Brij® 58 increase the dominance of the higher curvature structures, such as the $\mathrm{H_I}$ phase. This observation is most likely due to the expansion

between the ethylene oxide headgroups of the Brij® 58 and the HCPA, as illustrated in Figure 3.7.

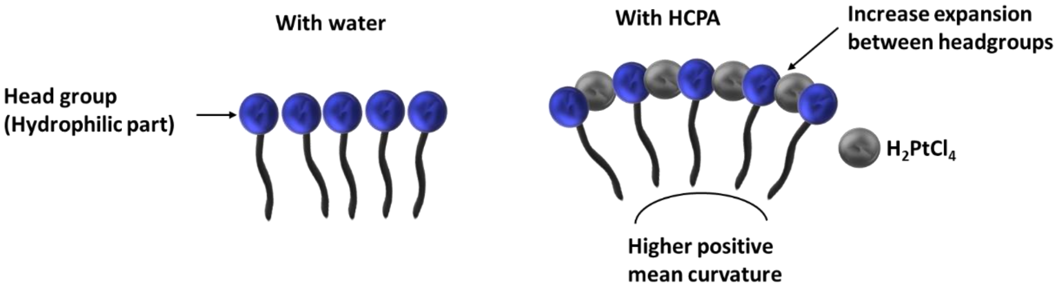

Figure 3.7 The expansion between HCPA and head groups of Brij® 58 resulting in the arrangement of high curvature aggregates

- The Brij® 58/HCPA mixtures with compositions from 30 wt% to 60 wt% exhibited reactivity at high temperatures. A chemical reaction happened when the Brij® 58 /HCPA mixture overheated at a high temperature (80 °C) after two days of preparation. This reaction was observed by changing the colour of the mixture from orange to black. More discussion of the reactivity of Brij 58/HCPA mixtures is presented in section 3.3.2.

It is essential to compare these findings with the earlier studies which investigated the effect of HCPA on the phase behaviour of Brij® 56.[71,127] The results agreed with the previous investigations in some aspects, such as stabilising the high curvature phases as the $\mathrm{H_I}$ phase over high temperatures. However, this study showed unusual phase behaviour of Brij® 58 at lower compositions in the presence of HCPA, emphasising the unique influence of HCPA on Brij® 58 due to its large head group size.

Further analysis has been done to measure and compare the lattice parameters for different phases in each system, and the details for the lattice parameter measurements are discussed in Chapter 2. The lattice parameters for Brij® 56/ water, Brij® 58/water, and Brij® 58/HCPA were measured from the data in Figure 3.6 and presented in Figure 3.8.

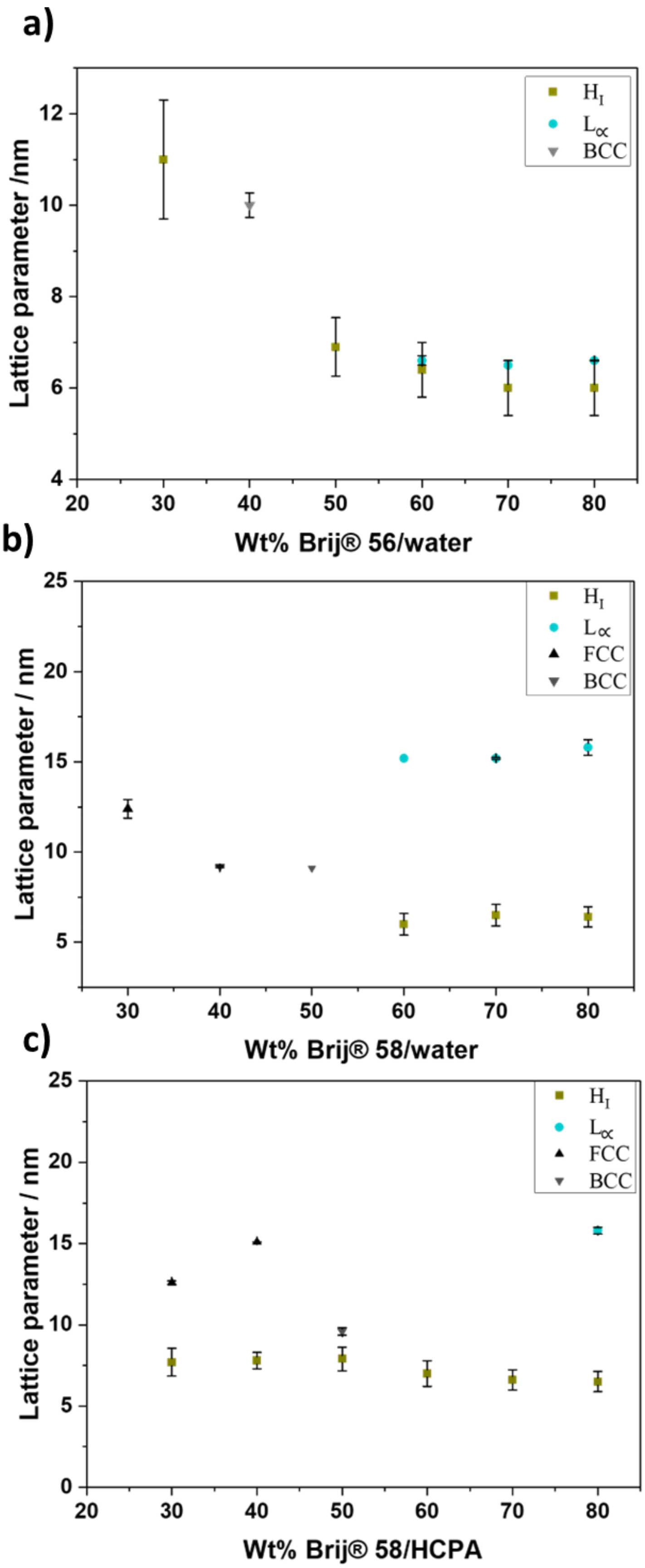

Figure 3.8 The lattice parameter for each phase of a) Brij® 56 in water, b) Brij® 58 in water and c) Brij® 58 in HCPA at different concentrations for different phases.

Figure 3.8 a) shows the lattice parameter of the Brij® 56/water system. The $\mathrm{H_I}^*$ phase at 30 wt% of Brij® 56/water shows the lattice parameter $a_{\mathrm{H_I}} = 11 \pm 1.3$ nm. The BCC phase at 40 wt% of Brij® 56/water shows the lattice parameter a_{BCC} = 9.8 $\pm$ 0.27 nm. At 50 wt% of Brij® 56/water displayed $\mathrm{H_I}$ phases, and the $a_{\mathrm{H_I}}$ showed 7.0 $\pm$ 0.64 nm, which is similar to the previous study that reported 7.5 nm.[71] At a higher wt% of Brij® 56 (from 60% to 80%), the samples show a biphasic nature consisting of the $\mathrm{H_I}$ and $\mathrm{L_\propto}$ structures with similar values of the lattice parameters. The $\mathrm{H_I}$ phase shows a slight decrease in the $a_{\mathrm{H_I}}$with the increase in wt % for Brij® 56 with values of 6.4 $\pm$ 0.60, 6.0 $\pm$ 0.60 and 6.0 $\pm$ 0.60 nm for 60, 70, and 80 wt%, respectively. Likewise, the $\mathrm{L_\propto}$ phase for 60, 70 and 80 wt% of Brij® 56 show values of $a_{\mathrm{L_\propto}}$= 6.6, $\pm$ 0.1, 6.5 $\pm$ 0.01 and 6.5$\pm$ 0.01 nm, respectively, which is slightly larger than the previous study that exhibited 5.7 nm for the $\mathrm{L_\propto}$ phase.[71] Asghar *et al*. reported a model that explains how the Brij® 56 volume fraction determines the lattice parameter of $\mathrm{H_I}$ and gyroid structures.[71] They showed that the lattice parameter decreases as the volume fraction increases. The findings of this study for the $\mathrm{H_I}$ lattice parameter followed the reported model.

Figure 3.8 b) reveals the lattice parameter of Brij® 58/ water mixtures. The FCC structure at 30 wt% Brij® 58/water shows a_{FCC} = 12.4 $\pm$ 0.52 nm, close to prior research that showed 13.0 nm for the FCC phase.[74] The BCC phase at 40 and 50 wt% Brij® 58/water show a_{BCC} = 9.1 $\pm$ 0.06 nm agrees with the previous study[74], which reported 9.2 nm. At higher concentrations from 60 wt% to 80 wt% Brij® 58/ water, the samples show the biphasic of the $\mathrm{L_\propto}$ and $\mathrm{H_I}$ structures. The $\mathrm{H_I}$ phase displays $a_{\mathrm{H_I}}$ = 6.0 $\pm$ 0.60, 6.5 $\pm$ 0.60 and 6.4 $\pm$ 0.55 nm while the $\mathrm{L_\propto}$ phase indicates $a_{\mathrm{L_\propto}}$= 15.2 $\pm$ 0.01, 15.2 $\pm$ 0.05 and 15.8 $\pm$ 0.44 nm for 60, 70 and 80 wt% Brij® 58/ water, respectively. These values are similar to the previous study [72], which exhibited $a_{\mathrm{H_I}}$ = 7.1 and $a_{\mathrm{L_\propto}}$=16.5 nm. Surprisingly, the results for the lattice parameter of the

$\mathrm{H_I}$ phase in Brij® 58/ water system did not follow the model reported by Asghar *et al.*[71] This is perhaps to be expected given the ill-defined nature of Brij® 58 micelles' surface (hairy micelles), which differ from the well-defined hard sphere micelles of Brij® 56. This difference may indicate why the reported model applies for Brij® 56 but not for Brij® 58.

Figure 3.8 c) shows the lattice parameters for the Brij® 58/HCPA. The FCC phase shows a_{FCC} =12.7 $\pm$ 0.1 nm and 15.1 $\pm$ 0.01 nm which are larger than the FCC phase for Brij® 58/water. The new regions of the $\mathrm{H_I}$ phase that were presented at concentrations 30, 40 and 50 wt% Brij® 58/HCPA show $a_{\mathrm{H_I}}$ = 7.7 $\pm$ 0.86 , 7.8 $\pm$0.95 and 7.9 $\pm$ 0.05 nm, respectively. However, the $\mathrm{H_I}$ phase at 60, 70 and 80 wt% Brij® 58/HCPA show a slight decrease with values of $a_{\mathrm{H_I}}$ = 7.0 $\pm$ 0.79, 6.7 $\pm$ 0.60 and 6.6$\pm$ 0.63 nm, respectively. The increase in the $a_{\mathrm{H_I}}$ at 30, 40 and 50 wt% Brij® 58/HCPA could be due to the size of the micelles for Brij® 58 that further increases in the presence of a high concentration of HCPA, as explained above in Figure 3.7.

When comparing the lattice parameters of the $\mathrm{L_\propto}$ and $\mathrm{H_I}$ phases at high concentrations from 60 to 80 wt% for both Brij® 56/water (Figure 3.8 a)) and Brij® 58/water (Figure 3.8 b)), it exhibited that the $a_{\mathrm{L_\propto}}$values are higher in Brij® 58 than Brij® 56. This difference is attributed to the larger hydrophilic head group of Brij® 58. Surprisingly, the $a_{\mathrm{H_I}}$ values are similar for both systems, contrary to expectations of having a larger value for the Brij® 58. As the $a_{\mathrm{H_I}}$ is determined by the distance between the centre of the two adjacent cylinders, it is speculated that the values are similar due to the thinner wall in the $\mathrm{H_I}$ phase of the Brij® 58 compared to Brij® 56. Although the $a_{\mathrm{H_I}}$of both systems show similar values; the size of the micelles differs, implying a variation in the pore size for the produced mesoporous materials. A schematic to explain this speculation is presented in Figure 3.9. The schematic illustrates a larger micelle size for the $\mathrm{H_I}$ phase of the Brij® 58 system with the lattice parameter that is similar to Brij® 56 which produces different wall thicknesses for Brij® 56 and Brij® 58.

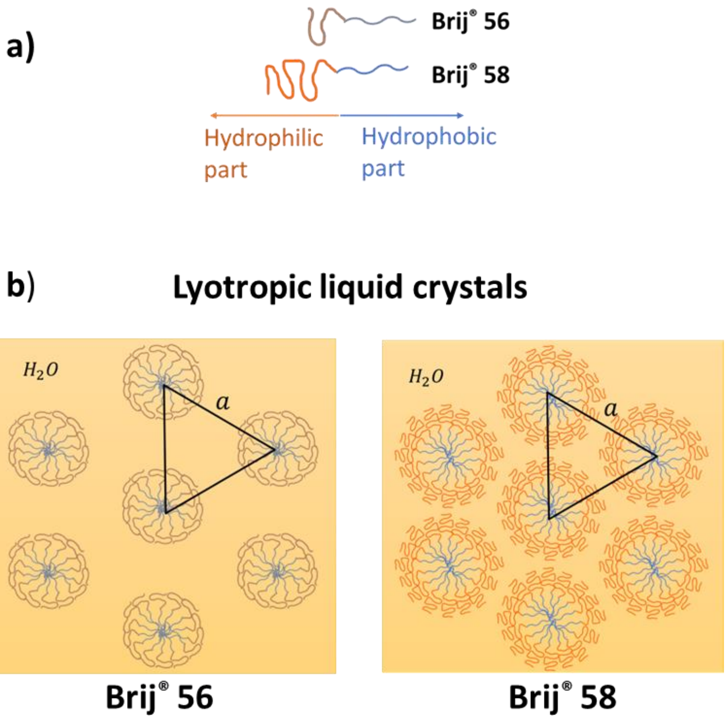

Figure 3.9. Schematic representation of the cross-sectional view model Brij® 58 and Brij® 56. a) show head groups and hydrocarbon chains for Brij® 56 and Brij® 58 b) representative model of hexagonal cylinders of lyotropic liquid crystals of Brij® 56 and Brij® 58 and "a" represents a lattice parameter.

It is important to note that the interaction between HCPA and the headgroup of surfactants is not required for nanostructured material templating. However, these behaviours have significant implications for selecting a template to produce nanostructured materials. From this investigation, 30% and 40 wt% of Brij® 58/HCPA were chosen to produce mesoporous platinum (discussed in chapters 4 and 5).

The following section discusses the reactivity property of Brij® 58 with HCPA detected at the compositions from 30 to 60 % Brij® 58/HCPA. This reactivity for the Brij® 58/HCPA template participated in the formation of platinum nanoparticles.

3.3.2 The investigation of the in-situ reactivity of Brij® 58 ≥ 30 wt%

The Brij® 58/HCPA mixtures were heated after two days of the preparation to mix and ensure that the mixtures were homogenous. Surprisingly, the colour of the mixtures changed from orange to black. This shifting in the colour indicates the sample's reactivity towards the fabrication of platinum nanoparticles. Therefore, additional samples were prepared (Table 3.5), and the details of the preparation process of the black mixtures are discussed in section 3.2.1. The production of platinum nanoparticles is indicated by the change in the colour of Brij® 58/HCPA mixtures from orange to black, as shown in Figure 3.10.

Figure 3.10 shows the evidence of the fabrication of platinum nanoparticles from the LLC of Brij® 58/HCPA mixtures at various concentrations while changing colour gradually over three days. On the first day, the mixtures were orange, and there was no indicator of the production of platinum nanoparticles. Then, on the second day, the colour of the mixtures at concentrations of 30, 40, 50 and 60 %wt of Brij® 58/HCPA changed to brownish after two cycles of heating for 20 minutes. The brownish colour indicates the initial reduction of HCPA and the formation of small platinum nanoparticles. Moving on to the third day, the Brij® 58/HCPA mixtures with concentrations of 50 and 60 wt% of Brij® 58/HCPA exhibited a noticeable colour change to black within 10 minutes of heating. Further heating was applied to the mixtures for 30 minutes, resulting in a colour change to black for the mixtures ranging from 30 to 60 wt% of Brij® 58/HCPA. The change of the colour to black indicates the growth of platinum nanoparticles to a larger size. As reported previously, platinum nanoparticles of a larger size can absorb more light, resulting in a change in colour from brownish to black.[147] However, the mixtures at higher concentrations of 70 and 80 wt% Brij® 58/HCPA did not exhibit any colour change, indicating no platinum nanoparticle formation at these concentrations. The likely explanation for not producing platinum particles in 70 wt% and

80 wt% of Brij® 58/HCPA is due to having less water compared to the other compositions. This agrees with previous studies showing that water could play an essential role in forming platinum nanoparticles as it leads to faster production and accelerates the rate of chemical reduction.[35,53] The faster reaction in the presence of water is due to an autocatalytic effect.

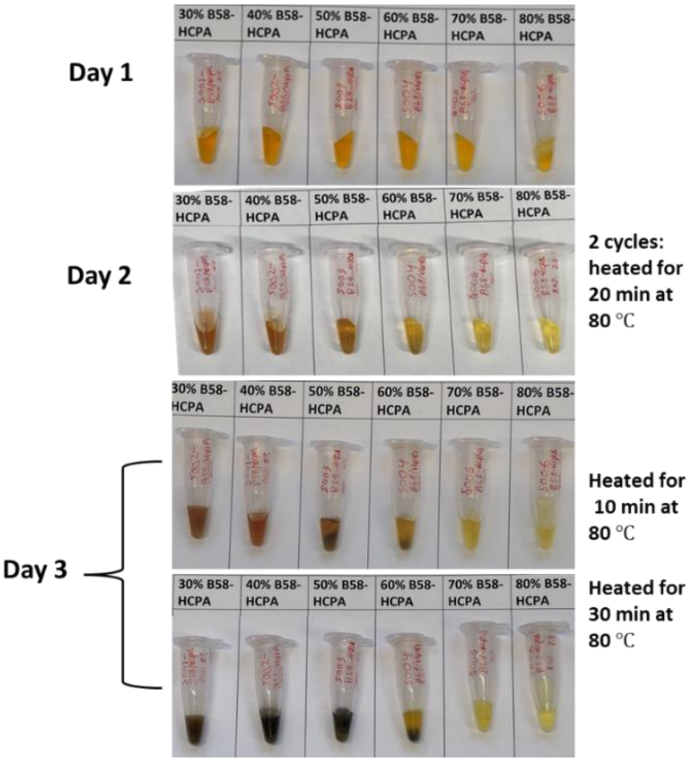

Figure 3.10 The chemical reaction over three days and a high temperature 80 ℃ for Brij® 58/HCPA at different compositions.

3.3.2.1 Small angle X-ray scattering

The black mixtures (the platinum nanoparticles with Brij® 58) at compositions of 30, 40, 50 and 60 %wt of Brij® 58/HCPA were studied by SAXS at room temperature and are shown in Figure 3.11.

Figure 3.11 a-d) show the 1D SAXS patterns which reveal three or four Bragg peaks indexed with either the FCC ($\sqrt{3}:\sqrt{4}$) or $\mathrm{H_I}$ ($1:\sqrt{3}:\sqrt{4}$) structures. The 2D SAXS data show rings confirming polydomain crystalline structures.

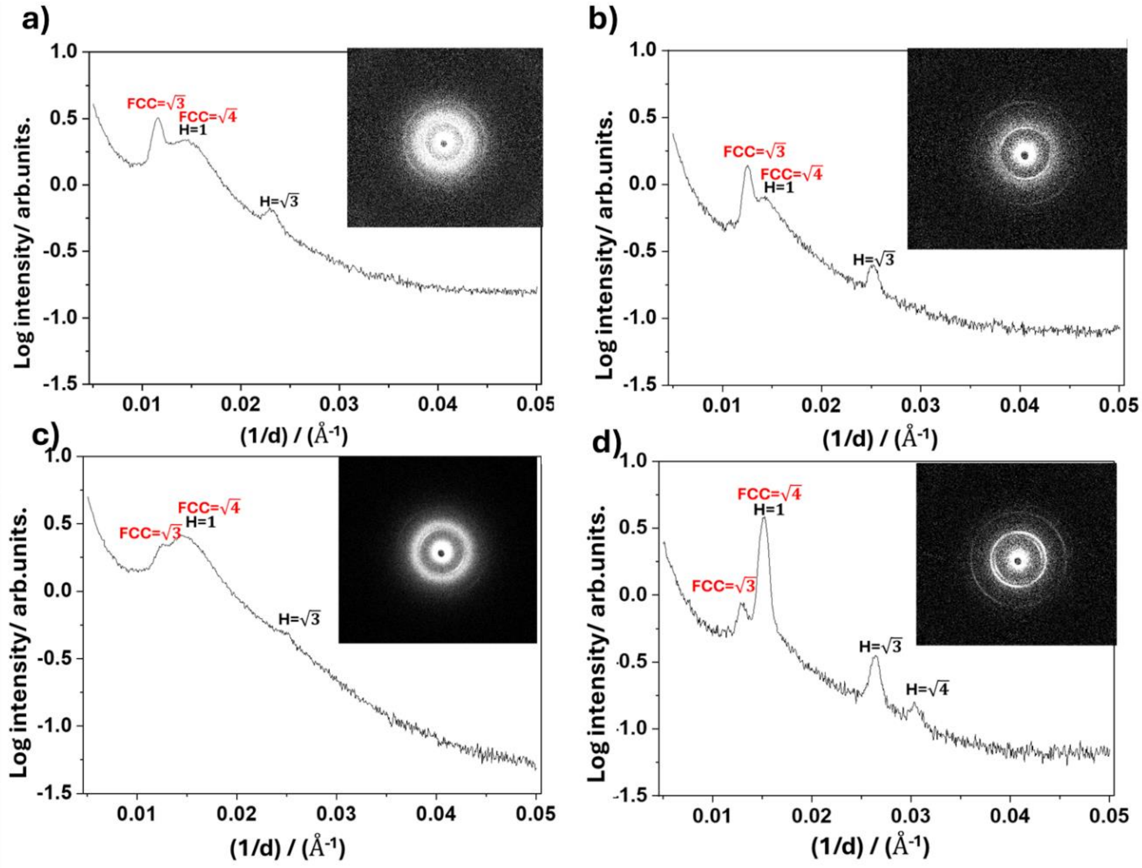

Figure 3.11 1D SAXS pattern of Brij® 58/HCPA mixtures after chemical reaction at different wt% a) 30 wt% , b) 40 wt%, c) 50 wt% and d) 60 wt %of Brij® 58/HCPA. The 2D SAXS patterns are inserted, and the relative peak position ratios are presented above the peaks. The SAXS measurements were collected at room temperature. The intensity profiles are plotted on the logarithmic scale.

The SAXS data for 30 and 40% Brij® 58/HCPA are in agreement with the data for 30 and 40% Brij® 58/HCPA without the chemical reaction shown previously in (Figure 3.6 c)) which exhibit a biphasic mixture of the FCC + $\mathrm{H_I}$ phases. However, the 50 and 60 wt% of Brij® 58/HCPA show different behaviour compared to the 50 and 60 wt% Brij® 58 /HCPA without the chemical reaction shown previously in (Figure 3.6 c) which revealed BCC+ $\mathrm{H_I}$ phase for 50 wt% and a pure $\mathrm{H_I}$ phase for 60 wt%. This change could be due to the chemical reaction. The SAXS data indicates that the formation of mesoporous platinum has not destroyed the template. The lattice parameter was measured from SAXS data for Brij® 58/HCPA without the chemical reaction (Figure 3.6) and after the chemical reaction (Figure 3.11) and is presented in Table 3.6.

Table 3.6 The lattice parameter measured from the SAXS data for each phase of Brij® 58 /HCPA with and without the chemical reaction.

Composition of Brij® 58/HCPA	Without chemical reaction				With chemical reaction			
	FCC	BCC	H_I	$L_\propto$	FCC	BCC	H_I	$L_\propto$
30%	12.7±0.1	--	7.7±0.86	--	14.7±0.27	--	7.7±0.64	--
40%	15.1±0.01	--	7.8±0.50	--	13.8±0.03	--	7.4±0.71	--
50%	--	9.6±0.25	7.9±0.73	--	13.9±0.06	--	7.3±0.74	--
60%	--	--	7.0±0.79	--	13.3±0.02	--	6.9±0.70	--

Table 3.6 shows slight variations in the lattice parameters for Brij® 58/HCPA without and with the chemical reaction. Therefore, this chemical reaction is believed to be true liquid crystal templating

3.3.2.2 Transmission electron microscopy

The TEM measurement was used to study the polydisperse mesoporous platinum nanoparticles produced at 30, 40, 50 and 60 wt% of Brij® 58/HCPA, as presented in Figure 3.12.

Figure 3.12 a-d) show the TEM images that provide visible conformation of the successful production of the porous morphology of polydisperse platinum nanoparticles from the LLC of Brij® 58/HCPA with concentrations from 30 to 60 wt%. The insert images in Figure 3.12 a-d) display magnified images to show the open porous structure. It is worth noting that the TEM images of porous platinum nanoparticles in this study reveal overlapped platinum nanoparticles, not spread spherical particles, which differs from what was shown in the literature.[28,40,41,148] The likely explanation is because of the different methods utilised to produce platinum nanoparticles.

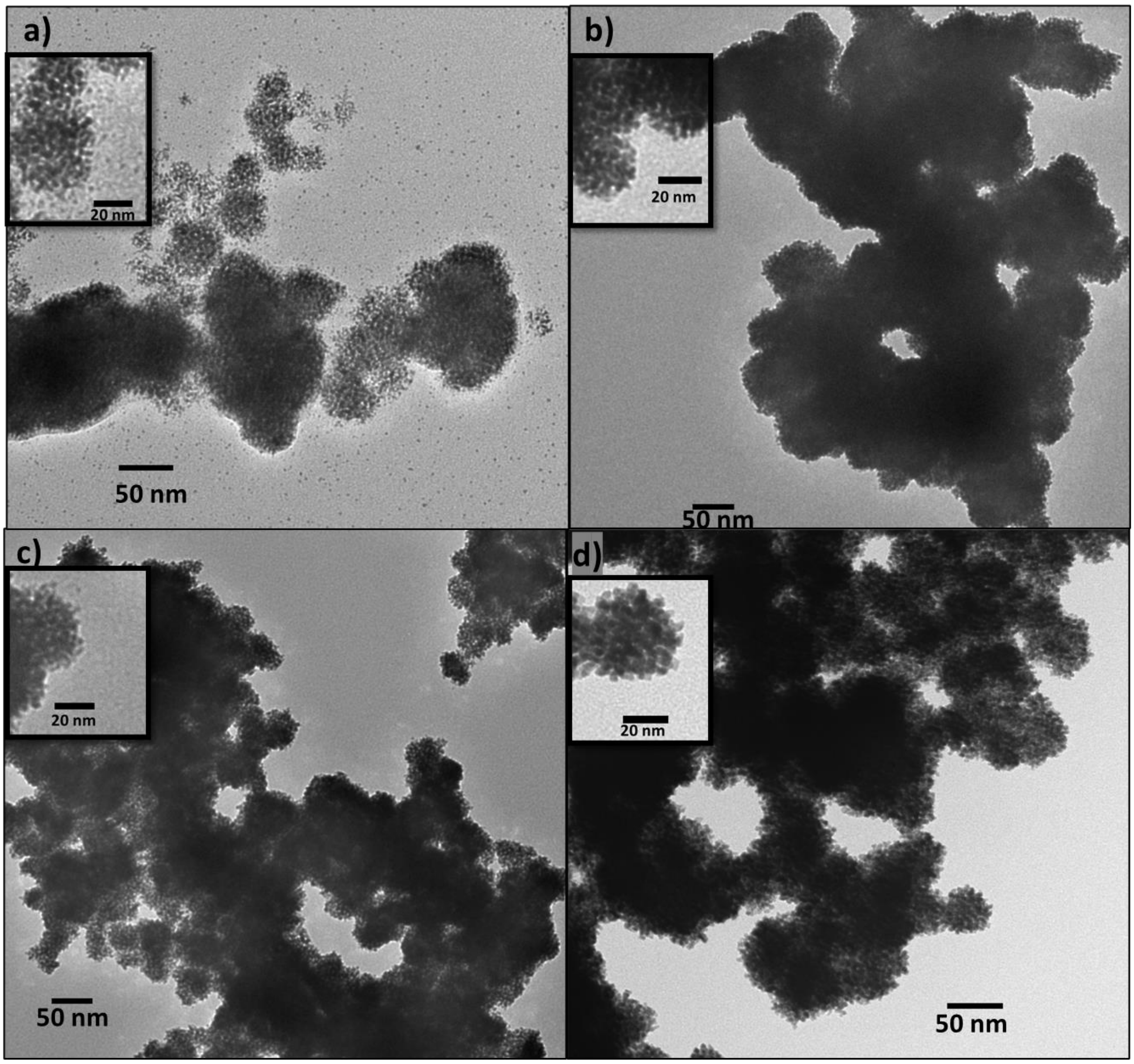

Figure 3.12 TEM images taken at different magnifications for platinum nanoparticles chemically fabricated: a) 30 wt%, b) 40 wt%, c)50 wt% and d)60 wt% of Brij®58/HCPA. The inserts show the zoomed area, and the image illustrates the scale bar.

In previous studies, the micelle assembly approach (low concentrations just above the CMC) typically with additional chemical reductants has been used, whilst in this study, the LLC approach (concentrations ≥ 30 wt%) with no additional reductant has been used to fabricate platinum nanoparticles. Although most previous studies concentrate on the stabilising role of surfactants in the fabrication of polydisperse platinum nanoparticles, this study displayed a supplemental role of Brij® 58, which have the capability to act as a reducing agent.

It is speculated that the reduction of platinum in this study happens in a similar way to polyol synthesis.[34] Thus, in the presence of water and high temperatures, polyethylene glycol (head group in Brij® 58) acts as a reducing agent, facilitating the reduction of platinum. The possible reaction of HCPA (H_2PtCl_6) with the ethanol group in Brij® 58 [149]:

$$\mathbf{2R[OCH_2CH_2]_nOCH_2CH_2OH + H_2PtCl_6 \rightarrow 2R[OCH_2CH_2]_nOCH_2CHO + Pt + 6H^+ + 6Cl^-}$$

Equation 3.1 possible chemical reaction of H_2PtCl_6 with Brij® compounds such as Brij® 58.

This is a general hypothesis for reducing platinum from HCPA to produce platinum nanoparticles. It is a challenge to understand the nucleation steps for platinum nanoparticle preparation due to the limitation of the detection measurements in this study, which has used only SAXS and TEM measurements to investigate the formed platinum nanoparticles. In contrast to common beliefs, the results of this study reveal that the functions of Brij® 58 can both stabilise and produce platinum particles. This discovery expands the knowledge and the roles of Brij® 58 in platinum nanoparticle synthesis. Further analysis was conducted to study the porosity using the TEM images, as shown in Figure 3.13.

Figure 3.13 a-d) present the TEM images for the platinum nanoparticles fabricated from 30, 40, 50 and 60 wt% Brij® 58/HCPA, respectively. The TEM images reveal fully open porous particles. However, the specific structure of these pores is unclear from the provided TEM images. The lattice parameter was analysed using Image J to determine the distance between one light spot and another. The average lattice parameter was found to vary with different concentrations of Brij® 58/HCPA, which show ~ 7.4 $\pm$ 0.12 nm, 7.4 $\pm$ 0.20 nm, 6.6 $\pm$ 0.28 nm and 5.9 $\pm$ 0.33 nm for 30, 40, 50 and 60 wt% Brij® 58/HCPA, respectively. The lattice parameter values decrease with the increase of Brij® 58 concentration. The lattice parameter from the TEM measurements reveals slightly smaller values compared with the lattice parameter for the $\mathrm{H_I}$ phase measured from SAXS, as shown in Table 3.6. The lattice parameter from the TEM data exhibits the same trend of reducing the values with an increase in the concentration of Brij® 58 (Table 3.6).

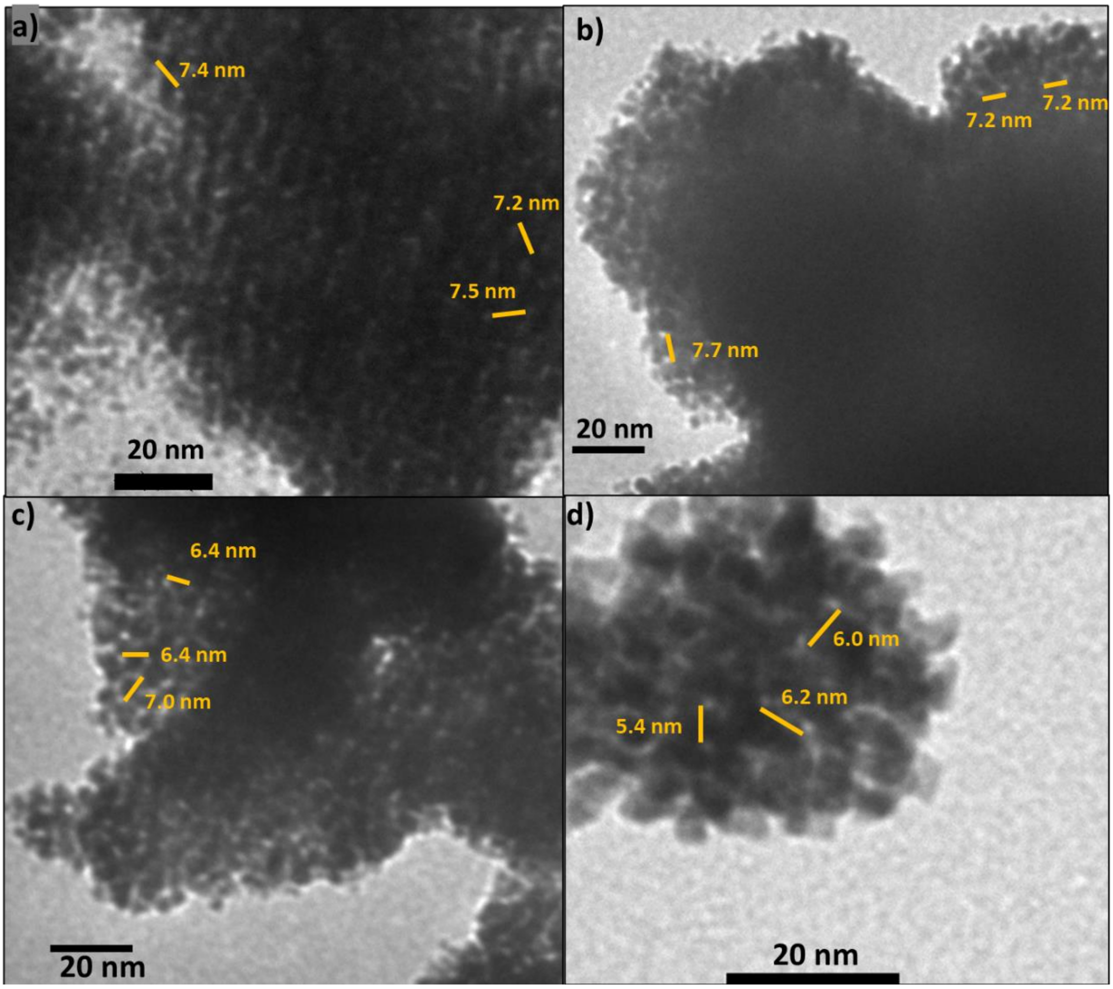

Figure 3.13 TEM images illustrating the lattice parameter for porous platinum nanoparticles at different concentrations a) 30 wt%, b) 40 wt%, c) 50 wt% and d) 60 wt% of Brij® 58/HCPA at scale bar 20 nm.

Further analysis for the mesoporous platinum particles was carried out, and histograms for the average particle diameter from the TEM images were created, as shown in Figure 3.14.

Figure 3.14 exhibits the TEM images that display a large amount of mesoporous platinum nanoparticles. Measuring the size of the mesoporous platinum nanoparticles showed that the particle diameter ranges depending on the composition of the template. It should be noted that some of the TEM images show overlapped particles, which caused issues in identifying the size of the particles. Therefore, the measurements were repeated for each sample using two different TEM images.

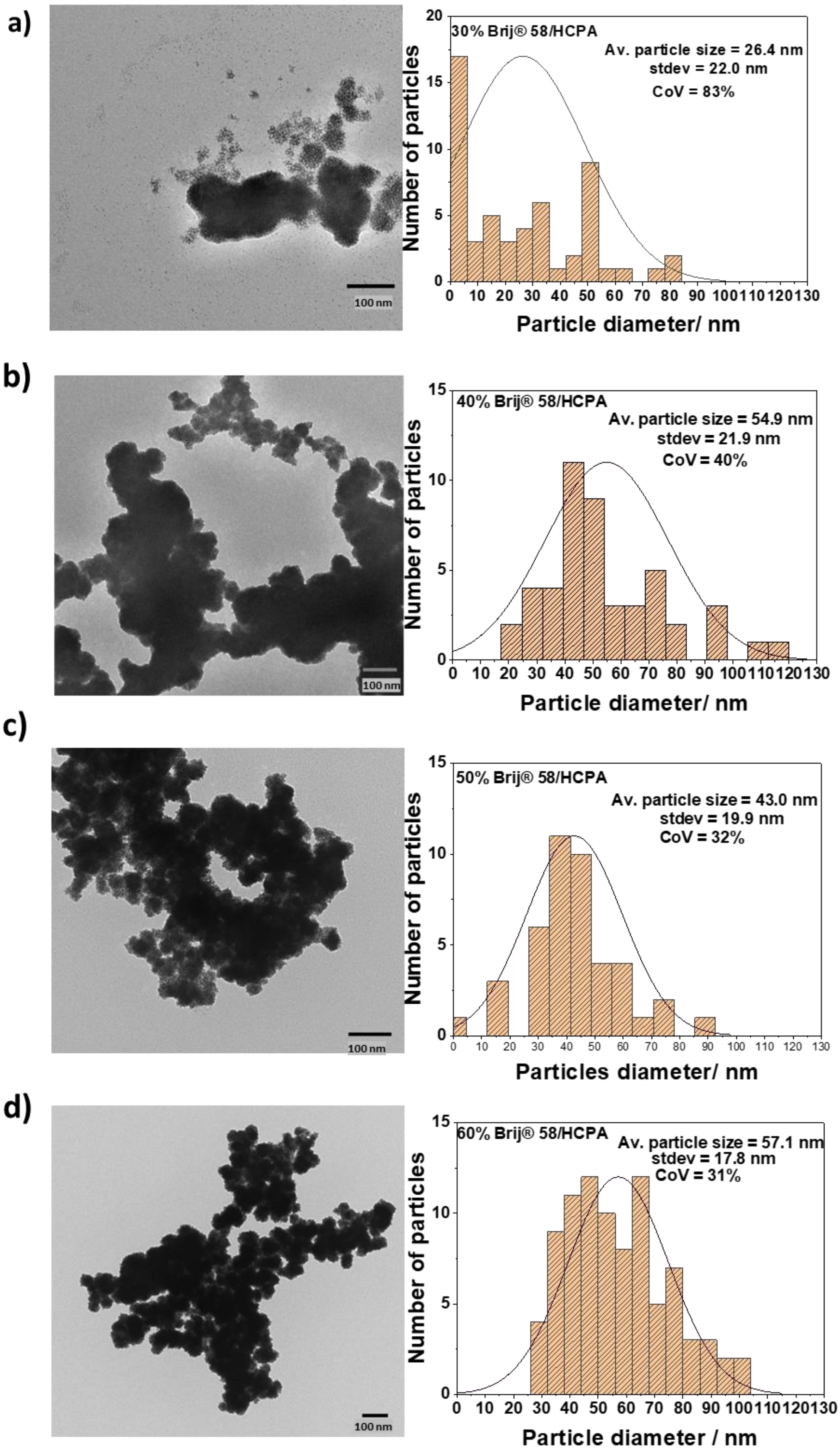

Figure 3.14 (left) TEM images (right) Histograms for platinum nanoparticles chemically fabricated from: a) 30 wt%, c) 40 wt%, e) 50 wt% and g) 60 wt% of Brij®58/HCPA. Histograms are an estimate based on manual measurement using image J for each platinum nanoparticle. The average particle size, the standard deviation (stdev) and the coefficient of variation (CoV) are shown in the plots.

In Figure 3.14 a) the TEM image for the mesoporous platinum nanoparticles fabricated from 30 wt% Brij® 58/HCPA indicates the presence of very small platinum particles (1-2 nm) that could be nucleated to produce larger sizes of mesoporous platinum nanoparticles. The histogram shows the average size to be 26.4 nm ± 22.0 nm, and the coefficient of variation (CoV) was 83%, meaning the particles have different sizes and are not evenly distributed.

In Figure 3.14 b-d), the TEM images for mesoporous platinum nanoparticles were produced from 40, 50, and 60 wt% Brij® 58/HCPA, respectively. These TEM images differ from Figure 3.14 a) and show only the large size of mesoporous platinum nanoparticles. The histograms show that the average particle diameter ranges from 41 to 57 nm, and the CoV ranges from 31 to 40 wt%.

The size of mesoporous platinum nanoparticles in this study is similar to the previous study by Yamauchi *et al.* [40], which used Brij® 58 in the presence of a chemical reductant to produce 60 nm dendritic platinum nanoparticles at 60 ℃. However, the size of the mesoporous platinum nanoparticles in this study exhibits a different trend compared to another previous study by Yamauchi *et al.* [41], which used several concentrations of Brij® 58, ranging from 0.01 wt% to 20 wt%.[41] Their results show that the increase of the Brij® 58 concentration leads to a decrease in the particle size due to increased viscosity at higher concentrations, which prevents the grain growth of platinum as the platinum species diffusion decreases and then reduces the particle size.[41] Their findings showed that at 0.01% Brij® 58, the size of platinum particles was 170 nm, while at 20% Brij®58 reduced significantly to 26 nm.[41] This study shows that the 30% Brij® 58 indicates a similar size to the 20% Brij® 58 in the previous study, which was 26 nm [41]. However, this study also explores higher concentrations of 40, 50 and 60 wt% of Brij®58 and shows larger particle sizes ranging from 41 to 57 nm. Therefore, these findings show that the relationship between particle size and Brij®58 concentration is non-linear and complex at high temperatures.

It should be noted that mesoporous platinum nanoparticles offer a high surface area and enhance the accessibility of species, which improves the electrocatalytic activity. The previous studies reported high electrocatalytic activity for platinum nanoparticles for catalytic applications such as methanol[28,41] and oxygen reduction[148]. Therefore, the mesoporous platinum particles fabricated in this study with an open porous structure may be highly beneficial for enhancing accessibility to the platinum surface and thus could potentially show high catalytic performance for catalytic applications. When preparing LLC phases for electrodeposition, this chemical reactivity was avoided by minimizing exposure to high temperatures.

3.4 Conclusion

The work reported in this chapter showed the differences in the phase behaviour of Brij® 58/ water and Brij® 56/water with different head group sizes. The results showed that the Brij® 58, which has a larger head group size compared to Brij® 56, prefers high-curvature structures such as FCC, BCC, and $\mathrm{H_I}$ phases. Also, the findings showed that the $a_{\mathrm{L}_\propto}$=15.8 nm for Brij® 58, while for Brij® 56, it was 6.5 nm, indicating a larger micelle size for Brij® 58. The results suggest that the $\mathrm{H_I}$ phase in Brij® 58 exhibits thinner wall thickness than that of Brij® 56, attributed to the larger micelles for Brij® 58 while maintaining a similar lattice parameter to Brij® 56 with a value of $\sim$ 6.8 nm. Besides, this study reports the effect of HCPA on Brij® 58 phase behaviour for the first time. The results demonstrated exciting behaviour, and the interaction between HCPA and the headgroup of Brij® 58 induced a new region of the $\mathrm{H_I}$ phase at lower concentrations of Brij® 58. The new $\mathrm{H_I}$ phase region was observed with either the FCC or BCC phase at 30, 40 and 50 wt% of Brij® 58/HCPA. Moreover, the presence of HCPA enhanced the stability of the $\mathrm{H_I}$ phase at larger concentrations of Brij® 58. Additionally, HCPA slightly swells the Brij® 58 micelles, which is attributed to the slight increase in the lattice parameter for Brij® 58 at different phases. At 60 wt% Brij® 58 $a_{\mathrm{H_I}}$ was 6.0 nm in water and increased to 7.0 nm in HCPA. Besides, the $a_{\mathrm{H_I}}$ showed slightly decreasing values from 7.8 nm to 6.5 nm with an increase in the Brij® 58 concentrations.

Moreover, this study showed the use of Brij® 58/HCPA at concentrations ≥ 30 wt% for producing mesoporous platinum nanoparticles for the first time. The production of mesoporous platinum nanoparticles was successfully achieved by heating the Brij® 58/HCPA mixtures at 80 °C without using common reducing agents. This investigation proposes a polyol synthesis-like mechanism for platinum reduction facilitated by polyethylene glycol in Brij® 58. The mesoporous platinum nanoparticles exhibited lattice parameters ranging from ~ 5.4 to 7.7 nm, corresponding to the lattice parameter of the $\mathrm{H_I}$ phase obtained from SAXS for the template. The mesoporous platinum particle demonstrated sizes ranging from ~ 23 to 57 nm.

Chapter 4- FCC$_{\text{Brij® 58}}$ templating of mesoporous platinum electrodes, their characterisation and electrocatalytic properties for ethanol oxidation

4.1 Introduction

This chapter focuses on the production of mesoporous platinum employing the Brij® 58 as a directing agent in the LLC templating with the FCC structure. Attard *et al*. demonstrated the effectiveness of direct templating from LLC, offering a straightforward, environmentally friendly and cost-effective way to fabricate ordered nanostructures with various morphologies.[6] Previous studies demonstrated the utilisation of Brij® 56 to create mesoporous metals with a 2D hexagonal array.[9,20,150] However, recent attention has shifted towards producing mesoporous materials with a 3D structure, which offer distinct advantages compared to other structures and could be achieved by employing bicontinuous cubic phases as a template.[8,151]

The utilisation of Brij® 58 which has larger micelles size than Brij® 56, favours highly curved phases such as the FCC and BCC and shows a slight swelling in the presence of HCPA, which could increase the possibility of producing mesoporous platinum with a larger pore size compared to the use of Brij® 56. In literature, the Brij® 58 has been used in a micellar approach (at a low concentration just above the CMC) to chemically synthesise porous platinum nanoparticles with 2-4 nm pore diameter in the presence of reducing agents.[28,40,41,148] Additionally, Brij® 58 was used previously at a low concentration just above the CMC at 1.0 wt% in electrochemical deposition to produce platinum–palladium alloy films with a pore size of 7 nm.[152] Yamauchi *et al*. also reported the fabrication of mesoporous platinum using various surfactants, including Brij® 58 at concentrations of 1.0 wt%, resulting in mesoporous platinum and ECSA of 43 m^2 g^{-1}.[153] Another study by Yamauchi *et al*. used the electrodeposition method employing various concentrations from 0.005 to 3.0 wt% of Brij® 58 to produce mesoporous Pt–Ru alloy, confirming that the Brij® 58 with the concentration less than the CMC did not produce the mesoporous structure while, the concentrations above the CMC created the mesoporous structure.[154] The produced mesoporous platinum and bimetallic mesoporous platinum indicated high catalytic activity towards methanol oxidation.[152–154]

However, there is limited literature on the specific application of LLC containing Brij® 58 with a high concentration for producing a distinct structure of mesoporous platinum films. Therefore, this current study investigated employing the FCC structure of 40 wt% Brij® 58 for the fabrication of mesoporous platinum for the first time. The initial focus was the structural analysis of 40 wt% Brij® 58 using SAXS and followed by an exploration of its ability to produce mesoporous platinum films by electrodeposition at various potentials. Furthermore, the electrocatalytic activity of the films towards ethanol oxidation was investigated.

Aims:

- To explore the potential of utilising the $FCC_{Brij® 58}$ as a template for depositing high surface area platinum films.
- To investigate how altering the deposition voltage using the $FCC_{Brij® 58}$ template impacts electrode morphology, surface area and catalytic activity

4.2 Methodology

The methodology is divided into two primary sections to align with the aims.

4.2.1 Potential utilising of the $FCC_{Brij^{®}\ 58}$ as a template for platinum deposition

The 40% Brij® 58/HCPA was prepared as described in Chapter 3, and Table 4.1 shows the amount of Brij® 58 and HCPA used in this study.

Table 4.1 Composition of Brij® 58/ HCPA used in this study.

Mass of Brij® 58 /g	Mass of HCPA /g	Wt.% of Brij® 58
0.401	0.601	40.00 ± 0.062%

Initially, the phase of this mixture was investigated using SAXS at room temperature. Then, CV investigated the optimum deposition potentials. The CV was conducted at a platinum electrode with an area of 3.142×10^{-2} cm^2 at room temperature and a scan rate of 10 mV s^{-1} between the limits +0.70 and -0.30 V vs Ag/AgCl.

4.2.2 Impact of deposition voltage using $FCC_{Brij^{®}\ 58}$ template on the electrode morphology, surface area and catalytic activity

The electrodeposition of platinum from the $FCC_{Brij^{®}\ 58}$ template was carried out on polished platinum electrodes with an area of 3.142×10^{-2} cm^2 and platinum foil with an area of ~ 0.2 - 0.5 cm^2 at room temperature. The potential was stepped from +0.60 V to various negative potentials at a fixed time (1800 s), as illustrated in Table 4.2.

Table 4.2 Variation of deposition potential from FCC$_{Brij^{®}\ 58}$ template and corresponding sample name. n= number of measurements. In all cases, the deposition time was 1800 s.

Deposition potential / V	**Sample name**
-0.15 (n=4)	MPE-0.15
-0.20 (n=4)	MPE-0.20
-0.23 (n=4)	MPE-0.23
-0.25 (n=4)	MPE-0.25

The morphology of MPEs was investigated using SEM and the morphology of the platinum foils was examined using TEM, AFM and XRD. The electrochemical characterisation for the MPEs was conducted using the CV in 0.5 M H_2SO_4 to determine the RSA. The catalytic activity towards ethanol oxidation of MPEs was also conducted using CV and EIS in 0.5 M H_2SO_4 + 0.5 M C_2H_5OH electrolyte. EIS was carried out at different applied potentials of 0.20 V, 0.60 V, and 0.80 V vs Ag/AgCl at room temperature. The frequency range applied was 100 kHz to 0.2 Hz, and the AC amplitude was 10 mV.

4.3 Results and discussion

The results are presented and discussed in two primary sections to align with the aims.

4.3.1 Potential utilising of the FCC$_{Brij^{®}\ 58}$ as a template for platinum deposition

4.3.1.1 SAXS characterisation of 40 wt% Brij® 58/HCPA mixture

SAXS was employed to investigate the phase of the 40 wt% Brij® 58/HCPA template before being used to fabricate MPEs. The SAXS patterns for 40 wt% Brij® 58 in water and HCPA are shown in Figure 4.1.

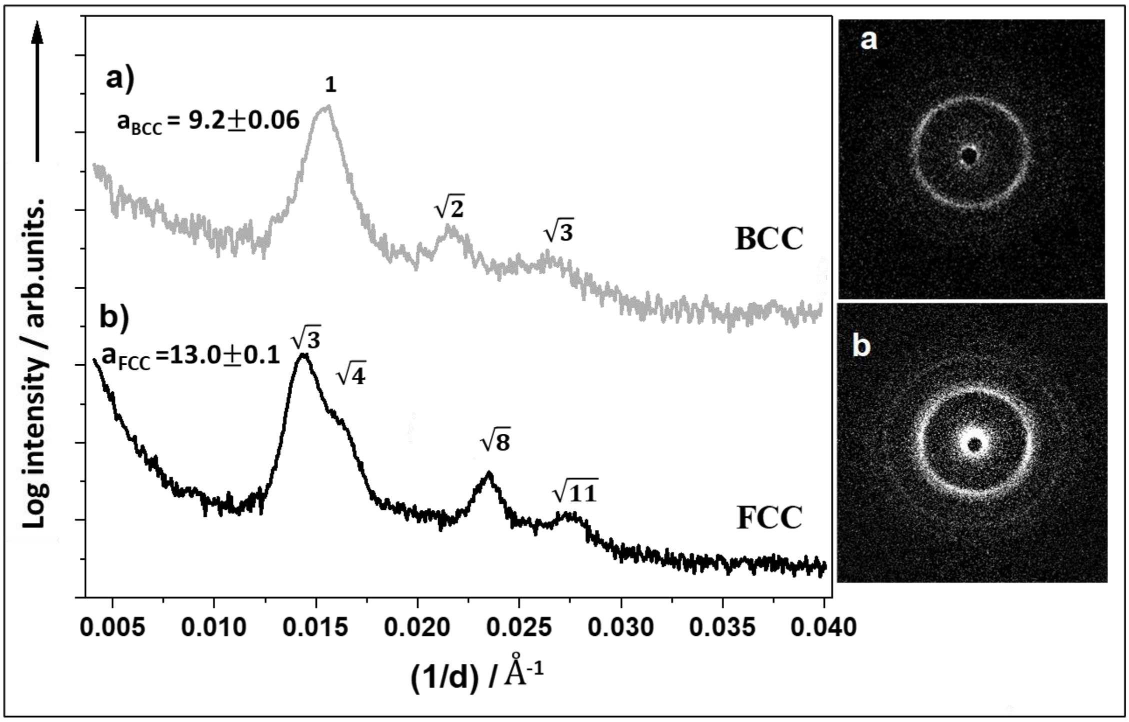

Figure 4.1 1D (left) and 2D (right) SAXS patterns for 40 wt% Brij® 58 in a) water and b) HCPA solution. The intensity of each 1D profile is plotted on a logarithmic scale; the relative peak positions are also noted, leading to the identification of the symmetry and lattice parameter as a_{BCC} water =9.2 ±0.06 nm and a_{FCC} HCPA =13.0±0.1 nm.

Figure 4.1 a) reveals the SAXS pattern for the 40 wt% Brij® 58 in water; the 2D SAXS pattern displays a ring, which often results from polydomain liquid crystalline structures. The structure was confirmed by the 1D SAXS pattern that shows three Bragg peaks corresponding to the BCC symmetry structure with a ratio of $1{:}\sqrt{2}{:}\sqrt{3}$. The calculated lattice parameter indicates a_{BCC}= 9.2 nm, which is in agreement with previous literature by Mahanthappa.[74]

Figure 4.1 b) displays the SAXS pattern for the 40 wt% Brij® 58 in HCPA. The 2D pattern shows three distinct rings, indicating the presence of multi-domain liquid crystalline structures. The SAXS data shows that the 40 wt% Brij® 58 in water with the BCC phase transferred to the FCC phase in the presence of HCPA. This was confirmed by the 1D SAXS pattern that reveals four Bragg peaks corresponding to the FCC structure with the ratio of $\sqrt{3}{:}\sqrt{4}{:}\sqrt{8}{:}\sqrt{11}$ and the lattice parameter a_{FCC} = 13.0 nm. The FCC structure for Brij® 58 in HCPA has not been previously reported. However, the previous studies showed that the FCC structure for Brij® 58 in water revealed a lattice parameter of 13.0 nm.[72,74]

Mahanthappa *et al.* reported that "LLC phases of packed micelles can be easily manipulated at the micelle, lattice, and grain size length scales by using relatively weak external forces." [155] These findings highlight the complexity of how additives can influence phase behaviour and microstructure compared to phase transformation in surfactant/water systems. One possible effect of the presence of HCPA is the ionic interaction with the micelles. Additionally, the physical interaction of HCPA with the micelles could play a significant role. Mahanthappa *et al.* also reported that the size of micelles changes with decreasing water content from 'hard' to 'hairy 'micelles, these hairy micelles are known to form the less dense BCC phase in water as was reported here.[74,155] When micelles are surrounded by a dehydrated PEO layer, the PEO chains extend, forming hairy micelles. Thus, a likely explanation for the transformation from BCC to FCC is the interaction of HCPA with the PEO groups and its physical insertion into the hairy micelles. Such physical interaction would lead to an increase in the Brij 58 effective headgroup size and this would favour the formation of the more highly curved FCC phase, as was reported here. Such favouring of highly curved phase in the presence of HCPA has previously been reported for other surfactant systems.[127]

It is essential to highlight that the SAXS data for 40 wt% Brij® 58 /HCPA in this chapter revealed a pure FCC phase, which is different compared to the biphasic $\mathrm{H_I}$+FCC structure presented in Chapter 3 for the same composition. It should be noted that the sample quantity in this chapter is larger than the samples used in Chapter 3. Subsequently, the likely explanation could be due to the natural variation in a mixing process of different volumes or due to the sample history and the conditions it has experienced over time, as reported by

Mahanthappa.[74] However, the recognition of the stable and pure FCC phase proposed that this mixture could be utilised as a template for producing of MPEs.

4.3.1.2 Electroreduction of the $FCC_{Brij^{®}\ 58}$ mixture

The CV in the 40 wt% Brij® 58 /HCPA ($FCC_{Brij^{®}\ 58}$) mixture was carried out at room temperature and a scan rate of 10 mV s^{-1}, as shown in Figure 4.2.

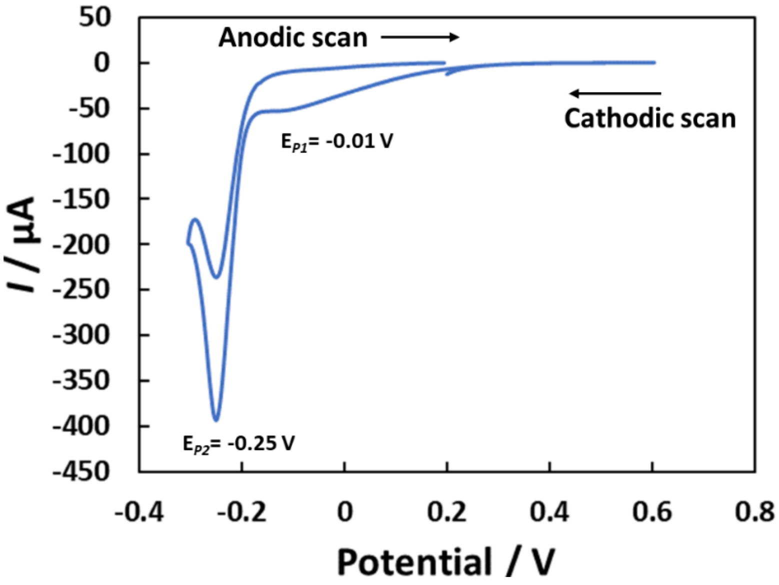

Figure 4.2 Cyclic voltammogram (CV) recorded in the $FCC_{Brij^{®}\ 58}$ mixture, recorded between 0.60 and -0.30 V vs Ag/AgCl t at scan rate of 10 mV s^{-1} and room temperature for a platinum polished electrode (cross-sectional area = 3.142 x 10^{-2} cm^2). The peaks are illustrated in the plot by E_{p1} and E_{p2}.

Figure 4.2 indicates the CV electroreduction of the $FCC_{Brij^{®}\ 58}$ mixture, which shows no current on the cathodic scan (forward scan) until +0.24 V. Then, two visible reduction peaks of high current are observed at potentials of E_{p1} = -0.01, and E_{p2} = -0.25 V. E_{p1} could be related to the reduction of $[PtCl_6]^{2-}$ to $[PtCl_4]^{2-}$, while E_{p2} is related to the reduction of $[PtCl_6]^{2-}$ to $[PtCl_4]^{2-}$ and then to Pt(0) species.[156] The E_{p2} reveals a very high current with a value of 400 µA, indicating the efficient reduction of platinum ions at this voltage. The anodic scan (reverse scan) appears different from the cathodic scan and shows one reduction peak. This behaviour is in agreement with the previous study by Elliott *et al*., which showed two waves in the platinum electrodeposition process.[7] The platinum electrodeposition from HCPA can occur via electron transfer from the mixture to the electrode's surface, which involves the two-electron transfer process (as shown in Equation 1.1 and Equation 1.2 in Chapter 1).[7,50,51]

These reactions indicate that the platinum reduction forms the intermediate $[PtCl_4]^{2-}$ and then forms the Pt(s).[24,157] Consequently, more than one peak in the current-voltage curve can be observed. Therefore, based on this mechanism, the voltages between -0.15 V and -0.25 V were selected for the electrodeposition of platinum, which will be discussed in the next section.

4.3.2 Impact of deposition voltage using $FCC_{Brij^{®}\ 58}$ template on the electrode morphology, surface area and catalytic activity

4.3.2.1 Electrochemical fabrication

The electrodeposition of platinum was carried out from the $FCC_{Brij^{®}\ 58}$ template at different voltages of -0.15 V, -0.20, -0.23 and -0.25 V at a fixed time for 1800 s, as shown in Figure 4.3.

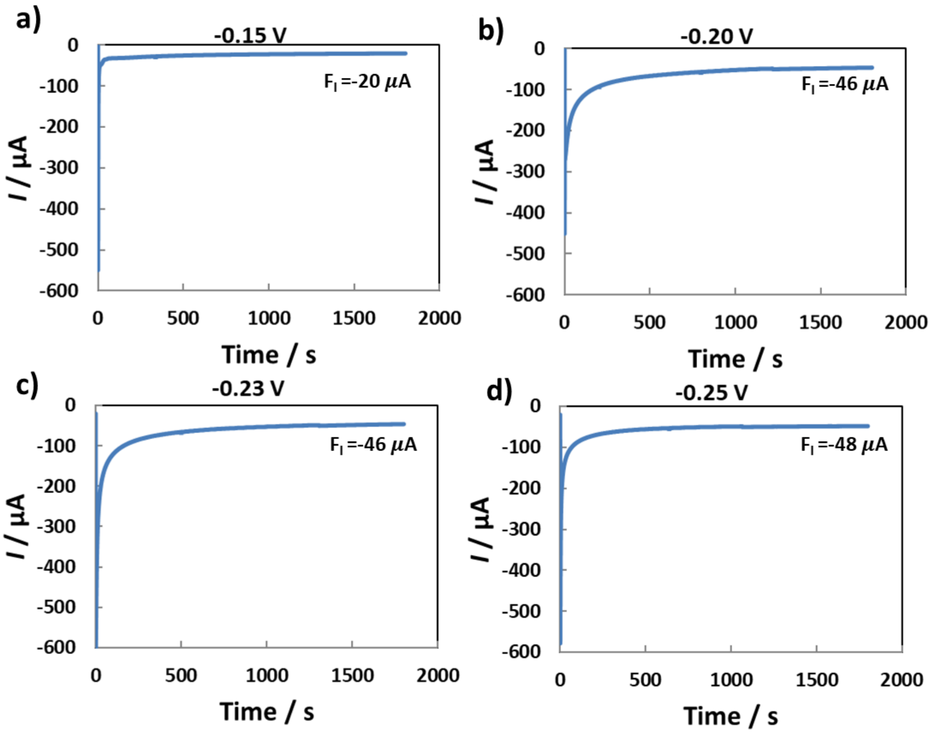

Figure 4.3 Representative electrodeposition transients recorded in the $FCC_{Brij^{®}\ 58}$ mixture at platinum electrodes (cross-sectional area = 3.142 x 10^{-2} cm^2) at room temperature and a fixed time for 1800 s with different potentials a) MPE-0.15, b) MPE-0.2, c) MPE-0.23, and d) MPE-0.25. F_I shows the final current.

From Figure 4.3, the deposition transients display different current magnitudes depending on the deposition potentials. Initially, the transients show a significant negative current that rapidly decays away to a steady deposition non-zero current as time passes. The initial large negative current relates to the stepping potential dropped from 0.60 V to the negative potentials (-0.15, -0.20, -0.23 and -0.25 V). The final current (F_l) increases as the deposition potential decreases to -0.25 V. After the deposition, the template was removed by soaking the electrodes in water. The washed electrode surfaces were dark grey/black in appearance.

For further investigation, Q_{dep} and the charge density (σ) were calculated and shown in Table 4.3. The Q_{dep} was directly obtained from the transient, and the σ was assessed from the charge passed divided by the geometric area of the electrode. The details of the calculation were expressed earlier in chapter 2.

Table 4.3 Variation in total deposition charge (Q_{dep}) and charge density (σ) for mesoporous platinum electrodes (MPEs) fabricated from $FCC_{Brij^{®}\ 58}$ template at different deposition potentials in a fixed time (1800 s). Values represent the mean ± SD of three independent depositions (n=3).

Electrodes	Q_{dep} / C	σ / C cm^{-2}
MPE-0.15	0.03 ± 0.015	0.83 ± 0.49
MPE -0.20	0.09 ± 0.026	2.80 ± 0.83
MPE -0.23	0.11 ± 0.010	3.50 ± 0.33
MPE -0.25	0.10 ± 0.008	3.26 ± 0.20

The data from Table 4.3 shows that the Q_{dep} and σ increase with the decrease of the deposition potentials. The lower values of Q_{dep} and σ were observed at less negative potentials for MPE- 0.15 due to the kinetically slow reaction at this potential. A further decrease in the deposition potential for MPE-0.25 shows a slight decrease in both Q_{dep} and σ values. The quantity of Q_{dep} and consequently σ are increased proportionately to the quantity of metal deposition, thus corresponding to the thickness of nanostructure films.[8,116] These results are in agreement with the previous study by Attard *et al.*, which showed a decline in the film thickness at a further decrease in the potential.[7] The reason was explained to be due to an initial increase in deposition efficiency as deposition potential was lowered, followed by a decrease in efficiency at very low values due to competing reactions, such as proton reduction.[7] From Table 4.3, the deposition from the $\mathrm{FCC}_{\mathrm{Brij}^{®}\ 58}$ template for MPE-0.15 and MPE- 0.20 show a larger error bar than MPE-0.23 and MPE-0.25. All the films produced were chosen for further study, and their characterisations are presented in the following section.

4.3.2.2 Characterisation of morphology and structure in the MPEs

XRD - The XRD provides information about the mesoporous structure, such as the crystal size. The MPEs deposited at different voltages and the blank platinum foil (PPE) were analysed using XRD, as shown in Figure 4.4.

Figure 4.4 a) shows the XRD data for blank platinum foil and the MPEs. The XRD for the PPE shows three peaks observed at 2θ= 46.5°, 67.7° and 81.4° indicating the FCC structure, which is in agreement with the International Centre for Powder Diffraction data file 00-004-0802 shown in Figure 4.4 b). The XRD for MPEs deposited at different potentials exhibits an increase in the number of peaks to five or six, indicating the FCC crystal of platinum. The increasing number of peaks could indicate that the MPE films have a well-defined structure. The XRD patterns show some variation in the intensity and the width of peaks for MPEs compared to PPE. The intensity of the peaks indicates the orientations of the platinum crystallites, even though all the samples have the same kind of platinum crystals. The intensities of peaks vary depending on the orientation of the pores, and some crystallographic planes are more aligned with the X-ray beam, producing highly intense peaks. The XRD does not give information about the mesostructure. However, performing SAXS will be an obvious next step to prove the structure.

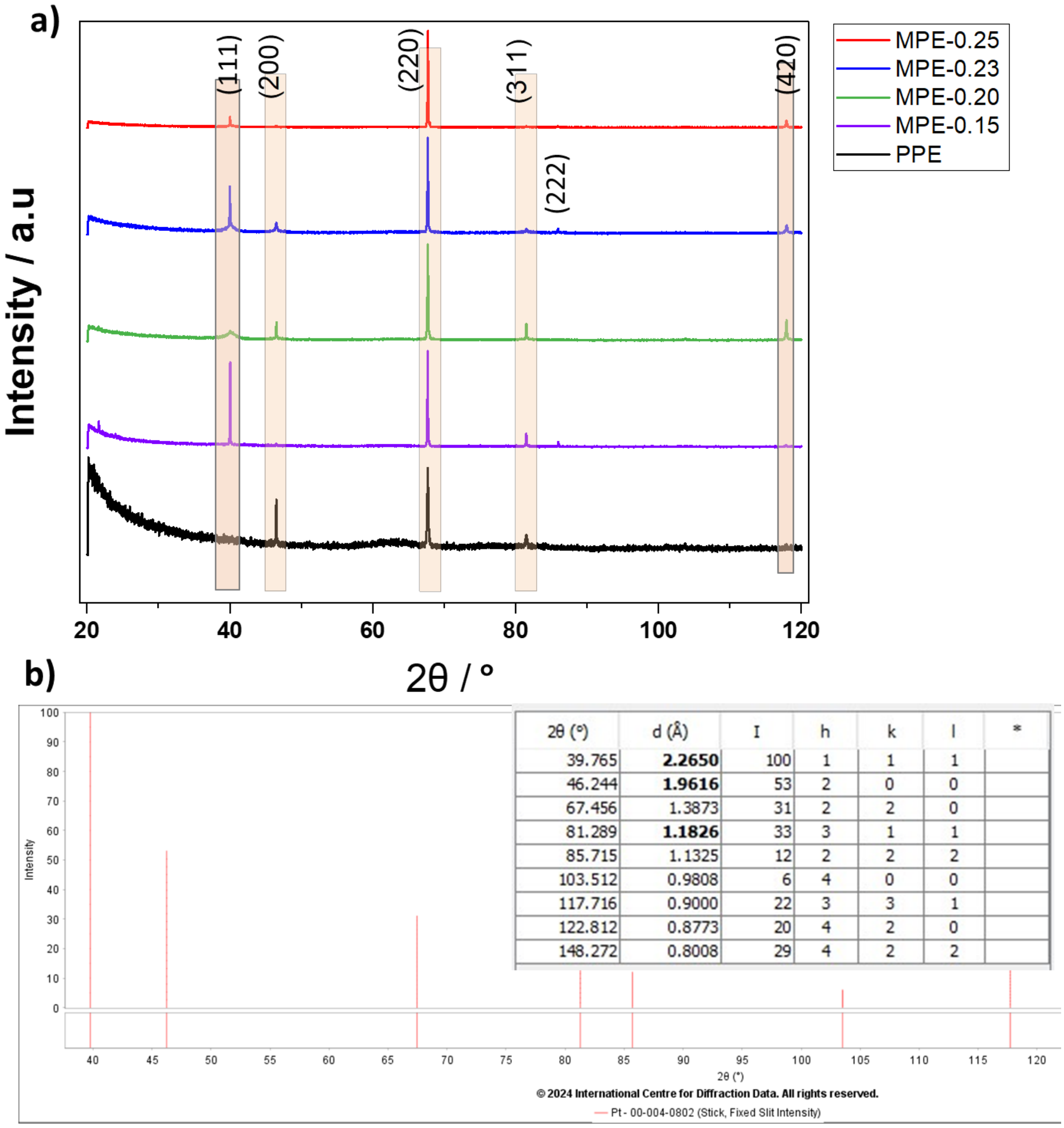

2θ (°)	d (Å)	I	h	k	l	*
39.765	**2.2650**	100	1	1	1	
46.244	**1.9616**	53	2	0	0	
67.456	1.3873	31	2	2	0	
81.289	**1.1826**	33	3	1	1	
85.715	1.1325	12	2	2	2	
103.512	0.9808	6	4	0	0	
117.716	0.9000	22	3	3	1	
122.812	0.8773	20	4	2	0	
148.272	0.8008	29	4	2	2	

Figure 4.4 a) XRD measurement for blank platinum foil (PPE) and mesoporous platinum foils (MPE) deposited from the FCC$_{Brij^{®}\,58}$ at different potentials MPE-0.15, MPE-0.20, MPE-0.23 and MPE-0.25.b) the platinum XRD data from International Centre for Powder Diffraction data file 00-004-0802

TEM - For the TEM analysis, the deposited platinum powder was separated from the platinum foils using a scalpel and placed in a carbon grid for TEM, as described in Chapter 2**.** The structure of the MPEs was investigated using the TEM technique and is presented in Figure 4.5.

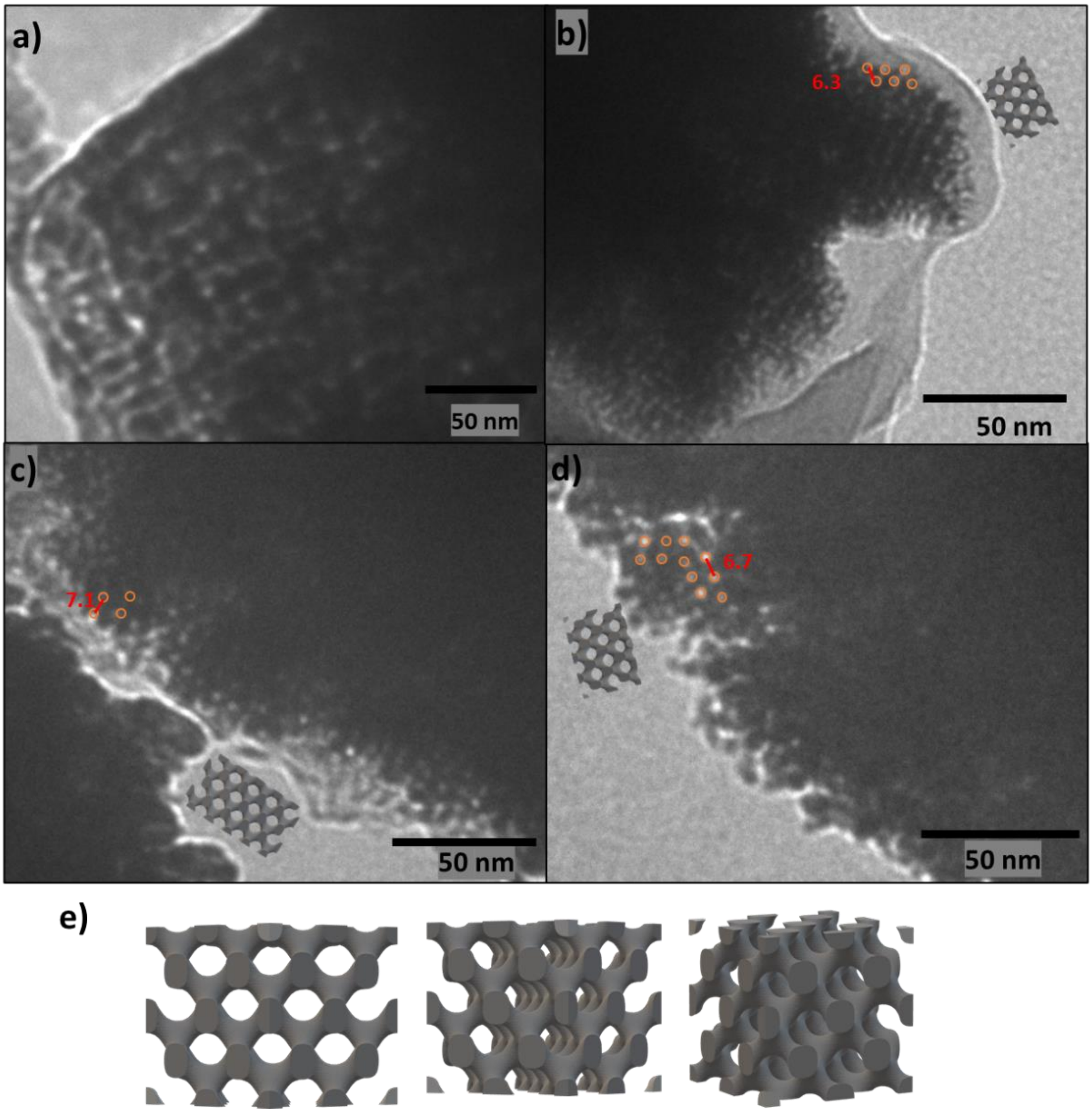

Figure 4.5a-d) TEM images for the mesoporous platinum films deposited from the FCC$_{Brij^{®}\ 58}$ at different potentials, a) MPE-0.15, b) MPE -0.20, c) MPE-0.23 and d) MPE-0.25; the inserts are the simulation projection for diamond structure. e) a simulation projection for diamond structure in different directions. The lattice parameter (distance from one pore to another) is inserted.

The TEM images show the 3D network of mesoporous platinum fabricated at different potentials. Figure 4.5 a) reveals the TEM image for MPE-0.15, which indicates some confirmation of porosity. However, the structure is unclear, probably due to the sample thickness. The other TEM images shown in Figure 4.5 b-d) for MPE-0.20, MPE-0.23 and MPE-0.25 indicate the 3D network with more regular pore structure. In general, the characterisation of the cubic structure relies on assessing the number of branches and nodes, which are essential parameters.[158] The template has a closely packed sphere with an FCC structure, and the platinum is assumed to be deposited in the channels between the micelles, which produce four branches in each node. Therefore, the produced materials will most likely be the diamond structure characterised by four branches for each node. Additionally, the TEM images show that the pore structure agrees with the diamond simulation projection and is the best match to the TEM images (as shown in the inserts). The diameter of pores ranged from 3.0 to 3.5 nm, and the lattice parameter shows 6.3 ± 0.3 nm, 6.7 ± 0.5 nm and 7.1 ± 0.7 nm for MPE-0.20, MPE-0.23 and MPE-0.25, respectively. Figure 4.5 e) illustrates the projections of the diamond structure simulated in various directions to aid interpretation.

It is essential to highlight the difficulty encountered in obtaining a clear TEM image under high voltage. It was noted that the high accelerating voltage damaged the fine details of the sample and produced a blurred TEM image. Unfortunately, the unavailability of the SAXS technique during this investigation hindered a comprehensive examination of the structure. As the SAXS measurement serves as a crucial method to validate the interpretation of TEM data.

SEM - The surface morphology of the MPEs was studied and compared to the surface of PPE using SEM, as shown in Figure 4.6.

Figure 4.6 a) displays the SEM image for the PPE surface. The SEM image shows a relatively smooth surface, attributed to the polishing process detailed in Chapter 2. It is worth noting that the small scratches are also due to the alumina polishing process employed for cleaning.

Figure 4.6 b) exhibits the SEM image for the MPE-0.15, which reveals smooth layers (the zoomed area illustrates the presence of more than one layer). Interestingly, Figure 4.6 c) presents the SEM image for the MPE-0.20, which shows exciting features consisting of spherical particles and smooth layers with fissures.

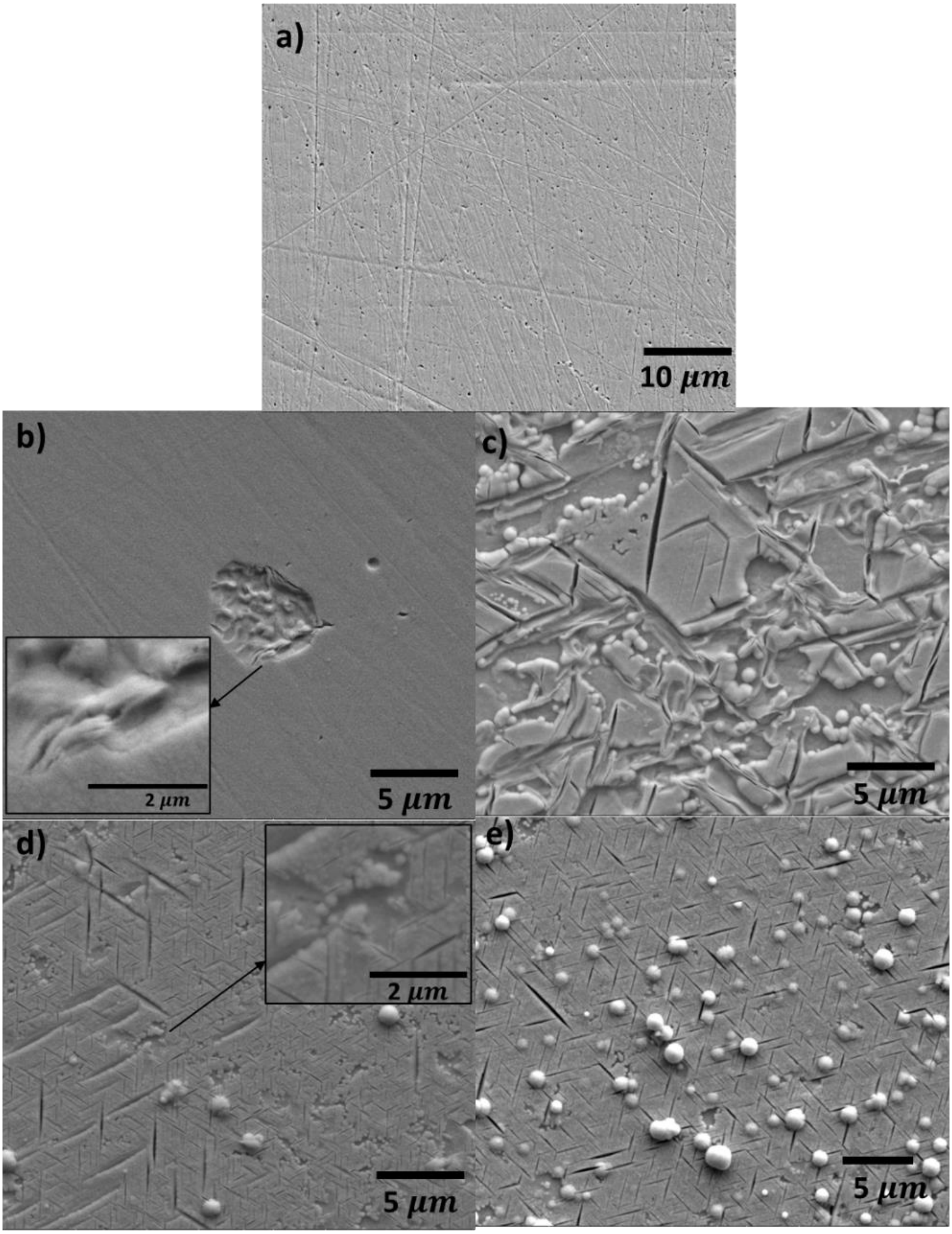

Figure 4.6 SEM images of a) polished platinum electrode (PPE) and mesoporous platinum electrodes (MPEs) deposited from the FCC$_{\text{Brij® 58}}$ *at different voltages, b) MPE-0.15, c) MPE-0.20, d) MPE-0.23, and e) MPE-0.25.*

Figure 4.6 d) and e) display the SEM images for MPE-0.23 and MPE-0.25, respectively. The SEM images show very interesting features similar to the MPE-0.20 surface, but the fissures cover the surface entirely in a specific direction and have some additional surface spherical features. The magnified area in Figure 4.6 d) confirms that the spherical particles are assembled in a specific way to create the layer. In Figure 4.6 e), large spherical particles above the fissures are observed. Further investigation of the morphological structure was conducted on platinum foil deposited at the same conditions. The blank platinum foil was dipped in the $\mathrm{FCC}_{\mathrm{Brij}^{®}\,58}$, and the deposition was carried out at -0.23 V. The SEM images were collected at various platinum foil parts and shown in Figure 4.7.

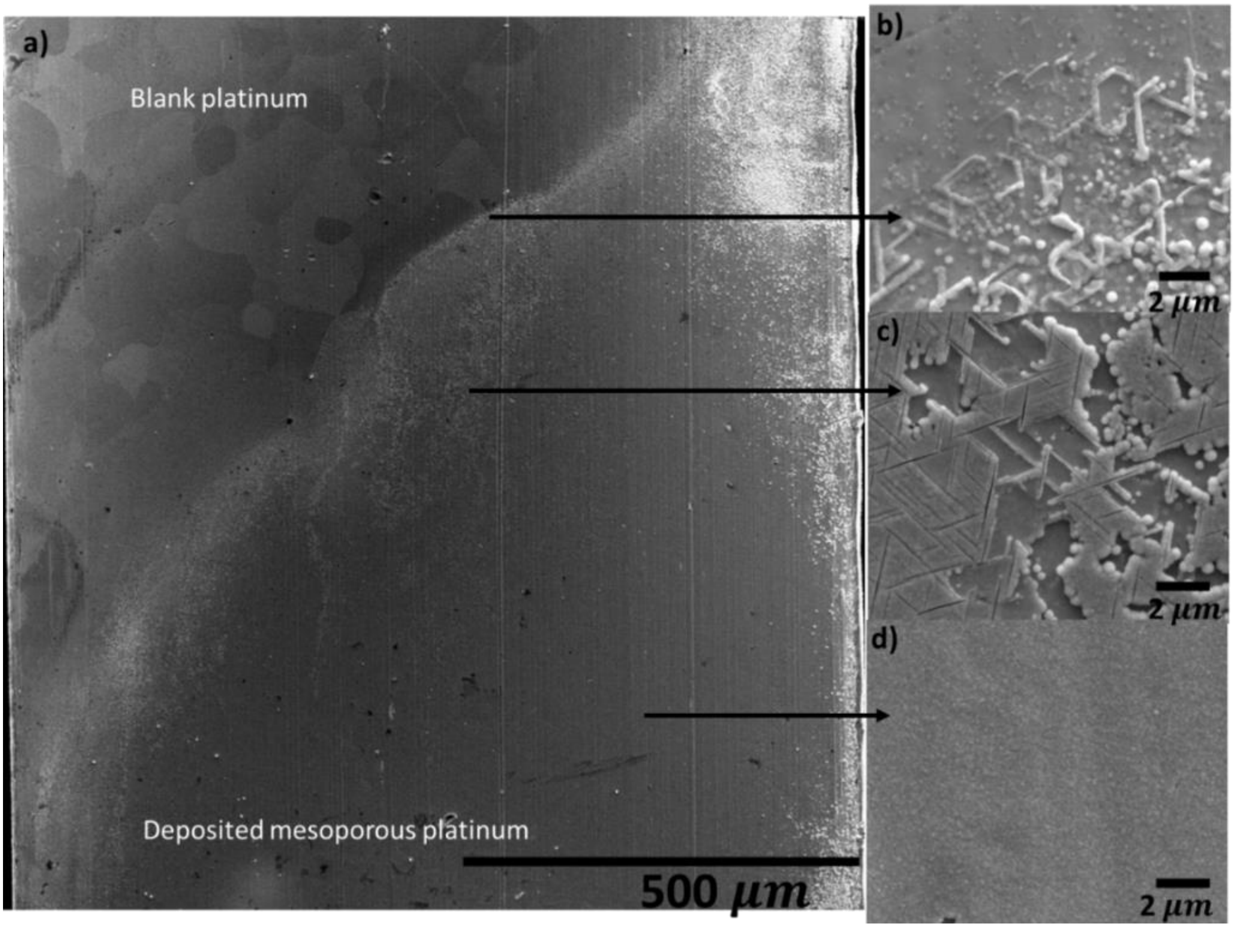

Figure 4.7 SEM images of mesoporous platinum deposited at -0.23 V in platinum foil, illustrating the blank and the mesoporous platinum regions. b), c) and d) are zoomed SEM images at various parts.

Figure 4.7 a) shows the SEM image for the platinum foil that illustrates the two regions of blank platinum and deposited mesoporous platinum. Figure 4.7 b-d) show the magnified SEM images at different parts of the deposited mesoporous platinum region. Interestingly, Figure 4.7 b) exhibits the SEM image at the border of the deposited mesoporous platinum, showing spheres arranging themselves in a specific structure. Figure 4.7 c) reveals that more layers with fissures were produced, proving that the spherical particles are arranged and creating this layer. Notably, Figure 4.7 d) shows the creation of thicker layers comprised of dense spheres. This thick part of the deposited mesoporous films was chosen for further study using AFM, as shown in the following section. Understanding the exact mechanism of this deposition could be achieved through future work involving detailed nucleation and growth studies.

AFM - The AFM images for mesoporous platinum films deposited at different voltages -0.15, -0.20, -0.23 and -0.25 V are shown in Figure 4.8.

Figure 4.8 a) shows that the AFM image for PPE reveals a smooth platinum surface without the presence of any features. Remarkably, Figure 4.8 b-e) show the 3D images of the AFM that express the highest and lowest points on the surface, revealing different roughness for the MPEs.

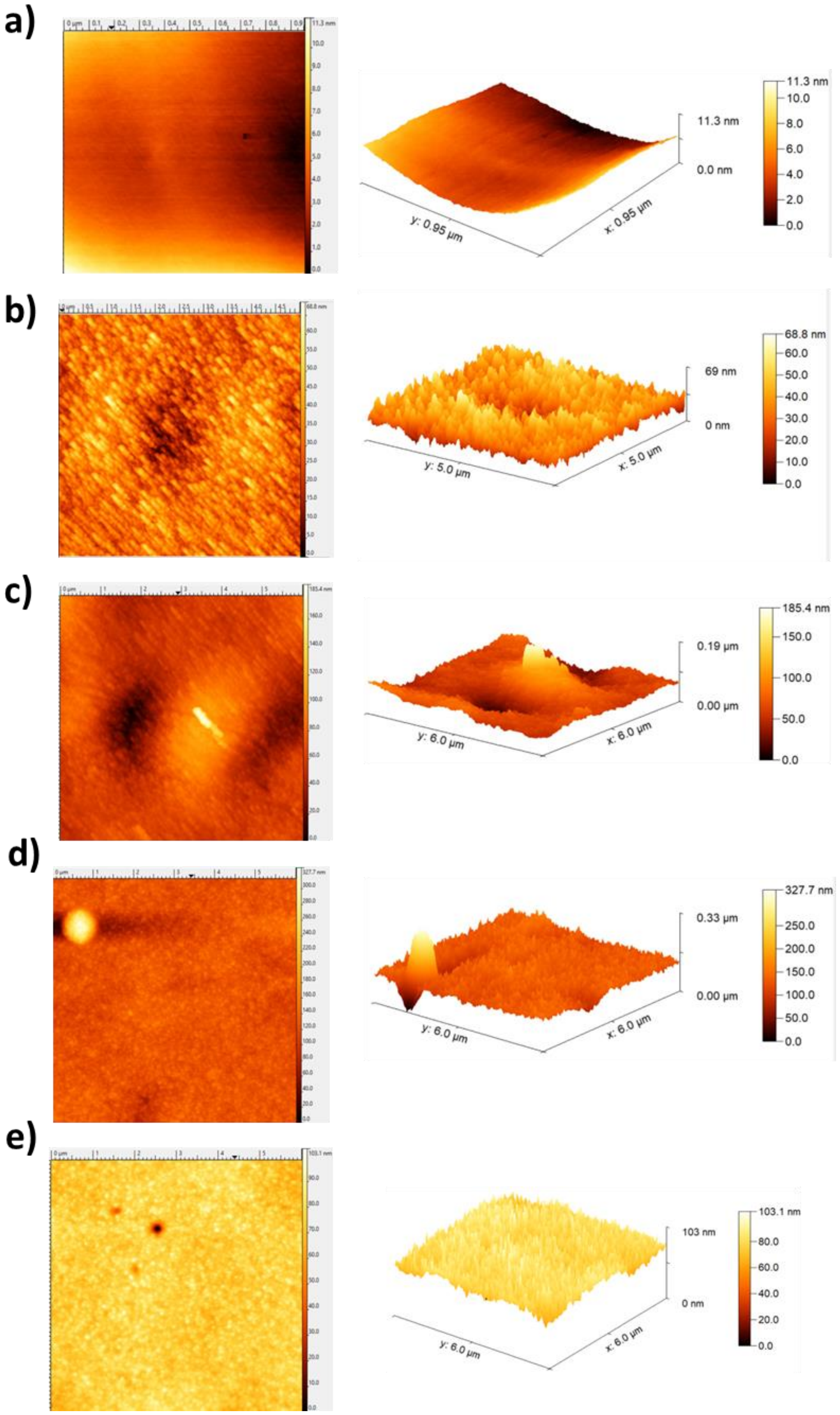

Figure 4.8 2D and 3D AFM images of a) polished platinum electrode (PPE) and mesoporous platinum electrodes (MPEs) deposited from the FCC$_{\text{Brij® 58}}$ at different voltages, b) MPE-0.15, c) MPE-0.2 V, d) MPE-0.23 and e) MPE-0.25

The roughness of the MPEs increased with the increase of the deposition potential from -0.15 V to -0.23 V, as shown in Table 4.4. Interestingly, the further decrease of the potential to -0.25 V shows a decrease in the roughness of the MPE-0.25. These findings agree with the Q_{dep} and σ that indicated an increase with a decrease in the voltage to -0.23 and then a slight decrease at -0.25. The average feature size (AFS) shows the same trend as shown in Table 4.4.

Table 4.4 The mean square roughness (RMS) and the average feature size (AFS) for PPE and MPEs deposited from the $FCC_{Brij^{®} 58}$ at different potentials.

Electrodes	RMS / nm	AFS / nm
PPE	1.87± 0.50	-
MPE-0.15	8.20 ± 0.13	80 ± 0.5
MPE-0.20	18.38 ±0.65	115 ± 0.8
MPE-0.23	20.23± 2.97	140 ± 1.2
MPE-0.25	5.74± 0.60	118 ± 0.8

4.3.2.3 Electrochemical characterisation of the MPEs

CV in sulfuric acid - The MPEs were cleaned using CV in 0.5 M H_2SO_4 aqueous solution to remove impurities. After this, the clean MPEs and PPE were further cycled in 0.5 M H_2SO_4 aqueous solution between -0.30 and 1.2 V vs Ag/AgCl, as shown in Figure 4.9.

The CVs for the PPE and MPEs fabricated at different voltages display the classic signal expected for platinum in acid. The CVs for the MPEs indicate significantly increased current compared to the PPE. This enhancement in the current is related to creating platinum films with a significant amount of electrochemically active surface area. The peaks in the Hydrogen underpotential (H_{upd}) region reveal hydrogen adsorption on the crystal faces of platinum. The representative CVs are consistent with earlier studies for the formation of high surface area platinum electrodes.[7,8] This indicates the successful production of platinum nanostructured film with a high surface area.

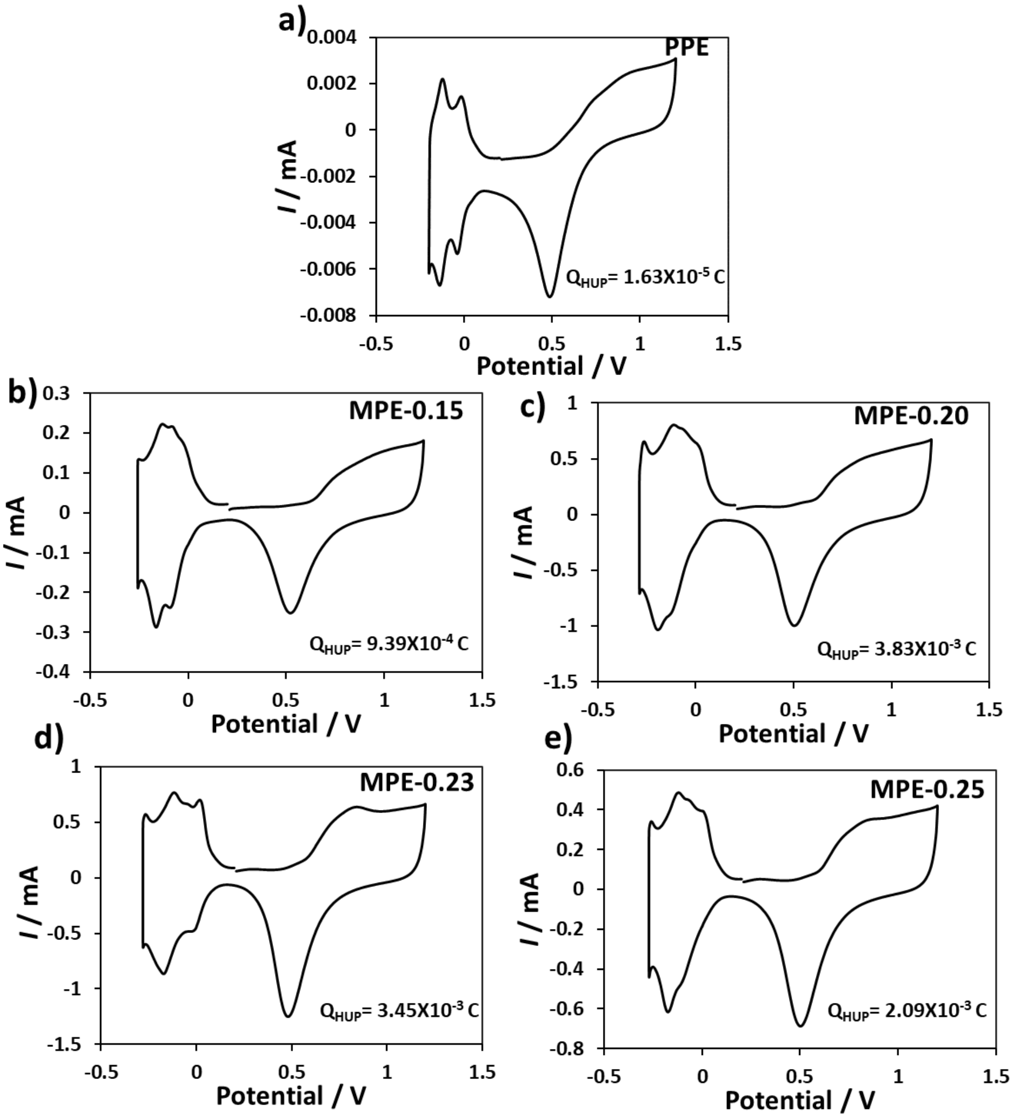

Figure 4.9 Cyclic voltammograms (CVs) recorded in 0.5 M H_2SO_4, at room temperature and 50 mV s^{-1} for a) polished platinum electrode (PPE) and a series of mesoporous platinum electrodes(MPEs) (cross-sectional area = 3.142 x 10^{-2} cm^2) fabricated from the $FCC_{Brij^{®}\ 58}$ with different deposition potentials: b) MPE-0.15, c) MPE-0.20, d) MPE- 0.23 and e) MPE-0.25. Q_{HUP} means the charge for hydrogen underpotential region.

Further analyses of the MPEs were carried out to investigate the RF values were calculated by dividing the Q_{HUP} by the electrode area,[106] as detailed in Chapter 2. Also, the ECSA values were calculated using the Attard *et al*.[150] method, which measures the area from the Q_{HUP} with the Q_{dep} as described previously in Chapter 2. The RSA, RF and ECSA for the three independent depositions (n=3) are shown in Table 4.5.

Table 4.5 The real surface area (RSA), roughness factor (RF) and electrochemical active surface area (ECSA) for the polished and mesoporous platinum electrodes (MPEs) deposited from the FCC$_{Brij^{®}\ 58}$ at different deposition potentials. ± SD of n=3.

Electrodes	RSA / cm^2	RF	ECSA / m^2 g^{-1}
PPE	0.08	2.5	-
MPE-0.15	1.68 $\pm$ 2.41	54 $\pm$ 77	9.06 $\pm$ 9.91
MPE-0.20	11.2 $\pm$ 6.31	346 $\pm$206	23.99 $\pm$ 6.97
MPE-0.23	14.58 $\pm$ 3.45	464 $\pm$ 111	27.58 $\pm$ 2.25
MPE-0.25	10.44 $\pm$ 0.45	333 $\pm$ 14	20.06 $\pm$ 1.57

From Table 4.5, the MPEs show different RSA, RF and ECSA values, which Initially increase with the decrease of the deposition potential for the MPEs. These findings are consistent with the Q_{dep} and σ values shown in Table 4.3. Thus, as the σ increased, the RF values increased, confirming the stability and uniform accessibility of the pores throughout the film thickness. From Table 4.5, the further decrease in the deposition potential to -0.25 V shows a decrease in the RSA, RF and ECSA values, which could be due to the reduction in the deposition efficiency because of the presence of competing reactions such as proton reduction.[7] The highest value of ECSA was observed for the MPE -0.23 to be 27.58 $\pm$ 2.25 m^2 g^{-1}. The ECSA values are greater in comparison to the previous value reported by Elliott for hexagonal platinum nanostructured, which was 22 m^2 g^{-1}.[6] However, the values here are smaller than the value observed previously for single diamond cubic platinum nanostructure, which showed a value > 40 m^2 g^{-1} by Akbar *et al*.[8]

CV in ethanol under acidic media - The catalytic responses to ethanol oxidation for the PPE and MPEs were evaluated through CV. Before the ethanol oxidation investigation, the PPE and MPEs were cycled in dilute acid for further cleaning. Then, the RF, RSA and ECSA were calculated from the clean CVs in acid for the MPEs used in this study and presented in Table 4.6.

Table 4.6 The total deposition charge (Q_{dep}), real surface area (RSA), Roughness factor (RF) and electrochemical active surface area (ECSA) for the polished and mesoporous platinum electrodes deposited from the $FCC_{Brij^{®} 58}$ at different deposition potentials. n=1

Electrodes	Q_{dep} / C	RSA / cm^2	RF	ECSA / $m^2 g^{-1}$
PPE	-	0.08	2.5	-
MPE-0.15	0.043	3.14	100	14.4
MPE-0.20	0.118	12.60	401	21.1
MPE-0.23	0.120	11.23	358	18.5
MPE-0.25	0.104	6.90	219	13.2

Table 4.6 represents the RSA, RF and ECSA values for a single deposition (n=1), while the data in Table 4.5 correspond to three independent depositions (n=3). Notably, the data are slightly different, and the RF and ECSA are slightly smaller due to multiple CV cycles of the MPEs, which reduced their values. These RSA were employed to determine current density (J), facilitating a direct comparison of different electrodes' catalytic activity.

The CV in 0.5 M H_2SO_4 + 0.5 M C_2H_5OH electrolyte was used for the investigation of the electrocatalytic activity of the MPEs. The CVs of each electrode became similar and stable after the third cycle. The resulting CVs from the third cycle in 0.5 M H_2SO_4 + 0.5 M C_2H_5OH electrolyte are shown in Figure 4.10.

Figure 4.10 a) and b) show the CVs for MPEs and PPE to demonstrate the catalytic response to ethanol oxidation, which is indicated by the peaks observed in forward and backward scans and the suppression of the hydrogen adsorption/desorption peaks. Figure 4.10 a) indicates the CVs for the PPE and the MPEs at different voltages in ethanol in terms of current (I). The CVs show an increase in the I for the MPEs when compared to PPE for ethanol oxidation. This increase in the current could be due to the enlarged surface area of the MPEs compared to PPE. The CVs exhibit that the current for the forward (I_F) and backward (I_B) oxidation peaks vary with the different RF for the MPE and MPE-0.23 shows the highest I_F and I_B.

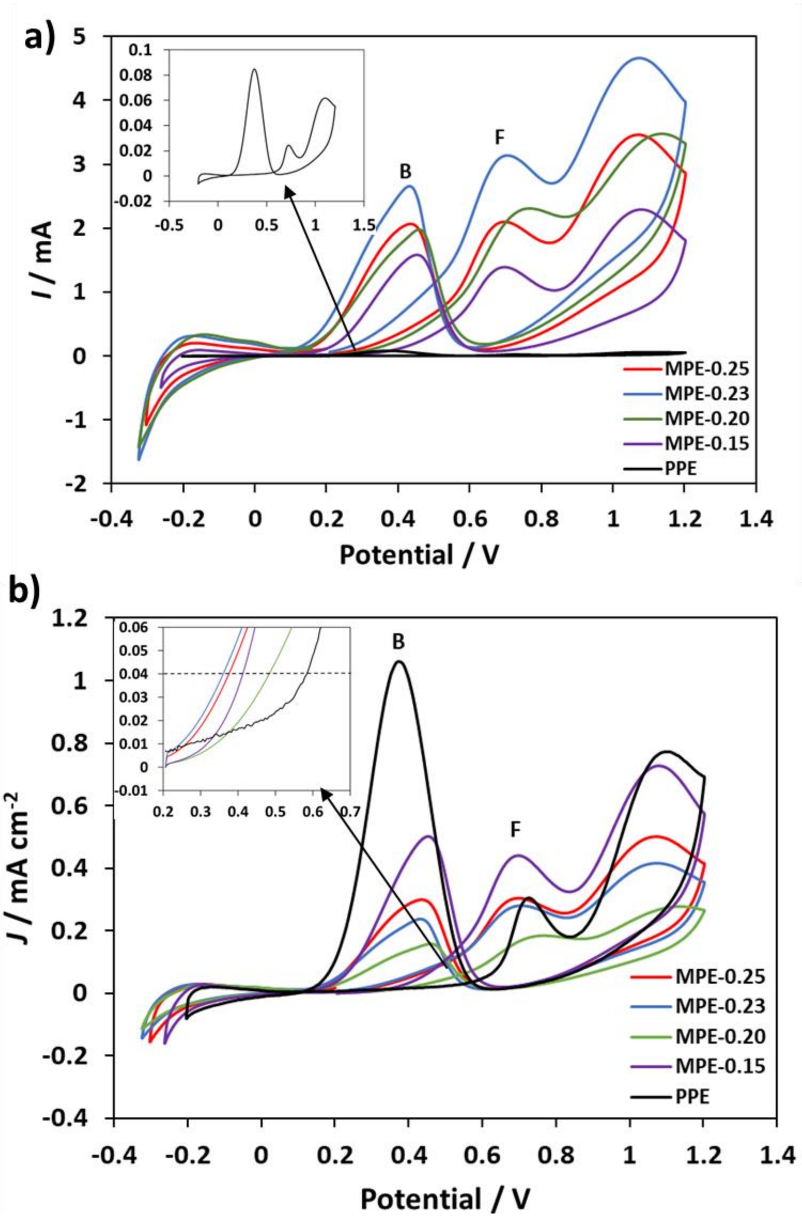

Figure 4.10 Cyclic voltammograms (CVs) in 0.5 M H_2SO_4 + 0.5 M C_2H_5OH solution a) current (I) and b) current density calculated from the RSA (J) recorded at room temperature at a scan rate of 50 mV s^{-1} of the polished platinum electrode (PPE) and mesoporous platinum electrodes (MPEs) deposited from the $FCC_{Brij® 58}$ at different potentials, MPE-0.15, MPE-0.20, MPE-0.23 and MPE-0.25.. The insert exhibits a) the CV of PPE and b) the magnification of the plot and the horizontal dotted line shows the J for the onset potential. The forward and backward peaks are illustrated by F and B in the plot.

Figure 4.10 b) shows the CVs of ethanol oxidation in terms of *J* for the MPEs and PPE. Surprisingly, the data exhibits different behaviour towards ethanol oxidation compared to Figure 4.10 a), and the CVs show similar *J* values for the MPEs compared to PPE. The current densities of forward (J_F) and backward (J_B) oxidation peaks decrease with an increase in RF for MPEs. For illustration, the highest J_F and J_B are observed for the MPE-0.15, which has the lowest RF = 100, while the lowest J_F and J_B are observed for the MPE-0.20, which has the highest RF = 401. The magnified plot in Figure 4.10 b) exhibits the E_{onset} which means the voltage at which electrochemical oxidation begins to occur, indicated by the increase in the current for the peak F. The plot shows an increase in the current at ~ 0.3 V; however, the E_{onset} was collected at a fixed *J* value (0.04 mA cm^{-2}) for more accuracy. A shift to the left (lower potential values) was observed for the MPEs compared to the PPE, which signifies more facile electrochemical reaction at the surface.

A previous study by Cheng *et al*. reported that the oxidation peak in the backward scan revealed the elimination of carbonaceous species that were not completely oxidised during the forward scan and accumulated on the surface of the catalysts.[113] Therefore, the *I* or *J* ratio for the F to the B peak can be evaluated to assess the CO-tolerance of the catalysts. A low F to B peak ratio indicates poor ethanol oxidation to the final product and extensive residual carbonaceous species on the catalyst surface. In contrast, a high F to B peak ratio value indicates higher CO tolerance. The ratio of the F to the B peak value and catalytic activity for the MPEs and the PPEs, measured from the CVs in Figure 4.10 a) and b), are shown in Table 4.7.

Table 4.7 The catalytic activity of the polished platinum electrode (PPE) and mesoporous platinum electrodes (MPEs) (cross-sectional area = 3.142 x 10^{-2} cm^2) deposited from the FCC$_{Brij® 58}$ at different voltages towards the ethanol oxidation in terms of current (I) and current density (J). The I_F means forward peak in current, I_B means backward peak in current, the J_F means forward peak in current density, and the J_B means backward peak in current density. Onset potential (E_{onset}) data are collected at 0.04 mA cm^{-2}.

Electrode	RF	I_F / mA	I_B / mA	J_F / mA cm^{-2}	J_B / mA cm^{-2}	J_F / J_B	E_{onset} / V
PP	2.5	0.02	0.08	0.25	1.05	0.24	0.58
MPE -0.15	100	1.38	1.58	0.44	0.50	0.88	0.41
MPE -0.20	400	2.30	1.93	0.18	0.15	1.19	0.48
MPE -0.23	357	3.13	2.65	0.28	0.24	1.18	0.35
MPE -0.25	219	2.09	2.06	0.30	0.30	1.02	0.37

Table 4.7 shows the catalytic activity data for the MPEs and PPE in terms of the I and J. The I_F and I_B increase as the RF for the MPEs increases, while the J_F and J_B decrease with increased RF values for the MPEs. The J_F/J_B show an increase with the rise of RF for the MPEs. The highest J_F/J_B value was 1.19, observed for MPE-0.20 with the highest RF (400), while the lowest value was 0.24 for PPE with RF of 2.5. Moreover, the E_{onset} indicates low values for the MPEs compared to PPE and the lowest value (0.35 V) was observed for MPE-0.23. This proves the easy oxidation of the ethanol on the MPEs compared to the PPE. The MPEs fabricated from the $FCC_{Brij® 58}$ show excellent performance towards ethanol oxidation compared to PPE.

Thus, there is some difference between the catalytic activity data for the MPEs and PPE in terms of the I and J forms. For instance, the value of I_F and I_B exhibit a positive correlation with the rising RF; however, the J_F and J_B decline as the RF increases. Increasing the RF could mean an expansion in the thickness of the porous film. Therefore, this lessening in the J_F and J_B with the elevation of the RF could be due to the fast oxidation of ethanol. This phenomenon was previously observed by Chung *et al.*[116], who explained that ethanol oxidation is a fast reaction and becomes diffusion-controlled; therefore, the process takes place only on the surface, as shown in Figure 4.11

Figure 4.11 illustrates a visual representation of how the ethanol molecules penetrate into the surface of the MPEs with different RF during ethanol oxidation. It is clear from this schematic that not all areas of the MPEs participate in the reaction. Therefore, as the RF increases, there is a reduction in the J_F and J_B value.

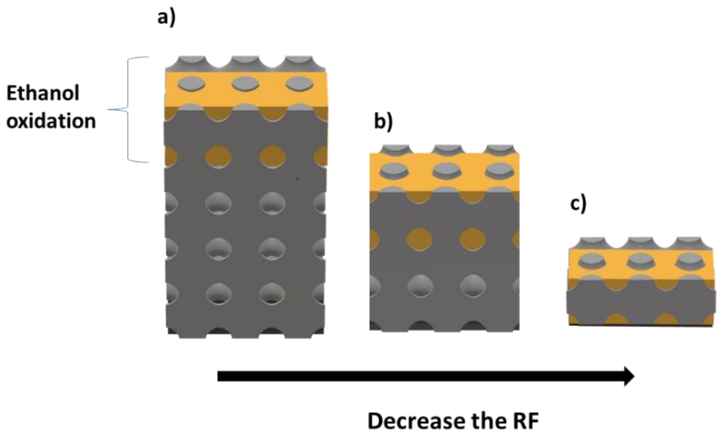

Figure 4.11 Schematic cross-sectional view of mesoporous platinum films with different RF. a) and b) with larger RF reveal partial pores participate in the ethanol oxidation reaction. c) shows mesoporous platinum film with a small RF that indicates entire pores participate in the ethanol oxidation reaction. The grey presents the mesoporous platinum film, and the orange indicates the ethanol oxidation.

For more investigation, the effect of the scan rate on the peak current at the MPEs and PPE was studied. The results showed that the J_F in all the CVs increased linearly with the square root of the scan rate, suggesting a diffusion-controlled electrochemical reaction (figures are not shown here).

Additional assessments were applied to investigate the stability and long-term activity of the MPEs and PPE towards the ethanol electro-oxidation process. Therefore, over 100 cycles were applied in 0.5 M H_2SO_4 + 0.5 M C_2H_5OH solution between -0.3 and 1.2 V vs Ag/AgCl at 50 mV s^{-1} and are shown in Figure 4.12.

Figure 4.12 a) shows PPE's stability towards the ethanol oxidation over 100 CVs. The first 20th CVs show an increase in the J_F (shown in red). Then, further CVs exhibit a clear decrease in ethanol oxidation with each scan until the 100th CV. This reduction indicates that the PPE surface accumulated reaction by-products and loses its stability. Figure 4.12 b-e) reveal the stability of the MPEs deposited at different potentials towards the ethanol oxidation over 100 CVs. The CVs indicate good stability for all the MPEs over 100 CVs.

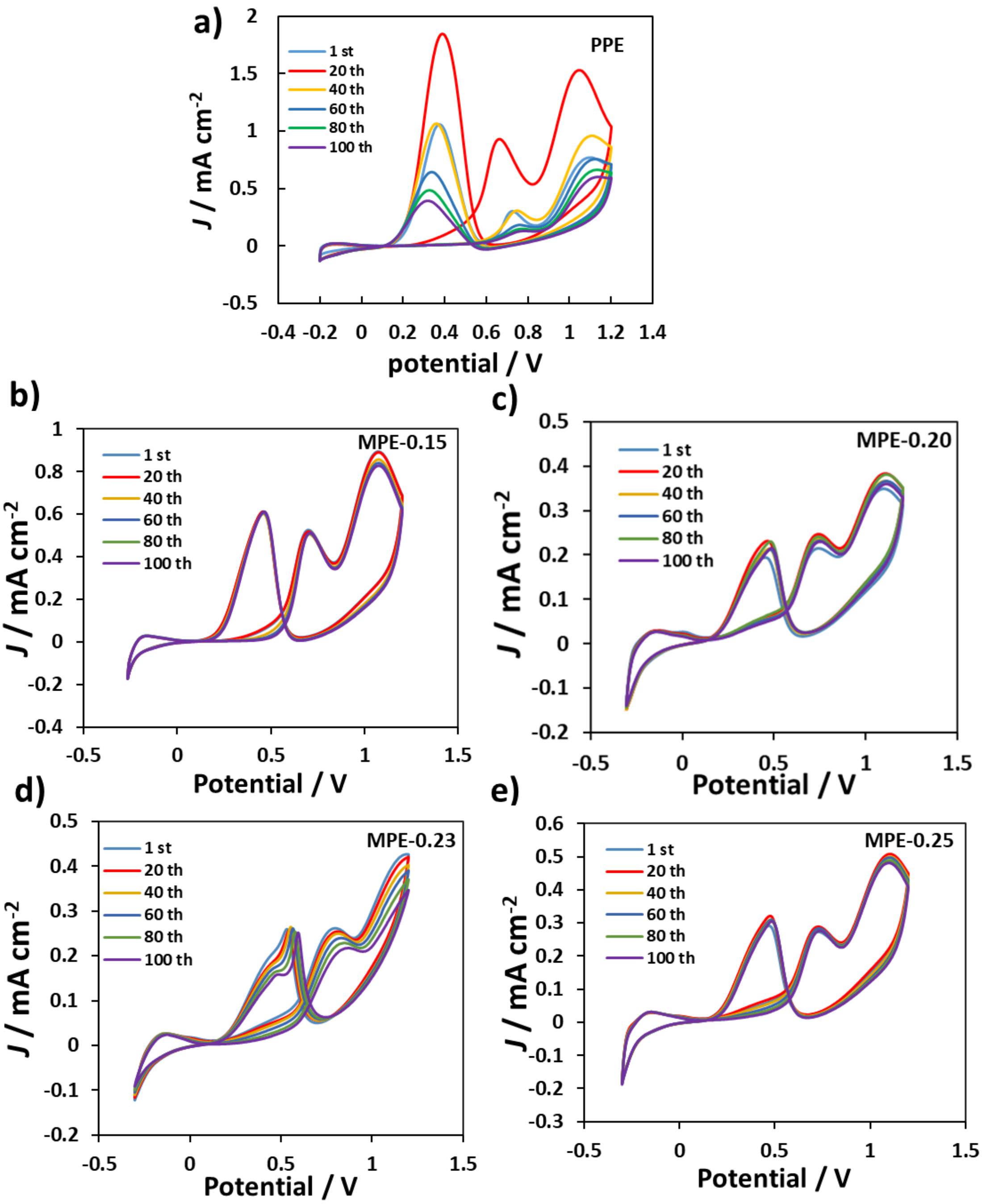

Figure 4.12 Cyclic voltammograms (CVs) over 100 cycles, in 0.5 M ethanol + 0.5 M H_2SO_4 solution at room temperature and 50 mV s^{-1} for a) polished platinum electrode and mesoporous platinum electrodes(MPE) deposited from the $FCC_{Brij® 58}$ at different voltages b) MPE-0.15, c) MPE-0.20, d) - 0.23 MPE, and e) MPE-0.25. Every 20 cycles are shown, and each colour presents the number of cycles.

Surprisingly, Figure 4.12 d) reveals an extra peak in the reverse scan. A previous study by Yanhui *et al.*[98] reported a hidden peak on the low potential side of the oxidation peak, which has the same origin as the oxidation peak observed in the reverse scan. This explanation could be applied to the data shown here, therefore whilst the shape is unusual it probably arises from the same electrochemical process. Further assessment of the J_F for the 1st and 100th cycles, the stability of the electrodes and the enhancement factor compared to polished electrodes are described in Table 4.8.

Table 4.8 The stability of the polished platinum electrodes (PPE) and mesoporous platinum electrodes (MPEs) fabricated from the $FCC_{Brij^{®}\ 58}$ at different voltages over 100 scans; J_F means the current density of the forward peak. The stability factor (1) is the percentage change calculated from the $J_{F100th\ scan}$ to the $J_{F1st\ scan}$ for each electrode. The enhancement factor (2) is a percentage comparison of the J_{F100th} for the MPEs to the J_{F100th} for PPE. It is calculated by dividing the J_{F100th} value of the MPEs by the J_{F100th} value of PPE.

Electrodes	**RF**	**$J_{F\ 1st\ scan}$ / mA cm^{-2}**	**$J_{F\ 100th\ scan}$ / mA cm^{-2}**	**Stability factor (1)**	**Enhancement factor (2)**
PPE	2.5	0.30	0.13	43%	100%
MPE-0.15	80	0.52	0.51	96%	390%
MPE-0.20	336	0.21	0.23	109%	180%
MPE-0.23	332	0.26	0.22	85%	170%
MPE-0.25	208	0.27	0.27	100%	210%

Table 4.8 shows that the MPEs deposited at different potentials reveal excellent stability compared to the PPE. The highest value of stability factor (109%) was observed for the MPE-0.20, which also has the highest RF. The enhancement factor compares the J_F for the 100th CV for PPE with the 100th CV for each MPE which displays significant insights into the performance of the MPEs. The highest value (390%) was observed for the MPE-0.15 V, with the smallest RF value among the MPEs.

EIS in ethanol under acidic media- Initially, the MPEs and PPE were cleaned electrochemically by CV in 0.5 M H_2SO_4 to ensure that any possible impurities in the electrode's surface were removed. A comparison of the CV in 0.5 M H_2SO_4 to that in 0.5 M H_2SO_4 + 0.5 M C_2H_5OH revealed that the ethanol oxidation started at ~ 0.30 V, as indicated by the current increase for the ethanol CVs. At 0.60 and 0.80 V, the current increased significantly compared to the

CV in acid, indicating ethanol oxidation. Also, the CV in 0.5 M H_2SO_4 showed the formation of platinum oxide at 0.8 V. Therefore, it is expected for both ethanol oxidation and platinum oxide formation to occur at 0.8 V.

EIS measurement was performed in 0.5 M H_2SO_4 + 0.5 M C_2H_5OH at three different potentials 0.20 V, 0.60 V, and 0.80 V at room temperature for the MPEs and PPE. The Nyquist plots for PPE and MPEs are shown in Figure 4.13.

Figure 4.13 a-e) show the Nyquist plots for PPE and the MPEs, which reveal different behaviour at different applied potentials. The Nyquist plots for PPE and the MPEs at an applied potential of 0.20 V indicate the impedance data to be in a clockwise mode as the applied frequency declines for all the electrodes. As the applied potential increases to 0.60 V, the impedance data show negative values for the real impedance when the applied frequency declines for all the electrodes. This was observed previously for ethanol oxidation and was suggested to be unstable behaviour in the electrochemical system.[98,159] The Nyquist plots at an applied potential of 0.80 V show a semicircle in clockwise mode as the applied frequency declined. The impedance values for these MPEs are much lower than PPE due to the greater surface area displayed by the nanostructure.

From the Nyquist plots, 0.80 V shows a semicircle with different diameters for the MPEs and PPE, reflecting the charge transfer resistance for ethanol oxidation. The smallest diameter suggests enhancement of a charge transfer during the ethanol oxidation and improves the catalytic activity.

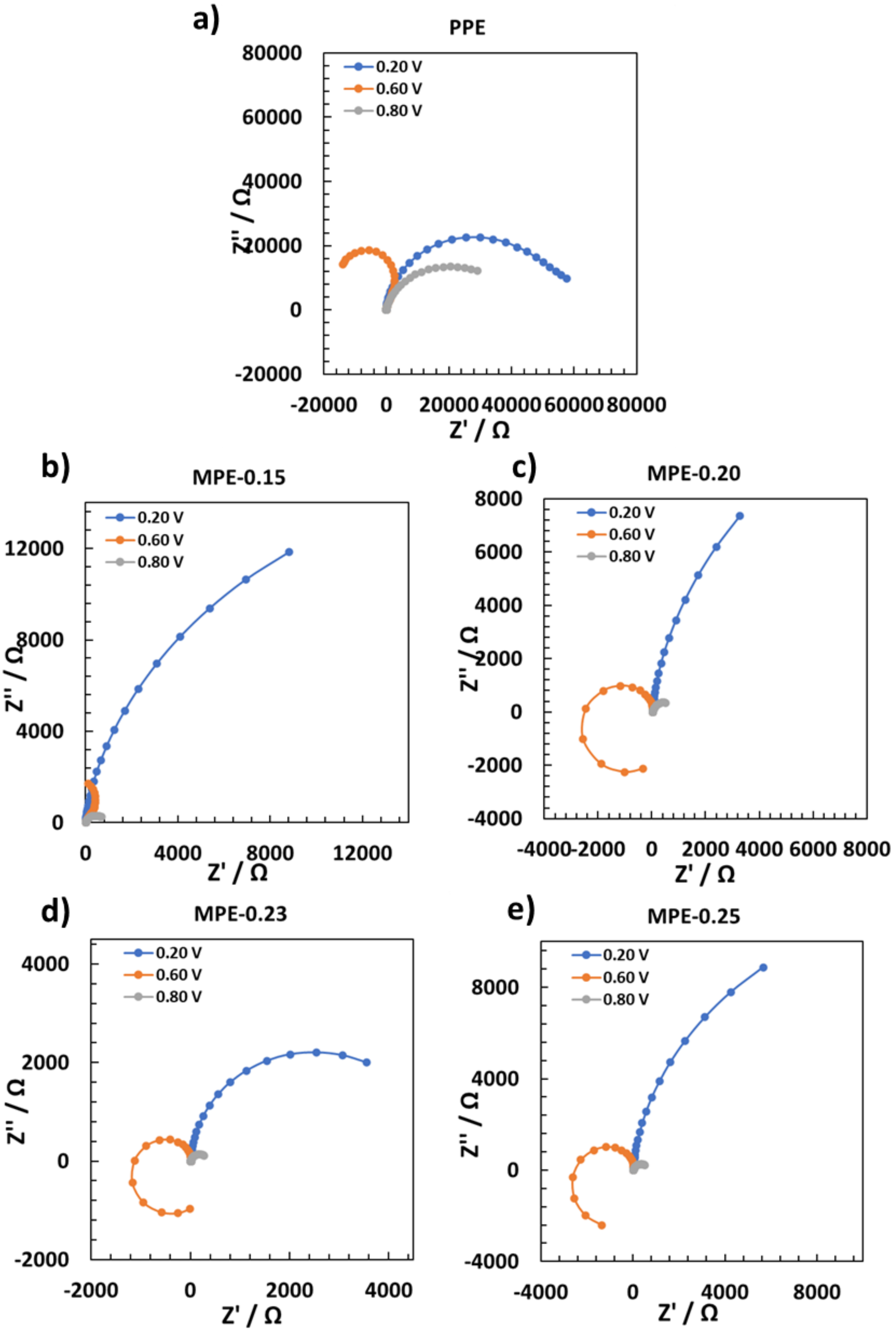

Figure 4.13 Electrochemical impedance in 0.5 M H_2SO_4 + 0.5 M C_2H_5OH solution at different applied potentials 0.20, 0.60 and 0.80 V of a) polished platinum electrode (PPE) and mesoporous platinum electrodes (MPEs) deposited from the $FCC_{Brij® 58}$ at different potentials, b) MPE-0.15, c) MPE-0.20, d) - 0.23 MPE, and e) MPE-0.25. The frequency range was 100 kHz to 0.2 Hz, and the AC amplitude was 10 mV.

The impedance data, at 0.80 V, displayed noteworthy trends that encouraged the application of circuit modelling for a more comprehensive understanding. Initially, the simple circuit R(RC) was evaluated, but the data did not give the best fitting. Therefore, the circuit with Q was proven to be the most appropriate for expressing the complexity of the electrode-electrolyte interface.[117] The R(RQ) circuit elements and other elements are described in Chapter 2. The x^2 values express the accuracy of the agreement between the model circuit and experimental data.[120] The fitted impedance data at 0.80 V for the MPEs and PPE are shown in Figure 4.14.

Figure 4.14 a) exhibits the equivalent circuit model R(RQ), which employs the Q parallel with a resistor to analyse the EIS data for the electrodes immersed in 0.5 M H_2SO_4 + 0.5 M C_2H_5OH. This circuit simplifies the representation of the electrochemical system. The solution resistance (Rs) indicates the electrolyte's resistance, which is influenced by electrolyte conductivity and electrode spacing factors. The charge transfer resistance (R_{ct}) at the electrode-electrolyte interface represents resistance linked to the kinetics of electrochemical reactions. Higher R_{ct} suggests slower charge transfer, influenced by reaction rate constants and electrode properties. The constant phase element (Q) replaces a capacitor and represents non-ideal capacitive behaviour, such as rough or porous electrodes. This circuit simplifies the analysis of complex electrochemical systems, capturing key aspects like electrolyte resistance, charge transfer kinetics, and non-ideal capacitive effects.

Figure 4.14 b) shows the Nyquist plot for PPE, demonstrating agreement with the fitting data. This was indicated by x^2 value of 0.0051 shown in Table 4.9. The insert plot shows the impedance at the high frequency range, revealing the near-vertical slope with a slight curvature near the low frequency. This behaviour is similar to the observed behaviour of polished electrode in dilute acid reported by Elliott *et al.*[114]

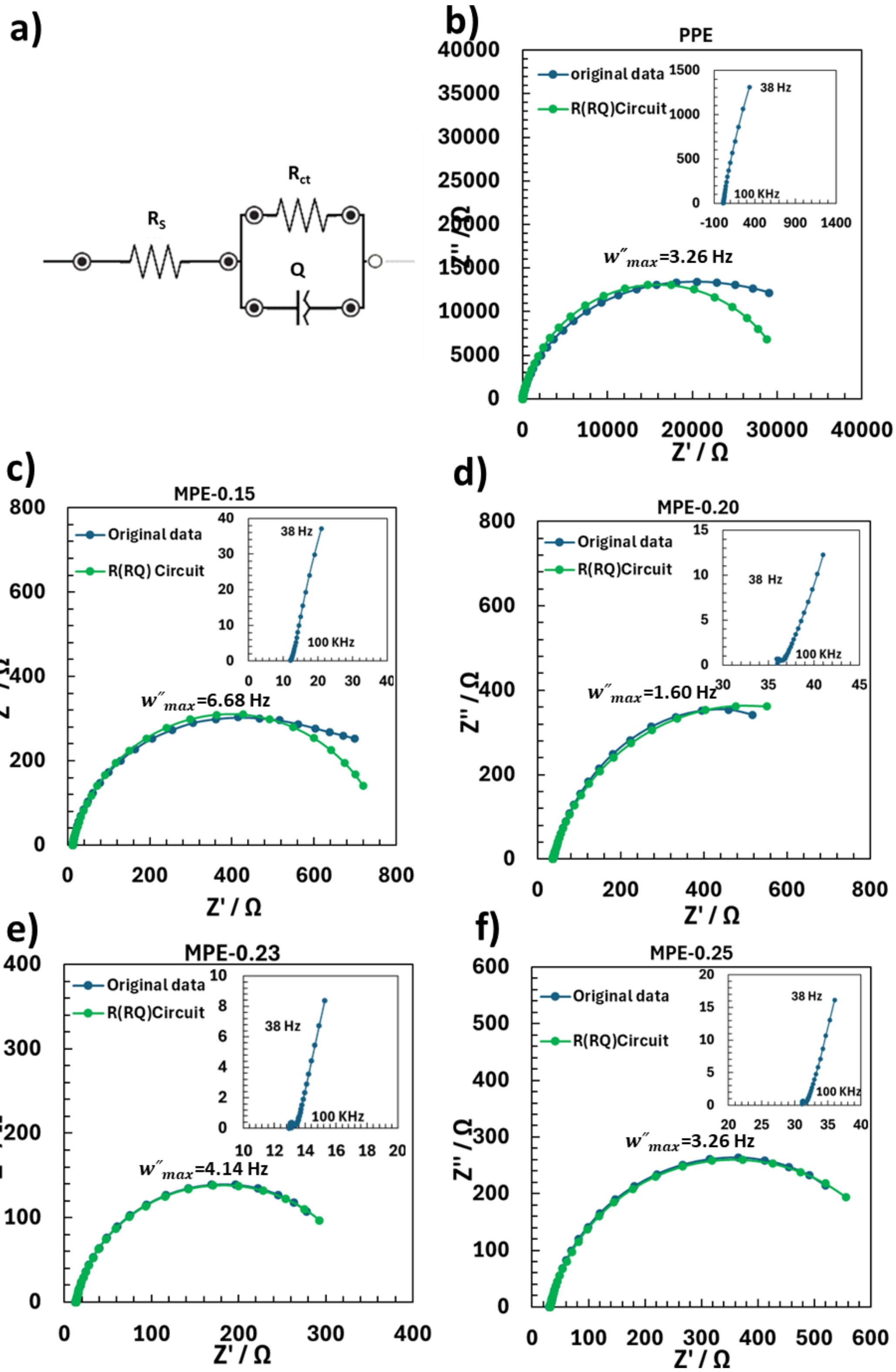

Figure 4.14 The fitted impedance spectra overlaid on the electrochemical impedance spectroscopies in 0.5 M H_2SO_4 + 0.5 M C_2H_5OH solution at applied potential of 0.80 V for different electrodes. a) The equivalent model circuit R(RQ), b)PPE and mesoporous platinum electrodes (MPEs) deposited from the $FCC_{Brij® 58}$ at different potentials, b) MPE-0.15, c) MPE-0.20, d) MPE-0.23 and e) MPE -0.25. The frequency range was 100 kHz to 0.2 Hz, and the AC amplitude was 10 mV. The insert plots show the impedance at higher frequencies, and the frequency of maximum imaginary impedance Z'' (w''_{max}) is shown in the plots.

Figure 4.14 c-f) show the Nyquist plots for MPE-0.15, MPE-0.20, MPE-0.23 and MPE-0.25, respectively. The accuracy of fitting with the R(RQ) circuit is indicated by the values of x^2 (as shown in Table 4.9); the smallest values are observed for MPE-0.20, MPE-0.23 and MPE-0.25 indicating better quality fits. The smallest semicircle diameter was observed for MPE-0.23. The insert plots present the magnified impedance at high frequencies and the shape at very high frequencies is unusual. This behaviour differs from the previous study by Elliott *et al.*, which studied the impedance for porous electrodes in dilute acid.[114] Their findings indicated that the porous electrodes with cylindrical pores revealed a Warburg impedance area with a slope $<$ 45° at high frequencies, which was explained by the transmission line model proposed by De Levie. De Levie's model represents a series of resistance and capacitance combinations at higher frequencies.[117,119] A possible explanation for why the results in Figure 4.14 vary from the standard Warburg model is likely due to different pore shape as explained by Cooper *et al*.[160] The De Levie model describes the impedance of a porous electrode with a cylindrical shape, which is different from the 3D pores in this study. The results presented here could be interpreted as evidence for a pore system with narrow openings as reported by Cooper *et al*.[160] ; it is also possibly due to artifacts from instrumental noise.[119]

The analysis of the EIS using the R(RQ) shows some key parameters, including R_s, R_{ct}, Y_0, n, C_{dl} and x^2, which were extracted, as shown in Table 4.9.

Table 4.9 surprisingly displays different R_s values for the MPEs and PPE. The R_s values for MPE- 0.15 and MPE-0.23 are similar, both smaller than those observed for MPE-0.20 and MPE- 0.25. These variations in R_s values could be due to the differences in the distance between the reference electrode and the working electrodes in each experiment.

Table 4.9 The RF, solution resistance (R_s), charge transfer resistance (R_{ct}) pre-exponent term (Y_0), exponent term (n), double layer capacitance (C_{dl}) and chi-squared (x^2) for PPE and MPEs deposited from the $FCC_{Brij^{®}\,58}$ at applied potential of 0.80 V.

Electrode	RF	R_s / Ω	R_{ct} / Ω	Y_0/ s^n $Ω^{-1}$	n / ϕ	C_{dl} / F	x^2
PPE	2.5	13	31870	4.49×10^{-6}	0.877	5.61×10^{-6}	0.0051
MPE-0.15	97	12	768	2.28×10^{-4}	0.866	1.76×10^{-4}	0.0024
MPE-0.20	346	37	939	7.77×10^{-4}	0.839	7.21×10^{-4}	0.0004
MPE-0.23	341	13	336	9.22×10^{-4}	0.877	7.75×10^{-4}	0.0004
MPE-0.25	209	32	651	5.24×10^{-4}	0.859	4.43×10^{-4}	0.0005

The R_{ct} values show that the MPEs exhibit smaller values compared to PPE, suggesting a faster and more efficient reaction for the MPEs than the PPE. The smallest R_{ct} (336 Ω) is detected for MPE-0.23, while the highest R_{ct} (31870 Ω) is observed for PPE due to the fewer active sites. Additionally, the MPEs demonstrate higher Y_0 values than the PPE, and these data were used to determine the C_{dl}, as explained in Equation 2.9 (Chapter 2). The w''_{max} values used in the C_{dl} measurement are presented in Figure 4.14 above. Table 4.9 indicates that the MPEs have larger C_{dl} values compared to the PPE, which recommends enhanced energy storage capacity linked to the enlarged area for the MPEs.

4.4 Conclusion

This chapter reported that the potential study investigating the use of the FCC structure of 40 wt% Brij® 58/HCPA with a_{FCC}= 13.0 nm as a template was effective as identified by the high passed current (400 µA) observed from the CV.

The successful electrodeposition through the $FCC_{Brij^{®}\,58}$ template at different potentials revealed increased Q_{dep} and σ values as the deposition voltage decreased until -0.23 V and then a slight decrease at -0.25 V probably due to the declined deposition efficiency and the presence of competing reactions. The morphology characterisation through the SEM images demonstrated interesting spherical particles assembled in a specific way to create layers with fissures in a specific direction. The AFM images showed that the RMS and AFS have the trend as the same Q_{dep} and σ values. Further investigation confirmed the porosity of the deposited platinum, with pore diameters ranging from 3.0 to 3.5 nm as indicated by TEM images. TEM analysis supports a regular diamond-like pore structure with lattice parameters varied from 6.3 ± 0.3 nm to 7.1 ± 0.7 nm. The CV investigation in dilute acid indicated high RF values which increased with respect to the σ value, suggesting the stability and uniform accessibility of their internal structure. The ECSA values ranged from 9.0 to 27.6 $m^2\ g^{-1}$ at different deposition potentials. The subsequent analysis for the MPEs presented promising catalytic activity towards ethanol oxidation in acidic media compared to PPE identified by the high J_F/J_B ratio with a maximum of 1.18, low E_{onset} minimising to 0.35 V and long-term stability.

Moreover, the EIS measurement for the ethanol oxidation in acidic media revealed various behaviours in Nyquist plots as the applied potential changed. Nyquist plots of EIS demonstrated a semicircle in clockwise mode at the potential of 0.20 and 0.80 V, but at 0.60 V, the data appeared in counterclockwise mode due to the unstable electrochemical system at this voltage. The R(RQ) circuit demonstrated an excellent fitting to the majority of the experimental data at 0.80 V. The EIS data at very high frequencies likely supports a pore system with narrow openings. The R_{ct} showed much smaller values for the MPEs compared to the PPE, due to their increased number of active sites. The MPEs revealed enhanced capacitance linked to their enlarged area compared to the PPE. This indicated encouraging catalytic activity for the MPEs towards ethanol oxidation compared to PPE.

Chapter 5- BCC$_{\text{Brij® 58}}$ templating of mesoporous platinum electrodes, their characterisation and electrocatalytic properties for ethanol oxidation

5.1 Introduction

This chapter focuses on utilising the BCC structure of Brij® 58 as a structural directing agent to produce mesoporous platinum films via the direct electrodeposition of LLC. The previous chapter highlighted the novel fabrication of 3D nanostructured platinum employing Brij® 58 with the FCC structure as a template, producing a diamond-like structure with pore diameter between 3.0 and 3.5 nm and lattice parameters ranging from 6.3 to 7.1 nm, based on TEM data. This achievement increases the interest in exploring the use of Brij® 58 in the LLC approach with alternative mesophases such as the BCC.

Therefore, this chapter employs a novel method employing the BCC structure of Brij® 58 for producing mesoporous platinum films with 3D morphology. The BCC structure has a space group of Im3m, and the Im3m is also considered a space group for the P-surface bicontinuous cubic phase and the tricontinueous cubic phase.[67] This suggests that the BCC template is expected to reveal similar behaviour to the bicontinuous (Im3m) template which was previously reported by Akbar *et al*.[26] In their recent work, Akbar *et al*. demonstrated the employment of phytantriol with Brij® 56 to form the Im3m template as a structuring agent via chemical and electrochemical deposition for the fabrication of mesoporous platinum films with a primitive (Pm3m) structure for the first time.[26] In their method, the reduction of platinum species occurred in one of the aqueous channels, leading to the fabrication of an ordered 3D platinum nanowire with a single primitive structure Pm3m symmetry. The findings revealed that the 3D platinum nanowire showed an extensive surface area, excellent accessibility, and electrochemical stability, highlighting their potential for catalytic applications.[26]

In this study, mesoporous platinum films are fabricated for the first time via the direct electrodeposition of LLC containing 30 wt% of Brij® 58 with BCC structure. Initially, attention was directed towards the structure assessment of 30 wt% Brij® 58 using SAXS, and after that, an examination of its capability to create mesoporous platinum films at various potentials. Then, the characterisation of the mesoporous platinum films was carried out employing different techniques, and the electrocatalytic activity towards ethanol oxidation was examined. Through this study, the objective was also to explore how the deposition time and film thickness alterations influence the morphology, electrode area and catalytic activity.

Aims:

- To investigate the feasibility of using the $\mathrm{BCC_{Brij^{®}\,58}}$ mixture as a template for depositing high area platinum films.
- To examine the effect of varying deposition voltage from the $\mathrm{BCC_{Brij^{®}\,58}}$ template upon electrode morphology, area and catalytic activity.
- To explore the effect of changing deposition time/film thickness from the $\mathrm{BCC_{Brij^{®}\,58}}$ template upon electrode morphology, area and catalytic activity.

5.2 Methodology

The methodology is presented in three main sections to align with the aims.

5.2.1 Feasibility study for using the $BCC_{Brij^{®}\ 58}$ mixture as a template for platinum deposition.

The 30 wt% Brij® 58 in HCPA solution was prepared as explained in Chapter 3. The amount of Brij® 58 and HCPA used in this study are shown in Table 5.1.

Table 5.1 Composition of Brij® 58/ HCPA used in this study.

Mass of Brij® 58 /g	**Mass of HCPA /g**	**Wt% of Brij® 58**
0.303	0.696	30.33 ± 0.082%

The 30 wt% Brij® 58/HCPA structure was investigated using SAXS at room temperature. Also, the possibility of deposition from this mixture was studied using CV. The CV was carried out in a polished platinum electrode with an area of 3.142×10^{-2} cm^2 at room temperature between the limits +0.70 and -0.30 V vs Ag/AgCl at a scan rate of 10 mV s^{-1}.

5.2.2 Effect of varying deposition voltage using the $BCC_{Brij^{®}\ 58}$ template upon the electrode morphology, surface area and catalytic activity

The electrodeposition of platinum from the $BCC_{Brij^{®}\ 58}$ template was carried out at platinum electrodes with an area of 3.142×10^{-2} cm^2 and platinum foils with an area of ~ 0.2 - 0.5 cm^2. The deposition was at room temperature and potential from +0.60 V to various negative potentials at a fixed time (1800 s), as shown in Table 5.2.

Table 5.2 Variation of deposition potential from BCC$_{Brij^{®} 58}$ template and corresponding sample name. n= number of measurements. In all cases, the deposition time was 1800.

Deposition potential/ V	Sample name
-0.15 (n=4)	MPE-0.15
-0.20 (n=4)	MPE-0.20
-0.23 (n=4)	MPE-0.23
-0.25 (n=4)	MPE-0.25

The morphology of the MPEs was investigated using SEM and the morphology of the platinum foils was examined using SAXS, TEM and XRD. Additionally, the electrochemical characterisation of the electrode area for the MPEs was carried out using CV in 0.5 M H_2SO_4. The catalytic activity towards ethanol oxidation of the MPEs was also conducted using CV in 0.5 M H_2SO_4 + 0.5 M C_2H_5OH electrolyte.

5.2.3 Impact of changing deposition time/film thickness from the BCC$_{Brij^{®} 58}$ template upon the morphology, electrode area and catalytic activity

Different film thicknesses were prepared through the electrodeposition of the 30 wt% Brij® 58/HCPA(BCC$_{Brij^{®} 58}$) template. The amount of Brij® 58 and HCPA used in this investigation is shown in Table 5.3.

Table 5.3 Composition of Brij® 58/ HCPA used in this study.

Mass of Brij® 58 /g	Mass of HCPA /g	Wt.% of Brij® 58
0.301	0.696	30.19 ± 0.083%

The deposition was carried out on platinum electrodes with an area of 3.142 x 10^{-2} cm^2 at room temperature and fixed potential -0.15 V over various durations, as shown in Table 5.4.

Table 5.4 Variation of deposition times from $BCC_{Brij^{®}\,58}$ template and corresponding sample name. n= number of measurements. In all cases, the deposition potential was -0.15 V.

Deposition time / s	Sample name
3600 (n=1)	MPE_3600
1800 (n=3)	MPE_1800
900 (n=1)	MPE_0900
300 (n=1)	MPE_0300
180 (n=2)	MPE_0180
120 (n=2)	MPE_0120
60 (n=2)	MPE_0060
30 (n=2)	MPE_0030
10 (n=1)	MPE_0010

The surface morphology of the MPEs fabricated at different durations was studied using SEM. The MPEs area was studied using CV in in 0.5 M H_2SO_4. The MPEs catalytic activity towards ethanol oxidation was investigated using CV in 0.5 M H_2SO_4 + 0.5 M C_2H_5OH electrolyte.

5.3 Results and discussion

The results are presented and discussed in three main sections to align with the aims.

5.3.1 Feasibility study for using the $BCC_{Brij^{®}\,58}$ mixture as a template for platinum deposition.

5.3.1.1 SAXS characterisation of the 30 wt% Brij® 58/HCPA mixture

SAXS was used to examine the structure and calculate the lattice parameter of the 30 wt% Brij® 58/HCPA mixture. The SAXS data of 30 wt% Brij® 58 in water and HCPA are revealed in Figure 5.1.

Figure 5.1 a) shows the SAXS pattern for 30 wt% Brij® 58 in water. The 2D SAXS pattern is composed of three sharp rings, indicating the presence of well-defined polydomain liquid crystalline structures. The SAXS data show the formation of the FCC phase, and this was confirmed by the 1D SAXS pattern that shows four Bragg peaks corresponding to the FCC symmetry structure with the ratio of $\sqrt{3}:\sqrt{4}:\sqrt{8}:\sqrt{11}$. The calculated lattice parameter of 30 wt% Brij® 58 in water was 12.4 nm, which agrees with the literature.[72,74] It has been reported by Mahanthappa *et al.* [74] that as the % water content increases, the micelle structure become 'hard' and consequently prefers to pack into the dense FCC phase, as was observed here.

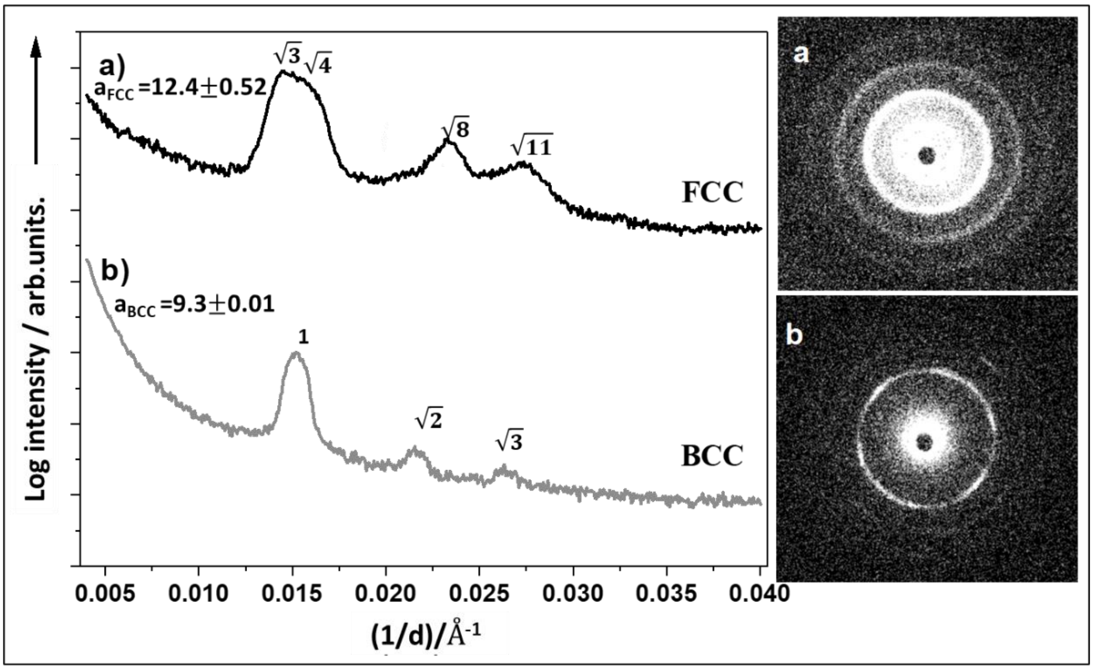

Figure 5.1 1D (left) and 2D (right) SAXS patterns for 30 wt% Brij® 58 in a) water and b) HCPA solution. The intensity of each 1D profile is plotted on a logarithmic scale; the relative peak positions are also noted, leading to the identification of the symmetry and lattice parameter as a_{FCC} water =12.4±0.52 nm and a_{BCC} HCPA =9.3 ±0.01 nm.

Figure 5.1 b) shows the SAXS pattern for 30 wt% Brij® 58 in aqueous HCPA. The 2D SAXS pattern reveals the weak arcs within the ring, showing some structural order within the polydomain LLC structures. The SAXS data show that the FCC phase for Brij® 58 in the presence of water was converted to the BCC structure in the presence of HCPA. The 1D SAXS pattern reveals three Bragg peaks with the ratios of $1:\sqrt{2}:\sqrt{3}$, which is typical for the BCC structure, and the calculated lattice parameter was 9.3 nm. The BCC structure for Brij® 58 in HCPA has not been reported previously, however, a previous study by Mahanthappa showed that the

BCC structure for Brij® 58 in water revealed a lattice parameter of 9.17 nm.[74] This transformation, from FCC to BCC, can be attributed to two possible reasons: first an ionic and second a physical interaction of the HCPA with Brij® 58 micelles. The most likely reason for this transformation at this composition is the ionic interaction of HCPA, which acts as a dehydrating agent, thereby reducing the effective hydration of Brij® 58 micelles. Therefore, the FCC phase is transformed into the lower packing fraction BCC structure, which is more compact and requires less hydration compared to the FCC phase in the water system.

It is essential to highlight that the SAXS data for 30 wt% of Brij® 58/HCPA in this chapter revealed a pure BCC structure, which is a different phase compared to the SAXS data presented previously in Chapter 3, which showed the mixed phase of the H_I+FCC structure. This difference in the phase behaviour was also observed previously in Chapter 4 and was explained to be possibly due to the sample history and sample preparation, as reported by Mahanthappa.[74] Another possible reason is a natural variation in the mixing process of different volumes, as the samples in this chapter have larger quantities than those in Chapter 3. However, the identification of the stable and pure BCC phase suggested that this mixture could be used as a template for the production of MPEs.

5.3.1.2 Electroreduction of the $BCC_{Brij® 58}$ mixture

To investigate the ideal deposition potential of the $BCC_{Brij® 58}$ mixture, the CV was employed at room temperature and a scan rate of 10 mV s^{-1}, as shown in Figure 5.2.

Figure 5.2 shows the CV for electroreduction of the $BCC_{Brij® 58,}$ which presents two visible electroreduction peaks E_{p1}=-0.01 V and E_{p2}=-0.23 V. This behaviour is similar to the electroreduction of the $FCC_{Brij® 58}$ mixture previously shown in Chapter 4. However, this CV indicates that the E_{p2} has a higher current (550 µA) than the $FCC_{Brij® 58}$ template, which showed

(400 µA) reported in Chapter 4. Additionally, the position of E_{p2} is at a more positive voltage (E_{p2}= -0.23 V) than the FCC$_{\text{Brij® 58}}$ template which revealed (E_{p2}= -0.25 V). From this CV, voltages between -0.15 V and -0.25 V were chosen for the electrodeposition of platinum.

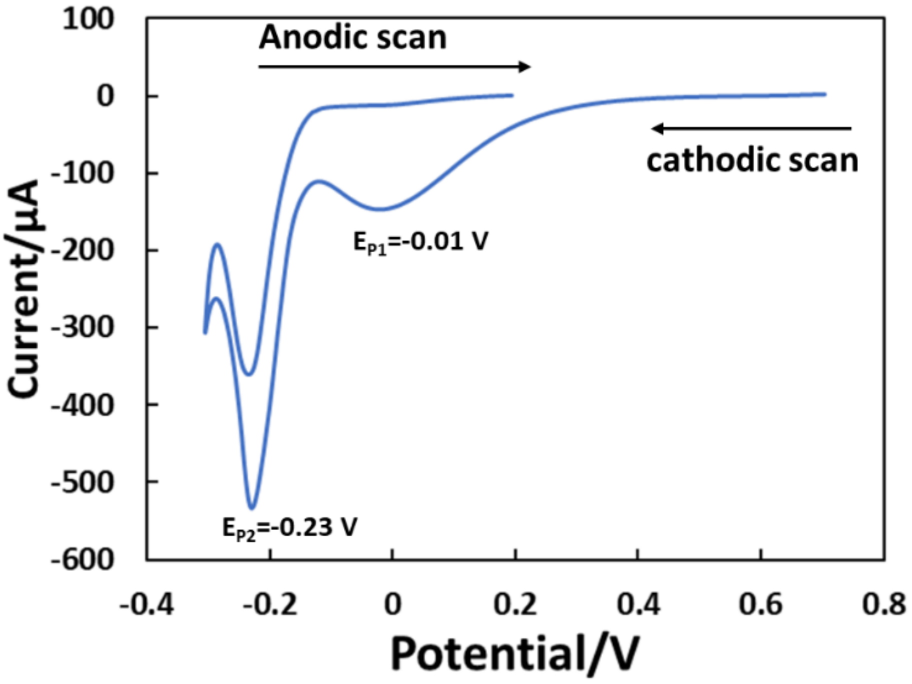

Figure 5.2 Cyclic voltammogram (CVs) recorded in the BCC$_{\text{Brij® 58}}$ mixture, recorded between 0.70 and -0.30 V vs Ag/AgCl at a scan rate of 10 mV s^{-1} and room temperature for a platinum polished electrode (cross-sectional area = 3.142 x 10^{-2} cm^2). The peaks are illustrated in the plot by E_{p1} and E_{p2}.

5.3.2 Effect of varying deposition voltage using the BCC$_{\text{Brij® 58}}$ template upon the electrode morphology, surface area and catalytic activity

5.3.2.1 Electrochemical fabrication

The electrodepositions were carried out at selected deposition potentials varying from -0.15 to -0.25 V for a fixed time of 1800 s using the BCC$_{\text{Brij® 58}}$ template; the corresponding deposition transients are shown in Figure 5.3.

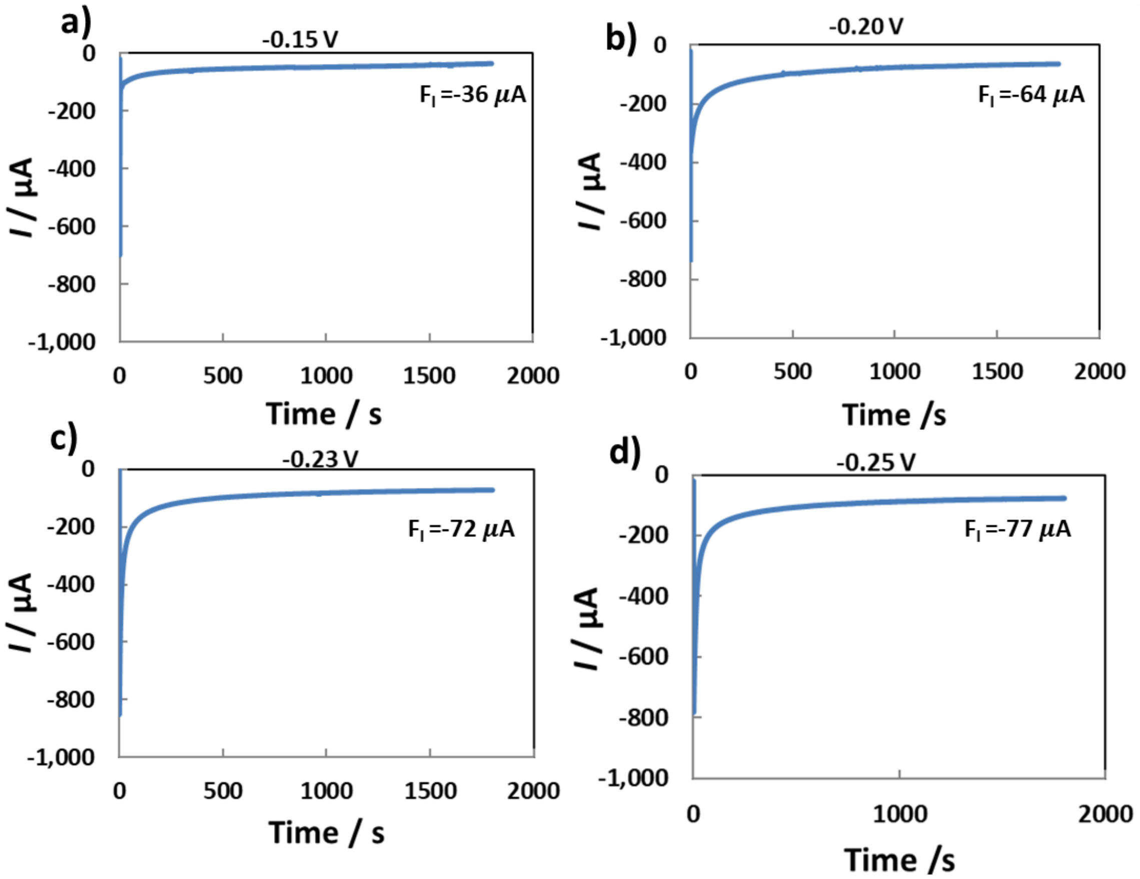

Figure 5.3 Representative electrodeposition transients recorded in the BCC$_{Brij^{®}\ 58}$ mixture at platinum electrodes (cross-sectional area = 3.142 x 10^{-2} cm^2) at room temperature and a fixed time for 1800 s with different potentials a) MPE-0.15, b) MPE-0.2, c) MPE-0.23 and d) MPE-0.25 V. F$_I$ shows the final current.

Figure 5.3 shows that the electrodeposition transients reveal different currents depending on the deposition potentials. The transients show an initial large negative current that rapidly declines and stabilises at non-zero current values as time passes. As described in Chapter 4, the initial large negative current is associated with the stepping potential from 0.60 V to negative potentials. The F$_I$ shows the smaller value for the potential at -0.15 V. Larger F$_I$ values are observed from the electrodeposition using the BCC$_{Brij^{®}\ 58}$ compared to the electrodeposition from the FCC$_{Brij^{®}\ 58}$ template reported in Chapter 4. This is in agreement with the current flowing during the CV deposition of the BCC$_{Brij^{®}\ 58}$ mixture (shown in Figure 5.2).

After the deposition, the template was removed by soaking the electrodes in water. Then, the washed electrode surfaces showed a dark grey to black appearance, similar to the colour observed for the MPEs fabricated from $FCC_{Brij^{®}\ 58}$ in Chapter 4. Further analyses of Q_{dep} and the σ using the transients at different deposition potentials are shown in Table 5.5.

Table 5.5 Variation in total deposition charge (Q_{dep}) and charge density (σ) for mesoporous platinum fabricated from the BCC $_{Brij^{®}\ 58}$ template at different deposition potentials in a fixed time (1800 s). Values represent the mean ± SD of n=3

Electrodes	Q_{dep} / C	σ / C cm^{-2}
MPE-0.15	0.10 ± 0.02	3.20 ± 0.51
MPE-0.20	0.18 ± 0.02	5.33 ± 0.54
MPE-0.23	0.17 ± 0.01	5.45 ± 0.44
MPE-0.25	0.16 ± 0.05	5.23 ± 1.59

Table 5.5Table 4.3 reveals that the Q_{dep} and σ differ depending on the deposition potentials. As the deposition potential decreased, both Q_{dep} and σ increased. The smaller values of Q_{dep} and σ for MPE-0.15 V are due to the slower kinetic reaction at this potential. For MPE-0.25, there is a slight decrease for both Q_{dep} and σ values. This trend of Q_{dep} and σ values is similar to the deposition from the $FCC_{Brij^{®}\ 58}$ mixture reported previously in Chapter 4, but the values here are larger. The depositions from $BCC_{Brij^{®}\ 58}$ for MPE-0.15, MPE-0.20 and MPE-0.23 indicate reproducibility. However, the MPE-0.25 V shows a large error bar. These films were selected for further studies, and the morphology of the produced platinum films at different potentials was conducted and is presented in the following section.

5.3.2.1 Characterisation of morphology and structure in the MPEs

TEM and SAXS - The structure of fabricated mesoporous platinum films using the $BCC_{Brij^{®}\ 58}$ template was studied using SAXS and TEM analysis, as shown in Figure 5.4.

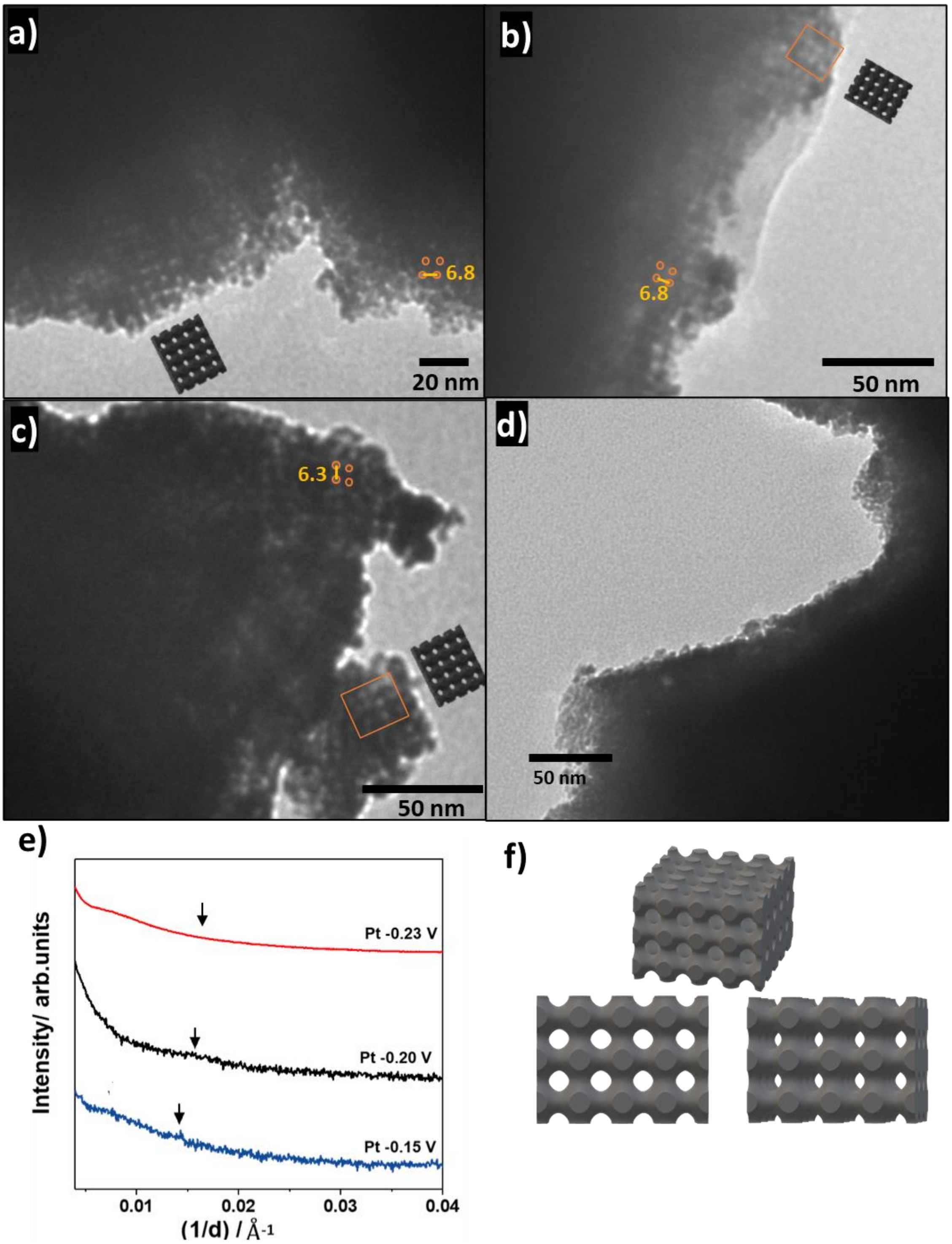

Figure 5.4 a-d) TEM images for the mesoporous platinum films deposited from the BCC$_{Brij^{®}\,58}$ at different potentials, a) MPE-0.15, b) MPE-0.2, c) MPE-0.23 and d) MPE-0.25 V the inserts are the simulation projections for a primitive structure. e)1D SAXS pattern for mesoporous platinum films deposited at - 0.15, -0.20 and -0.23 V, the intensity of each 1D profile is plotted on a logarithmic scale. f) a simulation projection for primitive Pm3m structure in different directions.

Figure 5.4 a-c) show the TEM image for MPE-0.15, MPE-0.20 and MPE-0.23, respectively.

These TEM images show similar shapes and display 3D networks with regular pore structures.

As the BCC template has a structure of closely packed spheres, the platinum could be deposited in the aqueous channel between the micelles, producing branches in each direction; making six branches in each node corresponding to the primitive space group Im3m.[158] Additionally, the pore structure from the TEM best matches the primitive structure simulation inserted in the TEM images. The measured lattice parameters for MPE-0.15, MPE-0.20 and MPE-0.23 are 6.8 ± 0.9, 6.8 ± 0.7 and 6.4 ±0.5 nm, respectively, with pore diameter estimated to be from 3.0 to 3.5 nm for all materials. The mesoporous platinum shows a structure in agreement with the phytantriol study by Akbar *et al.*; however, the lattice parameters from Brij® 58 are smaller than those from phytantriol (14.8 ± 0.8 nm).[26]

Figure 5.4 d) reveals the TEM image for MPE-0.25, which demonstrates a 3D network with an irregular porous structure. Therefore, as mentioned previously, the low applied potential in the deposition process could degrade the mesoporous platinum network's structure and morphology due to the side reactions, such as the evolution of gas, which led to the disruption of the nanostructure.[7,24] Elliott *et al*. and Akbar *et al*. reported a gradual structural loss for mesoporous platinum films deposited at more negative potentials than - 0.20 V using the hexagonal[7] and cubic (Q229) template.[24]

Figure 5.4 e) shows the 1D SAXS pattern for MPE-0.15, MPE-0.20 and MPE-0.23. However, the SAXS analysis of MPE-0.25 was unfortunately not feasible as the SAXS instrument became inoperative during this study. The SAXS plot is featureless, and the arrows point approximately to features representative of the spacing from the TEM. As these data do not show clear peaks, it was difficult to determine the exact symmetry from the provided SAXS data. Several projections were simulated in different directions, and the model of the primitive structure was found to best match the TEM images (shown in Figure 5.4 f)).

XRD - The XRD data is expected to show the FCC structure for platinum. The XRD can also provide some information about the effect of the mesoporous structure, such as the crystal size. The blank platinum foil was analysed using XRD and compared to the nanostructured platinum films, as shown in Figure 5.5.

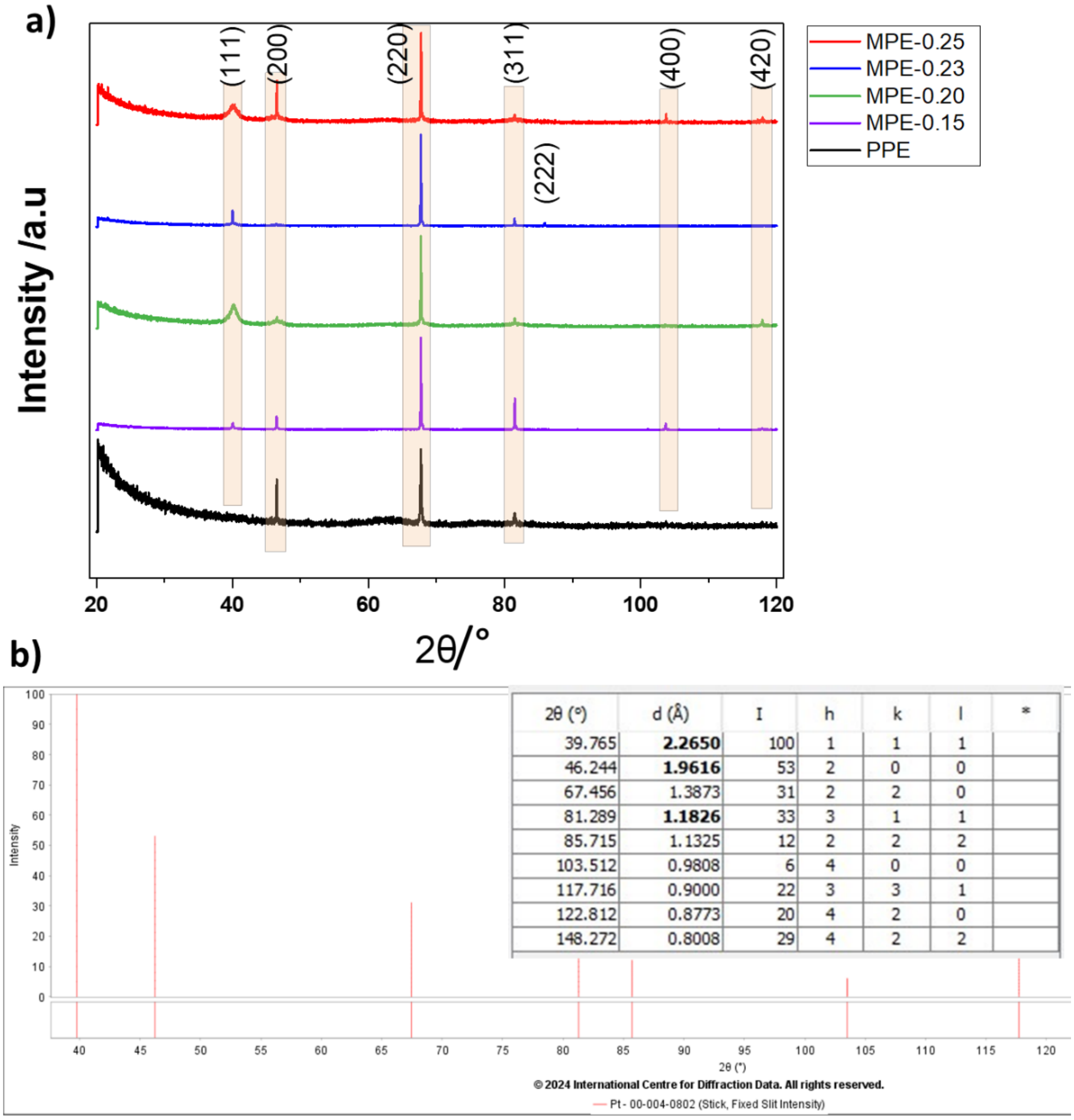

2θ (°)	d (Å)	I	h	k	l	*
39.765	**2.2650**	100	1	1	1	
46.244	**1.9616**	53	2	0	0	
67.456	1.3873	31	2	2	0	
81.289	**1.1826**	33	3	1	1	
85.715	1.1325	12	2	2	2	
103.512	0.9808	6	4	0	0	
117.716	0.9000	22	3	3	1	
122.812	0.8773	20	4	2	0	
148.272	0.8008	29	4	2	2	

Figure 5.5 a) XRD measurement for the platinum foil (PPE) and the mesoporous platinum foils (MPE) deposited from the BCC$_{Brij^{®}\ 58}$ at different potentials -0.15 V, -0.20 V, -0.23 V and -0.25 V. b) the platinum XRD data from International Centre for Powder Diffraction data file 00-004-0802

Figure 5.5 a) shows the XRD pattern for the PPE and the MPEs deposited at different potentials. The XRD patterns show notable differences between the blank platinum foil and the MPEs. The XRD for the PPE displays only three characteristic peaks corresponding to the

FCC crystal structure, which were observed at 2θ= 46.5°, 67.7° and 81.4°, respectively. The structure was checked by comparison through the International Centre for diffraction data's powder diffraction file 00-004-0802 shown in Figure 5.5 b). The XRD patterns for the MPEs exhibit five to six peaks that also indicate the FCC crystal of platinum. The hkl values for the FCC structure are shown in the plot. These XRD data show similar results to the previous XRD data reported for the MPEs prepared from the $FCC_{Brij^{®}\ 58}$ template in Chapter 4. There is some variation in the number of peaks and intensities.

SEM - The SEM images were obtained with various magnifications for the MPEs surfaces deposited at different voltages, as shown in Figure 5.6.

Figure 5.6 a) shows the SEM image for the PPE surface, which is similar to the image discussed in the previous chapter (Chapter 4). This image again confirms the polished surface, emphasising the smooth nature of the platinum surface with visible polishing lines.

Figure 5.6 b) and c) show the SEM images for the MPE-0.15 and MPE-0.20, respectively. The SEM reveal interesting morphological features compared to the PPE. These SEM images show that the growth of the platinum nanostructure started with an aggregation of small spherical particles in a specific structure to create a layer with visible cracks in a uniform pattern (as shown in the insert image in Figure 5.6 c)). Interestingly, Figure 5.6 d) and e) reveal the SEM images for the MPE-0.23 and MPE-0.25, respectively, and indicate the same growth behaviour observed for MPE-0.15 and MPE-0.20. However, the spherical particles were larger and more noticeable (as shown in the insert image in Figure 5.6 e)). These SEM images are similar to the SEM images for the MPEs deposited from the $FCC_{Brij^{®}\ 58}$ template reported in Chapter 4, however, the SEM data here show denser features. For further investigation, the EDX was used, and the results(not shown here) confirmed that the surface was covered with platinum only and there was no presence of other materials on the surface.

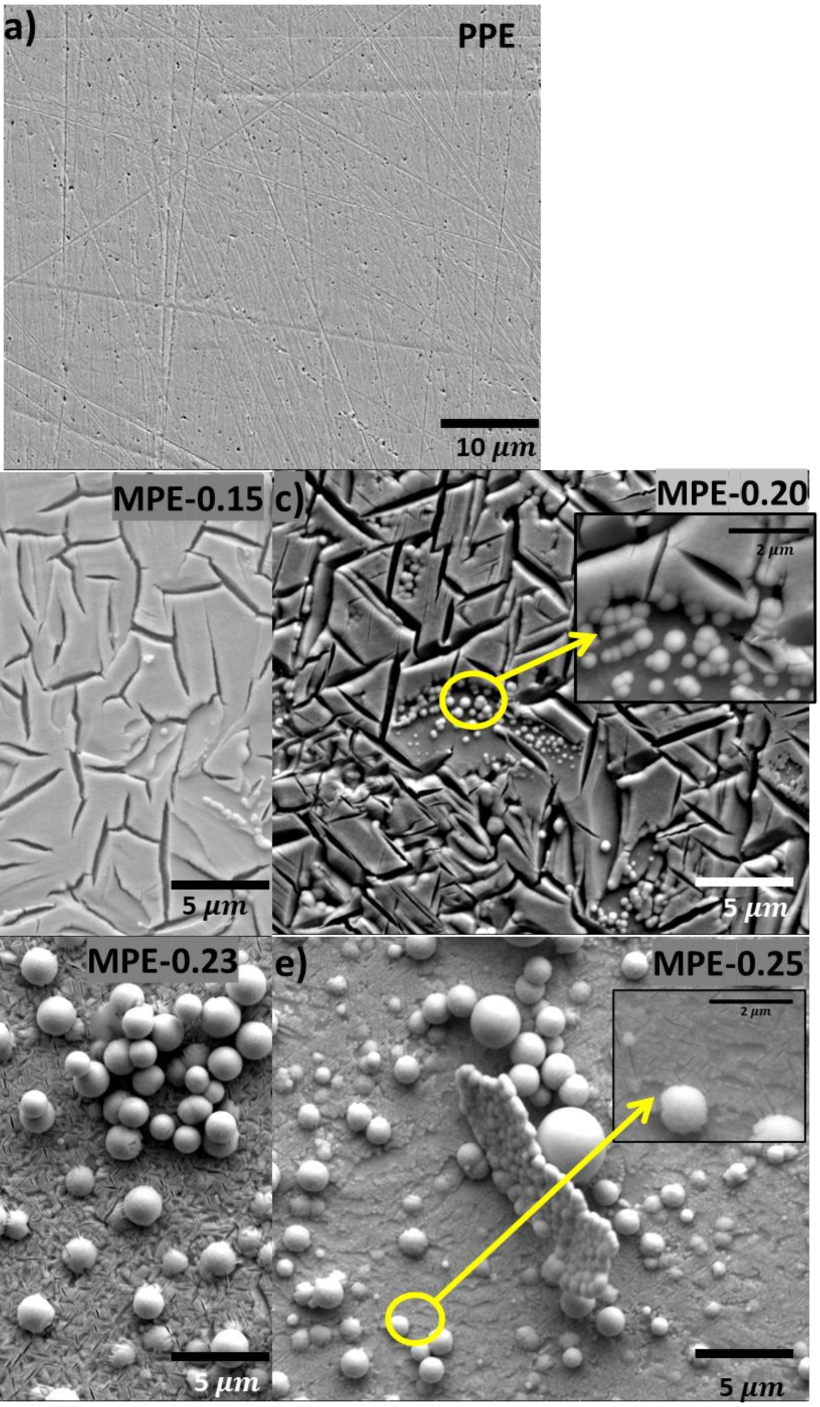

Figure 5.6 SEM images of a) polished platinum electrode (PPE) and mesoporous platinum electrodes (MPEs) deposited from the $BCC_{Brij^{®}\,58}$ *at different voltages, b) MPE-0.15, c) MPE-0.2, d) MPE-0.23, and e) MPE-0.25.*

5.3.2.2 Electrochemical characterisation of the MPEs

CV in sulfuric acid - this technique was used for further cleaning and to remove any impurities from the surfactant used as a template. The clean CVs of the MPEs and PPE were recorded at 50 mV s^{-1} and shown in Figure 5.7.

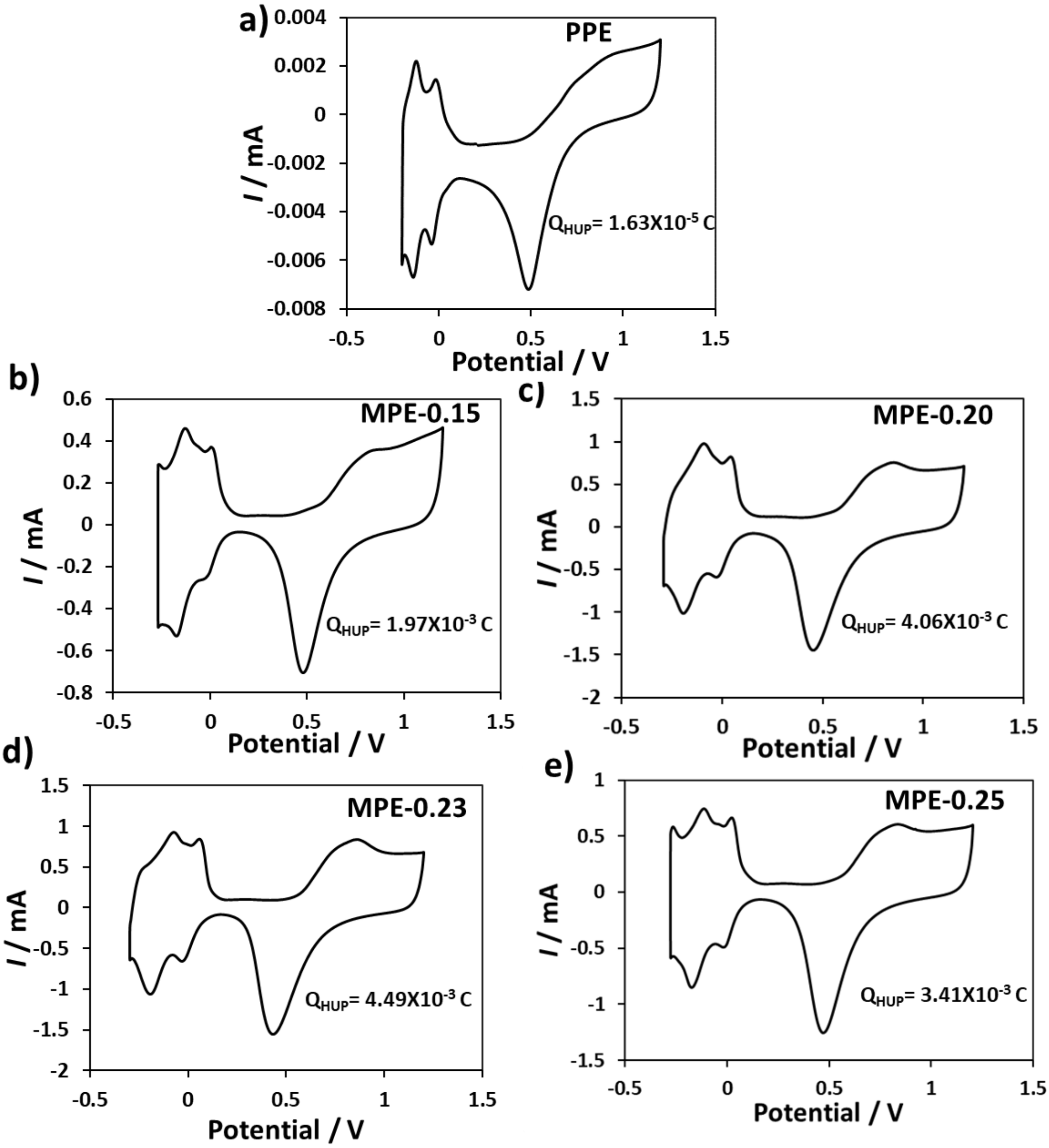

Figure 5.7 Cyclic voltammograms (CVs) recorded in 0.5 M H_2SO_4, at room temperature and 50 mV s^{-1} for a) polished platinum electrode (PPE) and a series of mesoporous platinum electrodes (MPEs)(cross-sectional area = 3.142 x 10^{-2} cm^2) fabricated from the BCC$_{Brij® 58}$ with different deposition potentials at b) MPE-0.15, c) MPE-0.20, d) MPE-0.23 and e) MPE-0.25. Q$_{HUP}$ means the charge for hydrogen underpotential region.

Figure 5.7 shows the CVs for the MPEs and PPE reveal the typical adsorption/desorption features in H_{upd} region. The MPEs exhibit a larger current than the PPE, indicating the successful production of mesoporous platinum films with a high surface area. The CVs present slightly different shapes with various deposition potentials, depending on the growth of the deposited platinum. Further analyses to determine the RSA, RF and ECSA values from the Q_{HUP} and the Q_{dep} (as explained in chapter 2) for all the MPEs prepared at different voltages from three independent depositions (n=3) were carried out and are shown in Table 5.6

Table 5.6 The real surface area (RSA) roughness factor (RF) and electrochemical active surface area (ECSA) for the polished electrode (PPE) and mesoporous platinum electrodes(MPEs) (cross-sectional area = 3.142 x 10^{-2} cm^2) deposited from the $BCC_{Brij^{®}\ 58}$ at different potentials. ± SD of n=3

Electrodes	RSA /cm^2	RF	ECSA /$m^2\ g^{-1}$
PPE	0.08	2.5	-
MPE-0.15	8.63 ± 2.06	275 ± 66.6	16.76 ± 2.84
MPE-0.20	19.31 ± 2.30	615 ± 74.5	22.73 ± 0.42
MPE-0.23	19.89 ± 1.35	634 ± 34.3	23.03 ± 1.24
MPE-0.25	14.89 ± 5.91	488 ± 189.6	17.40 ± 2.96

Table 5.6 shows that the RSA, RF and ECSA values vary depending on the deposition potential for the MPEs, and show an increase with decreasing deposition potential from -0.15 to -0.23 V. However, the MPE-0.25 shows an apparent decrease of the RF as well as the ECSA. This was identified to be due to reduced deposition efficiency at lower potentials.[7] This trend agrees with the previous results of the MPEs templated from the $FCC_{Brij^{®}\ 58}$ mixture in Chapter 4. The RF values for the MPEs from Table 5.6 increase with the increase of both Q_{dep} and σ as reported in Table 4.3, which suggests uniform accessibility of pores throughout the film thickness.

CV in ethanol under acidic media -The catalytic responses to ethanol oxidation for PPE and the MPEs deposited at various potentials were assessed through the CV. The MPEs were cycled in dilute acid before the ethanol oxidation study, and the RF, RSAs and ECSA values were recalculated and are presented in Table 5.7.

Table 5.7 The total deposition charge (Q_{dep}) roughness factor (RF), real surface area (RSA), and electrochemical active surface area (ECSA) for the polished platinum electrode (PPE) and mesoporous platinum electrodes (MPEs) (cross-sectional area = 3.142 x 10^{-2} cm^2) deposited from the $BCC_{Brij^{®}\,58}$ at different potentials. n=1

Electrode	Q_{dep} / C	RSA / cm^2	RF	ECSA / $m^2\,g^{-1}$
PPE	-	0.08	2.5	-
MPE-0.15	0.09	7.98	254	16.8
MPE-0.20	0.17	15.14	482	17.5
MPE-0.23	0.18	16.75	533	19.0
MPE-0.25	0.19	10.11	322	10.3

Table 5.7 show the RSA, RF and ECSA values for one deposition (n=1), while the data in Table 5.6 are values for three depositions (n=3). Therefore, some differences in the values are observed because the MPEs were cycled several times, reducing the values.

The RSA values of the MPEs were used to produce *J*. These MPEs were utilised as catalysts in 0.5 M H_2SO_4 + 0.5 M C_2H_5OH electrolyte using the CV. The third cycle of the CVs in 0.5 M H_2SO_4 + 0.5 M C_2H_5OH electrolyte are shown in Figure 5.8.

Figure 5.8 a) shows the CVs for ethanol oxidation in terms of *I*. The MPEs exhibit a higher current for ethanol oxidation than the PPE owing to the enlarged surface area of the MPEs. The CVs display that the I_F and I_B increase with the increase of RF for the MPEs. For instance, the MPE-0.23 with the highest RF shows the highest I_F and I_B for ethanol oxidation.

Figure 5.8 b) shows the CVs of ethanol oxidation with the in terms of *J* for the MPEs and PPE. The data exhibits that the J_F and J_B decrease with increased RF for the MPEs. The highest J_F and J_B were observed for the MPE-0.15 and MPE-0.25, which have the lowest RF. The insert shows that the curves of peak F reveal a shift to the left (lower potentials) for the MPEs compared to PPE. This confirms that the ethanol oxidation reaction occurs more easily on the MPE surfaces than on the PPE surface.

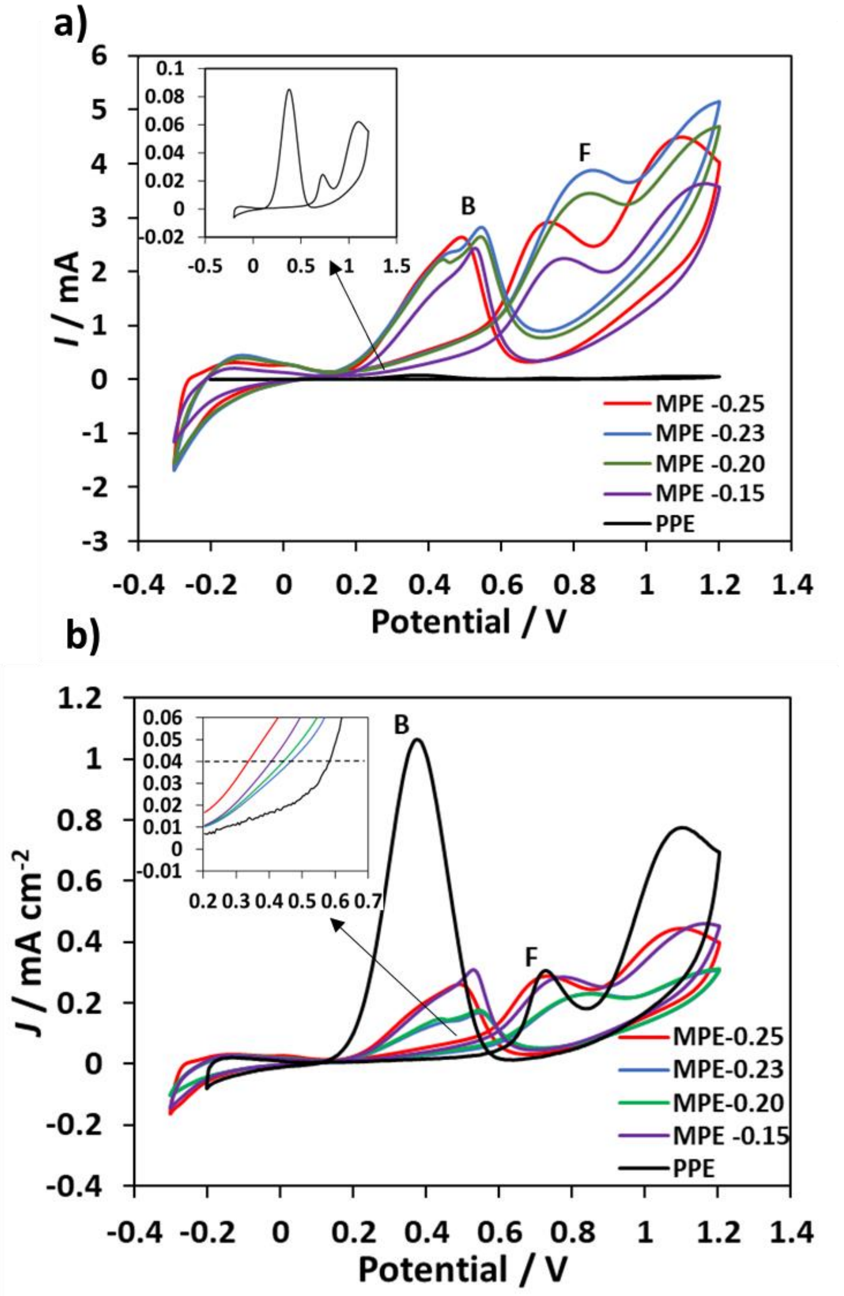

Figure 5.8 Cyclic voltammograms (CVs) in 0.5 M H_2SO_4 + 0.5 M C_2H_5OH solution a) current (I) and b) current density calculated from the RSA (J) recorded at room temperature at a scan rate of 50 mV s^{-1} of the polished platinum electrode (PPE) and mesoporous platinum electrodes (MPEs) deposited from the $BCC_{Brij® 58}$ at different potentials, MPE-0.15, MPE-0.2, MPE-0.23 and MPE-0.25. The insert exhibits a) the CV of the PPE and b) shows the magnification of the plot and the horizontal dotted line shows the J for the onset potential. The forward and backward peaks are illustrated by F and B in the plot.

Further analysis of catalytic activity examining J_F/J_B and E_{onest} for the MPEs and the PPE was carried out and data are shown in

Table 5.8.

Table 5.8 The catalytic activity of the polished platinum electrode (PPE) and mesoporous platinum electrodes (MPEs) (cross-sectional area = 3.142 x 10^{-2} cm^2) deposited from the $BCC_{Brij® 58}$ at different voltages towards the ethanol oxidation in terms of current (I) and current density (J). The I_F means forward peak in current, I_B means backward peak in current, the J_F means forward peak in current density, and the J_B means backward peak in current density. Onset potential (E_{onset}) data collected at 0.04 mA cm^{-2}, n=1

Electrode	Rf	I_F / mA	I_B / mA	J_F / mA cm^{-2}	J_B / mA cm^{-2}	J_F / J_B	E_{onset} / V
PPE	3	0.02	0.08	0.25	1.05	0.24	0.58
MPE-0.15	254	2.23	2.36	0.28	0.30	0.94	0.40
MPE-0.20	482	3.42	2.60	0.23	0.17	1.32	0.44
MPE-0.23	533	3.87	2.80	0.23	0.16	1.38	0.46
MPE-0.25	322	2.90	2.60	0.29	0.26	1.12	0.33

Table 5.8 shows the catalytic activity data for the MPEs and PPE in terms of *I* and *J* which indicates that the I_F and I_B increase as the RF for the MPEs increases, whilst the J_F and J_B decrease. The highest J_F and J_B were observed for the MPE-0.15 and MPE-0.25, which have the smallest RF. This is similar to the behaviour of the MPEs fabricated from the $FCC_{Brij® 58}$ in Chapter 4, and the reason was explained as likely due to the fast reaction of ethanol oxidation.[116] Therefore, ethanol species oxidise easily when they hit the electrode surface and do not penetrate deeply into thick films. Consequently, further investigation regarding the effect of the thickness of films fabricated from the $BCC_{Brij® 58}$ template towards ethanol oxidation was conducted and this is shown in section 5.3.3.

In contrast, the ratio of J_F/J_B show an increase with increase of the RF values. The highest ratio of J_F/J_B was obtained for MPE-0.23 (1.38), with the highest RF value of 533. The high J_F/J_B ratio for all MPEs suggests enhanced ethanol oxidation to the final product compared to PPE, most likely owing to an increase of available platinum sites. Moreover, the E_{onset} at J = 0.04 mA cm^{-2}

demonstrates that the MPEs reveal lower values than the PPE, suggesting a faster reaction towards ethanol, with the best performance from MPE-0.25 (0.33 V).

Repeated cycling was used to evaluate the stability and long-term activity of the MPEs and PPE towards ethanol electro-oxidation. Over 100 cycles were applied in 0.5 M H_2SO_4 + 0.5 M C_2H_5OH solution, and the CVs recorded between -0.3 and 1.2 V at 50 mV s^{-1} are shown in Figure 5.9.

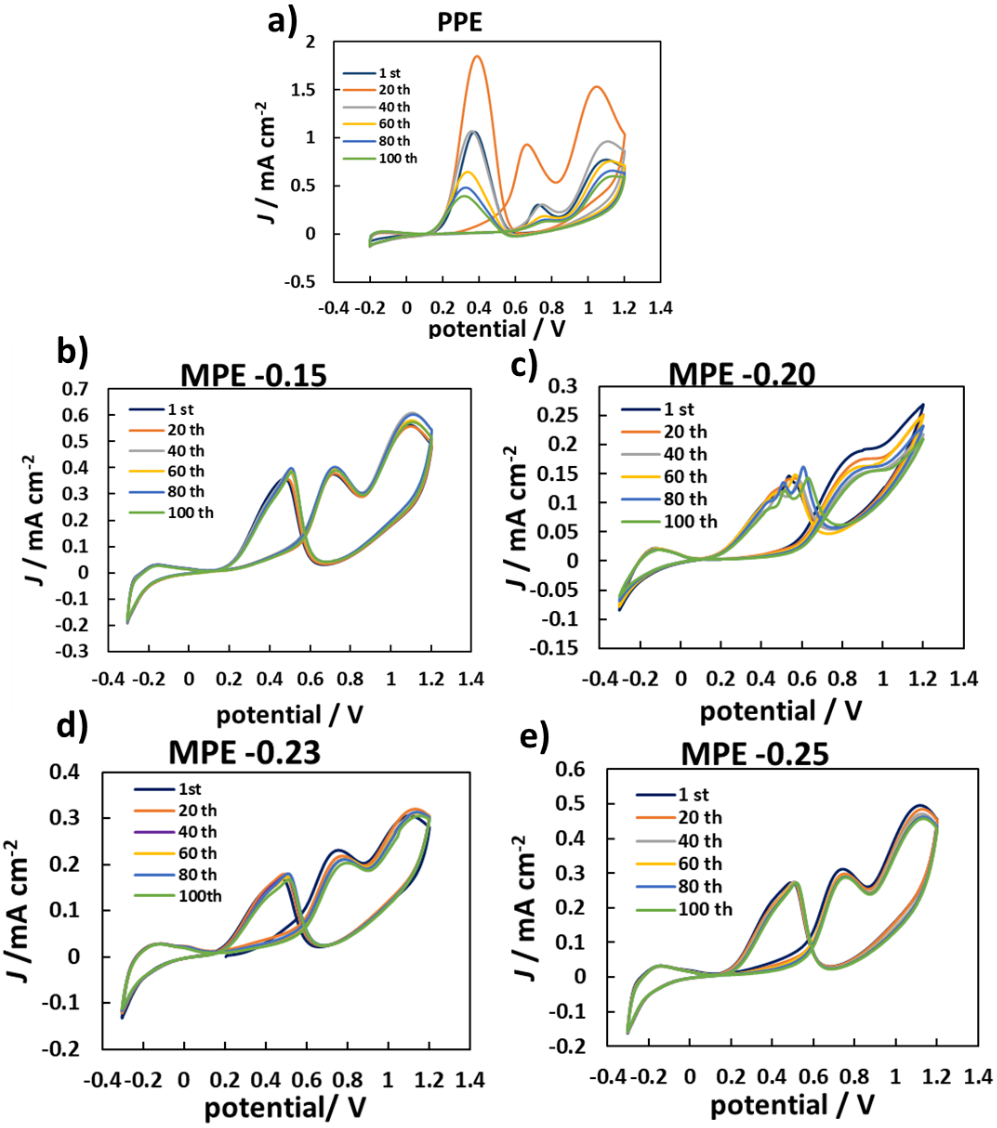

Figure 5.9 Cyclic voltammograms (CVs) over 100 cycles, in 0.5 M ethanol + 0.5 M H_2SO_4 solution at room temperature and 50 mV s^{-1} for a) polished platinum electrode and mesoporous platinum electrodes(MPE) deposited from the BCC$_{\text{Brij® 58}}$ at different voltages b) MPE-0.15, c) MPE-0.20, d) MPE-0.23, and e) MPE-0.25 V. Every 20 cycles are shown, and each colour presents the number of cycles.

Figure 5.9 a) the CV for PPE demonstrates that the J_F increases up to the 20th cycle, followed by a subsequent decrease in J_F to the 100th cycle. The decrease in the J_F over 100 CVs is most likely due to catalyst poisoning.

Figure 5.9 b-e) show the CVs for the MPEs deposited at different voltages, indicating good stability compared to the PPE over 100 CVs. Further analyses comparing the J_F for the 1st and 100th cycles, the stability and enhancement factors are presented in Table 5.9

Table 5.9 The stability of the polished platinum electrodes (PPE) and mesoporous platinum electrodes (MPEs) fabricated from the $BCC_{Brij^{®}\ 58}$ at different voltages over 100 scans; J_F means the current density of the forward peak. The stability factor (1) is the percentage change calculated from the $J_{F100th\ scan}$ to the $J_{F1st\ scan}$ for each electrode. The enhancement factor (2) is a percentage comparison of the J_{F100th} for MPEs to the J_{F100th} for PPE. It is calculated by dividing the J_{F100th} value of MPEs by the J_{F100th} value of PPE.

Electrodes	RF	$J_{F\ 1st\ scan}$ / mA cm^{-2}	$J_{F\ 100th\ scan}$ / mA cm^{-2}	Stability factor (1)	Enhancement factor (2)
PPE	2.5	0.30	0.13	42%	100%
MPE-0.15	207	0.37	0.39	104%	311%
MPE-0.20	417	0.19	0.15	82%	123%
MPE-0.23	477	0.23	0.20	88%	162%
MPE-0.25	295	0.31	0.28	93%	226%

The data in Table 5.9 reveal that the MPEs show remarkable stability factor over the 100th CVs compared to the PPE. Additionally, the enhancement factor demonstrates excellent efficiency and effectiveness of the MPEs. The highest stability and enhancement factor was observed for the MPE-0.15 with 104% and 311% values, respectively. Interestingly, this MPE-0.15 has the smallest RF (207) compared to other MPEs.

In order to investigate the MPE behaviour for different thicknesses of films, the deposition potential was fixed at -0.15V, and the time was varied. The following section discusses different thicknesses of mesoporous films prepared at -0.15 V.

5.3.3 Effect of changing the deposition time/film thickness from the $BCC_{Brij® 58}$ template upon the electrode morphology, area and catalytic activity

5.3.3.1 Electrochemical fabrication

The electrodeposition process was carried out using the $BCC_{Brij® 58}$ at a fixed potential of - 0.15 V, and the time was varied from 3600 to 10 s to create different thicknesses of the MPEs.

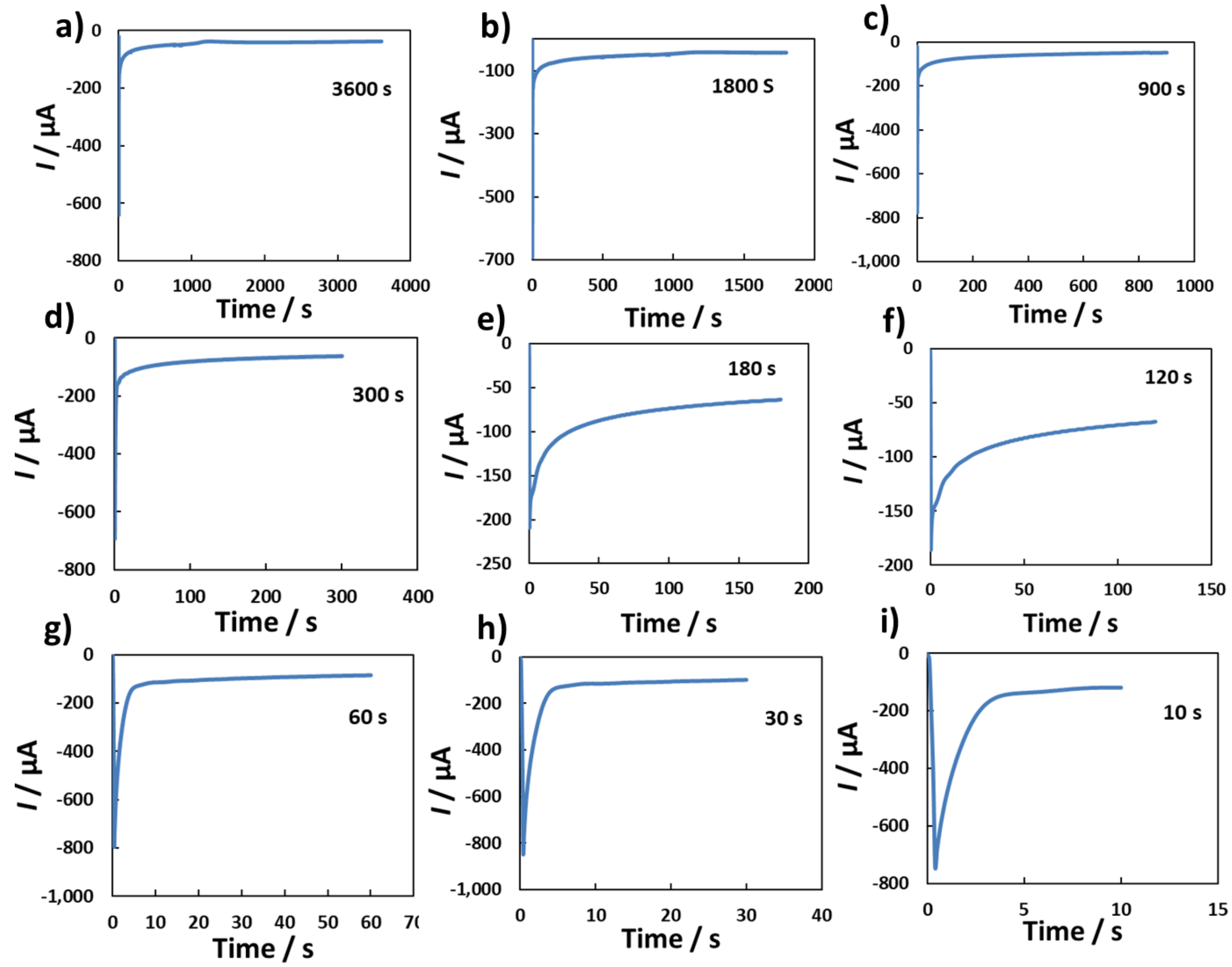

Figure 5.10 Representative electrodeposition transients recorded in the $BCC_{Brij® 58}$ mixture at platinum electrodes (cross sectional area = 3.142 x 10^{-2} cm^2) at room temperature and a fixed potential -0.15V vs Ag/AgCl with different deposition times a) 3600 s, b) 1800 s, c) 900 s, d) 300s, e) 180 s, f) 120 s, g) 60 s, h) 30 s and i) 10 s.

Figure 5.10 demonstrates the transients of the depositions at -0.15 V for different lengths of time. All the transients show that after an initial decrease the current became stable at negative values, indicating a steady rate of electrodepostion. The transients were used to calculate σ as shown in Figure 5.11.

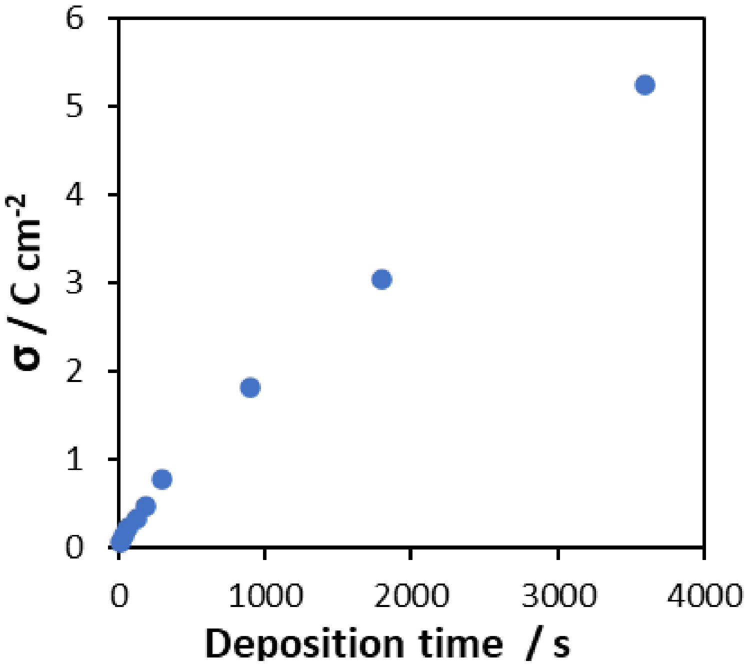

Figure 5.11 The charge density (σ) for the mesoporous platinum electrodes (MPE) deposited from the BCC$_{Brij^{®}58}$ at -0.15 V and different deposition times at room temperature. Data for MPE_3600, MPE_1800, MPE_0900, MPE_0300, MPE_0180, MPE_0120, MPE_0060, MPE_0030 and MPE_0010.

Figure 5.11 shows the σ value increases with deposition time. The highest σ was observed for MPE_3600. This increase in the σ values with increased deposition time suggests a corresponding increase in the film thickness, in accordance with Faraday's law.[161] It was expected that MPE_3600 had the largest film thickness and MPE_0010 the smallest.

5.3.3.2 Characterisation of morphology in the MPEs - SEM

SEM analyses were carried out to investigate the surface morphology of the MPEs, and the results are shown in Figure 5.12.

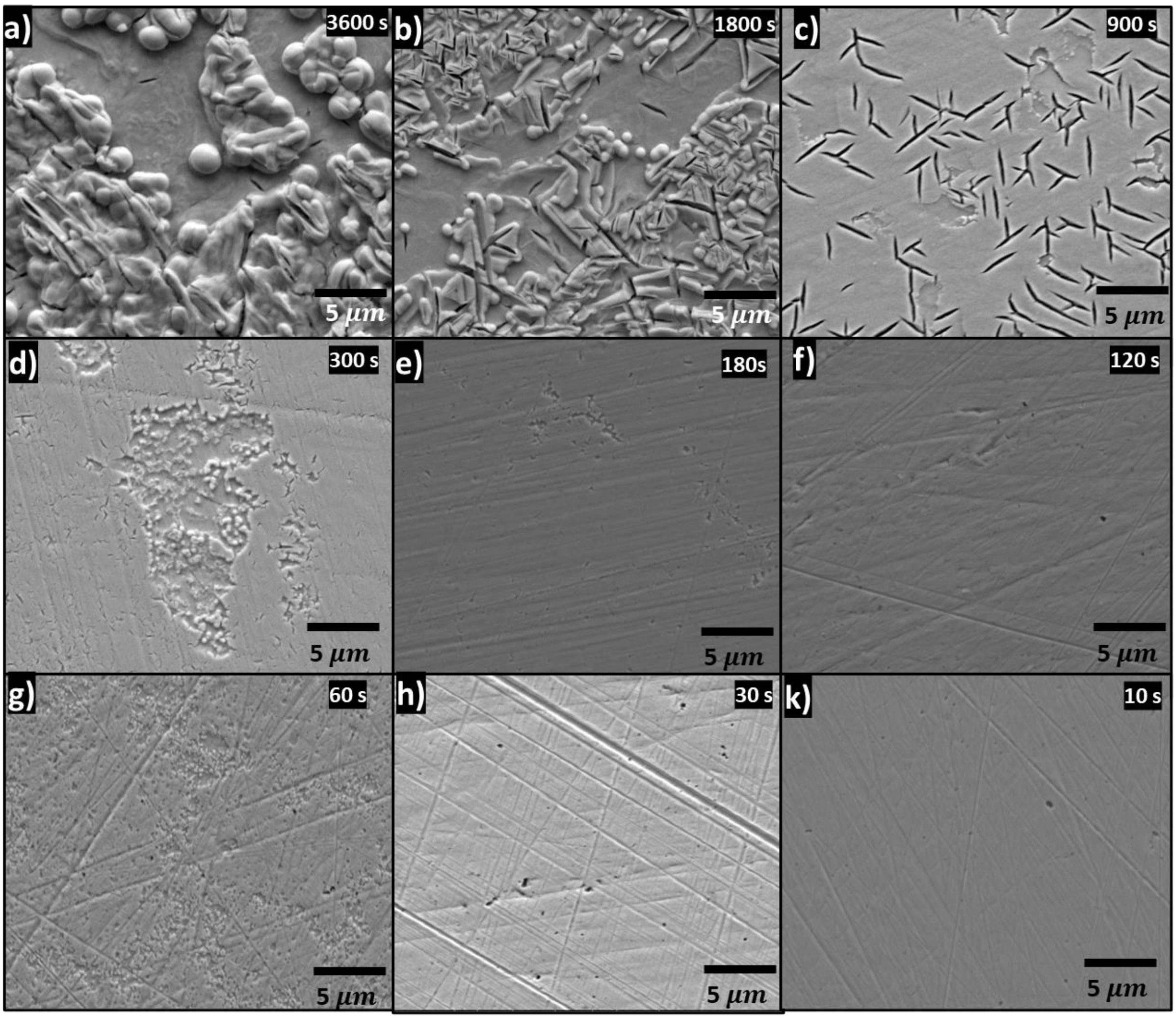

Figure 5.12 SEM images of mesoporous platinum electrodes (MPEs) fabricated from the BCC$_{Brij^{®}\ 58}$ at room temperature on the platinum electrode with an area of 3.142 x 10^{-2} cm^2 at different times a) MPE_3600, b) MPE_1800, c) MPE_0900, d) MPE_0300, e) MPE_0180, f) MPE_0120, g) MPE_0060, h) MPE_0030 and k) MPE_0010.

Figure 5.12 shows the SEM images for the MPEs and indicate different morphological structures depending on the deposition duration. The decrease in the deposition time shows a decrease in the number of features that coat the surface. In Figure 5.12 a), the MPE_3600 demonstrates the roughest morphology observed. A further decrease in the deposition time created films with fewer and smaller features and this makes the films appear flatter and smoother.

5.3.3.3 Electrochemical characterisation of the MPEs

CV in ethanol under acidic media - CV in 0.5 M H_2SO_4 was carried out for all the mesoporous films at room temperature and shown in Figure 5.13.

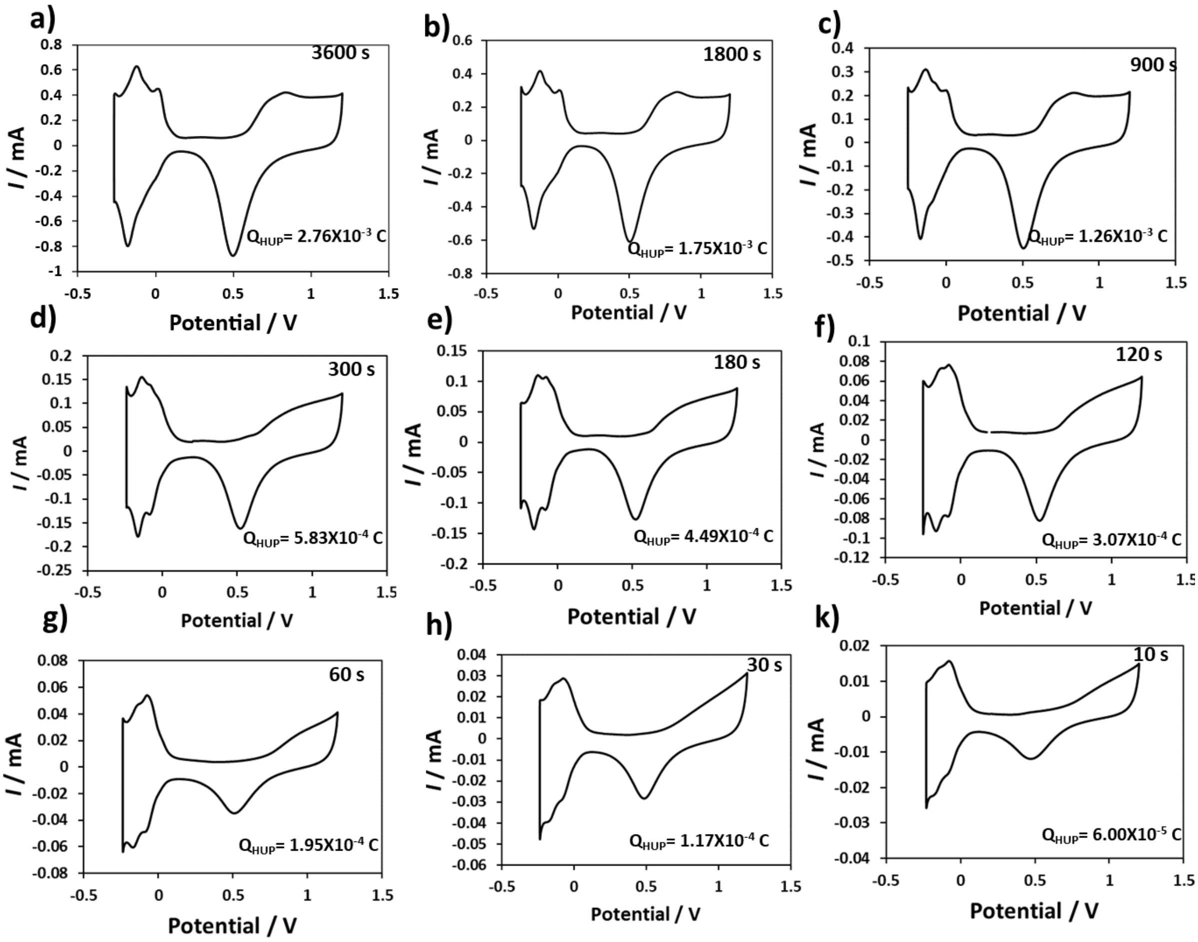

Figure 5.13 Cyclic voltammograms (CVs) recorded in 0.5 M H_2SO_4, at room temperature and 50 mV s^{-1} for a series of mesoporous platinum electrodes (cross-sectional area = 3.142 x 10^{-2} cm^2) fabricated from the $BCC_{Brij^{®}58}$ with different deposition times a) MPE_3600, b) MPE_1800, c) MPE_0900, d) MPE_0300, e) MPE_0180, f) MPE_0120, g) MPE_0060, h) MPE_0030 and k) MPE_0010. Q_{HUP} means the charge for hydrogen underpotential region.

Figure 5.13 reveals the CVs for all the MPEs which show the classic signals for platinum electrodes. The current was observed to decrease with a decrease in deposition time. This was expected because the current passed is directly related to the accessible area. The RF and the RSA values were calculated from these CVs, while the Q_{dep}, σ and M_{Pt} were calculated from transients in Figure 5.10, and the data are presented in Table 5.10.

Table 5.10. The Roughness factor (RF), total deposition charge (Q_{dep}), charge density (σ), mass of platinum (M_{Pt}) and the electrochemical active surface area (ECSA) for the mesoporous platinum electrodes fabricated from the $BCC_{Brij^{®}58}$ with different deposition times from 3600 s to 10 s.

Electrodes	Q_{dep} / C	σ / C cm^{-2}	RF	M_{Pt} / g	ECSA / m^2 g^{-1}
MPE_3600	0.164	5.25	429	8.28×10^{-5}	16.3
MPE_1800	0.095	3.04	265	4.80×10^{-5}	17.4
MPE_0900	0.057	1.84	191	2.88×10^{-5}	21.0
MPE_0300	0.025	0.80	88	1.26×10^{-5}	22.0
MPE_0180	0.015	0.48	68	7.58×10^{-6}	28.1
MPE_0120	0.010	0.33	47	5.05×10^{-6}	29.6
MPE_0060	0.007	0.22	30	3.54×10^{-6}	26.0
MPE_0030	0.004	0.14	18	2.02×10^{-6}	27.2
MPE_0010	0.002	0.06	9	9.6×10^{-7}	31.2

Table 5.10 indicates that the Q_{dep} and σ decrease with the decrease of the deposition times from 3600 to 10 s. Also, the RF values show a gradual decrease with the decrease of the deposition times, and the highest RF was observed for MPE_3600 (429), while the lowest RF was observed for MPE_0010 (9). Therefore, the deposition here is controlled, and the longer deposition time allows more platinum to be deposited onto the electrode surfaces, leading to thicker but porous films.

Interestingly, the ECSA values indicates an increase with decreasing deposition time. The highest ECSA value was observed for the thinner film: MPE_0010 (31.2 m^{2}g^{-1}). In contrast, the lowest ECSA value was obtained for the thicker film: MPE_3600 (16.3 m^{2}g^{-1}). The increase in ECSA, with a decrease in Q_{dep}, is likely due to increased pore accessibility for thinner and smoother films (as shown in the SEM images in Figure 5.12).

CV in ethanol under acidic media - The different thicknesses of the MPEs and PPE were utilised to investigate the ethanol oxidation as shown in in Figure 5.14.

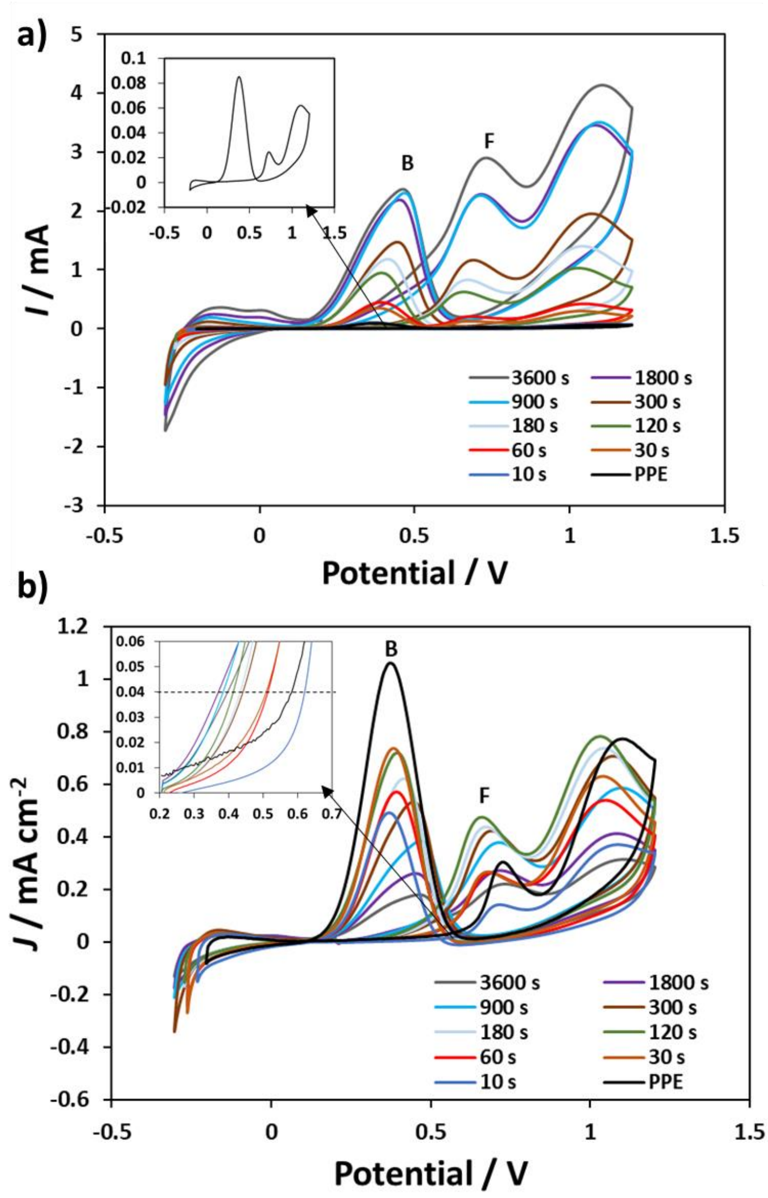

Figure 5.14 Cyclic voltammograms (CVs) in 0.5 M H_2SO_4 + 0.5 M C_2H_5OH solution a) current (I) and b) current density calculated from the RSA (J) recorded at room temperature and a scan rate of 50 mV s^{-1} of the polished platinum electrode (PPE) and mesoporous platinum electrodes (MPEs) fabricated from the BCC $_{Brij^{®}\ 58}$ at different deposition times from 3600 to 10 s. The insert exhibits the CV of the polished electrode. The forward and backward peaks are illustrated by F and B in the plot.

Figure 5.14 a) shows the CVs for ethanol oxidation that are presented in terms of *I* /mA for PPE and the MPEs with different deposition times. The CVs exhibit the I_F and I_B increase, and the position slightly shifts to more positive potential as the deposition time of the MPE increases compared to the PPE (insert plot). The highest I_F was observed for the thicker film (MPE_3600, shown in grey).

Figure 5.14 b) exhibits the CVs for ethanol oxidation displayed in terms of *J* for PPE and the MPEs with different deposition times. The CVs show that the position of J_F and J_B shifts slightly to the right with increases in the deposition time of the MPEs. Interestingly, the J_F and J_B exhibit a decrease as the deposition time of MPE increases, which is similar to the trend observed in Figure 5.8. The highest J_F and J_B were obtained for the MPE_0120 (shown in green). The insert of the magnified area for the peak F show that the curve shifts to more positive potential as the deposition time increases. Further analysis of the CV data is reported in Table 5.11.

Table 5.11 Table 5.12 The catalytic activity of the polished platinum electrode (PPE) and mesoporous platinum electrodes (MPEs) (cross-sectional area = 3.142 x 10^{-2} cm^2) deposited from the BCC $_{Brij^{®}\ 58}$ at different times towards the ethanol oxidation in terms of current (I) and current density (J). The I_F means forward peak in current, I_B means backward peak in current, the J_F means forward peak in current density, and the J_B means backward peak in current density. Onset potential (E_{onset}) data collected at 0.04 mA cm^{-2} n=1

Electrode	Rf	I_F / mA	I_B / mA	J_F / mA cm^{-2}	J_B / mA cm^{-2}	J_F / J_B	E_{onset}
PPE	2.5	0.02	0.084	0.25	1.07	0.24	0.58
MPE_3600	429	2.90	2.36	0.22	0.18	1.23	0.39
MPE_1800	265	2.28	2.36	0.27	0.28	0.97	0.37
MPE_0900	191	2.27	2.27	0.38	0.38	1.00	0.38
MPE_0300	88	1.17	1.43	0.42	0.52	0.82	0.44
MPE_0180	68	0.81	1.17	0.38	0.55	0.69	0.43
MPE_0120	47	0.62	0.92	0.42	0.62	0.67	0.41
MPE_0060	30	0.20	0.44	0.21	0.47	0.45	0.51
MPE_0030	18	0.13	0.35	0.23	0.62	0.37	0.51
MPE_0010	9	0.03	0.11	0.11	0.39	0.27	0.60

Table 5.10 shows the catalytic activity data for the MPEs. The J_F/J_B for all the MPEs indicate larger values than the PPE, due to having more active sites compared to the PPE. Examining J_F/J_B ratio in more detail shows a good maximum value for MPE_3600 (1.23) which steadily decreases with deposition time down to a minimum value for MPE_0010 (0.27). The E_{onset}

values show a steady increase in value with decrease in deposition time thus the thicker films perform better.

A stability study was conducted using CV over 100 cycles in 0.5 M H_2SO_4 + 0.5 M C_2H_5OH solution at a scan rate of 50 mV s^{-1}. Subsequently, the J_F was compared every 20 cycles and is shown in histograms in Figure 5.15.

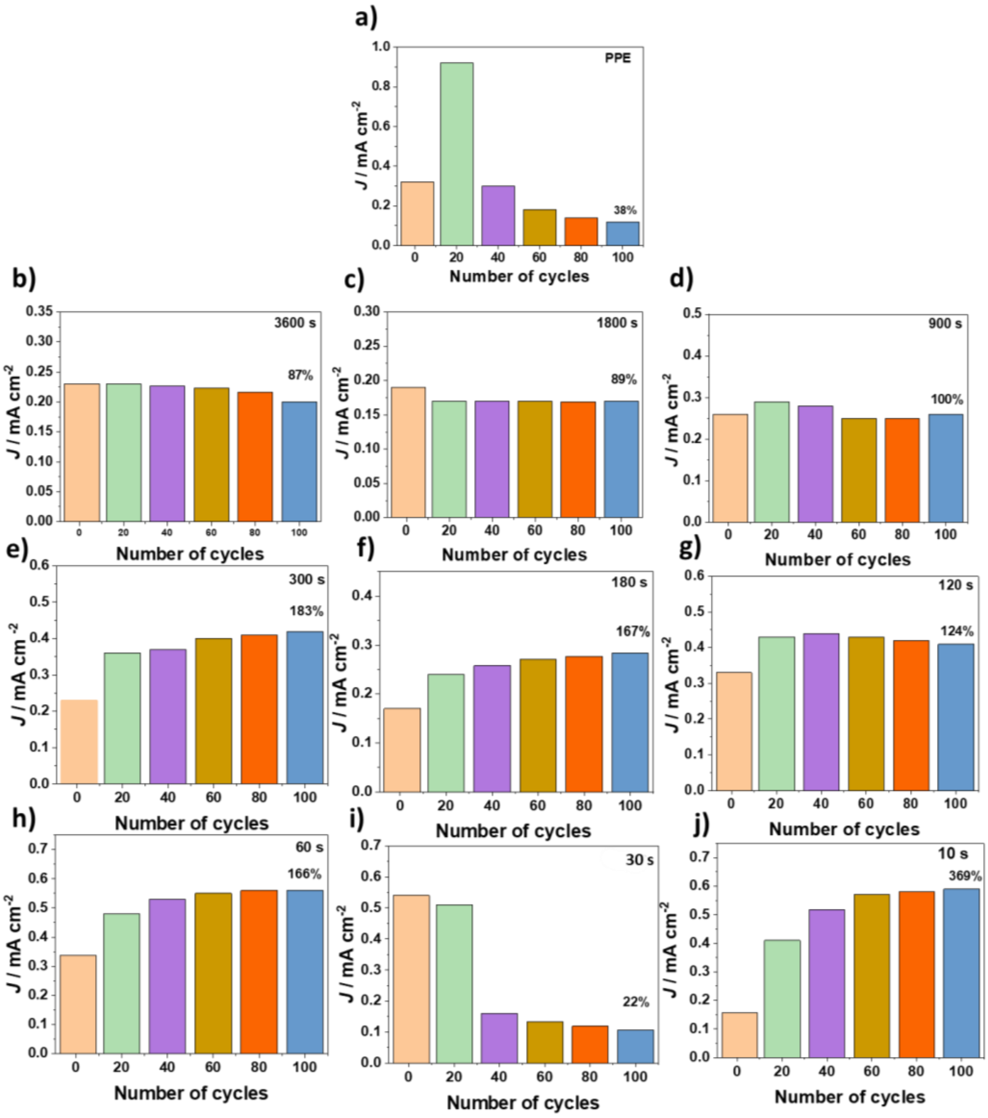

Figure 5.15 Histograms show the stability over 100 CVs towards ethanol oxidation for a) PPE and mesoporous platinum electrodes (MPEs) deposited from the $BCC_{Brij^{®}\ 58}$ at different deposition times, b) MPE_3600, c) MPE_1800, d) MPE_0900, e) MPE_0300, f) MPE_0180, g) MPE_0120, h) MPE_0060, i) MPE_0030 and j) MPE_0010. Each colour indicates the number of cycles, and the stability factor (%) calculated by comparing J_{F100th} to J_{F1st}.

Figure 5.15 a) shows the stability of J_F for the PPE to increase initially for the 20th cycle followed by a sharp decline and a subsequent further diminishing occurs with each scan until the 100th (38%). Figure 5.15 b-d) show a slight decrease in the J_F with each cycle for these electrodes and the good stability percentages are MPE_3600 (87%), MPE_1800 (89%) and MPE_0900 (100%), respectively.

Figure 5.15 e-j) shows that the stability for MPEs deposited at shorter deposition times demonstrate a gradual increase of the J_F. The stability percentages for these MPEs show values greater than 100% of and the greatest stability was observed for MPE_0010 (369%). However, the stability of MPE_0030 (Figure 5.15 i) displays unusual behaviour, the J_F decreased to 22%, this may be due to a real effect and instability of the film or due to solution contamination. Thus, the MPEs deposited at shorter times (thinner films) generally indicate better stability than at the longer deposition times (thicker films).

5.4 Conclusion

This chapter reported that the feasibility study investigating the use of the BCC structure of 30 wt% Brij® 58/HCPA with a_{BCC}= 9.3 nm as a template was successful as indicated by the high passed current (550 µA) observed from the CV.

The deposition at different potential showed an increase of both Q_{dep} and σ with a decrease of the deposition potential from -0.15 to -0.23 V with slightly smaller value at -0.25 V. The TEM investigation suggested a primitive structure with lattice parameter values ranging from 6.4 $\pm$ 0.5 nm and 6.8 $\pm$ 0.9 nm and pore diameters between 3.0 and 3.5 nm. The findings also revealed a gradual loss of the primitive structure for the MPE-0.25 V. Interesting features of spherical particles that aggregate in a specific way and build layers with fissures were observed from the SEM analysis. Moving to the CV investigations in dilute acid, the MPEs displayed high controllable surface area indicated by the increase of the RF values with respect to the σ, which also suggested stability and uniform accessibility of their internal structure. The ECSA values ranged from 16.74 ± 4.01 to 22.7 ± 1.56 $m^2\ g^{-1}$ for the MPEs. The subsequent catalytic examination displayed remarkable activity of the MPEs towards ethanol oxidation in acid media as evidenced by the J_F/J_B ratios reaching up to a maximum of 1.38, low E_{onset} values with a minimum of 0.33 and long-term stability.

The MPEs with different areas/thicknesses were successfully fabricated at - 0.15 V and various deposition times from 3600 to 10 s. The findings showed that the Q_{dep} and σ decreased with deposition time, indicating a decrease in the film thickness of the MPEs. Subsequently, the SEM investigation confirmed a decrease in the number of surface features with a decrease in the deposition time. Following this analysis, the CV study in dilute acid revealed that the RF and ECSA values varied depending on the deposition times. Interestingly, the RF decreased with the decrease of the Q_{dep} and σ values; however, the ECSA values increased from 16.3 to 31.2 $m^2\ g^{-1}$, likely due to increased pore accessibility for thinner and smoother films. Shifting the focus to their catalytic activity performance towards ethanol oxidation in acid, they exhibited excellent catalytic activity, indicated by high J_F/J_B ratios reaching up to a maximum of 1.23, low E_{onset} values diminishing to a minimum of 0.37 V and remarkable long-term stability.

Chapter 6- BCC$_{F127}$ templating of mesoporous platinum electrodes, their characterisation and electrocatalytic properties for ethanol oxidation

6.1 Introduction

This chapter explores the use of F127, a copolymer with an elongated PEO block, to produce mesoporous platinum films with a cubic structure. F127 is known for its large micelles structure with a radius of 10 nm[82,162], and is therefore often selected for its potential to yield larger pore sizes. The size and structure of pores play an important role in influencing the mass transport within porous materials. Larger pore sizes enhance the accessibility to active sites and facilitates the accommodation and transport of larger species.[163] Similarly a 3D cubic architecture also enhances the transport through the structure and further investigation for the creation of cubic platinum structure coupled with large pores is desirable.

When self-assembled F127 forms various phases in aqueous conditions, and its phase behaviour in water was reported in the literature and investigated using CPLM[87] and SAXS[164,165]. Previous studies showed that certain additives, such as SDS and urea in the aqueous solution of F127, can influence the PPO's hydrophobicity and the PEO's hydrophilicity.[166] Considering the impact of the additives on F127, it seems clear that understanding the phase behaviour of F127 systems in the presence of HCPA would be advantageous in developing its use as a template. Therefore, this study investigates the effect of HCPA on the phase behaviour of F127 for the first time.

F127 was previously used at low concentrations just above the CMC in the creation of multimetallic mesoporous spheres with sizes of 18.5 ± 0.5 nm via the chemical reduction of metal salts in the presence of ascorbic acid.[167] These mesoporous particles exhibited a lattice parameter value of 26.8 nm, and ECSA values ranging from 13.5 to 31.6 m^2 g^{-1}.[167] A similar approach of utilising a low concentration of F127 was also employed previously to produce mesoporous platinum nanospheres with a large pore size of 11 $\pm$ 1 nm and lattice parameter of 20 to 21 nm with an ECSA value of 25.1 m^2 g^{-1}.[168] On the other hand, a higher concentration (50 wt%) of F127 was reported by Corti *et al*. to produce mesoporous platinum and platinum/ruthenium alloy via the electrodeposition of metal salts.[19,169] The 0.1 M HCPA and 0.1 M $RuCl_3$ + 0.1 M HCPA metal salts were reduced by applying different voltages; at -0.30 V for mesoporous platinum and -0.40 V for platinum/ruthenium alloy.[169] The results showed a large pore size of 9-10 nm with a $\mathrm{H_I}$ structure and lattice parameter of 13.7 ± 0.2 nm.[19,169] The ECSA values for mesoporous platinum deposited at -0.30 and -0.40 V were 25.1 and 40.7 m^2 $g^{-1,}$ respectively, while the platinum/ruthenium indicated 40.1 and 47.1 m^2 g^{-1} at -0.40 and -0.43 V, respectively.[169] These mesoporous materials enhanced electrochemical activity towards a methanol oxidation reaction [21,167,168] and an oxygen reduction reaction[168].

Moreover, the cubic phase, known for its stability in aqueous F127[162], was also utilised previously to fabricate orderd mesoporous silica materials employing the BCC (Im3m) symmetry and the FCC (Fm3m) symmetry under varying synthesis conditions and the use of a different additives.[170,171] However, no prior investigation has explored the application of F127 with the BCC structure to create mesoporous platinum materials. As mentioned previously a related study by Akbar *et al*.[26] employed the phytantriol + Brij® 56 Im3m phase to produce mesoporous platinum films with a primitive structure and since the BCC phase shares the Im3m space group, this study provides a relevant basis for comparison.

In this current study a novel approach to producing platinum with 3D morphology is applied via the electrodeposition of 50 wt % F127/HCPA template with the BCC structure as a template. The initial focus was directed towards investigating the effect of HCPA on the phase behaviour of F127. Followed by electrodeposition at different potentials from - 0.10 to - 0.26 V allowing the methodical creation of a series MPEs. These MPEs were characterised using various techniques and the electrocatalytic activity of the films towards ethanol oxidation was studied.

Aims:

- To study the effect of HCPA on the phase behaviour of F127.
- To investigate the feasibility of employing the BCC_{F127} mixture as a template for the deposition of platinum films with a high surface area.
- To examine the effect of varying the deposition voltage with the BCC_{F127} template on the electrode surface area, structure, and catalytic performance.

6.2 Methodology

The methodology is presented in three main sections in accordance with aims.

6.2.1 Effect of HCPA on phase behaviour of F127

LLC of F127 with water and HCPA (0.195 M) at different compositions (from 30 wt% to 80 wt%) were prepared. The F127 becomes liquid at temperatures less than 5 °C; therefore, the cooling method was used in the preparation process. For F127 mixtures, an appropriate amount of F127 and ultra-pure deionised water or HCPA were placed in plastic vials. The sealed vials were heated using a dry bath at 70 °C for 10 minutes and then centrifuged for 10 minutes. After that, the vials were cooled in a fridge at 4 °C for one hour and then centrifuged for about 20 minutes. Following this, the samples were left overnight in the fridge at 4 °C. On the following day, the samples were centrifuged for about 20 minutes and mixed using a glass rod for about 3 minutes until the mixtures became homogenous. SAXS and CPLM were used to study the phase behaviour of F127 mixtures with water and HCPA. The details of the SAXS and CPLM analyses are described in Chapter 2. The exact amounts of F127 and solvents used are presented in Table 6.1 and Table 6.2. Also, 50 wt% F127/HCPA mixture was prepared in a larger quantity to prepare mesoporous platinum, as shown in Table 6.3.

Table 6.1 Different compositions of F127 and water mixtures used in this study.

Mass of F127 / g	**Mass of H_2O / g**	**Wt% F127**
0.149	0.350	29.86 ± 0.168
0.201	0.307	39.57± 0.124
0.250	0.248	50.20± 0.100
0.298	0.206	59.13± 0.084
0.351	0.158	68.96± 0.071
0.398	0.099	80.08± 0.063

Table 6.2 Different compositions of F127 and HCPA mixtures used in this study.

Mass of F127 / g	**Mass of HCPA / g**	**Wt% F127**
0.152	0.350	30.28 ± 0.165
0.201	0.296	40.44± 0.124
0.247	0.254	49.30± 0.101
0.296	0.194	60.41± 0.085
0.339	0.152	69.10± 0.074
0.398	0.105	79.12± 0.063

Table 6.3 50 wt% composition of F127 and HCPA mixture used in this study

Mass of F127 / g	Mass of HCPA / g	Wt.% F127
0.501	0.502	49.95± 0.049

6.2.2 Feasibility study for employing the BCC$_{F127}$ mixture as a template for platinum deposition.

The specific 50 wt% F127/HCPA (BCC$_{F127}$) mixture from Table 6.3 was studied using SAXS at room temperature to confirm the template structure prior to electrodepostion. Deposition from the BCC$_{F127}$ mixture was investigated using CV at a polished platinum electrode with an area of 3.142 x 10^{-2} cm^2 at room temperature between the limits +0.70 and -0.30 V vs Ag/AgCl at a scan rate of 10 mV s^{-1}.

6.2.3 Effect of variable deposition voltage utilising the BCC$_{F127}$ template on the electrode structure, surface area and catalytic performance

Platinum electrodeposition was carried out using the BCC$_{F127}$ mixture (50 wt% F127/HCPA) as a template. The deposition was carried out at platinum electrodes with an area of 3.142 x 10^{-2} cm^2 and platinum foils with an area of ~ 0.2 - 0.5 cm^2 at room temperature. The potential was stepped from +0.6 V to various negative potentials vs Ag/AgCl, as shown in Table 4.2.

Table 6.4 Variation of deposition potentials from BCC$_{F127}$ template and corresponding sample name. n= number of measurements. In all cases deposition time was 1800s.

Deposition potential/ V	Sample name
-0.10 (n=1)	MPE-0.10
-0.20 (n=2)	MPE-0.20
-0.22 (n=2)	MPE-0.22
-0.24 (n=2)	MPE-0.24
-0.26 (n=2)	MPE-0.26

Following the deposition, the template was eliminated by washing with ultra-pure water and soaking the electrodes overnight in ultra-pure water. Then, more cleaning was carried out by scanning the modified electrodes using CV in dilute acid. The morphology of the fabricated MPEs was investigated using SEM and the morphology of the platinum foils was investigated using TEM. Additionally, the electrochemical characterisation of the electrode area for the MPEs was carried out using CV in 0.5 M H_2SO_4. The catalytic activity towards ethanol oxidation of the MPEs was also conducted using CV, and EIS in 0.5 M H_2SO_4 + 0.5 M C_2H_5OH electrolyte at room temperature. The EIS was carried out at 0.4 V vs Ag/AgCl, the frequency range from 100 kHz to 0.2 Hz, and the AC amplitude of ± 10 mV. This voltage was chosen because it represents the beginning of the ethanol oxidation process.

6.3 Results and discussion

The results and discussion are presented in three primary sections in accordance with aims.

6.3.1 Effect of HCPA on the phase behaviour of F127

The phase behaviour of F127 in water (F127/water) and HCPA (F127/HCPA) at different compositions from 30 to 80 wt% was studied using SAXS and CPLM. However, only SAXS data are presented in this study (shown in Figure 1.1), however CPLM was used to confirm the phases.

Figure 6.1 a) shows that the intensities of the F127/water mixtures are very low, and only a few Bragg peaks can be seen. This creates difficulties in the analysis of the potential crystallographic space groups. Therefore, all the possible structures and the most common space groups reported for F127 in the literature were considered. The 30 wt% F127/ water shows very low intensity, and no peaks are observed; therefore, specifying the phase type at this composition is not possible based on SAXS. However, this sample showed the $\mathrm{I_I}$ isotropic phase under CPLM (image is not reported here). Also, the previous study by Chio *et al.*[165], which used the SAXS technique, reported the mixed phase of the BCC+FCC structure at this composition.

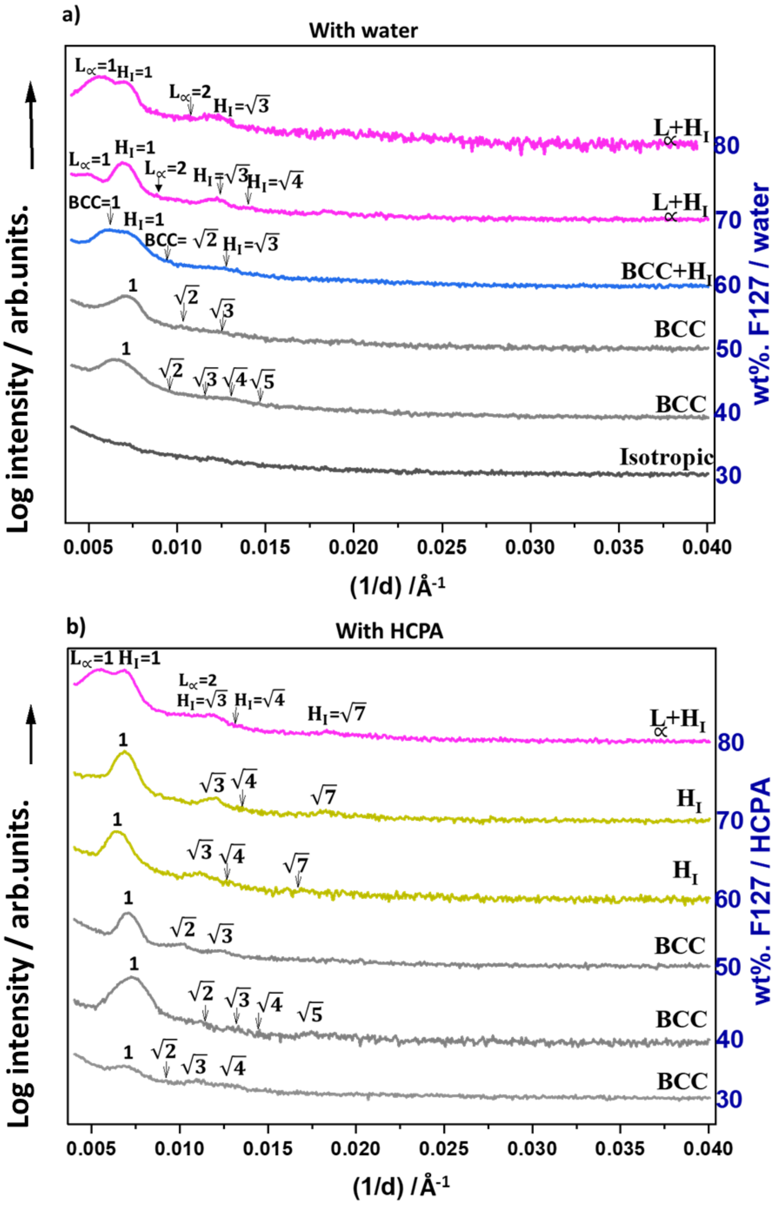

Figure 6.1 SAXS intensities of F127 in a) water and b) HCPA at different compositions and room temperature. The relative peak position ratios are presented in the plots for hexagonal (H_I) lamellar ($L_{\propto}$), face centred cubic (FCC) and body centred cubic (BCC). The intensity profiles are plotted on the logarithmic scale.

From Figure 6.1 a), as the concentration increases to 40 and 50 wt%, the intensity of the peaks enhances slightly, and peak positions reveal a ratio of $1{:}\,\sqrt{2}{:}\,\sqrt{3}{:}\,\sqrt{4}$ corresponding to the BCC phase. At 60 wt %, the mixed phase of the BCC+ $\mathrm{H_I}$ occurs, which is indicated by the positions of Bragg peaks with the ratio of BCC $(1{:}\sqrt{2})$ and $\mathrm{H_I}$ $(1{:}\sqrt{3}{:}\sqrt{4})$. Further increases of concentrations from 70 to 80 wt% show Bragg peaks that can be indexed with either the $\mathrm{H_I}$ $(1{:}\sqrt{3}{:}\sqrt{4})$ or $\mathrm{L}_\propto$ (1: 2: 3) phases. These data are consistent with those of earlier studies.[87,164,165]

Figure 6.1 b) reveals the SAXS diffraction pattern of F127/ HCPA at different compositions. Interestingly, the presence of HCPA enhances the intensities of the Bragg peaks. The BCC phase dominates the behaviour from 30 wt% to 50 wt% of F127/ HCPA, as shown by three or four peaks with a ratio of $1{:}\sqrt{2}{:}\sqrt{3}{:}\sqrt{4}$. Further increases in the compositions to 60 wt% and 70 wt% show four peaks with a ratio of $1{:}\sqrt{3}{:}\sqrt{4}{:}\sqrt{7}$ that correspond to the $\mathrm{H_I}$ phase. By increasing the compositions to 80 wt% of F127/ HCPA, new peaks are revealed along with the $\mathrm{H_I}$ peaks. All the Bragg peaks at 80% F127/HCPA can be indexed with either the $\mathrm{H_I}$ $(1{:}\sqrt{3}{:}\sqrt{4})$ or $\mathrm{L}_\propto$ (1: 2: 3) phases. Calculating the lattice parameter for the different phases of F127 with water and HCPA from the SAXS pattern was essential. The lattice parameters are summarised in Table 6.5.

Table 6.5 The lattice parameter for each phase of F127 with water and with HCPA.

Composition	**With water**			**With HCPA**		
	BCC	**$\mathrm{H_I}$**	**$\mathrm{L}_\propto$**	**BCC**	**$\mathrm{H_I}$**	**$\mathrm{L}_\propto$**
30%	--	--	--	20.9±0.49	--	--
40%	21.2±0.28	--	--	19.1±0.49	--	--
50%	19.8±0.44	--	--	20.1±0.21	--	--
60%	22.2±0.23	14.6±1.6	--	--	16.6±1.6	--
70%	--	15.8±1.5	19.9±0.09	--	15.7±1.5	--
80%	--	15.8±1.5	18.1±0.24	--	16.1±1.5	17.5±0.66

The visible variations in the phase behaviour of F127 in water and the presence of HCPA are discussed further below:

- HCPA enhanced the intensity of the Bragg peaks of F127 mixtures compared to the F127 in water. For instance, 30 wt% of F127 in water exhibited no presence of any peaks; however, HCPA showed some peaks identifying the BCC structure.
- The presence of HCPA increased the dominance of the higher curvature structures like the BCC and $\mathrm{H_I}$ phase. For instance, the pure $\mathrm{H_I}$ phase was revealed for 60 wt% and 70 wt% for F127 in the presence of HCPA, while F127/water showed a biphasic of the $\mathrm{L_\propto}$ and $\mathrm{H_I}$ phases. The presence of HCPA was assumed to extend the F127 PEO chains and favour the high-curvature structures. This performance was also observed in the Brij® 58 behaviour in the presence of HCPA (Chapter 3).
- The lattice parameters for different phases of F127 in water were in agreement with the previous study by Chio *et al.*[165], and in this study, similar lattice parameters were observed in the presence of HCPA.

The 50 wt% of F127/ HCPA was chosen as a template for mesoporous platinum production, and a larger quantity was made prior to electrodeposition; SAXS was carried out as shown in Figure 6.2.

Figure 6.2 a) and b) show the SAXS data for the 50 wt% of F127 in water and HCPA, respectively. The 2D SAXS patterns reveal rings, confirming multiple crystalline domains. The 1D SAXS pattern presents the peaks with a ratio of 1: $\sqrt{2}$: $\sqrt{3}$ confirming the BCC structure. The calculated lattice parameter a_{BCC} water (19.8 nm), is in agreement with previous literature by Chio *et al.* (20 nm) [165] for the BCC phase in water. The lattice parameter for a_{BCC} HCPA (21.0 nm) is slightly larger than that for the mixture in water. The identification of the stable and pure BCC phase suggested that this mixture could be used as a template for the fabrication of MPEs.

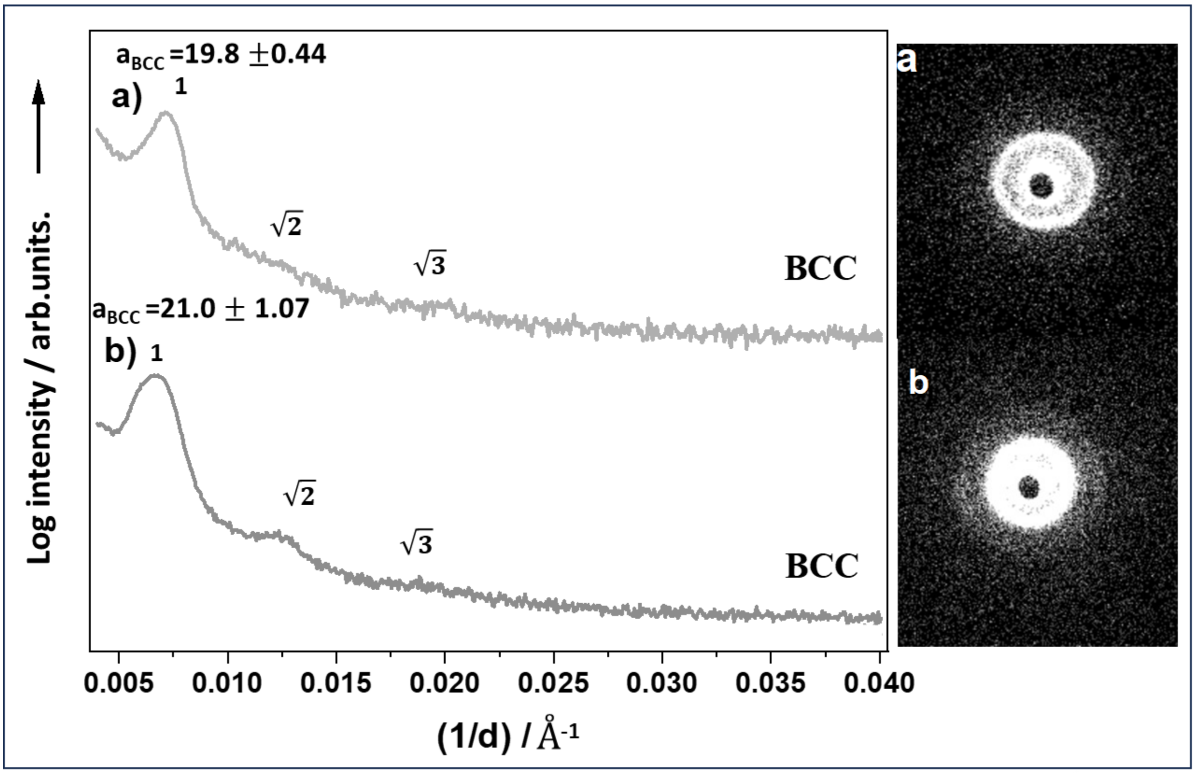

Figure 6.2 1D (left) and 2D (right) SAXS patterns for 50% F127 in a) water and b) HCPA solution. The intensity of each 1D profile is plotted on a logarithmic scale; the relative peak positions are also noted, leading to the identification of the symmetry and lattice parameter as a_{BCC} water =19.8 ±0.44 nm and a_{BCC} HCPA =21.0 ±1.07 nm.

6.3.2 Feasibility study for employing the BCC $_{F127}$ mixture as a template for platinum deposition

6.3.2.1 Electroreduction of the BCC $_{F127}$ mixture

The deposition of platinum from the 50 wt% of F127/ HCPA (BCC$_{F127}$) mixture by CV was carried out at room temperature and a scan rate of 10 mV s^{-1}, as presented in Figure 6.3.

Figure 6.3 shows the CV in the BCC$_{F127}$ mixture, revealing two peaks in the cathodic scan that differ from the anodic scan. The peaks are observed at the potentials E_{p1} = -0.10 and E_{p2} = - 0.26 V. The number of peaks observed from this CV is similar to those in the FCC$_{Brij^{®}\ 58}$ and the BCC$_{Brij^{®}\ 58}$ mixtures reported in Chapter 4 and 5, respectively; however, the positions of the peaks here are shifted to more negative values and the current observed for E_{p2} here is much smaller (150 µA). The BCC_{F127} template indicates a larger lattice parameter (21.1 nm) (Figure 6.2 b)), compared to the $BCC_{Brij® 58}$ template (9.3 nm) (Chapter 5, Figure 5.1). The current observed here is much smaller than the $BCC_{Brij® 58}$ mixture, which suggests a thinner aqueous channel and supports the formation of a larger pore size in this case. Voltages between -0.10 V and -0.26 V were selected for the electrodeposition of platinum and will be discussed in the next section alongside a full structure analysis .

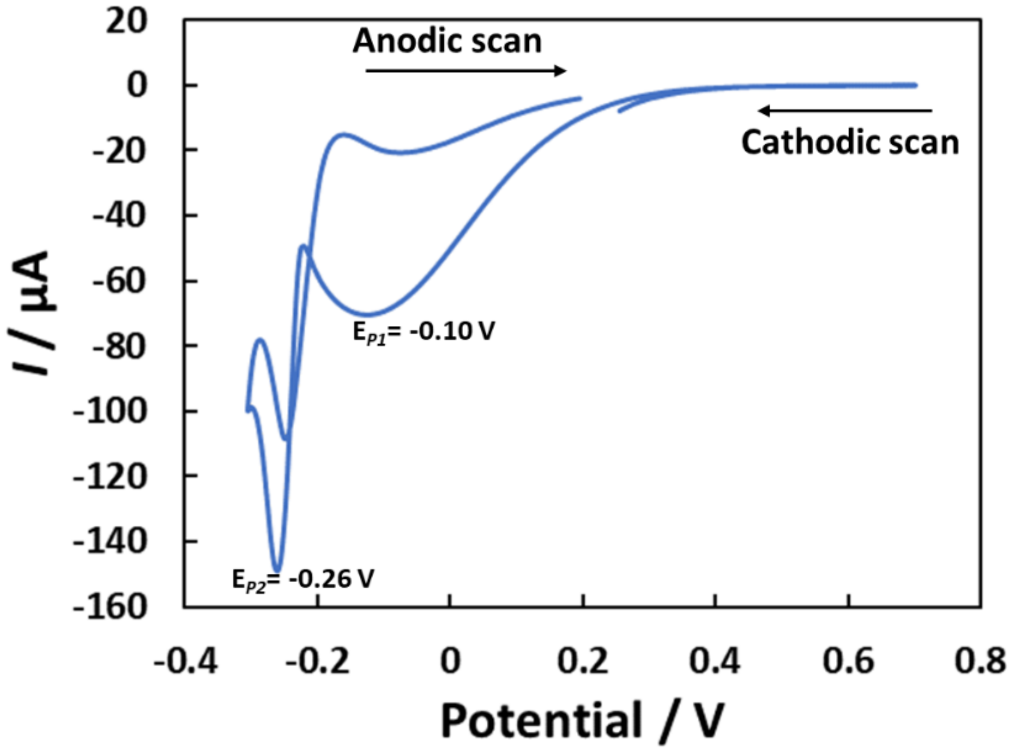

Figure 6.3 Cyclic voltammogram (CVs) recorded in the BCC_{F127} mixture, recorded between 0.70 and -0.30 V vs Ag/AgCl at a scan rate of 10 mV s^{-1} and room temperature for a platinum polished electrode (cross-sectional area = 3.142 x 10^{-2} cm^2). The peaks are illustrated in the plot by E_{p1} and E_{p2}.

6.3.3 Effect of variable deposition voltage utilising the BCC$_{F127}$ template on the electrode structure, surface area and catalytic performance

6.3.3.1 Electrochemical fabrication

The electrodeposition of platinum was carried out from the BCC$_{F127}$ template at different voltages of -0.10, -0.20, -0.22, -0.24 and -0.26 V at a fixed time of 1800 s; the electroreduction transients are shown in Figure 6.4.

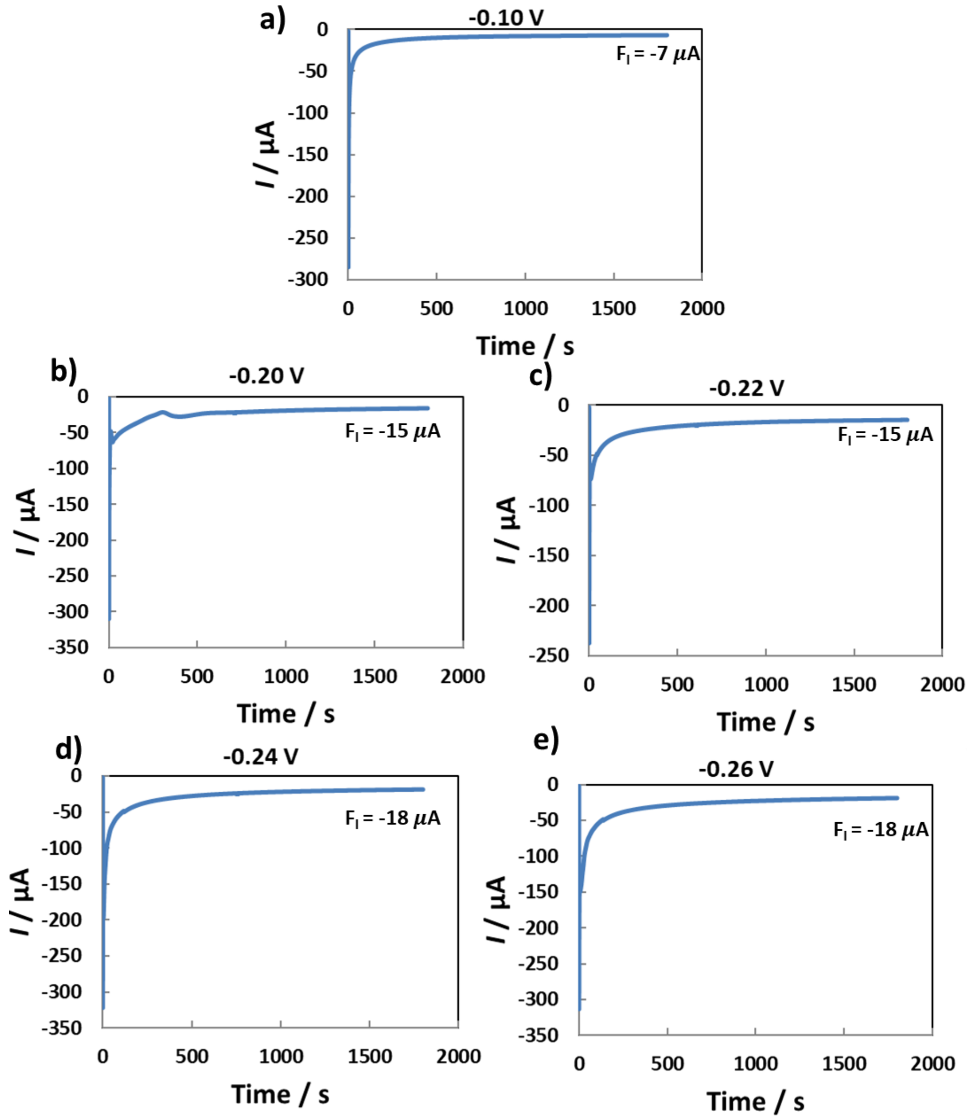

Figure 6.4 Representative electrodeposition transients recorded in BCC$_{F127}$ mixture at platinum electrodes (cross-sectional area = 3.142 x 10^{-2} cm^{2}) at room temperature and a fixed time for 1800 s with different potentials a) MPE-0.10, b) MPE-0.20, c) MPE-0.22, d) MPE-0.24 and e) MPE-0.26. F_I shows the final current.

All the transients show the same behaviour, revealing a high negative current followed by a decrease in the current stabilising at a non-zero value. Figure 6.4 a) shows the transient for MPE-0.10, which reveals the smallest passed current and the F_l shows only -7 µA. While Figure 6.4 b) and c) for MPE-0.20 and MPE-0.22, respectively, illustrate similar passed currents with similar F_l values (-15 µA). Surprisingly, a comparable trend is also noted with decreasing the deposition potentials for MPE-0.24 and MPE-0.26, but the values are slightly larger to be F_l =- 18 µA as shown in Figure 6.4 d) and e), respectively. These results indicate that as the potential is lowered the deposition is facilitated.

It should be noted that the F_l values of the electrodeposition from the BCC_{F127} template are much smaller than those observed from the $FCC_{Brij® 58}$ and the $BCC_{Brij® 58}$ templates in Chapters 4 and 5. This corresponds with the data from the CV deposition in Figure 6.3, which revealed less current for E_{P2}. Therefore, less platinum is expected to be deposited from the BCC_{F127} template than from the $FCC_{Brij® 58}$ and the $BCC_{Brij® 58}$ templates.

The deposition process was repeated on platinum foil at different voltages, and it demonstrated its reproducibility. However, calculating Q_{dep} and σ from the platinum foils was not feasible. Therefore, Table 6.6 shows the Q_{dep} and σ data obtained from the MPES, as presented in Figure 6.4.

Table 6.6 Variation in total deposition charge (Q_{dep}) and charge density (σ) for mesoporous platinum prepared from BCC_{F127} using different deposition potentials in a fixed time (1800 s). n=1.

Electrodes	Q_{dep} / C	σ / C cm^{-2}
MPE-0.10	0.019	0.62
MPE-0.20	0.041	1.32
MPE-0.22	0.037	1.19
MPE-0.24	0.051	1.63
MPE-0.26	0.053	1.69

Table 6.6 shows various values for the Q_{dep} and σ depending on the deposition potential. Both Q_{dep} and σ show a gradual increase with the decrease of the potentials. It is worth noting that the Q_{dep} and σ from the BCC_{F127} show smaller values than the $FCC_{Brij® 58}$ and $BCC_{Brij® 58}$ templates (chapters 4 and 5) and have not decreased with decreasing the deposition potential. These films were further investigated, and the examination of the structure morphology is presented in the following section.

Following the deposition, the template was eliminated by immersing the electrodes in water. Then, the electrode surface showed a dark grey appearance, which appeared less intense than the colour observed for the MPEs fabricated from the $FCC_{Brij® 58}$ and $BCC_{Brij® 58}$ templates. This also indicates the depositing of less platinum and likely smoother films than the films prepared from the $FCC_{Brij® 58}$ and the $BCC_{Brij® 58}$ templates.

6.3.3.2 Characterisation of morphology and structure in the MPEs

SEM - The surface morphology of the MPEs was studied and compared to the surface of PPE using SEM, as shown in Figure 6.5 and Figure 6.6. (the zoomed images).

Figure 6.5 a) and Figure 6.6 a) show the SEM for PPE, which reveals the smooth surface of the electrode, as presented in the previous chapters. Interestingly, Figure 6.5 b) and Figure 6.6 b) exhibit the SEM image for MPE-0.10, which also indicates a smooth surface and a thin layer, as shown by the presence of the polishing lines. The presence of this thin layer corresponds to the small values of Q_{dep} and σ shown in Table 6.6.

Figure 6.5 c) and Figure 6.6 c) reveal the SEM results for MPE-0.20, which show exciting surface features and the presence of the worm-like structure for the platinum, suggesting a high surface area compared to MPE-0.10. Figure 6.5 d-f) and Figure 6.6 d-f) demonstrate the SEM data for MPE-0.22, MPE-0.24 and MPE-0.26, respectively. The SEM images for these MPEs are similar and indicate the presence of the spherical particles that assemble to create the smooth layers that cover the surface.

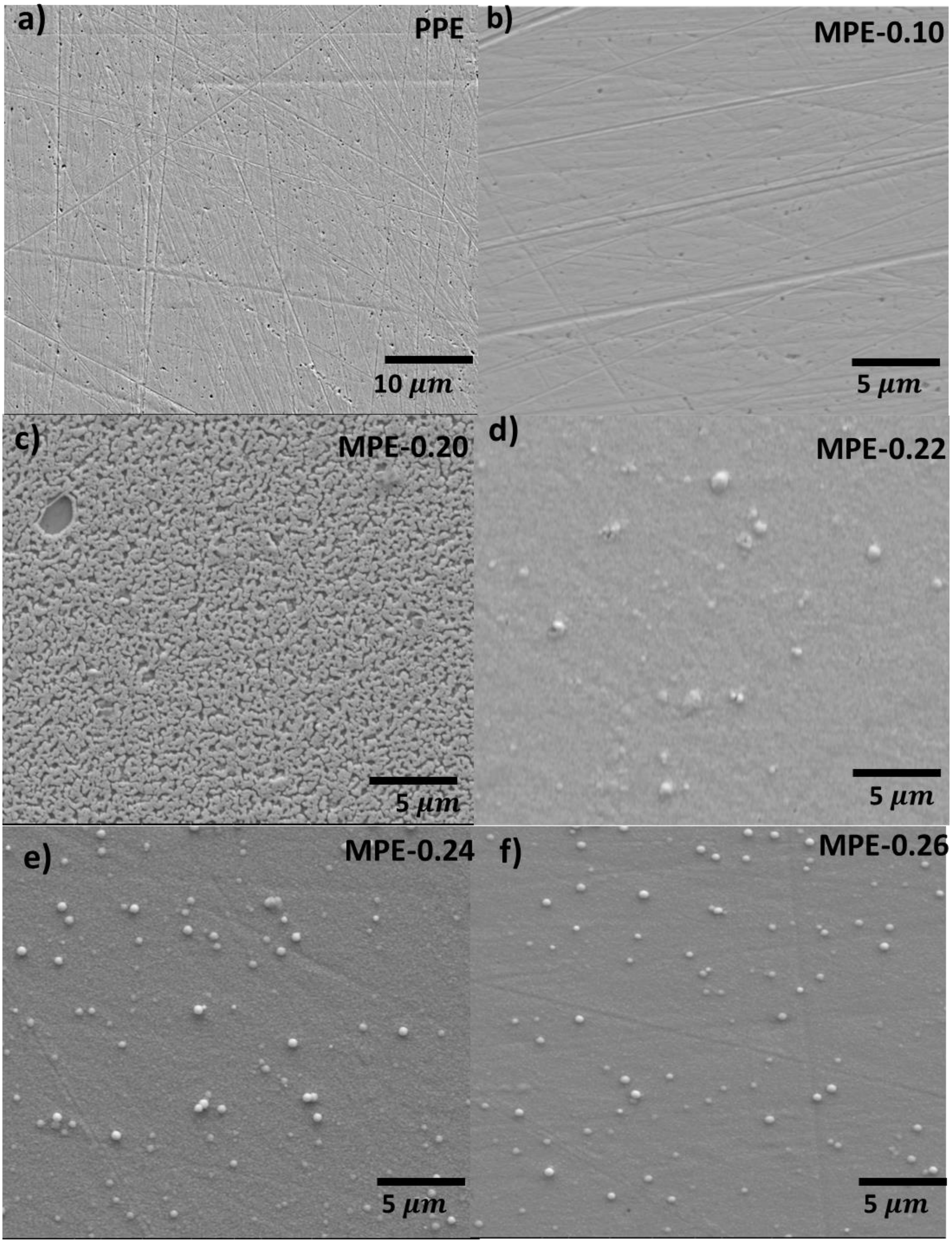

Figure 6.5 SEM images of a) polished platinum electrode (PPE) and mesoporous platinum electrodes (MPEs) deposited from BCC $_{F127}$ at different voltages, b) MPE-0.10, c) MPE-0.20, d) MPE-0.22, e) MPE- 0.24 and f) MPE-0.26.

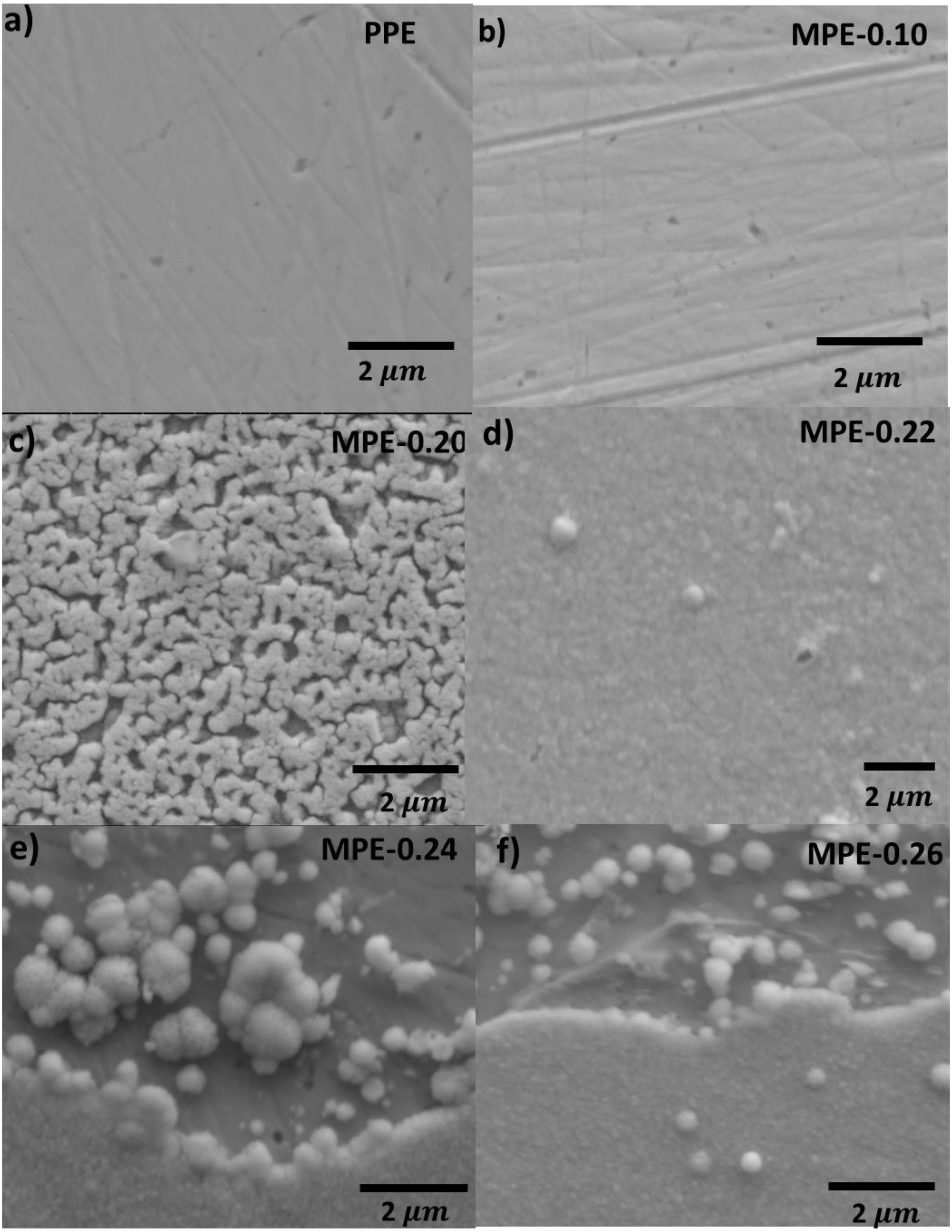

Figure 6.6 SEM images of a) polished platinum electrode (PPE) and mesoporous platinum electrodes (MPEs) deposited from the BCC $_{F127}$ at different voltages, b) MPE-0.10, c) MPE-0.20, d) MPE-0.22, e) MPE- 0.24 and f) MPE-0.26.

It is worth noting that these SEM images show different morphology compared to the MPEs fabricated from the FCC$_{\text{Brij® 58}}$ and BCC$_{\text{Brij® 58}}$ templates presented in Chapters 4 and 5, respectively; the current images exhibit only spherical features but no fissures.

TEM - The structure of fabricated MPEs using the BCC$_{F127}$ template was studied using TEM analysis, as shown in Figure 6.7. The MPE-0.10 was not included in the TEM analysis as the film was very thin, and extracting the platinum powder from it was not possible.

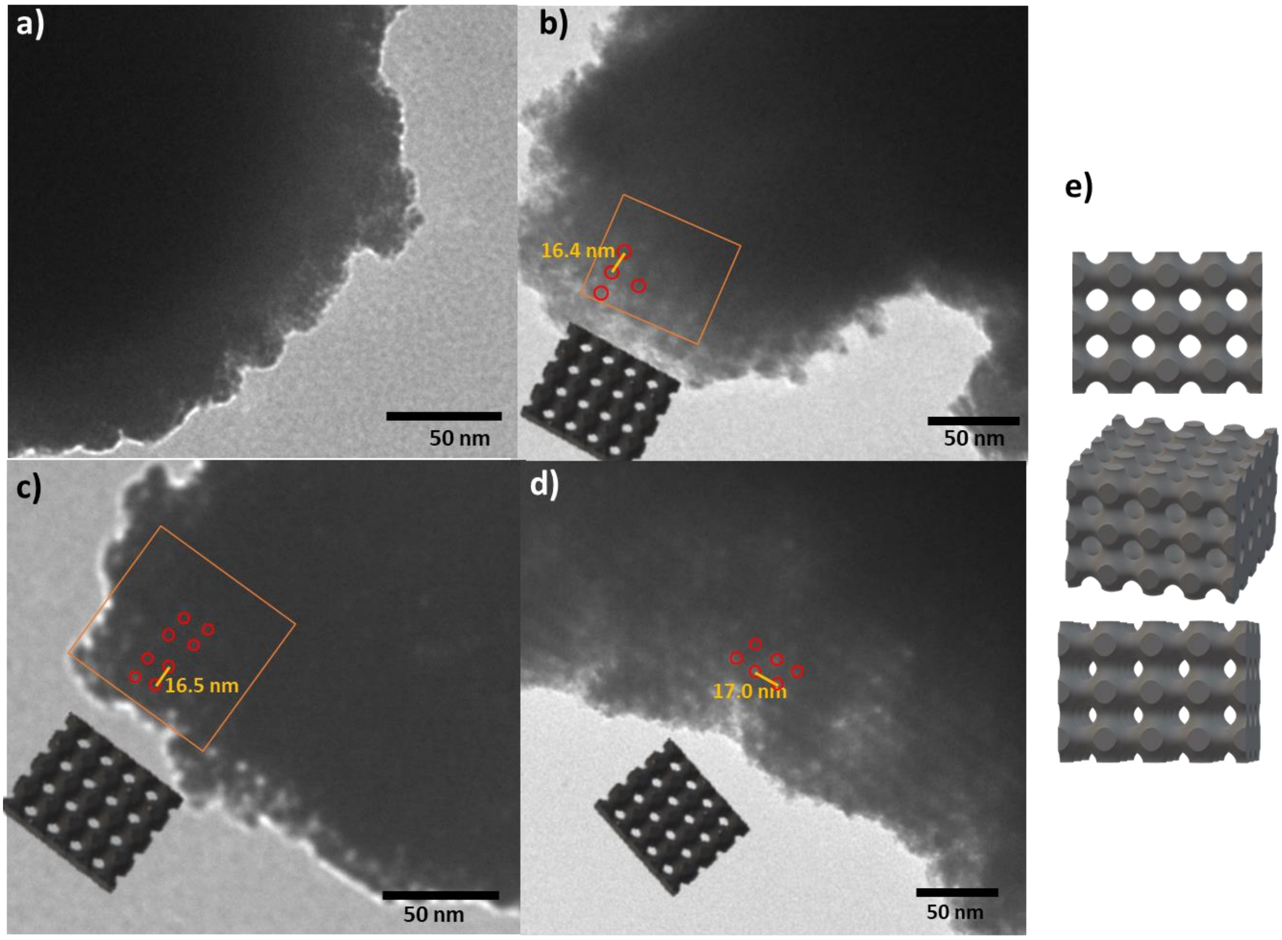

Figure 6.7 TEM images for the mesoporous platinum films deposited from BCC $_{F127}$ at different potentials, a) MPE-0.20, b) MPE-0.22, c) MPE-0.24 and d) MPE-0.26; the inserts are the simulation projection for primitive Pm3m structure. The red circles show the pores, and the lattice parameters measure the distance from the middle of one pore to the another, as shown in the image.

Figure 6.7 a) shows the TEM image for MPE-0.20, indicating some evidence of porosity near the edge. However, the thickness of the sample negates a full understanding of the periodicity of the structure. Figure 6.7 b-d) show the TEM images for MPE-0.22, MPE-0.24 and MPE-0.26, respectively. The TEM images reveal the same structure and could exhibit 3D networks with a regular pore structure. Interestingly, these TEM images appear to be consistent with the primitive model Pm3m symmetry. Figure 6.7 e) exhibits the simulation of primitive model in different directions which gives a good match to the structure in the TEM images. These films were expected to have a primitive structure similar to the results reported in Chapter 5 for the MPEs fabricated from the $BCC_{Brij^{®}\ 58}$. However, the pore diameter here is larger, with values between 7.8 and 8.2 nm compared to 3.0 to 3.5 nm from the $BCC_{Brij^{®}\ 58}$. Also, the lattice parameters here are 16.4 ± 1.7 nm, 16.5 ± 0.4 nm, and 17.0 ± 0.3 nm for MPE-0.22, MPE-0.24 and MPE-0.26, respectively, these values are slightly smaller than the lattice parameter from the template (21.1 nm) (Figure 6.2 b).

While these TEM images exhibited the primitive structure of the MPEs fabricated from the BCC_{F127}, confirmation of these findings through the SAXS would have been a valuable additional method; unfortunately, it was unavailable during this study.

6.3.3.3 Electrochemical characterisation of the MPEs

CV in sulfuric acid - The CV was employed in 0.5 M H_2SO_4 aqueous solution for additional cleaning and to remove any impurities from the surface. The resulting CV profiles of the clean MPEs and PPE recorded at 50 mV s^{-1} are shown in Figure 6.8.

Figure 6.8 shows the CVs for PPE and MPEs deposited at different voltages. The CVs exhibit the classic signals for the platinum electrode. The H_{upd} region shows a slight variation depending on the deposition potential. The MPEs show higher current than the PPE due to increased surface area. From Figure 6.8 the Q_{HUP} and M_{Pt} are used to measure the RF and the ECSA. The details of the calculations are described in Chapter 2. The RSA, RF and ECSA data for all the MPEs prepared at different voltages are shown in Table 6.7

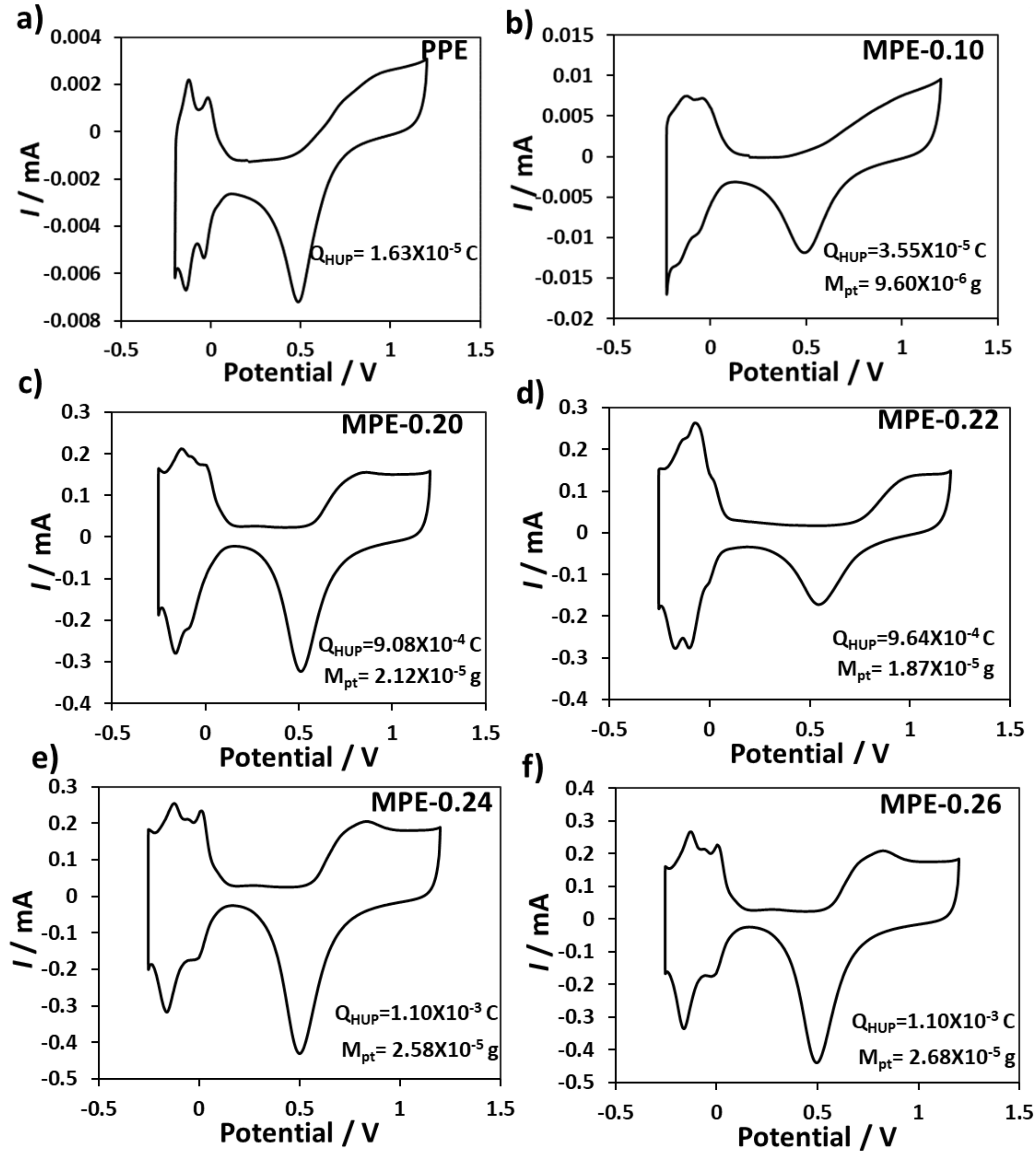

*Figure 6.8 CVs recorded in 0.5 M H_2SO_4, at room temperature and 50 mV s^{-1} for a) polished platinum electrode (PPE) and a series of mesoporous platinum electrodes (cross-sectional area = **3**.142 x 10^{-2} cm^2) fabricated from the BCC_{F127} with different deposition potentials b) MPE-0.10, c) MPE-0.20, d) MPE-0.22, e) MPE- 0.24 and f) MPE-0.26.Q_{HUP} represents the charge for the hydrogen underpotential region, and M_{pt} means the mass of platinum.*

Table 6.7 shows the RF value generally increases with the decrease of the deposition potential. The highest ECSA value was observed for MPE-0.22 (24.5 m^2 g^{-1}). The RF values are smaller than those reported for MPEs fabricated previously from $FCC_{Brij^{®}\ 58}$ and $BCC_{Brij^{®}\ 58}$ template in

Chapters 4 and 5 but interestingly, the ECSA values are comparable which could illustrate an increase in pore accessibility.

Table 6.7 The real surface area (RSA), Roughness factor (RF) and electrochemical active surface area (ECSA) for the polished and mesoporous platinum electrodes (MPEs) fabricated from BCC$_{F127}$ at different deposition potentials. n=1

Electrodes	RSA / cm^2	RF	ECSA / m^2 g^{-1}
PPE	0.08	2.5	-
MPE-0.10	0.16	5	1.7
MPE-0.20	4.30	137	20.2
MPE-0.22	4.59	146	24.5
MPE-0.24	5.22	166	20.2
MPE-0.26	5.25	167	19.6

CV in ethanol under acidic media - The catalytic efficiency of the MPEs fabricated at different potentials was assessed using the CV measurement for ethanol oxidation. Immediately before this investigation, the MPEs were evaluated in 0.5 M H_2SO_4 to clean the electrodes and recalculate the RF, RSA and ECSA, as shown in Table 6.8

Table 6.8 The real surface area (RSA), Roughness factor (RF) and electrochemical active surface area (ECSA) for the polished and mesoporous platinum electrodes (MPEs) fabricated from BCC$_{F127}$ at different deposition potentials. n=1

Electrodes	RF	RSA / cm^2	ECSA / m^2 g^{-1}
PPE	2.5	0.08	-
MPE-0.10	5.0	0.16	1.8
MPE-0.20	115	3.61	17.4
MPE-0.22	126	3.96	20.8
MPE-0.24	144	4.52	17.5
MPE-0.26	153	4.80	18.7

Table 6.8 indicates that the RSA, RF and ECSA values are slightly smaller than those presented in Table 6.7. The decrease in these values is due to the repetitive CVs. These RSA values for the MPEs were used to convert the data from *I* to *J* for the comparison of the catalytic activity.

The electrocatalytic activity of the MPEs for ethanol oxidation was characterised by CV in 0.5 M H_2SO_4 + 0.5 M C_2H_5OH electrolyte at a scan rate of 50 mV s^{-1}. The CV of each electrode became similar and stable after the third cycle. The resulting CVs from the third cycle are shown in Figure 6.9.

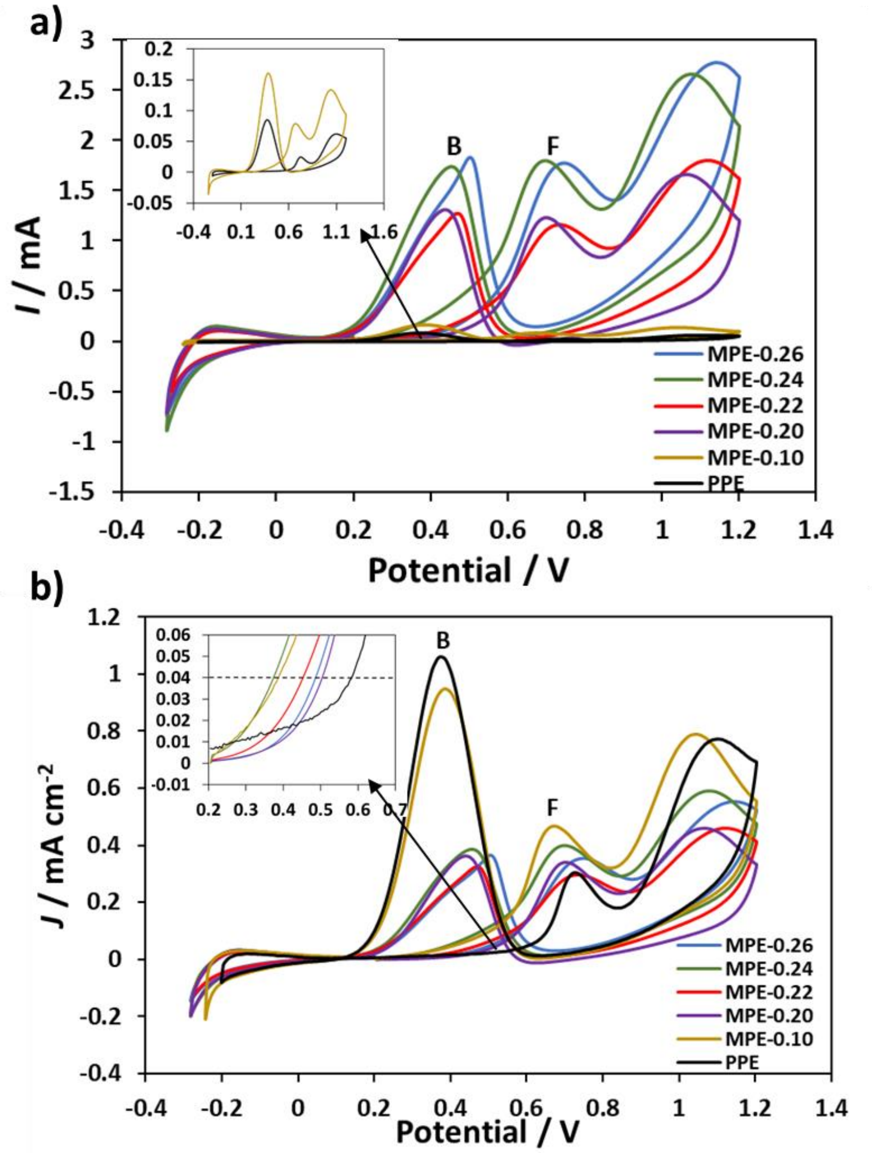

Figure 6.9 Cyclic voltammograms (CVs) in 0.5 M H_2SO_4 + 0.5 M C_2H_5OH solution a) current (I) and b) current density calculated from the RSA (J) recorded at room temperature at a scan rate for 50 mV s^{-1} of the polished platinum electrode (PPE) and mesoporous platinum electrodes (MPEs) deposited from the BCC $_{F127}$ at different potentials, MPE-0.10, MPE-0.20, MPE-0.22, MPE-0.24 and MPE-0.26. The insert in a) exhibits the CV of the PPE and MPE-0.10 and b) the magnification of the plot and the horizontal dotted line shows the J for the onset potential (E_{onset}). The forward and backward peaks are illustrated by F and B in the plot.

Figure 6.9 a) indicates the CVs for ethanol oxidation in terms of I for the MPEs and PPE. The CVs show that I_F and I_B increase with an increase of the RF value for the MPEs. Since the MPE- 0.24 and MPE-0.26 have similar RF values, they show similar values of I_F and I_B. Also, similar behaviours of I_F and I_B are observed for MPE-0.20 and MPE-0.22.

Figure 6.9 b) shows the CVs for ethanol oxidation in terms of J for the MPEs and PPE. The CVs reveal that as the RF value for the MPEs increases, both the J_F and J_B decrease. The MPE- 0.10 with the smallest RF (5) indicates the highest J_F and J_B values. Moreover, the insert plot shows that the corresponding peak F potential moves to lower voltages for the MPEs compared to PPE, suggesting faster reaction kinetics towards ethanol oxidation. Additional analysis of catalytic activity, the J_F and J_B ratio and E_{onset} evaluated from the CVs in Figure 6.9 a) and Figure 6.9 b),is shown in Table 6.9.

Table 6.9 The catalytic activity of the polished platinum electrode (PPE) and mesoporous platinum electrodes (MPEs) (cross-sectional area = 3.142 x 10^{-2} cm^2) deposited from the BCC$_{F127}$ at different voltages towards the ethanol oxidation in terms of current (I) and current density (J). The I_F indicates forward peak in current, I_B means backward peak in current, the J_F means forward peak in current density, and the J_B means backward peak in current density. Onset potential (E_{Onest}) means the magnitude potential at J_F 0.04 mA cm^{-2}.

Electrode	RF	I_F / mA	I_B / mA	J_F / mA cm^{-2}	J_B / mA cm^{-2}	J_F / J_B	E_{Onest} / V
PP	**2.5**	0.02	0.084	0.25	1.05	0.24	0.58
MPE -0.10	**5**	0.08	0.16	0.47	0.94	0.50	0.39
MPE -0.20	**115**	1.23	1.30	0.34	0.36	0.95	0.50
MPE -0.22	**126**	1.15	1.23	0.29	0.32	0.93	0.45
MPE -0.24	**144**	1.79	1.70	0.40	0.38	1.05	0.37
MPE-0.26	**153**	1.77	1.83	0.35	0.37	0.97	0.48

Table 6.9 shows that the I_F and I_B for the MPEs increase with the increase of RF, and the highest values are observed for MPE-0.26 and MPE-0.24. In contrast, the J_F and J_B values increase with the decrease of RF and the highest values are observed for MPE-0.10. This behaviour is similar

to the previous chapters that exhibited a decrease in J_F and J_B values with increasing RF values, possibly due to the fast reaction of ethanol oxidation at the electrodes' surface.

Table 6.9 reveals that the J_F/J_B show an increase with the increase of the RF value, and the highest value is observed for MPE-0.24 (1.05). This increase in the J_F/J_B indicates higher CO tolerance, while the low J_F/J_B for PPE indicates poor ethanol oxidation to the final product.[113] This confirms that the MPEs have better catalytic performance than PPE due to the greater number of accessible platinum sites. Moreover, the E_{onset} also proves the improved electrocatalytic activity, showing lower values for the MPEs compared to PPE. The smallest E_{onset} value is observed for MPE-0.24 (0.37 V), which exhibits the easy oxidation of ethanol. The trends for ethanol oxidation agree with the MPEs fabricated from the $FCC_{Brij^{®}\ 58}$ and the $BCC_{Brij^{®}\ 58}$ in chapters 4 and 5.

The long-term stability of the MPEs and PPE was conducted using CV over 100 cycles in 0.5 M H_2SO_4 + 0.5 M C_2H_5OH solution at a scan rate of 50 mV s^{-1}. Subsequently, the J_F was compared every 20 cycles, as shown in the histograms in Figure 6.10.

Figure 6.10 a) reveals the stability of PPE over 100 CVs towards ethanol oxidation. An increase in the J_F happens for the initial 20 cycles (shown in green), and then a decline in J_F occurs until the 100th cycle, showing only 38% of the first scan.

Figure 6.10 b-f) demonstrate the stability towards ethanol oxidation for MPE-0.10, MPE-0.20, MPE-0.22, MPE-0.24 and MPE-0.26, respectively. The results show good stability compared to the PPE. The highest stability was observed for MPE-0.20, which shows an increase in J_F over the 100 CVs, showing 128% of the first scan.

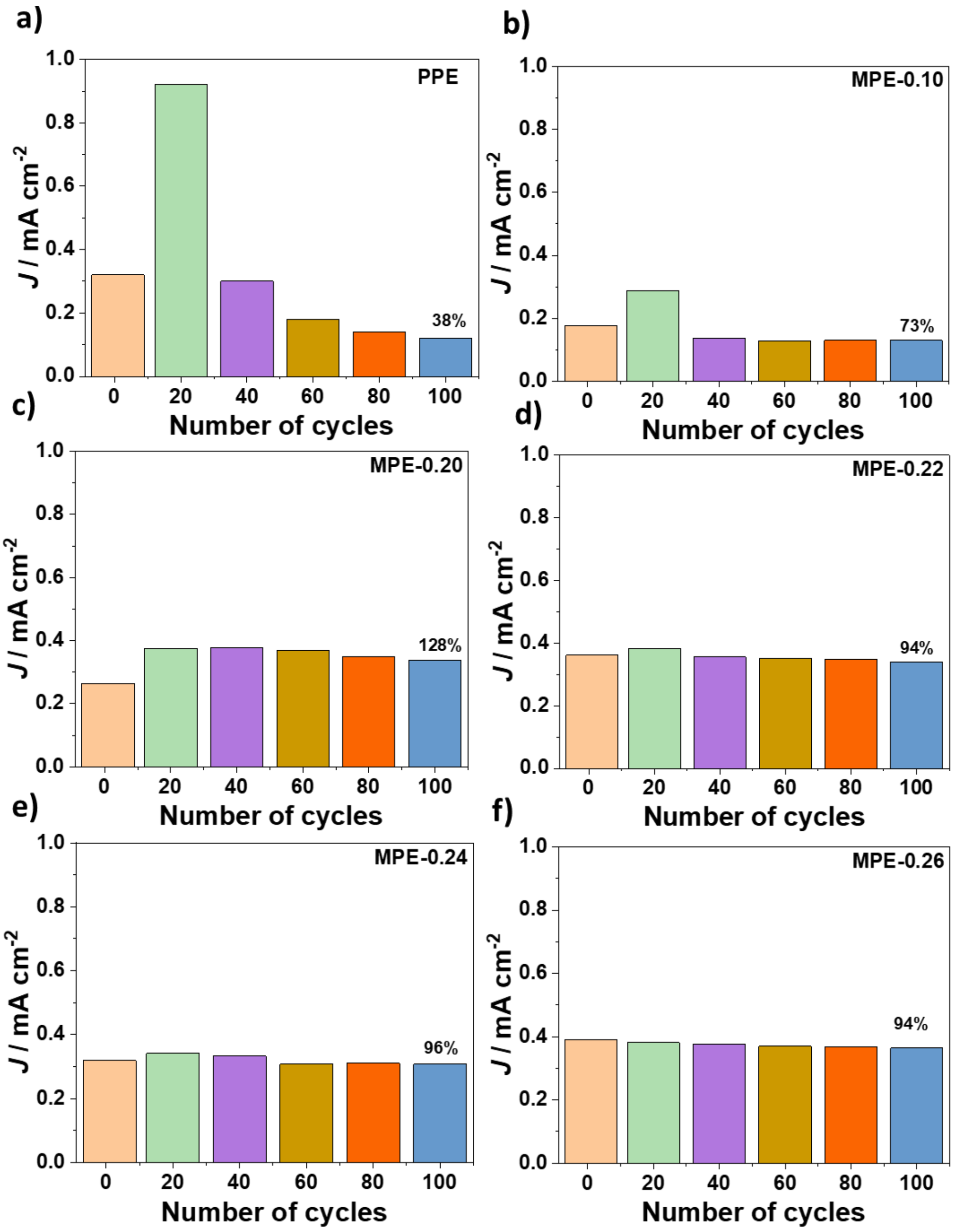

Figure 6.10 Histograms show the stability for J_F over 100 CVs towards ethanol oxidation for a) polished platinum electrode (PPE) and mesoporous platinum electrodes (MPEs) fabricated from the BCC $_{F127}$ with different deposition potentials at b) MPE-0.10, c) MPE-0.20, d) MPE-0.22 V, e) MPE-0.24 and f) MPE-0.26. Each colour indicates the number of cycles, and the stability factor (%) calculated by comparing J_{F100th} to J_{F1st}.

EIS in ethanol under acidic media - The MPEs were cleaned electrochemically using CV in 0.5 M H_2SO_4 solution. This step was taken to eliminate any impurities from the surface of the electrodes. Subsequently, EIS was carried out in 0.5 M H_2SO_4 + 0.5 M C_2H_5OH at a constant applied potential of 0.4 V. The 0.4 V is just above the E_{onset}, and when comparing the CVs in acid and ethanol, it became evident that ethanol oxidation occurs at this voltage. This was concluded by the noticeable increase in current detected in the CV for ethanol compared to that obtained in the acid. The Nyquist plots of all the MPEs at 0.4 V are shown in Figure 6.11.

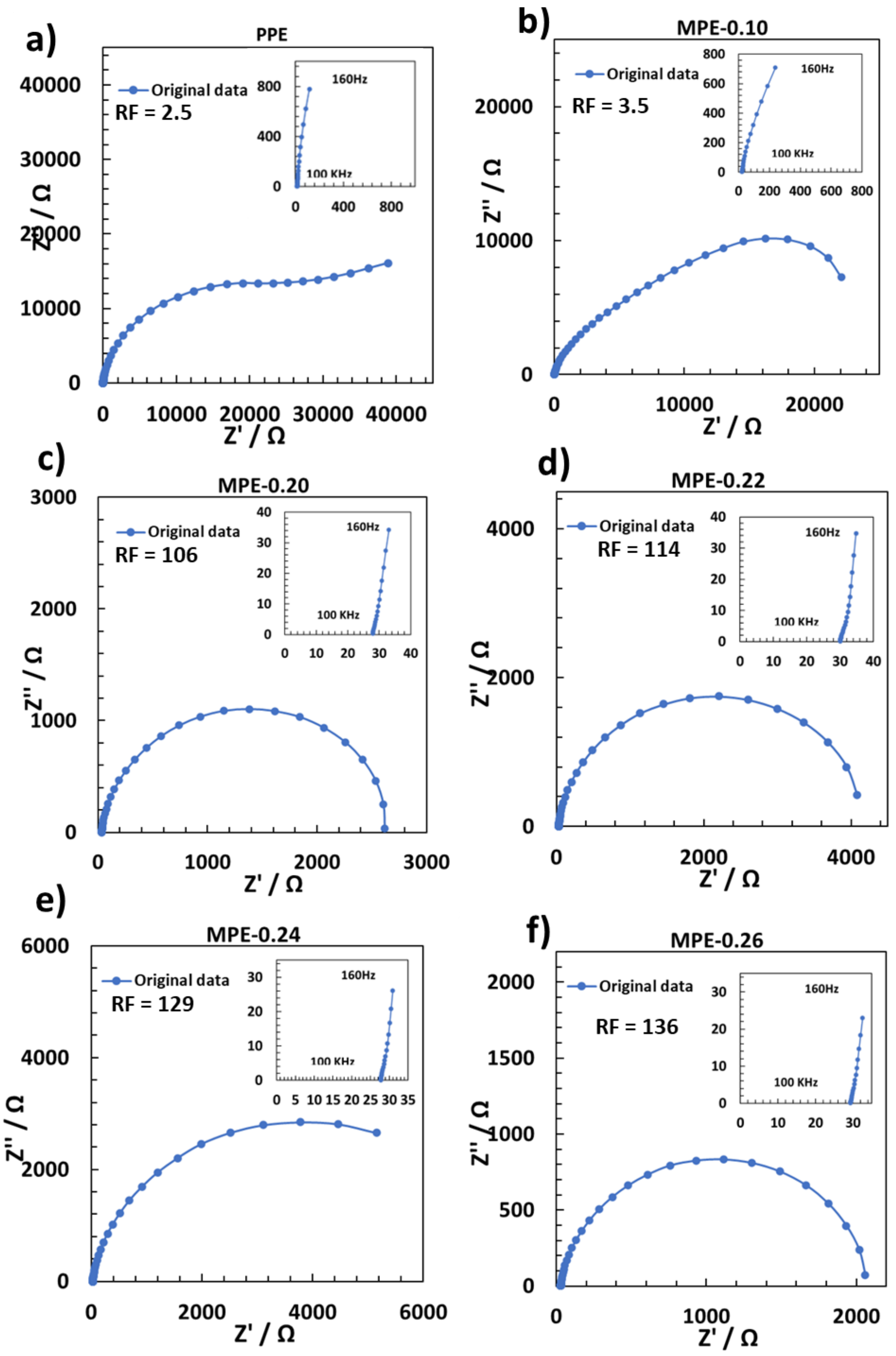

Figure 6.11 The electrochemical impedance spectroscopies in 0.5 M H_2SO_4 + 0.5 M C_2H_5OH solution at a fixed potential of 0.40 V and at frequencies from 100 KHz to 0.2 Hz for different electrodes. a)PPE and mesoporous platinum electrodes (MPEs) deposited from the BCC_{F127} at different potentials, b) MPE-0.10, c) MPE-0.20, d) MPE-0.22, e) MPE -0.24, and f) MPE-0.26. The insert plots show the impedance at higher frequencies, from 100 KHz to 160 Hz.

Figure 6.11 a) reveals the Nyquist plot for the PPE at 0.4 V, which indicates a large impedance value with a semicircle at the middle frequencies. The insert plot reveals the impedance at higher frequencies from 160 Hz to 100 KHz that reveal the near-vertical slope with slight curvature as the frequncy decreases. This behaviour is in agreement with the polished electrode behaviour in dilute acid reported by Elliott *et al.*[114] Interestingly, the Nyquist plot for MPE-0.10, which has the lowest RF, shows evidence for two semicircles, as illustrated in Figure 6.11 b). This observation suggests the possibility of an additional adsorption process occurring at different rate on these smaller area electrodes, which shows more prompt poisoning than larger area electrodes. Additionally, the insert plot for the impedance at high frequencies reveals behaviour similar to PPE.

Figure 6.11 c-f) indicate the Nyquist plots for the MPE-0.20, MPE-0.22, MPE-0.24 and MPE- 0.26, respectively. Interestingly, these MPEs show similar behaviour to one another, indicating a semicircle in a clockwise direction. The impedance values for these MPEs are much lower than the PPE and MPE-0.10 due to higher RF. Moreover, the insert plots show that the impedance at higher frequencies, from 160 Hz to 100 KHz, reveals a slope $>$ 45° line at higher frequencies, transforming into a nearly vertical line.[117] This behaviour is similar to the impedance data for the MPEs fabricated from the $\mathrm{FCC}_{\mathrm{Brij®}\ 58}$ as shown in Chapter 4. This behaviour differs from the model of hexagonal mesoporous electrodes in dilute acid by De Levie, which showed a Warburg impedance region with a slope of 45° at high frequency.[114,117,119] This variation from the standard Warburg model is due to the different pore shapes as explained by Cooper *et al.*[160] They reported that the pore shape affects the mid and high-frequency range, and the Warburg element with a phase $>$ 45° appeared for the porous geometries with a narrow opening.

These impedance data, presented in Nyquist plots, displayed distinctive features that prompted the application of circuit modelling for a more comprehensive understanding. As the PPE revealed a nearly vertical line for Warburg impedance at the low frequencies, the Randel circuit was chosen for fitting to the experimental data. The MPEs here show the best fitting to circuit model R(RQ) circuits that feature Q, describing the complexities of the electrode-electrolyte interface.[117] However, the presence of two semicircles for MPE-0.10 requires the addition of another R and Q to the R(RQ) circuit to make R(RQ)(RQ). The physical meaning of these circuits lies in their ability to capture the behaviour of the electrode-electrolyte interface, where the resistors and constant phase elements represent the various processes involved, such as solution resistance, charge transfer and Warburg Impedance (Z_w). The Z_w represents the diffusion of ions in the electrolyte towards the electrode surface. The description of these circuits is demonstrated in Chapter 2 and 4, and the Randel circuits for PPE R(RQ) and R(RQ)(RQ) circuits for the MPEs are shown in Figure 6.12.

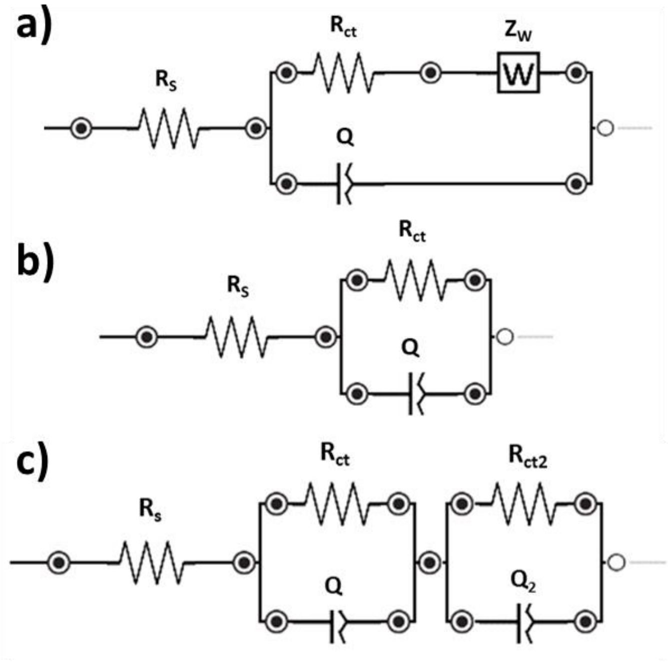

Figure 6.12 a) Randel circuit for the PPE, b) R(RQ) circuit for MPEs and R(RQ)(RQ) circuit for MPE-0.10.

The selection of the suitable model circuit was chosen to achieve good agreement with the experimental data as evidence by small x^2 values.[120] On this basis the chosen impedance model data are overlayed on the EIS data and are shown in Figure 6.13.

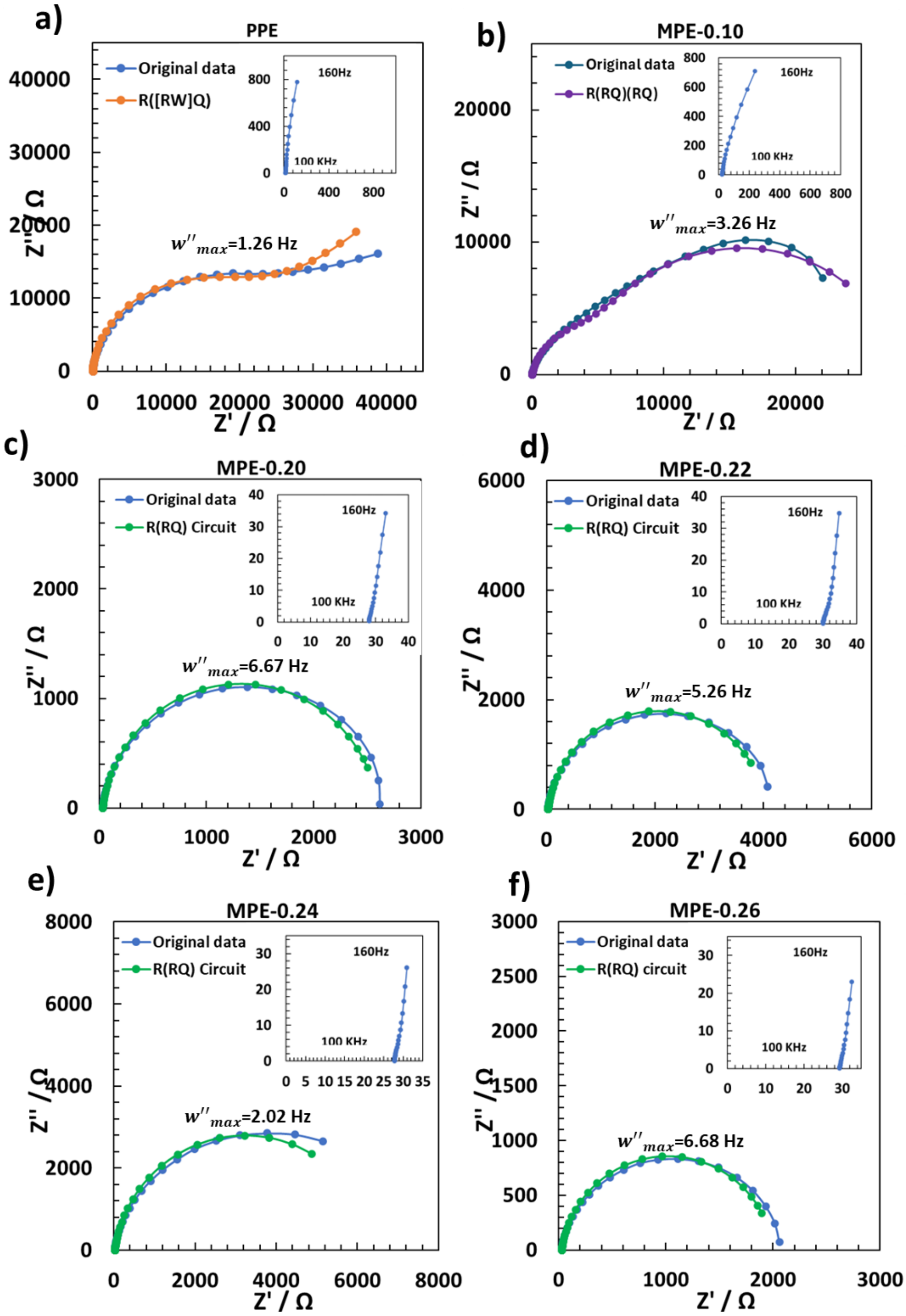

Figure 6.13 The chosen fits overlaid on the electrochemical impedance spectroscopies in 0.5 M H_2SO_4 + 0.5 M C_2H_5OH solution at a fixed potential of 0.40 V. The frequency range was 100 kHz to 0.2 Hz. a)PPE and mesoporous platinum electrodes (MPEs) deposited from the BCC_{F127} at different potentials, b) MPE-0.10, c) MPE-0.20, d) MPE-0.22, e) MPE -0.24, and f) MPE-0.26. The frequency of maximum imaginary impedance Z'' (w''$_{max}$) is shown in the plots.

Figure 6.13 a) represents the impedance spectra for the PPE that matches the Randel circuit, which is indicated by the small value of x^2. Figure 6.13 b) for MPE-0.10 indicates the agreement of the impedance data to the R(RQ)(RQ) circuit, which is indicated by x^2 (0.0028) (shown in Table 4.9). The two semicircles, almost appearing as one semicircle, could be due to the presence of different adsorption processes and the close time constants of the two separate processes, leading to the merging of the two semicircles.[117]

Figure 6.13 c-f) show the Nyquist plots for the MPE-0.20, MPE-0.22, MPE-0.24 and MPE-0.26, respectively. These plots show the same behaviour, and the successful integration of the R(RQ) circuit was evident as the fitted impedance spectra closely aligned with the EIS data with small x^2 values (shown in Table 4.9).

The analysis of the EIS using the R(RQ) and Randel circuits shows some key parameters are shown in Table 6.10.

Table 6.10 The RF, solution resistance (R_s), charge transfer resistance (R_{ct}) and (R_{ct2}), Warburg diffusion element (Z_W), pre-exponent term (Y_0 and (Y_0), exponent term (n) and (n_2), double layer capacitance(C_{dl}) and chi-squared (x^2) for PPE and the MPEs deposited from the BCC_{F127} at different potentials.

Electrode	RF	R_s /Ω	R_{ct} /Ω	Z_W/σ	Y_0/ s^n $Ω^{-1}$	n / ϕ	C_{dl} / F	x^2
PPE	2.5	14	21940	1.91×10^{-4}	1.73×10^{-6}	0.954	1.71×10^{-6}	0.0014
MPE-0.10	3.5	21	R_{ct}= 23960 R_{ct2}=4373	--	Y_0=1.63×10^{-5} Y_{02}=4.10×10^{-6}	n= 0.842 n_2=0.893	1.13×10^{-5}	0.0028
MPE-0.20	106	34	2572	--	4.82×10^{-5}	0.920	4.14×10^{-5}	0.0011
MPE-0.22	114	30	4043	--	4.69×10^{-5}	0.924	4.14×10^{-5}	0.0010
MPE-0.24	129	28	6406	--	6.61×10^{-5}	0.913	6.22×10^{-5}	0.0009
MPE-0.26	136	29	1978	--	7.66×10^{-5}	0.911	6.47×10^{-5}	0.0013

Table 6.10 shows larger R_s for the MPEs with higher RF than MPE-0.10 with RF of 3.5 and PPE. This increase in the R_s for the MPEs with high RF could be due to the position of the working

electrode to the reference electrode. Conversely, the MPEs with high RF reveal smaller R_{ct} than PPE, which suggests a more efficient and faster reaction due to more pathways for charge transfer. The lowest R_{ct} (1978) was observed for the MPE-0.26, which has the highest RF and, therefore, more active sites that may facilitate the reaction. The MPEs with higher RF exhibit higher Y_0 values than PPE, and these values with *n* and w''_{max} (shown in the plot from Figure 6.13) were used to calculate C_{dl} utilising Equation 2.9 (shown in Chapter 2). The C_{dl} show larger values for the MPEs compared to PPE, suggesting enhanced capacitance linked to the higher RF and expanded surface area. Conversely, the PPE exhibits a diminished Y_0 value, suggesting reduced capacitance. It should be noted that Equation 2.9 is applied to the R(RQ) circuits, and since the PPE and MPE-0.10 reveal different circuits, this might introduce inaccurate data for the C_{dl}.

6.4 Conclusion

This chapter reported the phase behaviour of F127 in water, which agrees with previous reports in the literature. As the composition increased from 30 wt% to 80 wt% of F127 in the water system, a sequence of the phase transitions was observed: isotropic, BCC, BCC + $\mathrm{H_I}$ and $\mathrm{H_I}$ + $\mathrm{L_\propto}$ phases. On the other hand, the investigation of the presence of HCPA indicated an enhancement in the peak intensity and favoured highly curved structures such as the BCC and $\mathrm{H_I}$ phase. With an increase in the wt% composition, the phase transitions moved through a series of BCC, $\mathrm{H_I}$ and $\mathrm{H_I}$ + $\mathrm{L_\propto}$ phases in the presence of HCPA. The average lattice parameter for the BCC, $\mathrm{H_I}$ and $\mathrm{L_\propto}$ of F127 in water indicated 20.8 nm, 16.6 nm and 18.9 nm, respectively, which are similar to HCPA systems that revealed 19.8 nm, 17.0 nm and 18. 2 nm, respectively.

The feasibility study investigating the use of the BCC structure of 50 wt% F127/HCPA with a_{BCC} (21.1) nm as a template was effective as evidenced by the high passed current (150 µA) observed from the CV.

The successful electrodeposition through the BCC_{F127} template at different potentials exhibited that the rate increased with the decrease of the deposition potential. The SEM analysis demonstrated the coverage of the surface with some spherical particles. The following examination through the TEM revealed the ordered 3D networks of the MPEs with primitive structure and large pore size between 7.8 and 8.2 nm with lattice parameters from 16.4 ± 1.7 to 17.4 ± 0.3 nm. The CV in dilute acid investigation exhibited that RF increased with the decrease in deposition potential. The ECSA value was 1.7 m^2 g^{-1} for MPE-0.10 and increased at other MPEs to show values ranging from 19.6 to 24.5 m^2 g^{-1}. The MPEs showed excellent catalytic activity towards ethanol oxidation in acid media compared to PPE identified by the high J_F/J_B reaching a maximum of 1.05, low E_{onset} with the lowest reaching 0.37 V and long-term stability. The subsequent inspection of the EIS measurements for the MPEs in ethanol in acid media at 0.4 V revealed Warburg impedance at low frequencies for PPE, while the MPEs with high RF showed semicircles in clockwise mode. The Randel circuit model illustrated the fitting to PPE, while the MPEs except MPE-0.10 revealed good fitting to the R(RQ) circuit model indicated by small values of x^2. The MPEs with higher RF demonstrated lower R_{ct}, recommending more efficient electrochemical reactions with increased active sites. MPE-0.26 confirmed the lowest R_{ct}, indicating improved reaction facilitation. The MPEs revealed increased capacitance associated with the expanded area compared to PPE. This suggested great catalytic activity for the MPEs towards ethanol oxidation compared to PPE due to the more platinum sites.

Chapter 7- General conclusion and future work

7.1 Conclusion

In summary, mesoporous platinum films with a high area and ordered 3D network were successfully produced using Brij® 58 and F127 cubic phases as structure-directing agents through LLC templating. The phase behaviour of Brij® 58 and F127 with water along with the influence of HCPA, was successfully investigated. The presence of HCPA induced an increase in the dominance of high curvature phases, such as FCC, BCC, and $\mathrm{H_I}$ phases for both Brij® 58 and F127. Interestingly, for Brij® 58, HCPA created an additional $\mathrm{H_I}$ phase co-existing at lower concentrations alongside FCC and BCC, and it slightly swelled the Brij® 58 micelle and corresponding lattice parameters across different phases. In contrast, the lattice parameter for F127 phases remained similar. When the lattice parameters for Brij® 58 and F127 phases were compared the latter were found to be significantly larger.

Interestingly, Brij® 58 with HCPA at concentrations ≥ 30 wt% when heated to 80 ℃ demonstrated chemical reactivity and produced mesoporous platinum nanoparticles. The successful production of these nanoparticles, achieved without conventional reducing agents, suggested a polyol synthesis-like mechanism facilitated by polyethylene glycol in Brij® 58. The polydisperse mesoporous platinum nanoparticles presented lattice parameters from ~ 5.4 to 7.7 nm and diameters ranging from ~ 23 to 57 nm.

The FCC and BCC phases of Brij® 58 and the BCC phase of F127 were utilised as structure-directing agents for platinum electrodeposition at different potentials. The fabricated films demonstrated interesting surface structure and 3D porous cubic morphology. The films produced from $\mathrm{FCC_{Brij^{®}\,58}}$ template demonstrated a diamond-like structure with pores diameters ranging from ~ 3.0 to 3.5 nm and lattice parameters from ~ 6.3 to 7.1 nm. Similar pore diameters and lattice parameter were observed for the films fabricated from $\mathrm{BCC}_{\mathrm{Brij}^{®}\ 58}$ template, but these demonstrated a primitive structure. On the other hand, larger pore diameters ranging from ~7.8 to 8.2 nm and lattice parameter ranging from ~16.4 to 17.4 nm were observed from films created from $\mathrm{BCC}_{\mathrm{F127}}$ with a primitive structure.

The MPEs fabricated from $\mathrm{FCC}_{\mathrm{Brij}^{®}\ 58}$, $\mathrm{BCC}_{\mathrm{Brij}^{®}\ 58}$ and $\mathrm{BCC}_{\mathrm{F127}}$ templates demonstrated maximum ECSA values of 27.6, 22.7 and 24.5 $m^2\ g^{-1}$, respectively. Moreover, the films exhibited excellent catalytic activity towards ethanol oxidation in dilute acid, demonstrating high J_F/J_B ratios, low E_{onset} and good long-term stability. The J_F/J_B ratios reached a maximum of 1.18, 1.38 and 1.05, and minimum E_{onset} values of 0.35, 0.33 and 0.37 V, respectively. The long-term stability also showed encouraging results with maximum stability factors of 109, 104 and 128 %, respectively. The effect of deposition time was also investigated for $\mathrm{BCC}_{\mathrm{Brij}^{®}\ 58}$ template and showed a maximum ECSA value of 31.2 $m^2\ g^{-1}$ and a remarkable stability factor of 396 % for the shortest deposition time.

EIS was found to be a useful technique for examining the catalytic performance, indicated by the ability to model R_{ct} and C_{dl} values and was applied to the MPEs from $\mathrm{FCC}_{\mathrm{Brij}^{®}\ 58}$ and $\mathrm{BCC}_{\mathrm{F127}}$. Different reaction conditions were explored however, all results indicated excellent performance. The R_{ct} represents the ability to catalyse the reaction and smaller values are preferred and were observed. C_{dl} represents the double-layer capacitance and is related to the area of the electrodes. The C_{dl} values demonstrated a maximum value of 7.75×10^{-4} F (at 0.80 V) and 6.47×10^{-5} F (at 0.40 V) for MPEs fabricated from $\mathrm{FCC}_{\mathrm{Brij}^{®}\ 58}$ and $\mathrm{BCC}_{\mathrm{F127}}$, respectively. The varied reaction conditions complicate direct comparisons between the films; however, they collectively support the presence of a large nanostructure area.

7.2 Future work

The exploration of the phase behaviour of Brij® 58 and F127 with HCPA through SAXS at room temperature was examined. However, further investigation into the phase transitions across a wider temperature range would extend the understanding and unveil invaluable insights into the dynamic behaviour of these systems under varying thermal conditions.

The mesoporous platinum nanoparticles with a highly porous structure and different sizes were successfully produced. However, further characterisation is required to obtain the structure, size, electrochemical active surface area, and catalytic activity. This can be performed using different techniques, such as UV–visible spectroscopy, SAXS, Dynamic Light Scattering, CV and EIS.

The fabricated mesoporous platinum films revealed a regular pore structure using TEM analysis. However, further structure confirmation is needed, which can be obtained from different techniques, such as SAXS. Additionally, detailed nucleation and growth studies could provide insights into the deposition mechanism. Moreover, these films could also be used for other catalytic systems.

References

1. Ciesla, U. & Schu, F. Ordered mesoporous materials. *Microporous and Mesoporous Materials* **27**, 131–149 (1999).

2. Everett, D. H. & Koopal, L. K. *International Union of Pure and Applied Chemistry Division of Physical Chemistry Manual of Symbols and Terminology for Physicochemical Quantities and Units Appendix Ii Definitions, Terminology and Symbols in Colloid and Surface Chemistry Part i*. (1971).

3. Yanagisawa, T., Shimizu, T., Kuroda, K. & Kato, C. The preparation of alkyltrimethylammonium-kanemite complexes and their conversion to microporous materials. *Bull Chem Soc Jpn* **63**, 988–992 (1990).

4. Bagshaw, S. A., Prouzet, E. & Pinnavaia, T. J. Templating of mesoporous molecular sieves by nonionic polyethylene oxide surfactants. *Science (1979)* **269**, 1242–1244 (1995).

5. Yang, P., Zhao, D., Margolese, D. I., Chmelka, B. F. & Stucky, G. D. Generalized syntheses of large-pore mesoporous metal oxides with semicrystalline frameworks. *Nature* **396**, 152–155 (1998).

6. Attard, G. S. *et al.* Mesoporous platinum films from lyotropic liquid crystalline phases. *Science (1979)* **278**, 838–840 (1997).

7. Elliott, J. M. *et al.* Nanostructured platinum (HI-ePt) films: Effects of electrodeposition conditions on film properties. *Chemistry of Materials* **11**, 3602–3609 (1999).

8. Akbar, S., Elliott, J. M., Rittman, M. & Squires, A. M. Facile production of ordered 3D platinum nanowire networks with ‘single diamond’ bicontinuous cubic morphology. *Advanced Materials* **25**, 1160–1164 (2013).

9. Asghar, K. A., Elliott, J. M. & Squires, A. M. 2D hexagonal mesoporous platinum films exhibiting biaxial, in-plane pore alignment. *J Mater Chem* **22**, 13311–13317 (2012).

10. Whitehead, A. H., Elliott, J. M. & Owen, J. R. Nanostructured tin for use as a negative electrode material in Li-ion batteries. *J Power Sources* **81**, 33–38 (1999).

11. Meynen, V., Cool, P. & Vansant, E. F. Microporous and Mesoporous Materials Verified syntheses of mesoporous materials. *Microporous and Mesoporous Materials* **125**, 170–223 (2009).

12. Walcarius, A. Mesoporous materials and electrochemistry. *Chem Soc Rev* **42**, 4098–4140 (2013).

13. Suib, S. L. A Review of Recent Developments of Mesoporous Materials. *Chemical Record* **17**, 1169–1183 (2017).

14. Walcarius, A. Mesoporous Materials-Based Electrochemical Sensors. *Electroanalysis* **27**, 1303–1340 (2015).

15. Yamauchi, Y., Suzuki, N., Radhakrishnan, L. & Wang, L. Breakthrough and future: Nanoscale controls of compositions, morphologies, and mesochannel orientations toward advanced mesoporous materials. *Chemical Record* **9**, 321–339 (2010).

16. Yamauchi, Y. & Kuroda, K. Rational design of mesoporous metals and related nanomaterials by a soft-template approach. *Chem Asian J* **3**, 664–676 (2008).

17. Taguchi, A. & Schu, F. *Ordered Mesoporous Materials in Catalysis*. vol. 77 (2005).

18. Bang, J. J., Han, D., Shin, J., Chung, T. D. & Bae, J. H. Selective Enhancement of Electrochemical Signal Based on the Size of Alcohols Using Nanoporous Platinum. *ChemElectroChem* **8**, 2407–2412 (2021).

19. Franceschini, E. A. *et al.* Mesoporous Pt electrocatalyst for methanol tolerant cathodes of DMFC. *Electrochim Acta* **71**, 173–180 (2012).

20. Elliott, J. M., Birkin, P. R., Bartlett, P. N. & Attard, G. S. Platinum Microelectrodes with Unique High Surface Areas. *Langmuir* **15**, 7411–7415 (1999).

21. Franceschini, E. A., Planes, G. A., Williams, F. J., Soler-Illia, G. J. A. A. & Corti, H. R. Mesoporous Pt and Pt/Ru alloy electrocatalysts for methanol oxidation. *J Power Sources* **196**, 1723–1729 (2011).

22. Park, S., Chung, T. D. & Kim, H. C. Nonenzymatic Glucose Detection Using Mesoporous Platinum. **75**, 3046–3049 (2003).

23. Kibsgaard, J., Gorlin, Y., Chen, Z. & Jaramillo, T. F. Meso-structured platinum thin films: Active and stable electrocatalysts for the oxygen reduction reaction. *J Am Chem Soc* **134**, 7758–7765 (2012).

24. Akbar, S., Elliott, J. M., Squires, A. M. & Anwar, A. Optimum conditions for electrochemical deposition of 3-D mesoporous platinum framework. *Journal of Nanoparticle Research* **22**, 1–9 (2020).

25. Akbar, S. *et al.* Control of Pore and Wire Dimensions in Mesoporous Metal Nanowire Networks through Curvature Modulation in Lipid Templates: Implications for Use as Electrodes. *ACS Appl Nano Mater* **4**, 5717–5725 (2021).

26. Akbar, S., Elliott, J. M., Squires, A. M. & Anwar, A. Use of cubic structure with primitive nanochannels for fabrication of free standing 3D nanowire network of Pt with Pm3m symmetry. *Nanotechnology* **33**, 195602 (2022).

27. Wang, L., Nemoto, Y. & Yamauchi, Y. Direct synthesis of spatially-controlled Pt-on-Pd bimetallic nanodendrites with superior electrocatalytic Activity. *J Am Chem Soc* **133**, 9674–9677 (2011).

28. Wang, L. & Yamauchi, Y. Synthesis of mesoporous Pt nanoparticles with uniform particle size from aqueous surfactant solutions toward highly active electrocatalysts. *Chemistry - A European Journal* **17**, 8810–8815 (2011).

29. Tan, H. *et al.* A facile surfactant-assisted synthesis of carbon-supported dendritic Pt nanoparticles with high electrocatalytic performance for the oxygen reduction reaction. *Microporous and Mesoporous Materials* **280**, 1–6 (2019).

30. Zhang, G. *et al.* Porous dendritic platinum nanotubes with extremely high activity and stability for oxygen reduction reaction. *Sci Rep* **3**, 1–8 (2013).

31. Xiong, Y. *et al.* PtAl truncated octahedron nanocrystals for improved formic acid electrooxidation. *Chemical Communications* **54**, 3951–3954 (2018).

32. Moghaddam, R. B. & Pickup, P. G. Support effects on the oxidation of ethanol at Pt nanoparticles. *Electrochim Acta* **65**, 210–215 (2012).

33. Wang, L. & Yamauchi, Y. Block copolymer mediated synthesis of dendritic platinum nanoparticles. *J Am Chem Soc* **131**, 9152–9153 (2009).

34. An, K. & Somorjai, G. A. Size and Shape Control of Metal Nanoparticles for Reaction Selectivity in Catalysis. *ChemCatChem* **4**, 1512–1524 (2012).

35. Quinson, J. & Jensen, K. M. Ø. From platinum atoms in molecules to colloidal nanoparticles: A review on reduction, nucleation and growth mechanisms. *Adv Colloid Interface Sci* **286**, 102300 (2020).

36. Harada, M., Okamoto, K. & Terazima, M. Diffusion of platinum ions and platinum nanoparticles during photoreduction processes using the transient grating method. *Langmuir* **22**, 9142–9149 (2006).

37. Ullah, M. H., Chung, W. S., Kim, I. & Ha, C. S. PH-selective synthesis of monodisperse nanoparticles and 30 dendritic nanoclusters of CTAB-stabilized platinum for electrocatalytic O2 reduction. *Small* **2**, 870–873 (2006).

38. Siani, A., Wigal, K. R., Alexeev, O. S. & Amiridis, M. D. Synthesis and characterization of Pt clusters in aqueous solutions. *J Catal* **257**, 5–15 (2008).

39. Chang, F. C., Li, Y. C., Wu, R. J. & Chen, C. H. Pt-Pd Floating Nanoarrays Templated on Pluronic F127 Micelles as Effective Surface-Enhanced Raman Scattering Sensors. *ACS Appl Nano Mater* **4**, 2515–2524 (2019).

40. Shim, K. *et al.* Synthesis and Cytotoxicity of Dendritic Platinum Nanoparticles with HEK-293 Cells. *Chem Asian J* **12**, 21–26 (2017).

41. Li, C., Imura, M. & Yamauchi, Y. A universal approach to the preparation of colloidal mesoporous platinum nanoparticles with controlled particle sizes in a wide range from 20 nm to 200 nm. *Physical Chemistry Chemical Physics* **16**, 8787–8790 (2014).

42. Wang, Y., Ren, J., Deng, K., Gui, L. & Tang, Y. Preparation of tractable platinum, rhodium, and ruthenium nanoclusters with small particle size in organic media. *Chemistry of Materials* **12**, 1622–1627 (2000).

43. Quinson, J., Kunz, S. & Arenz, M. Surfactant-Free Colloidal Syntheses of Precious Metal Nanoparticles for Improved Catalysts. *ACS Catal* **13**, 4903–4937 (2023).

44. Jeyaraj, M., Gurunathan, S., Qasim, M., Kang, M. H. & Kim, J. H. A comprehensive review on the synthesis, characterization, and biomedical application of platinum nanoparticles. *Nanomaterials* **9**, 1719 (2019).

45. Ryoo, R., Joo, S. H. & Jun, S. Synthesis of highly ordered carbon molecular sieves via template-mediated structural transformation. *Journal of Physical Chemistry B* **103**, 7743–7746 (1999).

46. Jun, S. *et al.* Synthesis of new, nanoporous carbon with hexagonally ordered mesostructure. *J Am Chem Soc* **122**, 10712–10713 (2000).

47. Shin, H. J., Ryoo, R., Liu, Z. & Terasaki, O. Template synthesis of asymmetrically mesostructured platinum networks. *J Am Chem Soc* **123**, 1246–1247 (2001).

48. Malgras, V. *et al.* Nanoarchitectures for Mesoporous Metals. *Advanced Materials* **28**, 993–1010 (2016).

49. Wang, C., Chen, D. & Jiao, X. Lyotropic liquid crystal directed synthesis of nanostructured materials. *Sci Technol Adv Mater* **10**, 023001 (2009).

50. Gollas, B., Elliott, J. M. & Bartlett, P. N. Electrodeposition and properties of nanostructured platinum films studied by quartz crystal impedance measurements at 10 MHz. *Electrochim Acta* **45**, 3711–3724 (2000).

51. Zubimendi, J. L. *et al.* Early stages of platinum electrodeposition on highly oriented pyrolitic graphite: Scanning tunneling microscopy imaging and reaction pathway. *Journal of Physical Chemistry* **97**, 5095–5102 (1993).

52. Bartlett, P. N. *Electrodeposition of Nanostructured Films Using Self-Organizing Templates*. (2004).

53. Chen, S. *et al.* Initial Reaction Mechanism of Platinum Nanoparticle in Methanol-Water System and the Anomalous Catalytic Effect of Water. *Nano Lett* **15**, 5961–5968 (2015).

54. Yamauchi, Y., Momma, T., Yokoshima, T., Kuroda, K. & Osaka, T. Highly ordered mesostructured Ni particles prepared from lyotropic liquid crystals by electroless deposition: The effect of reducing agents on the ordering of mesostructure. *J Mater Chem* **15**, 1987–1994 (2005).

55. Wu, C., Liu, T., Chu, B., Schneider, D. K. & Graziano, V. Characterization of the PEO-PPO-PEO triblock copolymer and its application as a separation medium in capillary electrophoresis. *Macromolecules* **30**, 4574–4583 (1997).

56. Zana, R. Dynamics of Surfactant Self-Assemblies: Micelles, Microemulsions, Vesicles and Lyotropic Phases,. *Surfactant Science* **125**, (2005).

57. Deng, Y., Wei, J., Sun, Z. & Zhao, D. Large-pore ordered mesoporous materials templated from non-Pluronic amphiphilic block copolymers. *Chem Soc Rev* **42**, 4045–4070 (2013).

58. Li, C. *et al.* Self-assembly of block copolymers towards mesoporous materials for energy storage and conversion systems. *Chem Soc Rev* **49**, 4681–4736 (2020).

59. Israelachvili, J. N. & Mitchell, D. J. A model for the packing of lipids in bilayer membranes. *BBA - Biomembranes* (1975) doi:10.1016/0005-2736(75)90381-8.

60. Khalil, R. A. & Zarari, A. H. A. Theoretical estimation of the critical packing parameter of amphiphilic self-assembled aggregates. *Appl Surf Sci* **318**, 85–89 (2014).

61. Stuart, M. C. A. & Boekema, E. J. Two distinct mechanisms of vesicle-to-micelle and micelle-to-vesicle transition are mediated by the packing parameter of phospholipid-detergent systems. *Biochim Biophys Acta Biomembr* **1768**, 2681–2689 (2007).

62. Rosen, M. J. & Kunjappu, J. T. *Surfactants and Interfacial Phenomena: Fourth Edition*. *Surfactants and Interfacial Phenomena: Fourth Edition* (2012).

63. Ghosh, S. Comparative studies on brij reverse micelles prepared in benzene/surfactant/ethylammonium nitrate systems: Effect of head group size

and polarity of the hydrocarbon chain. *J Colloid Interface Sci* **360**, 672–680 (2011).

64. Israelichvili, J. *Intermolecular and Surface Forces: Revised Third Edition*. *Academic Press, New York* (2011).

65. Salim, M., Minamikawa, H., Sugimura, A. & Hashim, R. Amphiphilic designer nano-carriers for controlled release: From drug delivery to diagnostics. *Medchemcomm* **5**, 1602–1618 (2014).

66. Iakimov, N. P. *et al.* Evaluation of critical packing parameter in the series of polytyrosine-PEG amphiphilic copolymers. *Colloid Polym Sci* **299**, 1543–1555 (2021).

67. Impéror-Clerc, M. Three-dimensional periodic complex structures in soft matter: Investigation using scattering methods. *Interface Focus* **2**, 589–601 (2012).

68. Pashley, R. M. & Karaman, M. E. *Applied Colloid and Surface Chemistry*. (J. Wiley, 2004).

69. Al-Saden, A. A., Whateley, T. L. & Florence, A. T. Poloxamer association in aqueous solution. *J Colloid Interface Sci* **90**, 303–309 (1982).

70. Alexandridis, P. & Alan Hatton, T. Poly(ethylene oxide)poly(propylene oxide)poly(ethylene oxide) block copolymer surfactants in aqueous solutions and at interfaces: thermodynamics, structure, dynamics, and modeling. *Colloids Surf A Physicochem Eng Asp* **96**, 1–46 (1995).

71. Asghar, K. A., Rowlands, D. A., Elliott, J. M. & Squires, A. M. Predicting Sizes of Hexagonal and Gyroid Metal Nanostructures from Liquid Crystal Templating. *ACS Nano* **9**, 10970–10978 (2015).

72. Fall, S., Pattier, B., Benyayia, L. & Gibaud, A. Binary phase diagram of water/Brij58 studied by SAXS. *Acta Phys Pol A* **121**, 388–396 (2012).

73. Ecjhao, C. Micellization Studies on Binary Mixture of Methionine with Polyoxyethylene (10) Cetyl Ether (Brij-56) and Polyoxyethylene (20) Cetyl Ether (Brij-58). *J Chem* **7**, 1578–1583 (2010).

74. Jayaraman, A., Zhang, D. Y., Dewing, B. L. & Mahanthappa, M. K. Path-Dependent Preparation of Complex Micelle Packings of a Hydrated Diblock Oligomer. *ACS Cent Sci* **5**, 619–628 (2019).

75. Seddon, J. M. *et al.* Pressure-jump X-ray studies of liquid crystal transitions in lipids. *Philosophical Transactions of the Royal Society A: Mathematical, Physical and Engineering Sciences* **364**, 2635–2655 (2006).

76. Fong, W. K., Hanley, T. L., Thierry, B., Kirby, N. & Boyd, B. J. Plasmonic nanorods provide reversible control over nanostructure of self-assembled drug delivery materials. *Langmuir* **26**, 6136–6139 (2010).

77. Tangso, K. J. *et al.* Novel spiropyran amphiphiles and their application as light-responsive liquid crystalline components. *Journal of Physical Chemistry B* **117**, 10203–10210 (2013).

78. Barauskas, J. & Landh, T. Phase behavior of the phytantriol/water system. *Langmuir* **19**, 9562–9565 (2003).

79. Boyd, B. J., Whittaker, D. V., Khoo, S. M. & Davey, G. Lyotropic liquid crystalline phases formed from glycerate surfactants as sustained release drug delivery systems. *Int J Pharm* **309**, 218–226 (2006).

80. Dong, Y. Da, Larson, I., Hanley, T. & Boyd, B. J. Bulk and dispersed aqueous phase behavior of phytantriol: Effect of vitamin E acetate and F127 polymer on liquid crystal nanostructure. *Langmuir* **22**, 9512–9518 (2006).

81. Alexandridis, P., Ivanova, R. & Lindman, B. Effect of glycols on the self-assembly of amphiphilic block copolymers in water. 2. Glycol location in the microstructure. *Langmuir* **16**, 3676–3689 (2000).

82. Aw, M. S., Gulati, K. & Losic, D. Controlling Drug Release from Titania Nanotube Arrays Using Polymer Nanocarriers and Biopolymer Coating. *J Biomater Nanobiotechnol* **02**, 477–484 (2011).

83. Malmsten, M. & Lindman, B. Self-Assembly in Aqueous Block Copolymer Solutions. *Macromolecules* **25**, 5440–5445 (1992).

84. Rill, R. L., Liu, Y., Winkle, D. H. Van & Locke, B. R. Pluronic copolymer liquid crystals : unique , replaceable media for capillary gel electrophoresis. **817**, 287–295 (1998).

85. Albano, J. M. R., Grillo, D., Facelli, J. C., Ferraro, M. B. & Pickholz, M. Study of the lamellar and micellar phases of pluronic F127: A molecular dynamics approach. *Processes* **7**, 1–11 (2019).

86. Wanka, G., Hoffmann, H. & Ulbricht, W. The aggregation behavior of poly-(oxyethylene)-poly-(oxypropylene)-poly-(oxyethylene)-block-copolymers in aqueous solution. *Colloid Polym Sci* **268**, 101–117 (1990).

87. Wanka, G., Hoffmann, H. & Ulbricht, W. Phase Diagrams and Aggregation Behavior of Poly(oxyethylene)-Poly(oxypropylene)-Poly(oxyethylene) Triblock Copolymers in Aqueous Solutions. *Macromolecules* **27**, 4145–4159 (1994).

88. Jang, H. S., Kim, T. H., Do, C., Lee, M. J. & Choi, S. M. Single-walled carbon nanotube induced re-entrant hexagonal phases in a Pluronic block copolymer system. *Soft Matter* **9**, 3050–3056 (2013).

89. Fierro, J. Metal oxides: chemistry and applications. *Materials* (2005).

90. Jiang, B. *et al.* Layer-by-Layer Motif Architectures: Programmed Electrochemical Syntheses of Multilayer Mesoporous Metallic Films with Uniformly Sized Pores. *Angewandte Chemie* **129**, 7944–7949 (2017).

91. Collinson, M. M. *et al.* Nanoporous Gold Electrodes and Their Applications in Analytical Chemistry. *ISRN Analytical Chemistry* **2013**, (2013).

92. Sun, Y. *et al.* Defects and Interfaces on PtPb Nanoplates Boost Fuel Cell Electrocatalysis. *Small* **14**, 1702259 (2018).

93. Tang, J., Liu, J., Torad, N. L., Kimura, T. & Yamauchi, Y. Tailored design of functional nanoporous carbon materials toward fuel cell applications. *Nano Today* **9**, 305–323 (2014).

94. Yuda, A., Ashok, A. & Kumar, A. A comprehensive and critical review on recent progress in anode catalyst for methanol oxidation reaction. *Catalysis Reviews* **64**, 126–228 (2020).

95. Yaqoob, L., Noor, T. & Iqbal, N. A comprehensive and critical review of the recent progress in electrocatalysts for the ethanol oxidation reaction. *RSC Adv* **11**, 16768–16804 (2021).

96. Vyas, A. N., Saratale, G. D. & Sartale, S. D. Recent developments in nickel based electrocatalysts for ethanol electrooxidation. *Int J Hydrogen Energy* **45**, 5928–5947 (2020).

97. Zheng, Y., Wan, X. & Cheng, X. Advanced Catalytic Materials for Ethanol Oxidation. *Catalysts* **10**, 166 (2020).

98. Han, L., Ju, H. & Xu, Y. Ethanol electro-oxidation: Cyclic voltammetry, electrochemical impedance spectroscopy and galvanostatic oscillation. *Int J Hydrogen Energy* **37**, 15156–15163 (2012).

99. Shen, S. Y., Zhao, T. S. & Wu, Q. X. Product analysis of the ethanol oxidation reaction on palladium-based catalysts in an anion-exchange membrane fuel cell environment. *Int J Hydrogen Energy* **37**, 575–582 (2012).

100. Bai, J., Liu, D., Yang, J. & Chen, Y. Nanocatalysts for Electrocatalytic Oxidation of Ethanol. *ChemSusChem* **12**, 2117–2132 (2019).

101. Shao, M., Peles, A. & Shoemaker, K. Electrocatalysis on platinum nanoparticles: Particle size effect on oxygen reduction reaction activity. *Nano Lett* **11**, 3714–3719 (2011).

102. Akbar, S., Anwar, A., Noon, M. Z. & Elliott, J. M. Platinum as an electrocatalyst : effect of morphological aspects of Pt / Pt-based materials. *Science and Technology,* **35**, 1–11 (2019).

103. Peng, Z. & Yang, H. Designer platinum nanoparticles: Control of shape, composition in alloy, nanostructure and electrocatalytic property. *Nano Today* **4**, 143–164 (2009).

104. Zhu, Y., Bu, L., Shao, Q. & Huang, X. Subnanometer PtRh Nanowire with Alleviated Poisoning Effect and Enhanced C-C Bond Cleavage for Ethanol Oxidation Electrocatalysis. *ACS Catal* **9**, 6607–6612 (2019).

105. Zhu, G., Zhao, Y., Su, L., Qiu, P. & Luo, W. Recent advances on the synthesis of mesoporous metals for electrocatalytic methanol oxidation. *Emergent Mater* **3**, 291–306 (2020).

106. Rogers, J. A., Maznev, A. A., Banet, M. J. & Nelson, K. A. *Electrochemical Methods Fundamentals and Applications*. *Annual Review of Materials Science* vol. 30 (2000).

107. Elgrishi, N. *et al.* A Practical Beginner's Guide to Cyclic Voltammetry. *J Chem Educ* **95**, 197–206 (2018).

108. Agrawal, K., Naik, A. A., Chaudhary, S., Parvatalu, D. & Santhanam, V. Prudent Practices in ex situ Durability Analysis Using Cyclic Voltammetry for Platinum-based Electrocatalysts. *Chem Asian J* **16**, 3311–3325 (2021).

109. Lukaszewski, M., Soszko, M. & Czerwiński, A. Electrochemical methods of real surface area determination of noble metal electrodes - an overview. *Int J Electrochem Sci* **11**, 4442–4469 (2016).

110. Wongbua-ngam, P., Veerasai, W., Wilairat, P. & Kheowan, O. U. Model interpretation of electrochemical behavior of Pt/H2SO4 interface over both the hydrogen oxidation and oxide formation regions. *Int J Hydrogen Energy* **44**, 12108–12117 (2019).

111. Daubinger, P., Kieninger, J., Unmüssig, T. & Urban, G. A. Electrochemical characteristics of nanostructured platinum electrodes-A cyclic voltammetry study. *Physical Chemistry Chemical Physics* **16**, 8392–8399 (2014).

112. Brummer, S. B., Ford, J. I. & Turner, M. J. *The Adsorption and Oxidation of Hydrocarbons on Noble Metal Electrodes. I. Propane Adsorption on Smooth Platinum Electrodes*. (1995).

113. Cheng, C. F. *et al.* Nanoporous gyroid platinum with high catalytic activity from block copolymer templates via electroless plating. *NPG Asia Mater* **7**, e170–e170 (2015).

114. Elliott, J. M. & Owen, J. R. Electrochemical impedance characterisation of a nanostructured (mesoporous) platinum film. *Physical Chemistry Chemical Physics* **2**, 5653–5659 (2000).

115. Bisquert, J. Influence of the boundaries in the impedance of porous film electrodes. *Physical Chemistry Chemical Physics* **2**, 4185–4192 (2000).

116. Park, S., Song, Y. J., Han, J. H., Boo, H. & Chung, T. D. Structural and electrochemical features of 3D nanoporous platinum electrodes. *Electrochim Acta* **55**, 2029–2035 (2010).

117. Srinivasan, R. & Fasmin, F. *An Introduction to Electrochemical Impedance Spectroscopy*. (2021).

118. Padha, B., Verma, S., Mahajan, P. & Arya, S. Electrochemical Impedance Spectroscopy (EIS) Performance Analysis and Challenges in Fuel Cell Applications. *Journal of Electrochemical Science and Technology* **13**, 167–176 (2022).

119. Lazanas, A. C. & Prodromidis, M. I. Electrochemical Impedance Spectroscopy–A Tutorial. *ACS Measurement Science Au* **3**, 162–193 (2023).

120. Laschuk, N. O., Easton, E. B. & Zenkina, O. V. Reducing the resistance for the use of electrochemical impedance spectroscopy analysis in materials chemistry. *RSC Adv* **11**, 27925–27936 (2021).

121. Bhattarai, J. K. *et al.* Electrochemical impedance spectroscopy study of Concanavalin A binding to self-assembled monolayers of mannosides on gold wire electrodes. *Journal of Electroanalytical Chemistry* **780**, 311–320 (2016).

122. Hsu, C. H. & Mansfeld, F. *Technical Note: Concerning the Conversion of the Constant Phase Element Parameter Y 0 into a Capacitance*. *CORROSION SCIENCE SECTION CORROSION* vol. 57 (2001).

123. Wolman, M. Polarized light microscopy as a tool of diagnostic pathology. A review. *Journal of Histochemistry and Cytochemistry* **23**, 21–50 (1975).

124. Frandsen, A. F. *Polarized Light Microscopy*. (2016).

125. Roychoudhuri, C. & Pedrotti, L. Basic Physical Optics. in *Fundamentals of Photonics* (2019).

126. Saadat, Y., Imran, O. Q., Osuji, C. O. & Foudazi, R. Lyotropic liquid crystals as templates for advanced materials. *J Mater Chem A Mater* **9**, 21607–21658 (2021).

127. Attard, G. S., Bartlett, P. N., Coleman, N. R. B., Elliott, J. M. & Owen, J. R. Lyotropic liquid crystalline properties of nonionic surfactant/H2O/hexachloroplatinic acid ternary mixtures used for the production of nanostructured platinum. *Langmuir* **14**, 7340–7342 (1998).

128. Figueiredo Neto, A. M. & Salinas, S. R. A. . *The Physics of Lyotropic Liquid Crystals: Phase Transitions and Structural Properties* vol. 62 (OUP Oxford, 2005).

129. Hamley, I. W. & Castelletto, V. *Small-Angle Scattering of Block Copolymers in the Melt, Solution and Crystal States*. *Progress in Polymer Science* vol. 29 (2004).

130. Robinson, I. Elements of Modern X-ray Physics. 46–66 (2002).

131. Gräwert, M. & Svergun, D. A beginner’s guide to solution small-angle X-ray scattering (SAXS). *Biochemist* **42**, 36–42 (2020).

132. de Jeu, W. H. & de Jeu, W. H. Basic Scattering by Particles. in *Oxford University Press* (2016).

133. Kulkarni, C. V., Wachter, W., Iglesias-Salto, G., Engelskirchen, S. & Ahualli, S. Monoolein: A magic lipid? *Physical Chemistry Chemical Physics* **13**, 3004–3021 (2011).

134. Ermrich, Martin., Opper, Detlef. & PANalytical (Almelo). *XRD for the Analyst : Getting Acquainted with the Principles*. (PANalytical, 2013).

135. Forty, A. J. The use of the scanning electron microscope by J. W. S. Hearle, J. T. Sparrow and P. M. Cross . *J Appl Crystallogr* **7**, 513–514 (1974).

136. Mohammed, A. & Abdullah, A. *Scanning Electron Microscopy (SEM): A Review*. (2018).

137. Zhou, W., Apkarian, R. P., Lin Wang, Z. & Joy, D. *Fundamentals of Scanning Electron Microscopy*.

138. Michler, G. H. *2 Transmission Electron Microscopy: Fundamentals of Methods and Instrumentation*. (2008).

139. Mo, K. & Sellevåg, S. R. *Adsorption and Degradation of Chemical Warfare Agents on Oxides*. (2011).

140. Paredes, J. I., Martínez-Alonso, A. & Tascón, J. M. D. Application of scanning tunneling and atomic force microscopies to the characterization of microporous and mesoporous materials. *Microporous and Mesoporous Materials* **65**, 93–126 (2003).

141. Zeng, C., Vitale-Sullivan, C. & Ma, X. In situ atomic force microscopy studies on nucleation and self-assembly of biogenic and bio-inspired materials. *Minerals* **7**, 158 (2017).

142. Nelson, P. A., Elliott, J. M., Attard, G. S. & Owen, J. R. Mesoporous nickel/nickel oxide - A nanoarchitectured electrode. *Chemistry of Materials* **14**, 524–529 (2002).

143. Ghanem, M. A., Al-Mayouf, A. M., Singh, J. P., Abiti, T. & Marken, F. Mesoporous Nickel/Nickel Hydroxide Catalyst Using Liquid Crystal Template for Ethanol Oxidation in Alkaline Solution. *J Electrochem Soc* **162**, H453–H459 (2015).

144. Shrestha, L. K. *et al.* Nonionic amphiphile nanoarchitectonics: Self-assembly into micelles and lyotropic liquid crystals. *Nanotechnology* **26**, 204002 (2015).

145. Huang, Y. & Gui, S. Factors affecting the structure of lyotropic liquid crystals and the correlation between structure and drug diffusion. *RSC Adv* **8**, 6978–6987 (2018).

146. Shigeta, K., Olsson, U. & Kunieda, H. Correlation between micellar structure and cloud point in long poly(oxyethylene)n oleyl ether systems. *Langmuir* **17**, 4717–4723 (2001).

147. Gharibshahi, E. & Saion, E. Influence of dose on particle size and optical properties of colloidal platinum nanoparticles. *Int J Mol Sci* **13**, 14723–14741 (2012).

148. Tan, H. *et al.* A facile surfactant-assisted synthesis of carbon-supported dendritic Pt nanoparticles with high electrocatalytic performance for the oxygen reduction reaction. *Microporous and Mesoporous Materials* **280**, 1–6 (2019).

149. Lin, C. S., Khan, M. R. & Lin, S. D. The preparation of Pt nanoparticles by methanol and citrate. *J Colloid Interface Sci* **299**, 678–685 (2006).

150. Attard, G. S. *et al.* Mesoporous Platinum Films from Lyotropic Liquid Crystalline Phases. *Science (1979)* **278**, 838–840 (1997).

151. Li, C. *et al.* Self-assembly of block copolymers towards mesoporous materials for energy storage and conversion systems. *Chem Soc Rev* **49**, 4681–4736 (2020).

152. Wang, H. & Yamauchi, Y. Synthesis of mesoporous platinum-palladium alloy films by electrochemical plating in aqueous surfactant solutions. *Chem Asian J* **7**, 2133–2138 (2012).

153. Wang, H. *et al.* Synthesis of mesoporous Pt films with tunable pore sizes from aqueous surfactant solutions. *Chemistry of Materials* **24**, 1591–1598 (2012).

154. Wang, H. *et al.* Electrochemical design of mesoporous Pt-Ru alloy films with various compositions toward superior electrocatalytic performance. *Chemistry - A European Journal* **18**, 13142–13148 (2012).

155. Valentine, C. S., Jayaraman, A., Mahanthappa, M. K. & Walker, L. M. Shear-Modulated Rates of Phase Transitions in Sphere-Forming Diblock Oligomer Lyotropic Liquid Crystals. *ACS Macro Lett* **10**, 538–544 (2021).

156. Georgolios, N., Jannakoudakis, D. & Karabinas, P. Pt electrodeposition on PAN-based carbon fibres. *Journal of Electroanalytical Chemistry* **264**, 235–245 (1989).

157. Goldberg, R. N. & Hepler, L. G. Thermochemistry and oxidation potentials of the platinum group metals and their compounds. *Chem Rev* **68**, 229–252 (1968).

158. Xiang, L. *et al.* Block Copolymer Self-Assembly Directed Synthesis of Porous Materials with Ordered Bicontinuous Structures and Their Potential Applications. *Advanced Materials* **35**, 2207684 (2023).

159. Koper, M. T. M. *Stability Study and Categorization of Electrochemical Oscillators by Impedance Spectroscopy '*. *Journal of Electroanalytical Chemistry* vol. 409 (1996).

160. Cooper, S. J., Bertei, A., Finegan, D. P. & Brandon, N. P. Simulated impedance of diffusion in porous media. *Electrochim Acta* **251**, 681–689 (2017).

161. Ojo, A. A. & Dharmadasa, I. M. Electroplating of semiconductor materials for applications in large area electronics: A review. *Coatings* **8**, 262 (2018).

162. Alexandridis, P. & Hatton, T. A. Poly(ethylene oxide)-poly(propylene oxide)-poly (ethylene oxide) block copolymer surfactants in aqueous solutions and at interfaces: thermodynamics, structure, dynamics, and modeling. *A: Physicochemical and Engineering Aspects* **96**, 46 (1995).

163. Huang, J., Sumpter, B. G. & Meunier, V. Theoretical model for nanoporous carbon supercapacitors. *Angewandte Chemie - International Edition* **47**, 520–524 (2008).

164. Ivanova, R., Lindman, B. & Alexandridis, P. Evolution in structural polymorphism of Pluronic F127 poly(ethylene oxide)-poly(propylene oxide) block copolymer in

ternary systems with water and pharmaceutically acceptable organic solvents: From `glycols’ to `oils’. *Langmuir* **16**, 9058–9069 (2000).

165. Jang, H. S., Kim, T. H., Do, C., Lee, M. J. & Choi, S. M. Single-walled carbon nanotube induced re-entrant hexagonal phases in a Pluronic block copolymer system. *Soft Matter* **9**, 3050–3056 (2013).

166. Desai, P. R., Jain, N. J., Sharma, R. K. & Bahadur, P. Effect of additives on the micellization of PEO/PPO/PEO block copolymer F127 in aqueous solution. *Colloids Surf A Physicochem Eng Asp* **178**, 57–69 (2001).

167. Jiang, B., Li, C., Imura, M., Tang, J. & Yamauchi, Y. Multimetallic Mesoporous Spheres Through Surfactant- Directed Synthesis. *Advanced Science* **2**, 1500112 (2015).

168. Jiang, B. *et al.* Mesoporous Pt nanospheres with designed pore surface as highly active electrocatalyst. *Chem Sci* **7**, 1575–1581 (2016).

169. Franceschini, E. A., Planes, G. A., Williams, F. J., Soler-illia, G. J. A. A. & Corti, H. R. Mesoporous Pt and Pt / Ru alloy electrocatalysts for methanol oxidation. *J Power Sources* **196**, 1723–1729 (2011).

170. Kerkhofs, S. *et al.* Self-Assembly of Pluronic F127 - Silica Spherical Core-Shell Nanoparticles in Cubic Close-Packed Structures. *Chemistry of Materials* **27**, 5161–5169 (2015).

171. Meynen, V., Cool, P. & Vansant, E. F. Verified syntheses of mesoporous materials. *Microporous and Mesoporous Materials* **125**, 170–223 (2009).